UNIVERSITÄT BONN

institut für geowissenschaften METEOROLOGIE

Climate variability and change in the Altai-Dzungarian region and its hydrological impact

Dissertation
zur
Erlangung des Doktorgrades (Dr. rer. nat.)
der
Mathematisch-Naturwissenschaftlichen Fakultät
der
Rheinischen Friedrich-Wilhelms-Universität Bonn

vorgelegt von

Oyunmunkh Byambaa

aus
Selenge (Mongolia)

Bonn, 2023

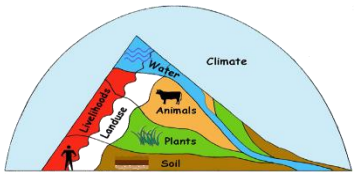

www.watercope.org

IFAD
INTERNATIONAL FUND FOR AGRICULTURAL DEVELOPMENT

This research was carried out as a part of the WATERCOPE project, funded by the International Fund for Agricultural Development (I-R-1284).

Climate variability and change in the Altai-Dzungarian region and its hydrological impact

Dissertation
zur
Erlangung des Doktorgrades (Dr. rer. nat.)
der
Mathematisch-Naturwissenschaftlichen Fakultät
der
Rheinischen Friedrich-Wilhelms-Universität Bonn

vorgelegt von

Oyunmunkh Byambaa

aus
Selenge (Mongolia)

Bonn, 2023

Angefertigt mit Genehmigung der Mathematisch-Naturwissenschaftlichen Fakultät
der Rheinischen Friedrich-Wilhelms-Universität Bonn

Gutachter/Betreuer: Prof. Dr. Clemens Simmer
Gutachter: Prof. Dr. Bernd Diekkrüger

Tag der Promotion: 29. August 2023
Erscheinungsjahr: 2023

ACKNOWLEDGEMENTS

First of all, I would like to express gratitude to Prof. Dr. Andreas Bürkert (University of Kassel) and Prof. Dr. Nergui Soninkhishig (National University of Mongolia), who accepted me to work with an interdisciplinary international research team and provided technical and financial assistance to gather a wonderful experience about the Altai Mountains and the Dzungarian Gobi Desert.

I would like to express my sincere thanks to my supervisor Prof. Dr. Clemens Simmer and co-supervisor Prof. Dr. Bernd Diekkrüger for their professional guidance and experienced support in my work. I also appreciated their warm welcome and their support whenever I need professional instruction.

I sincerely thank to PD Dr. Stef Weijers for his guidance in dendrochronology, his instructive advice, and reviewing parts of my work. I also thank Dr. Michael Russel for his proof-reading my dissertation and fruitful comments.

My special thanks go to Prof. Dr. Jörg Löffler (University of Bonn), Prof. Dr. Baatarbileg Nachin and Mrs. Suran Byambagerel (Tree Ring Laboratory of the National University of Mongolia) for their technical support and advice.

In addition, I am so grateful to Dr. Nyambayar Dashzeveg, Dr. Sven Gönster-Jordan, local administration and driver for their support during field work. I also thank Michael Frerkes, Frederik Kurzrock, Tuvshinbayar and Gantumur Batbold for field sampling, Sainbayar Gombo for assisting in laboratory work and Caroline Leland for her advice on analysis and references.

Furthermore, special thanks go to Mrs. Annemarie Debus and Dr. Insa Thiele-Eich (Institute of Geosciences, Section Meteorology) for their help with my documents and staying in Bonn. Also, thanks to my friends in Bonn, Mrs Munkhzul Baramsai (Mongolei Zentrum Bonn), Carsten Friede and his wife Munkhzul and Mrs. Bayardulam who shared pleasant and memorable time with me.

Finally, I express my deep thanks to my daughter and husband, Gerelmaa and Otgonbaatar, and my lovely mother Narantsetseg for their patience and unconditional support. In my mind, I always thank my lovely dad for his encouragement and support in my achievements even though he could not see the end of this exciting journey in my life.

TABLE OF CONTENTS

Summary

The southern Altai Mountain range and the Dzungarian semi-desert basin, located in a transition zone from the East to the Central Asian region, are characterized by semi-arid continental climate conditions with high intra-annual and diurnal temperature variation and unevenly distributed precipitation due to the orographic effect. Rivers of the Altai Mountains are recharged primarily by meltwater from glaciers and snow (51-63%), followed by rainfall (3-17%) and groundwater (31-40%).

The Sixth Assessment Report of the Intergovernmental Panel on Climate Change (2022) highlights that temperature has increased rapidly in recent decades, and seasonal weather patterns have changed in the mountain regions. Moreover, the warming rate is higher in drylands than in humid areas. Thus, the semi-arid Altai-Dzungarian region is highly sensitive to climate change.

Warming summer temperatures since the 1980s have resulted in an accelerated glacier recession in the Altai Mountains. The highest acceleration of glacier recession occurred from 1990 to 2000, followed by a period from 2010 to 2016; thus, the glacier contribution to total runoff decreased. Moreover, accumulated snow depth during the previous winter influences the high flows of the rivers in the southern Altai Mountains. From 1975 to 2007, warm winters reduced the duration of the snow cover in the Bulgan catchment, and the snow-to-rain ratio rapidly decreased in the southern Altai Mountains from 2000 to 2016.

As a result of the shortening of the freezing period, the ground temperature has increased at a rate of 0.15-0.18°C per decade in the Mongolian Altai Mountains since the 1980s. This has led to permafrost degradation and thickening of the active layer, increasing the water storage capacity. Increased groundwater storage has triggered an increase in winter baseflow in high-latitude permafrost regions, such as in the river basin in northwestern China in the 1990s. The end result of the consecutive warm years has been an acceleration in the regional hydrological cycle since the 1980s.

The World Meteorological Organization emphasizes that human-induced warming is more extensive than the annual variation of the global average triggered by naturally occurring climate drivers. As the effect of global warming differs region by region, understanding long-term regional climate variation and climate drivers is vital in interpreting the worldwide warming and future water availability in Asia. The Bulgan River in the semi-arid Altai-Dzungarian region is a transboundary water resource for irrigated agricultural production and mountain pastoralism in western Mongolia and northwestern China. The observed hydrological impacts of climate change in the Altai Mountains might lead to water shortage for livelihood security and agriculture in the Altai-Dzungarian region in the future.

This thesis aims to better understand long-term climate variability and change over the Altai-Dzungarian region and the hydrological impact of observed and future climate change on water availability and timing for this semi-arid region. This study answered the following three research questions.

Question 1: How has regional climate varied over the Altai-Dzungarian region during and after the Little Ice Age?

Question 2: How did the observed climate change impact the Bulgan River in the southern Altai Mountains between 1985 and 2015?

Question 3: How will future climate change influence the hydrological regime of the Bulgan River for the period of 2030-2050?

Climate variation over the Altai-Dzungarian region during and after the Little Ice Age

Long-term instrumental observations do not exist in desert and mountain areas; therefore, a climate proxy based on undisturbed tree rings in the Altai Mountains was used in the estimation of long-term climate variability and change of the Altai-Dzungarian region back to the Little Ice Age.

This study determined long-term (>400 years) climate variation over the Altai-Dzungarian region by reconstructing the longest time series of (611 years) temperature and (444 years) precipitation from tree-ring proxies. At upper and lower tree lines in the southwestern Mongolian Altai, 77 Larix sibirica Ledeb. trees were sampled, and temperature and precipitation were reconstructed. Based on tree ring-width chronologies, mean June-July air temperatures and June-December precipitation were reconstructed for the periods 1402-2012 and 1569-2012, respectively. These time frames extended the periods presented in previous studies from this area by 168 years for temperature and 191 years for precipitation.

The temperature and precipitation reconstructions explained 39.7% and 41.3% of the station observation variance during the periods 1977-2012 and 1963-2012, respectively. The precipitation reconstruction shows alternating extreme wet and dry conditions during the Little Ice Age (1580-1874), followed by more stable conditions until a late 20th century wetting. The temperature reconstruction shows cooler periods related to volcanic and low solar activities during the Little Ice Age, followed by a warm period in the 20th century, which was interrupted by two short cold periods.

Long-term climate variation and change over the Altai-Dzungarian region were inferred from the analysis of the combined temperature and precipitation reconstructions for the common period 1580-2012. Although this region has warmed since 1875, a positive phase of the Arctic Oscillation might have caused a late 20th-century cool and wet period by strengthening westerly winds in addition to volcanic-induced cooling over the Altai-Dzungarian region.

Moreover, cooling in the 1950s to the 1990s also found in previous temperature reconstructions from the Altai Mountains contrasts with a continuous 20th-century warming of the mean Northern Hemisphere.

The Altai-Dzungarian region is located at the junction between the North Atlantic climate system to the west and the Pacific climate system to the east. Various atmospheric circulation systems influence the regional climate. We analyzed relation of the reconstructed summer temperature and precipitation with the North Atlantic Oscillation (NAO), the Arctic Oscillation (AO), and the El Niño-Southern Oscillation on interannual and interdecadal time scales considering wind-induced interannual variation of the ocean surface condition and interdecadal changes in the oceans' heat storage and transport.

On the interannual time scale, prominent positive winter NAO ($r=-0.31$, $p<0.05$) and AO ($r=-0.32$, $p<0.05$) indices brought cool-wet summers in the Altai-Dzungarian region for the period 1960-2012 due to the northward shift of the polar jet and the intensified westerlies; in contrast, on the interdecadal time scale, the identified cool and wet summers more strongly correlated with negative April NAO (0.69 for cold temperature) and negative July NAO ($r=-0.65$ for more precipitation) than winter NAO ($r=-0.53$ for temperature and $r=0.44$ for precipitation) for 1900-2012. Moreover, summer July AO correlated only with precipitation ($r=-0.38$); however, positive winter AO strongly correlated with cool ($r=-0.72$) and wet ($r=0.41$) summer conditions over the Altai-Dzungarian region on the interdecadal time scale. Furthermore, positive preceding autumn - early winter NINO3.4 induced cool summer temperatures, and a positive summer NINO3.4 led to high precipitation over the Altai-Dzungarian region on the interdecadal time scale. This can be related to wet air transport from the tropical Indian Ocean with the southwesterly winds to Central Asia and southward shifts of the subtropical westerly jet.

Many studies have investigated the most prominent NAO and AO patterns in winter. They proposed a delayed influence of the winter NAO and AO on climate over East Asia. A few studies on summer NAO also found that a negative summer NAO brings cooler and wetter conditions over northwest China but warm and dry conditions over northwest and central Mongolia, and northeast China. Also, the summer AO was found to be negatively correlated with the West Asian subtropical westerly winds that enhance westerly flow over northwestern China.

Besides, we found sign and strength changes in interannual teleconnections of the prevailing natural climate drivers to the regional climate from 1900 to 2012. The significant inflection points of the teleconnections in the 1970s and late 1990s coincided with the beginning and end of the recent cool-wet period. In the late 1970, previous studies have also found the

same sign and strength changes in teleconnections between summer NAO and air temperatures of Middle East Asia related to the shift of the summer NAO mode from more westward to more eastward. Also, the NINO3.4-drought connection in Xinjiang significantly strengthened in 1997.

Our study added value to previous studies on teleconnections by suggesting changes in the strength of teleconnections of climate drivers characterizing the Altai-Dzungarian region on the longer time scales using the reconstructed temperature and precipitation from the tree-ring proxies.

Hydrological response of the Bulgan River to climate change in the southern Altai Mountains in the period 1985-2015

Climate and hydrological observations in the Bulgan catchment started in 1977 and 1984, respectively. During 1984-2015, a warming of 2.1°C and a decrease of 20% in annual precipitation was observed at stations. Autumn precipitation significantly decreased by 46% in the mountains and by 89% in the desert area; however, winter precipitation insignificantly increased by 21% in the mountains and by 25% in the desert area. Also, summer precipitation insignificantly declined by 10% over the same period. The reference ET_0 increased by 20% in winter but only by 6% in summer due to a decrease in summer ET_0 after a moderate upward trend that occurred until the mid-2000s.

The Altai Mountains' climate stations are sparse and all located in the valley; thus, we evaluated the interpolated APHRODITE dataset (0.25ºx0.25º) in our climate impact study. Compared to two available climate stations in the Bulgan catchment, the interpolated APHRODITE dataset slightly underestimates temperature and precipitation amounts over the southern Altai Mountains but overestimates precipitation for the desert area; so these biases are corrected for the hydrological simulations.

According to our developed regression models, the driving climate factors in the hydrological regime of the Bulgan River in the southern Altai Mountains are identified as accumulated snow amount from late autumn through winter and summer rainfall and temperature. As a result of a decrease in precipitation in summer and autumn, and an increase in summer temperature, annual discharges decreased by 34% at the upstream gauge and 20% at the downstream gauge for the period 1984-2015. In contrast, the winter discharge of the Bulgan River increased by 87% at the upstream area related to the increasing in July temperature. The same increase in the winter discharge has been observed in other high mountain permafrost regions and northwestern China, related to an increase in groundwater recharge to baseflow due to permafrost degradation and an increased soil storage capacity rather than glacier melt.

It is likely that the increase in baseflow has influenced river ice formation and break-up. The cold period from river ice formation to break-up was shortened by 33 days between 1984 and 2007, and the maximum water temperature of the Bulgan River increased by 1.4°C at the upstream and 6.9°C at the downstream gauges.

Changes in seasonal runoff and water balance of the Bulgan catchment in response to observed climate change were estimated by the rainfall-runoff HBV-Light model. Compared to the calibration period of 1985-2005, the simulated water balance of the Bulgan catchment in the validation period of 2006-2015 showed that river runoff declined by 17% and water storage decreased by 38% as a result of a decrease in total precipitation by 11% and an increase in potential evapotranspiration by 4%. Between 1985 and 2015, contributions of rain and snow to the annual runoff decreased by 36% and 51%, respectively. In contrast, glacier input to the annual runoff increased by 78% at $p<0.5$.

To include the seasonal thaw of the permafrost and glaciers in the hydrological simulation of the Bulgan catchment, we added a delayed response function and glacier variant to the standard model structure of the HBV model. Our attempt to conceptualize the permafrost condition of the Bulgan catchment with a delay response function in the model much improved the baseflow simulation of the Bulgan River, which was unsatisfactorily simulated by the SWAT model developed for water use in the irrigated downstream area of the Bulgan catchment.

Although our model efficiency was good (0.69) with a low absolute error of 7.6%, the high flows of the Bulgan River in wet years were underestimated and low flows in dry years were overestimated. Moreover, increasing winter flow since 2006 was not simulated well due to a lack of data on glacier area change and the simple conceptualization of the permafrost degradation. The uncertainty of the hydrological simulation for the Bulgan catchment might have originated from limited precipitation measurements for the complex terrain, errors in discharge measurement for the extreme years, lack of glacier and permafrost observation data, and model structure and parameters.

Using the optimized hydrological model of the Bulgan catchment, we run runoff sensitivity of the Bulgan River by changing precipitation and temperature input data. The runoff was more sensitive to changes in precipitation than to changes in temperature. An increase in the daily precipitation sums of 10% amplified the annual runoff by 22%, whereas a warming of +1°C in daily temperature reduced the annual runoff by 6%. When temperature increases, the runoff decreases during the snowmelt period from May to June and the cold period from October to March, but the runoff slightly increases in August due to an increase in groundwater from ice melt of glacier and frozen ground.

Projected climate and runoff changes for the Bulgan catchment for the period 2030-2050 under RCP4.5 and RCP8.5 climate scenarios

General Circulation Models (GCM) help to understand the uncertainty range of climate projections. Regional Climate Models (RCM) accurately show regional climate at fine-resolution geographic and temporal scales.

Future climate and runoff changes for the Bulgan catchment were projected based on dynamically and statistically downscaled RCMs (RegCM4 and SD-CanESM2) and their driving GCMs (HadGEM2-AO and CanESM2). First, we statistically downscaled CanESM2 at two stations in the Bulgan catchment using the SDSM tool. The statistical downscaling model skills for precipitation from CanESM2 were satisfactory (R^2=0.56) for the mountainous area but poor (R^2=0.24) for the desert area due to low rainfall frequency and extreme climate. However, the maximum and minimum temperatures of CanESM2 were downscaled well (R^2=0.95-0.96) at the two stations.

The original GCMs and dynamical RCM simulated too many drizzle days with low precipitation and warmer temperatures for the Altai Mountains. After post-processed using distribution mapping, local climate conditions were better represented with lower RMSE (0.2-0.5) and higher correlation coefficients with observation (r=0.98-1.00) for the baseline period of 1985-2005.

Compared to the baseline period from 1985 to 2005, the mean of the post-processed GCMs projected an increase of 14% (RCP4.5) and 28% (RCP8.5) in total precipitation and a warming in annual temperature of +1.8°C (RCP4.5) and +2.3°C (RCP8.5) from 2030 to 2050. Similarly, the means of RCMs projected an increase of 13% and 18% in annual precipitation and intensive warming in annual temperature of +2.4°C and +2.9°C under RCP4.5 and 8.5, respectively.

Seasonally, GCMs projected intensive warming by +2.0°C in summer and autumn and the highest increase in precipitation during spring of +29% (RCP4.5) and 50% (RCP8.5). In contrast, winter precipitation was likely to decrease by -11% under RCP4.5 but to increase slightly by +13% under RCP8.5. Contrary to the projection of GCMs, RCMs projected a high increase of +23% and +47% in winter precipitation and a more significant warming in spring by +2.7°C and +3.3°C in the 2040s under RCP4.5 and RCP8.5, respectively. However, precipitation was projected to decrease slightly in spring and summer.

The projected change in the summer temperature (+2.96±0.79°C) in the 2040s under RCP4.5 is similar to the reconstructed temperature (+2.94±0.96°C) in the 1900s; however, the impact of the continued warming on water resources can be more severe than the short-

term warming in the 1900s. The variation of the June-December precipitation sum will be high and extreme in the 2040s compared to the dry period after Little Ice Age.

With regards to the hydrological regime, all models projected the highest increase in the snowmelt runoff in April and May but the lowest increase in June. RCMs projected more intensive warming than GCMs' projections; thus, the impact of temperature on runoff simulation was more pronounced in the runoff prediction. Previous studies on future runoff change in the Altai Mountains also projected the largest increase in spring runoff but a decrease, or the smallest increase, in summer runoff in the region. This altered seasonal water allocation through the year might threaten the intensified agriculture along the Bulgan River with water shortages during the growing season.

Overall, the Altai-Dzungarian region has been intensively warming since 1985. This warming is projected to continue with a projected increase in precipitation in the 2040s, and the hydrological regime of the Bulgan River will be changed.

LIST OF TABLES

LIST OF FIGURES

ABBREVIATION

FAO	Food and Agriculture Organization
GCM	Global climate model
RCM	Regional climate model
WMO	World Meteorological Organization
RCP	Representative concentration pathways
IPCC	Intergovernmental Panel on Climate Change
IRIMHE	Research Institute of the Meteorology, Hydrology, and Environment of Mongolia
WWF Mongolia	World Wide Fund for Nature Mongolia Programme Office
TTOP	Temperature at the Top Of the Permafrost
scPDSI	Self-Calibrating Palmer Drought Severity Index
CRU	Climatic Research Unit
SST	Sea surface temperature
NAO	North Atlantic Oscillation index
AO	Arctic Oscillation index
ENSO	El Niño-Southern Oscillation
APHRODITE	Asian Precipitation-Highly-Resolved Observational Data Integration Towards Evaluation
CORDEX	Coordinated Regional Climate Downscaling Experiment
WCRP	World Climate Research Program
EPS	Expressed Population Signal
SDSM	Statistical DownScaling Model
a.s.l	above sea level
NAMHEM	National Agency of Meteorology, Hydrology and Environmental Monitoring
CNCDC	China National Climate Data Center
GHCN	Global Historical Climatology Network
FDC	Flow Duration Curve

CHAPTER 1. INTRODUCTION

"…There are fruit groves in the river valley.

In the oasis on the front side of the Altai Mountains,

All people are happy in their hometown…"

from "Bulgan River with Beavers" folk song

Photo: A midstream area of the Bulgan River, Oyunmunkh 2017

1.1 Motivation

The World Meteorological Organization (WMO, 2022) emphasizes that since the 1980s each decade has been warmer than the previous one. Despite being temporarily cooled by the 2020-2022 La Niña events, 2021 was recorded as the seventh consecutive warm year since 2015. Also, WMO is concerned that now human-induced long-term warming is more extensive than annual variations of global average temperatures triggered by naturally occurring climate drivers. Consequently, climate change has already accelerated the global hydrological cycle causing negative societal impacts, including water scarcity and water-related extreme events like floods and droughts (Pörtner et al., 2022).

In recent decades temperature has increased rapidly and seasonal weather patterns have changed in the mountain region; snow cover extent and duration has reduced in low elevation zones, and an increased permafrost thaw and loss of glacier mass are observed with high confidence. Also, the number and size of glacier lakes has increased in the mountainous area (Adler et al., 2022).

The southern Altai Mountain range and the Dzungarian semi-desert basin are characterized by semi-arid continental climate conditions with high intra-annual and diurnal temperature variation and unevenly distributed precipitation due to orographic effects (Kurzrock et al., 2017). The observed warming rate in drylands is higher than in humid areas due to the sparse vegetation cover and low soil moisture (Mirzabaev et al., 2022). Thus, the semi-arid Altai-Dzungarian region is very sensitive to climate change.

In the semi-arid Altai-Dzungarian region, the Bulgan River is an important transboundary water resource for intensified and irrigated agricultural production and mountain pastoralism in western Mongolia and northwestern China (Jordan, 2016). Rivers of the Altai Mountains are mainly fed by the meltwater of snow from April to June and the meltwater of glaciers from July to August (Davaa, 2015; Zhang et al., 2017). They are influenced by seasonal thaws of permafrost from May to September (Sharkhuu, 2003).

Glaciers in the Altai Mountains have retreated rapidly since the 1990s (Dmitry et al., 2017; Kadota and Gombo, 2007; Maria et al., 2010; Wei et al., 2015) and permafrost thaw has increased since the 1980s (Jambaljav, 2017). Warmer winters and springs result in earlier snowmelt and an advance in the timing of spring high floods by 20 days in the Altai Mountains. On the other hand, changes in the summer rainfall pattern cause a delay in the timing of summer floods. Thus, break-up dates of rivers start 10-30 days earlier, whereas freeze-up dates of rivers are delayed by 10-30 days. (Batima, 2006).

These observed hydrological impacts of climate change in the Altai Mountains might lead to water shortage for livelihood security and agriculture in the Altai-Dzungarian region in the

future. Hence, this study aims to help policymakers and researchers to better understand long-term climate variation and its drivers over the Altai-Dzungarian region in the past and present, also runoff changes as a result of human-induced climate change in the present and the near future. The following research needs are identified by reviewing the literature on regional climate change and impact studies.

Research need 1: Long-term climate reconstruction using temperature and precipitation sensitive tree-ring data from the Altai-Dzungarian region (AD)

According to the longest instrumental observations in Mongolia, the annual mean air temperature of rose by 2.24°C from 1940 to 2015, and the warming rate is higher in its mountainous regions than elsewhere (Batjargal, 2018). Under the influence of the continuous increase of air temperature since the 1970s, evapotranspiration has also intensified in Mongolia and semi-arid northwestern China (Yu et al., 2016; Wei and Wang, 2013). The warmest ten years have occurred since 2000. The number of consecutive hot days and the frequency of high-intensity rainfall events have also increased (Batjargal, 2018). In the southern Altai Mountains, warm-season precipitation slightly increased between 1961 and 2015, while it decreased in the northern Altai (Batjargal, 2018; Zhang et al., 2018).

These short-term human-induced climate changes might be accelerated or slowed down by effect of naturally occurring climate drivers. Thus, understanding long-term regional climate variation and climate drivers is vital in interpreting the regional difference in warming and water availability. The lack of long-term instrumental observations from such outback desert and mountain areas hinders the estimation of climate variability and change in these regions. Schwikowski et al. (2009) suggested that climate proxies based on tree rings, relict wood, lake sediments, and glaciers, which often can be found in such remote regions in still rather undisturbed states, should be used for exploring regional climate change and variability. Accordingly, tree rings from the Altai Mountain range are widely used as climate proxies to reconstruct the past variability of temperature, precipitation, and drought in Mongolia, China, and Russia (Chen et al., 2012; 2014; Davi et al., 2009; Loader et al., 2010; Panyushkina et al., 2005; Zhang et al., 2015; Buentgen et al., 2016).

Buentgen et al. (2016) reconstructed the so far longest summer temperature time series starting in the 6th century AD, using tree-ring chronologies from the Russian Altai. However, climate reconstructions for the southern Altai have so far only covered temperatures over the past 450 years and precipitation over the past 250 years. Moreover, up to now past studies for this area have usually reconstructed a single climate parameter, while reconstructions of different parameters have not yet been compared and combined.

This study determined long-term (>400 years) climate variation over the Altai-Dzungarian region by reconstructing the longest time series of (611 years) temperature and (444 years) precipitation from tree-ring proxies.

Research need 2: Teleconnections between large-scale atmospheric circulation patterns and regional climate variability over the Altai-Dzungarian basin

Climatologically, the Altai Mountains are influenced by both the North Atlantic climate system to the west and the Pacific climate system to the east (Zhang et al., 2018). The Altai-Dzungarian region is influenced by both the southwesterly monsoonal airflow from the Mediterranean Sea, Black Sea, Caspian Sea, and Aral Sea (Iwao and Takahashi, 2006; Zhao et al., 2014; Zhang et al., 2018), and the midlatitude westerly and northwesterly airflow from the Atlantic Ocean during summer (Iwao and Takahashi, 2006; Bohner, 2006; Chen et al., 2015; Zhang et al., 2018). The latter brings warm air and relatively high amounts of precipitation to the region during summer, but northerly and westerly winds of the Siberian thermal high-pressure system bring cold and dry airflow from Siberia and the Arctic during winter (Chen et al., 2015; Zhang et al., 2018).

Warming of sea surface temperatures over the North Atlantic and the Indo-West Pacific Oceans changed the position of westerly winds, which increased their strength over the Altai-Dzungarian basin and brought more rainfall over central Asia during the 1980s (Chen et al., 2014; Zhao et al., 2014; Wei et al., 2017). Simultaneously, the North Atlantic Oscillation (NAO) changed toward a positive phase resulting in increased storm tracks in the Northern Hemisphere from the 1960s till the 1990s and returning to its mean state between the mid-1990s and early 2000s (Hartmann et al.,2013). Furthermore, a positive phase of the Arctic Oscillation (AO) brought warmer and wetter winter conditions to Mongolia in the 1980s (He et al., 2017), followed by a strengthening of the dry and cold Siberian High and its expansion northwestward between 1998 and 2012 (Hartmann et al., 2013).

In general, various large-scale atmospheric circulations influence the regional climate variation. The focus of early research on these influences has been based on the prominent NAO and AO patterns in winter (Portis et al., 2001; Hurrel, 1995; Gong and Ho, 2003; Osborn, 2006). Recently, some researchers have examined the effects of the summer NAO on summer temperature and rainfall using instrumental data and tree-ring proxy data (Folland et al., 2009; Sun et al., 2008; Linderholm et al., 2011; Sun and Wang, 2012; Linderholm et al., 2013).

This study revealed variations in teleconnections between large-scale atmospheric circulation patterns and regional climate variability on annual and interdecadal time scales using reconstructed temperature and precipitation time series from the southern Altai Mountains.

Research need 3: Hydrological impacts of observed climate change in the southern Altai Mountains, in the Bulgan catchment in Mongolia from 1984 to 2005.

The rivers of the Mongolian Altai Mountains are mostly fed by meltwater from glaciers and snow (51-63%), followed by rainfall (3-17%) and groundwater (31-40%) (Davaa, 2015). Recent studies found critical impacts of climate change on these water sources.

On the global scale, after the Little Ice Age, glaciers globally retreated strongly in particular periods, such as the 1920s, 1940s, and the 1980s, with advancing conditions in the 1970s (Dmitry et al., 2017). Likewise, glaciers in the Altai Mountains have retreated rapidly since the mid-20th century (Dmitry et al., 2017; Kadota and Gombo, 2007; Maria et al., 2010; Wei et al., 2015). Warming summer temperatures since the 1980s have resulted in an accelerated glacier recession in the Russian Altai, northern Mongolian Altai, and Chinese southern Altai Mountains from 1995 to 2008 (Dmitry et al., 2017; Wei et al., 2015; Maria et al., 2010). In the Mongolian Altai Mountains, the highest acceleration of glacier recession occurred from 1990 to 2000, followed by another recession period from 2010 to 2016 (Pan et al., 2018); thus, glacier contribution to total runoff decreased from 18.7% in 2000 to 15.4% in 2016 (Pan et al., 2019).

The Bulgan River gets water from glaciers of the Munkhkhairkhan massif in the southern Altai Mountains. The dynamics of these small glaciers are significantly affected by regional temperature and precipitation variation (Krumweide, 2010). The total glaciated area of the Munkhkhairkhan peak decreased by 30% and 12% for the periods of 1991-2001 and 2001-2011, respectively (Kamp et al., 2013).

Moreover, accumulated snow depth during the previous winter influences the high flows of the rivers in the southern Altai Mountains (Davaa, 2015; Wu et al., 2021). 18.5% of total snowfall in this region is sublimated back into the air during winter (Wu et al., 2021). From 1975 to 2007, warm winters reduced the duration of the snow cover in the Bulgan catchment by 20-25 days (Odgarav and Munkhbat, 2013). Also, the snow-to-rain ratio rapidly decreased in the southern Altai Mountains from 2000 to 2016, despite an increase in total precipitation (Wu et al., 2021).

Furthermore, Mongolia is located on the southern boundary of the Siberian permafrost, having a ground temperature close to 0°C. Thus, the permafrost extent of Mongolia, especially the permafrost in the Altai Mountains, is very sensitive to climate change (Sharkhuu, 2003). Permafrost thaw has increased in the Mongolian Altai Mountains since the 1980s as the annual mean ground temperature has risen at a rate of 0.15-0.18°C per decade (Jambaljav, 2017).

This permafrost degradation reduces the thickness of the seasonally frozen ground (Dashtseren et al., 2014) and creates a thicker active layer with a larger water storage

capacity. Increased water storage has triggered an increase in winter baseflow in high-latitude permafrost regions, such as river basins of the Russian Arctic (Liljedahl et al., 2017; Wang et al., 2021), high mountain permafrost regions (Wang et al., 2019, Wang et al., 2017), and northwestern China since 1990 (Kong and Pang, 2012).

Overall, the observed climate change has negatively impacted the water resources of regional hydrological regimes since the 1980s. Many impact studies of climate change correlated seasonal air temperature and precipitation sum with seasonal river discharges, such as in the high mountains of the Qinghai-Tibet Plateau (Fan and He, 2015), and in the southwest and northwest China (Ma et al., 2008; Wang et al., 2019), whereas other studies applied different hydrological models in the Altai Mountains based on the concept of river discharge resulting from different catchment processes (Ma et al., 2008), for instance, glacier mass balance models (Khalzan et al., 2022; Zhang et al., 2016), a physically based snow model (Wu et al., 2021), a semi-distributed SWAT model (Lui et al., 2019), and an HBV model with permafrost parameterization (Heerema, 2013).

This study determined key climate factors in the seasonal variation of the Bulgan River by developing Stepwise Linear Regression models for each season. Also, the rainfall-runoff HBV-Light model is applied to simulate changes in the water balance of the Bulgan catchment regarding regional climate change. In this data-scarce region, the accuracy of the gridded APHRODITE dataset is also evaluated and used as an alternative to station data in a climate change analysis and hydrological simulation.

Research need 4: Future hydrological impact of climate change over the southern Altai Mountains, Mongolia

Natural and human-induced substances and processes in the atmosphere are drivers of climate change altering the energy budget of the Earth. The changes in energy fluxes, calculated at the top of the atmosphere, are quantified as Radiative Forcing (Wm^{-2}). An increase in greenhouse gases since 1750 has made the total radiative forcing of the Earth positive, triggering surface warming (IPCC, 2013). The warming is likely to continue in the future with the projected increase in greenhouse gas emissions by humans. Climate models simulate changes in the climate system based on representative concentration pathway (RCP) scenarios of anthropogenic forcing (IPCC, 2013).

Recent climate studies in the region of the study area have evaluated the performance of Global (GCM) and Regional Climate Models (RCM) in simulating the regional hydrological impacts of the projected climate change in different periods under different representative concentration pathways (RCPs) (usually RCP2.6, RCP4.5, and RCP8.5). For instance, Pan et al. (2020) and Lui et al. (2019) estimated future changes in climate and the water cycle for

Northwest China using the regional climate models HadGEM3-RA, SUN-MM5, and RegCM4, derived from the Coordinated Regional Climate Downscaling Experiment (CORDEX) for the east Asian domain. Zhang et al. (2016) calculated future glacier changes in the Altai Mountains over the period 2006-2100 using 12 GCMs outputs. And Heerema (2013) simulated the future discharge of the Buyant River in the Mongolian Altai Mountains for the period 2080-2100 using four GCMs.

According to the ensemble mean of climate projections from 12 GCMs for the Altai Mountains, from 2081 to 2100, air temperature is expected to increase by 2.5℃ for RCP4.5 and 5.3℃ for RCM8.5, and precipitation is likely to increase by 10.5% for RCP4.5 and 15.6% for RCP8.5 (Zhang et al., 2016). The RCM RegCM4 generally simulates observed precipitation and temperature better than other RCMs for this complex terrain region by correcting the cold bias of the driving GCM HadGEM2-ES (Pan et al., 2020). During the historical period of 1985-2004, RegCM4 underestimates annual mean temperature but overestimates daily mean precipitation for the Altai and other mountains, and vice versa for the Dzungarian basin.

According to the climate projection of RegCM4 over the Altai Mountains, the annual mean temperature will warm by 6℃ and total precipitation will increase by 50mm for the period 2081-2100 under the RCP8.5 scenario (Pan et. al., 2020). Increased precipitation might not compensate for the enhanced loss of glacier mass, so glacier loss will occur by 2050s and the total area of Altai glaciers will decrease by 26±10% for RCP4.5 and by 60±15% for RCP8.5 by 2100 (Zhang et al., 2016). Summer precipitation will decrease (Lui et al., 2019), and the number of summer days (>25℃) will increase in this region (Pan et. al., 2020). Spring runoff is likely to increase in the Altai Mountains with more snow accumulation during winter, and the warm and rainy spring; however, summer runoff is likely to decrease in the future (Heerema, 2013; Lui et al., 2019).

This study estimated future climate and runoff changes in the southern Altai Mountains under RCP4.5 and RCP8.5 scenarios from 2030 to 2050. As an alternative to the dynamically downscaled RegCM4, the general climate model CanESM2 is statistically downscaled at climate stations in the Bulgan catchment using the computationally cheap and flexible Statistically Downscaling Model (SDSM). Moreover, both statistically and dynamically downscaled RCMs and their driving GCMs are evaluated for this complex terrain and used in the hydrological impact assessment of future climate projections.

1.2 Conceptual research framework

This thesis aims to better understand long-term climate variability and change over the Altai-Dzungarian region, teleconnections with large-scale atmospheric patterns, and the hydrological impact of observed and future climate change on water availability and timing for this semi-arid region. Figure 1.1 shows a conceptual research framework of this study developed based on the following main research questions.

- Question 1 (Q1): How has regional climate varied over the Altai-Dzungarian region during and after the Little Ice Age (LIA)?
    - Question 1.1 (Q1.1): What do the tree-ring based temperature and precipitation reconstructions tell us about climate variation and change during and after LIA?
    - Question 1.2 (Q1.2): How are the large-scale atmospheric circulation patterns connected to the regional long-term climate variation?
- Question 2 (Q2): How did the observed climate change impact the Bulgan River in the southern Altai Mountains between 1985 and 2015?
    - Question 2.1 (Q2.1): How has temperature, precipitation, and evapotranspiration changed in the region?
    - Question 2.2 (Q2.2): How has runoff of the Bulgan catchment changed? What are the most influencing climate factors?
    - Question 2.3 (Q2.3): How does the HBV-Light model perform for the Bulgan catchment? What are potential uncertainties in this hydrological simulation?
    - Question 2.4 (Q2.4): How sensitive is runoff of the Bulgan catchment to changes in temperature and precipitation?
- Question 3 (Q3): How will future climate change influence the hydrological regime of the Bulgan River for the period of 2030-2050 under RCP4.5 and 8.5 climate scenarios?
    - Question 3.1 (Q3.1): What do GCMs and RCMs projections imply about temperature and precipitation change in the southern Altai Mountains in near (2030-2050) and far future (2080-2100) periods?
    - Question 3.2 (Q3.2): How does the statistical downscaling approach perform for the Bulgan catchment in the semi-arid Altai Mountains?
    - Question 3.3 (Q3.3): How does the bias correction method improve GCMs and RCMs outputs in representing local climate conditions?
    - Question 3.4 (Q3.4): How will the projected climate change impact on the hydrological regime of the Bulgan catchment from 2030 to 2050 under RCP4.5 and 8.5 climate scenarios?

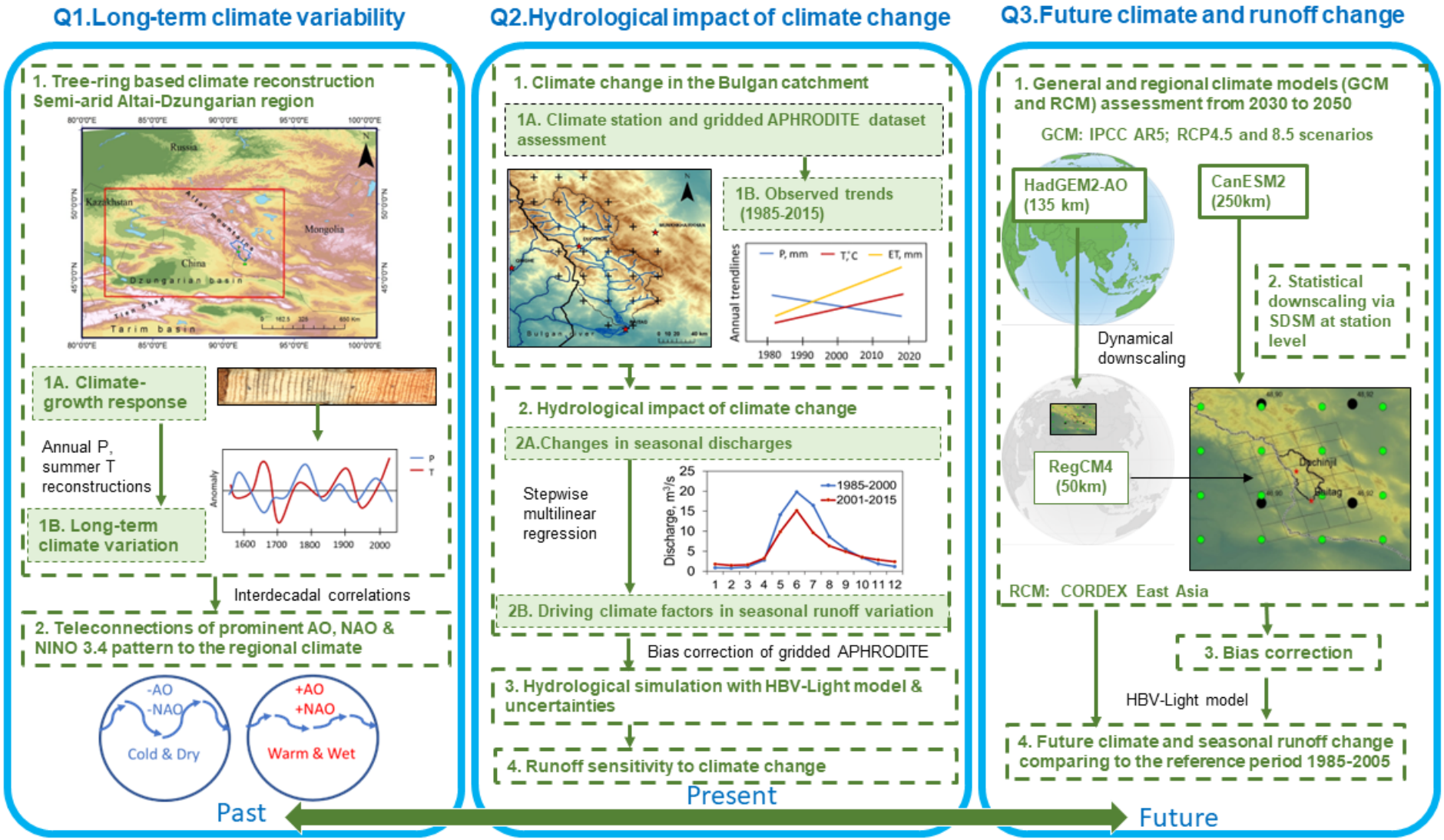

Figure 1.1: Conceptual research framework determining the long-term climate variability (Q1) and hydrological impact of climate change (Q2) as well as future climate and runoff change (Q3). For Q1.1, regional precipitation (P) and summer temperature (T) variations are reconstructed based on the response of tree growth to climate (Q1.1.1A). The long-term regional climate (Q1.1.1B) is determined by combining estimated P and T. Furthermore, relations of prominent large-scale circulations including North Atlantic Oscillation (NAO), Arctic Oscillation (AO), and Niño3.4 to the regional climate (Q1.2) are examined by

correlating them with the estimated long-term P and T time series on the interdecadal scale after relating them spatially to observations on the annual scale. For Q2.1, interpolated temperature and precipitation datasets of Asian Precipitation-Highly-Resolved Observational Data Integration Towards Evaluation (APHRODITE) are evaluated in this region (Q2.1.1A). Trends in precipitation, temperature, and evapotranspiration (ET_0) at the climate stations and the corresponding grids of the APHRODITE dataset are analyzed between 1984 and 2015 (Q2.1.1B). For Q2.2, the trends in seasonal runoff are analyzed (Q2.2A), and driving climate factors of runoff change are evaluated based on the Stepwise Multilinear Regression Model (Q2.2.2B). For Q2.3, the daily runoff and water balance of the Bulgan catchment are simulated by the conceptual rainfall-runoff model HBV-Light4.0 based on the station and the interpolated APHRODITE data. For Q2.4, the runoff sensitivity of the Bulgan catchment to climate change is determined using the established hydrological model. For Q3, future climate and runoff changes in the Bulgan catchment are projected for 2030-2050 under RCP4.5 and RCP8.5 and compared to the reference period 1985-2005. For Q3.1-3.2, CanESM2 is statistically downscaled at the climate station level using the Statistical Downscaling Model (SDSM). Both statistically and dynamically downscaled RCMs, and driving GCMs are evaluated for the Bulgan catchment. After correcting the biases in the climate model outputs (Q3.3), future runoff is simulated with the projected climate change for 2030-2050 under RCP4.5 and RCP8.5 scenarios (Q3.4).

1.3 Thesis outline

Chapter 1 introduces the research needs and motivation by reviewing previous studies, then presents the conceptual research framework. Chapter 2 describes the characteristics of the study area, the data collection, and its detailed analysis (subchapters 2.3.1-2.3.5).

In Subchapter 2.3.1 relationships between tree growth and climate are tested by examining the correlations between instrumental precipitation and temperature data and tree-growth chronologies from upper and lower tree lines. Based on a simple linear regression between temperature and precipitation-sensitive chronologies and climate data, transfer functions for reconstructing summer June-July temperature and June-December precipitation sum are developed. Afterwards, the effect of large-scale atmospheric circulation patterns on the regional climate is explored through annual and decadal correlation analyses of the North Atlantic Oscillation, the Arctic Oscillation, and NINO3.4 indices with observed and estimated long-term precipitation and temperature records in Subchapter 2.3.2.

In Subchapter 2.3.3, climate and hydrological changes over the period 1984-2015 are explored by testing the presence of monotonic increasing or decreasing trends in climate variables and upstream and downstream discharges of the Bulgan River with the Mann-Kendall test and Sen's slope.

To identify the hydrological impact of the observed regional climate change, key climate variables explaining the variation of upstream and downstream discharges are determined on the seasonal timescales using stepwise regression; moreover, rainfall-runoff conceptual HBV-Light model is simulated for evaluating changes in the water balance of the Bulgan catchment in Subchapter 2.3.4. Furthermore, the runoff sensitivity of the Bulgan River to climate change is tested based on the optimized hydrological model under different climate scenarios by increasing temperature and decreasing precipitation.

In Subchapter 2.3.5, projected changes in the seasonal temperature and precipitation for the Bulgan catchment are estimated from dynamical and statistical downscaled RCMs and their driving GCMs. A low-cost Statistically Downscaling Model (SDSM) is used to downscale outputs of CanESM2 at climate stations in the Bulgan catchment. Future runoff changes in the Bulgan catchment are simulated for the period 2030-2050 using the optimized HBV-Light model and bias-corrected GCMs and RCMs.

Chapter 3 presents and discusses the results. Chapter 4 concludes with a summary of the main findings and recommends some ideas for future study.

CHAPTER 2. STUDY AREA, DATA AND METHODS

“Mountain Ranges and the Gobi Desert are combined

A plenty of hays and crops are swinging…”

from “Bulgan River with Beavers” folk song

Photo: An upper treeline on a north slope of the Altai Mountains, Oyunmunkh 2014

2.1 Study area

2.1.1 Altai-Dzungarian region

The Altai Mountain range lies in the cross-border region of Kazakhstan, China, Mongolia, and Russia. The vegetation zones of this region follow moisture and temperature gradients with a decrease in moisture and an increase in temperature from North to South and from West to East (Zhang et al., 2015). The Dzungarian semi-desert basin is bounded by the Altai mountains in the north and the Tian Shan mountains in the south (Figure 2.1). In the vulnerable steppe and semi-desert ecosystems of the Altai Mountains and Dzungarian Desert Basin area, the WATERCOPE research project[1] was executed by a Sino-Mongolian-German consortium over the period 2012-2016 to develop, compare, and test-implement technologies to cope with climate change effects on the regional natural resources. In the scope of the WATERCOPE project, we conducted this hydrological impact study of climate change in the Altai-Dzungarian region for the Bulgan catchment.

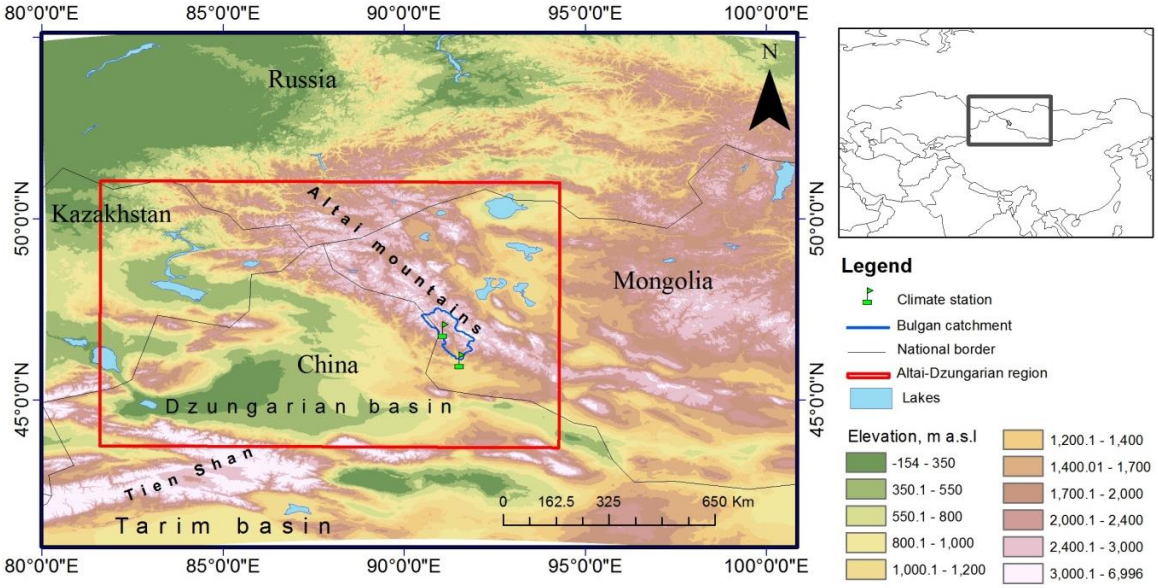

Figure 2.1: Geography of the Altai-Dzungarian region in Central Asia. The green flags indicate the location of the climate stations Duchinjil (46.93˚N, 91.08˚E, 1951 m a.s.l) and Baitag (46.09˚N, 91.55˚E, 1186 m a.s.l) in the Bulgan catchment, which is indicated by the blue line. The light blue polygons indicate large lakes. The color scale indicates elevations from low areas to high mountain ranges.

2.1.1.1 Climate

The Altai Mountain range and the Dzungarian semi-desert basin have semi-arid continental climate conditions with high intra-annual and diurnal temperature variation and unevenly distributed precipitation due to orographic effects (Kurzrock et al., 2017). Along the Bulgan River valley, two climate stations, Duchinjil (1951m a.s.l) and Baitag (1186m a.s.l) are located in the high mountains and the Gobi Desert, respectively, see Figure 2.1.

[1] http://www.watercope.org

The annual mean temperature is between -3.9°C and 0.3°C at the Duchinjil station in the valley of the mountainous area and between -0.2°C and 4.8°C at the Baitag station in the semi-desert area. Total annual precipitation varies from 68mm to 193mm at the Duchinjil, and from 24mm to 140mm at Baitag (own study, Figure 2.2).

At Duchinjil, monthly mean and maximum air temperatures in July reach 15.9°C and 22°C. Also, the monthly mean and minimum temperatures drop to -22°C and -27°C in January (Figure 2.2a). On average, 55% of total precipitation falls in the summer months June through August, but only 6% falls in the winter months December through February. At Baitag, the monthly mean temperature varies from –21°C in January to 20°C in July. The maximum temperature reaches 28°C in July, and the minimum temperature drops to -28°C in January (Figure 2.2b). On average, 45% of total precipitation falls as rainfall in summer and 13% as snow in winter.

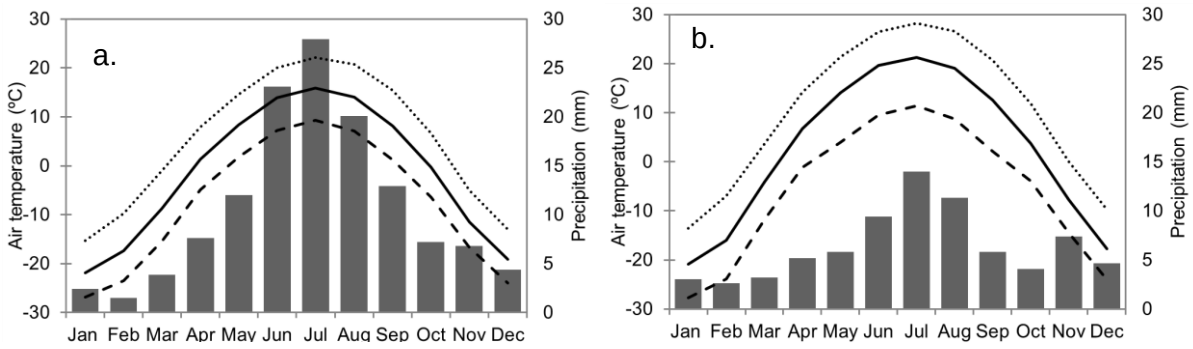

Figure 2.2: Climate diagrams for Duchinjil station (46.93˚N, 91.08˚E, 1951m a.s.l) for 1977-2017 (a) and Baitag station (46.09˚N, 91.55˚E, 1186m a.s.l.) for 1963-2017 (b). Monthly precipitation sums are shown by grey column bars. Monthly maximum, mean and minimum temperatures are illustrated by dotted, solid and dashed black lines, respectively.

One of the seven temporary climate stations of the WATERCOPE project located at different altitudes along the valley, Tsunkhul station at 2425m a.s.l, recorded an annual precipitation sum of 404 mm in 2013, but Duchinjil station at 1951m, a.s.l, only recorded 85mm. This large difference in precipitation sums at different elevations is explained by convective rainfall in the high mountains during summer (Kurzrock et al., 2017).

2.1.2 Bulgan catchment

The Bulgan River originates from the southern Altai Mountains, in the western region of Mongolia and flows southward for 203 km to the Bulgan-Baitag gauge station then veers westward 65km to the border with China (Figure 2.3). After passing the border with China, the Bulgan River merges with the Qinghe River and becomes the Urungu River, which flows northwestward and ends in the Ulungur Lake, China. 268 km of total river length (700km) passes through Mongolia. The Bulgan catchment is surrounded by the steep Altai Mountains, which are characterized by small glaciers and areas of permafrost. The upstream area

contains glacial and tectonic lakes with fresh and saline water; downstream saline lakes are also found.

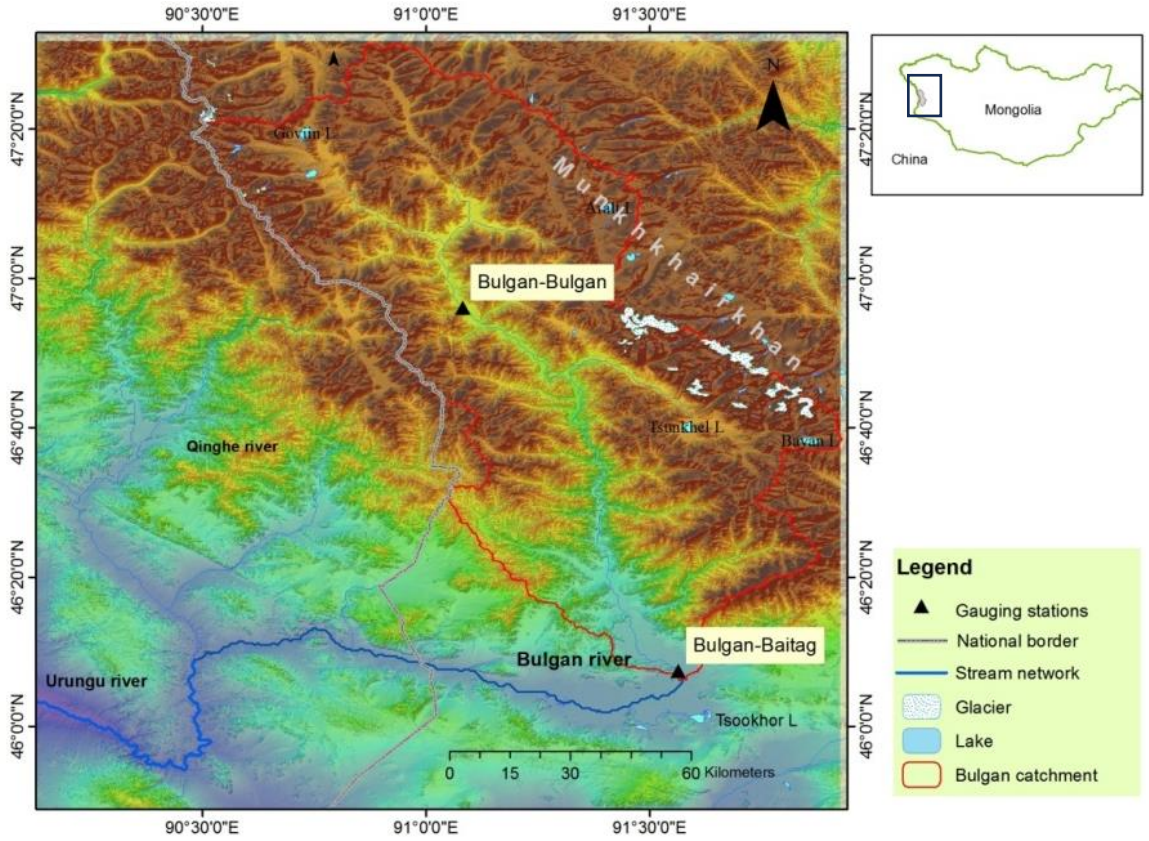

Figure 2.3: An overview of the Bulgan catchment in the Altai-Dzungarian region. Two hydrological gauging stations, Bulgan-Bulgan and Bulgan-Baitag, are located along the river.

Upstream, the north-facing slopes of the Altai Mountains are sparsely populated by *Larix sibirica* while downstream wide alluvial plains are found which emerge into the semi-arid Dzungarian Gobi Desert. Thus, the Bulgan catchment lies in the transition area between the high mountain zone and the desert zone.

Land cover characteristics of the Bulgan catchment are shown in Figure 2.4a and Table 2.1. Forest and glaciers occupy about 6.7% and 0.13% of the whole catchment area, respectively. Permafrost extends over 87% of the total area (Obu et al., 2018). The elevation of the catchment ranges from 1185m to 4160m above sea level and is divided into 15 elevation zones in this study (Figure 2.4b).

Rivers of the Altai Mountains are temperature-dependent and snow-fed; thus, they have low flows in the cold season and high flows in the warm season (Davaa, 2015).

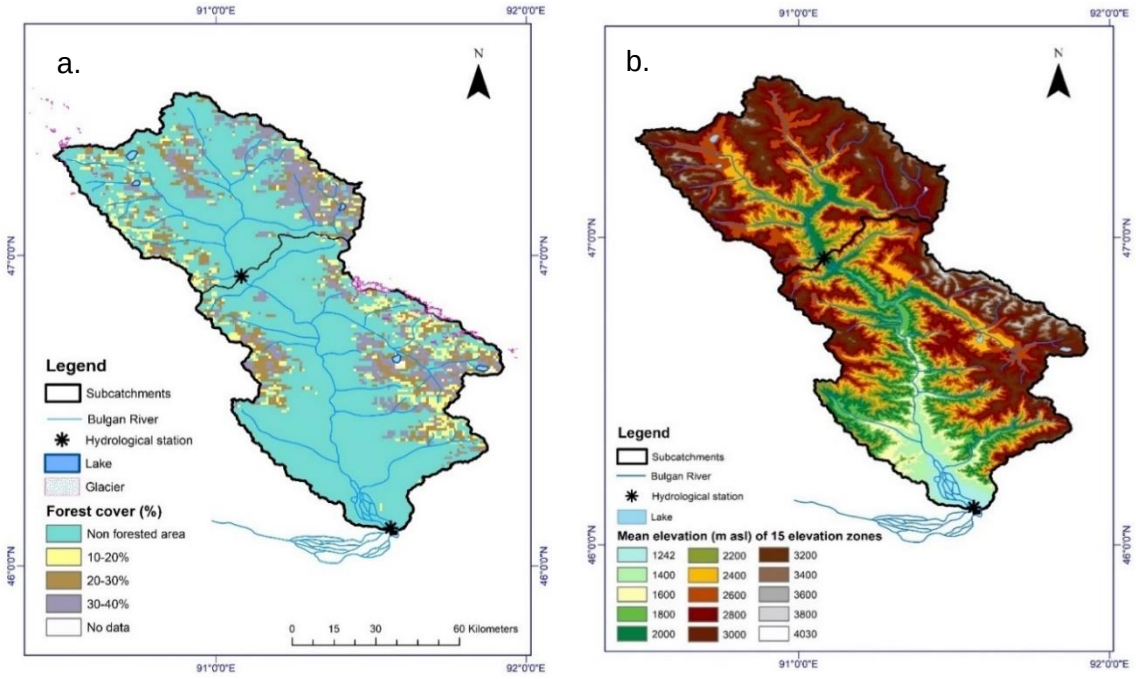

Figure 2.4: Land cover (a), and elevation zones (b) of the Bulgan catchment

Table 2.1: Land cover characteristics of the Bulgan catchment area.

Catchment	Area (km^2)	Forest[2] (%)	Glacier area[3] (km^2)	(%)	Permafrost (%)	Lake[4] (%)	Elevation[4] (m a.s.l) Min	Max	Mean
Upper subcatchment	2945.3	6.8	1.2	0.04	100	0.25	1925	3803	2787
Lower subcatchment	4643	6.7	8.3	0.19	77	0.12	1185	4160	2399
Whole catchment	7588.3	6.7	9.5	0.13	87	0.17	1185	4160	2552

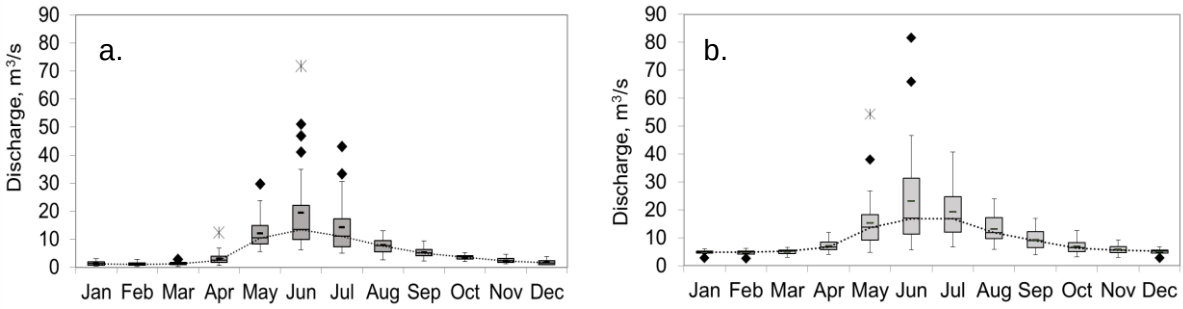

Figure 2.5: Monthly mean discharges of Bulgan River at the upstream (a) and the downstream hydrological stations (b) over the period 1984-2015. Outliers and extremes are marked by black rhombus and asterisks, respectively. Mean and median values are shown by minus symbol and dotted line, respectively.

After the peak snowmelt runoff by the end of May, a high flow of rainfall-runoff occurs in the Bulgan catchment between late June and late August (Figure 2.5a-b; Davaa 2015). Low flow sustained by groundwater increases at the lower elevation during the cold season.

[2] Geospatial Information Authority of Japan, Chiba University, accessed on 12 May 2019, https://globalmaps.github.io/ptc.html
[3] The database of Global Land Ice Measurements from Space, accessed 31 March 2019, http://www.glims.org/.
[4] WWF Mongolia database, accessed in January 2012, http://mongolia.panda.org/web_gis/

2.1.2.1 Glacier area changes

The Bulgan River is fed by snow, ice, and glaciers, extending on the south- and north-facing slopes of the Munkhkhairkhan Peak (4208m a.s.l) of the southern Altai Mountain. The glacierized area accounted for only 0.13% of the Bulgan catchment in 2001 according to Mongolian glacier outlines derived from a NIR(4)/SWIR(7) band ratio (Kamp et al., 2013). Krumweide (2010) found that the dynamics of the small glaciers in the Mongolian Altai Mountains are sensitive to the variation of the regional climate. Over the period 1991-2011, as shown in Figure 2.6a, the glacier area decreased by 38% and reduced from 39.66 to 27.55km^2 (Kamp et al., 2013). 30% and 12% of the total glacierized area was lost in the 1990s and the 2000s, respectively. Moreover, the Information and Research Institute of the Meteorology, Hydrology, and Environment of Mongolia (IRIMHE) found that the glacier area of the Munkhkhairkhan Mountain decreased by 22.4% over the period 2001-2019 (Figure 2.6b).

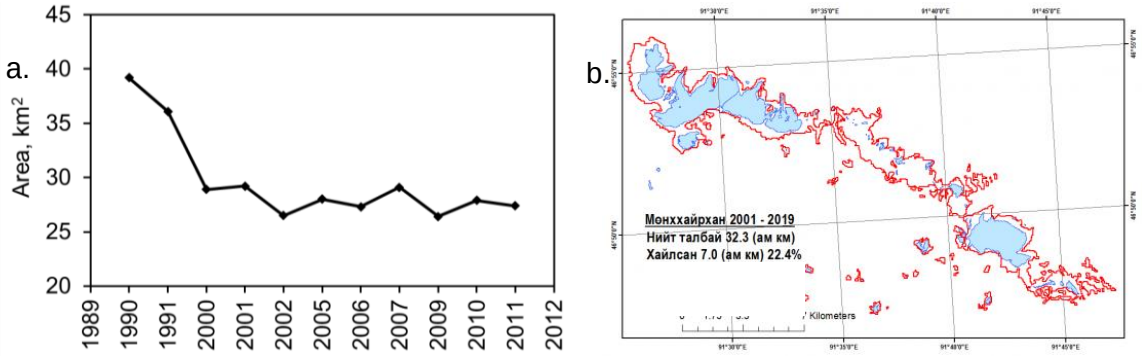

Figure 2.6: Recession of glacierized area of the Munkhkhairkhan Mountains from 1989 to 2011 (Kamp et al., 2013) (a) and from 2001 to 2019 (b) (IRIMHE, 2021). Glacier areas for 2001 and 2019 are marked by red and blue polygons, respectively.

In general, the loss of the glaciers in the Bulgan catchment was characterized by a large recession from 1990 to 2000 followed by a more gradual decline between 2001 and 2019.

2.1.2.2 Snow cover variation

Snow is one of the important water resources in the southern Altai Mountain. According to the snow camera shots of the WATERCOPE project stations throughout 2013-2014, snow falls in the high mountains starting mid-September and melts till late June.

In the flat semi-desert area, snow cover remains for 131 days from December through March and remains for 184 days in the valleys of the high mountains from November through April (Munkhbat, 2010). Maximum and mean snow depths are 20cm and 5cm at Baitag station, but 11cm and 8cm at Duchinjil station. In heavy snowy winters, the maximum snow depth reaches approximately 100cm (Odgarav and Munkhbat, 2013). More snow accumulates on the leeward north-, east-, and southeast-facing slopes in the Altai Mountains while less snow

accumulates on the windward west-, southwest- and south-facing slopes (Zhong et al., 2021).

Snow accumulated during winter generates runoff during spring depending on snow water equivalent and air temperature (Khadka et al., 2004). From 1975 to 2007, snow water equivalent was 24mm and the snow density was 0.18gr/cm^3 on average at Duchinjil station (Munkhbat, 2010). Moreover, the snow water equivalent of the Bulgan catchment reaches a maximum value of 100-200mm in late February. In early March 2014, snow depth along the river valley of Bulgan catchment was 9cm on average with a range of 1.7cm to 25cm; moreover, snow density varied from 0.15gr/cm^3 to 0.37gr/cm^3, and snow water equivalent was in the range of 17-22mm (Purevdagva, 2014).

The spatial variation of snow properties is determined by topography and vegetation. Elevation and latitude predominantly define snow depth and snow water equivalent, but longitude across Altai Mountain describes variation in snow density (Zhong et al., 2021). The lapse rate of snow depth is 6cm per 100m altitude change in the Bulgan catchment (Purevdagva, 2014) up to a certain altitude, then decreases towards the highest altitude (Grünewald et al., 2014).

In the Chinese Altai Mountains, snow thickness and duration slightly increased at the climate station from 1961 to 2015, with an abrupt rise since the late 1980s (Zhang et al., 2022). In contrast, snow cover of the Bulgan catchment declined in February but increased in March from 2001 to 2010, as shown in Figure 2.7 (Odgarav and Munkhbat, 2013). Odgarav and Munkhbat (2013) concluded that warming winters shortened the duration of the snow cover in the Bulgan catchment by 20-25 days over the period 1975-2007.

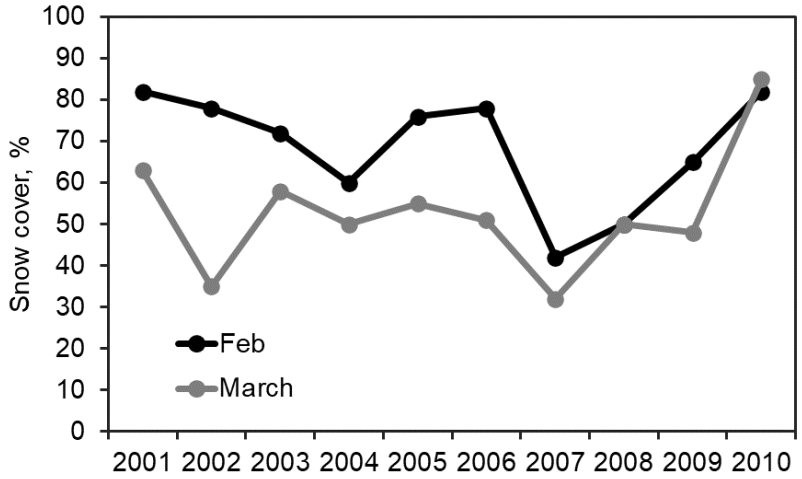

Figure 2.7: Snow cover variation (%) of Bulgan catchment in February and March based on estimation of MODIS satellite images (Odgarav and Munkhbat, 2013).

2.1.2.3 Permafrost extent

Permafrost, frozen soil, has a temperature close to 0°C and is very sensitive to climate change. Permafrost plays an essential role in the water balance of the catchments in the semi-arid mountainous area due to the freeze-thaw cycle (Zorigt et al., 2016; Yang et al., 2021). Seasonal thawing of permafrost occurs between May to September (Sharkhuu, 2003) and sustains soil moisture and river flow locally during the dry period (Dashtseren et al., 2014). Soil (active layer) above permafrost table thaws in the summer and starts refreezing in October and freezes in December. Abundant water in the deep soil layer delays soil refreezing by 30 days on average due to latent heat effect.

In winter, snow cover and duration control the seasonal freezing thickness of the ground; therefore, thin snow cover stays for a short period and leads to the deeper frozen ground due to a lack of thermal insulation (Dashtseren et al., 2014). In summer, downward shortwave radiation and air temperature control the thawing rate of seasonally frozen ground and the active layer depth of the permafrost; the surface temperature is higher on dry south-facing slopes than on north-facing slopes (Dashtseren et al., 2014).

Permafrost acts as a barrier to water flow in the soil system. Unfortunately, global warming increases the ground temperature resulting in permafrost thawing, thickening of the active layer, and shortening of the freezing period (Yang et al., 2021). Permafrost degradation reduces the thickness of seasonally frozen ground (Dashtseren et al., 2014) and results in more frequent transport of groundwater into different layers of aquifers than before (Figure 2.8). Moreover, a thicker active layer creates a larger water storage capacity and increases groundwater contribution to winter baseflow (Wang et al., 2021).

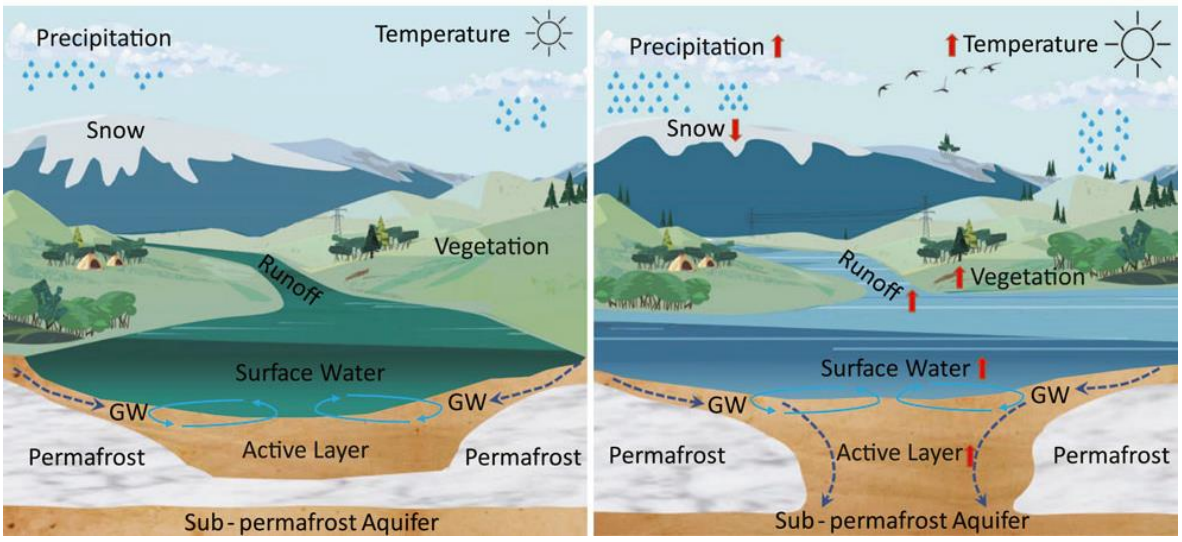

Figure 2.8: Groundwater (GW) and surface water interaction in cold region before (a) and after (b) global warming (Source: Yang et al., 2021).

According to Northern Hemisphere permafrost mapping based on the Temperature at the Top Of the Permafrost (TTOP) modeling for 2000-2016 at a 1km^2 scale (Obu et al., 2019), frozen soil accounts for 87% of the Bulgan catchment (Figure 2.9; Table 2.2). Ground temperature in Mongolia has increased since 1980 at a rate of 0.15°C-0.18°C per decade (Jambaljav, 2017). In the northern Altai Mountains, Zorigt et al. (2020) also revealed that ground temperature at 10m depth below the surface increased by 0.4°C on average over the whole period of 1980-2017; for instance, the Tsagaannuur borehole temperature increased from -1.2°C in 1983 to -0.5°C in 2017.

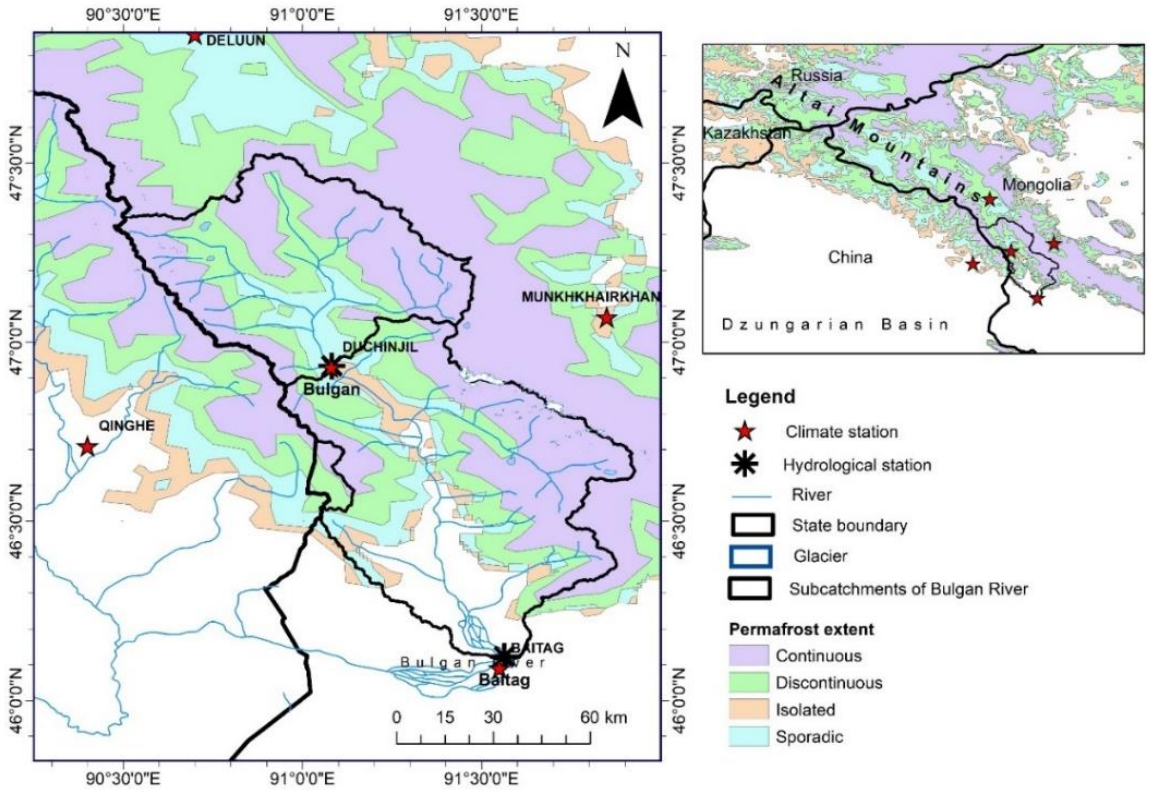

Figure 2.9: Permafrost extent of the Bulgan catchment in the Altai-Dzungarian region. Data source: Classes of permafrost are based on mean annual ground temperature (MAGT) and permafrost probability (MAGT<0°C), validated with observations and maps (Obu et al 2018)

Table 2.2: Permafrost extent of the Bulgan catchment based on the Permafrost map (Obu et al., 2018).

No	Permafrost Extent	Upper Subcatchment, %	Lower Subcatchment, %	Whole catchment, %
1	Continuous (-1.71 ± 0.48°C)	49	34	43
2	Discontinuous (-0.01 ± 0.37°C)	30	24	26
3	Sporadic (+1.46 ± 0.44°C)	15	12	5
4	Isolated patches (+2.62± 0.53°C)	6	7	13
5	Non frozen ground	-	23	13

2.2 Data collection

2.2.1 Tree-ring data and sampling site description

In the southern part of the Mongolian Altai Mountains (Figure 2.10c), patches of Siberian larch forest are often found on north-, west- and northwest-facing slopes (Figure 2.10a-b). Site selection is fundamentally important in dendroclimatology. Sites where growing season temperature limits tree growth are selected to reconstruct temperature, while to reconstruct precipitation, sites where moisture availability limits tree growth are chosen (Sheppard, 2010). Trees for sampling are chosen based on apparent age and the absence of evidence of any disturbance by non-climatic factors for instance fire, disease, wind, volcanic, earthquakes, insects, or humans to extract reliable climatic information from tree rings (Cook and Kairiukstis, 1990; Sheppard, 2010). Non-climatic disturbances change year-to-year ring width variability and create difficulties in cross-dating tree cores (Cook and Kairiukstis, 1990). Thus, to avoid potential disturbances local people were questioned about fire, disease, and human disturbances before selecting sites.

Not much is known about the impact of wildfires on these patchy forests. In the national fire statistics for the period 1963-1997, the majority of wildfires were reported from forested areas of central and eastern Mongolia after the snowmelt in March to mid-June and in autumn (Bayartaa, 2007). Regional grassland fire reconstructions based on charcoal analyses of sediments from 48 lakes in northwestern Mongolia with sediment influx from the Altai revealed no recent wildfire evidence (Umbanhowar et al., 2009).

During fieldwork in the area, local people asserted that the main disturbance has been intensive logging from the 1960s to 1990s and that in recent decades no widespread fires have occurred. The Mongolian Altai Mountain forest is also too cold for insect outbreaks (Dulamsuren and Khishigjargal, 2012). In the Russian northern Altai, a Siberian silk moth outbreak was confined to southern slopes with 11°-13° steepness located at approximately 400 m a.s.l (Khurah et al., 2016). Our sampling sites have steeper (25-33°) and colder northwestern slopes at higher altitudes than the silk moth favorable dry and hot conditions on the gentle southern slopes at the middle elevation (Kharuk et al., 2020).

Core samples from in total of 53 trees were taken at the sites Kargait (KAR), Khets (KET), and Gurt (GUR) located at upper treelines in July 2014. In addition, 20 trees at the sites Yolt (YLT), Shiregt (SHR), and Khudagt (KUD) located at the lower treeline of forest patches were sampled in July 2013. The positions of all sites are shown in Figure 2.10c; see also Table 2.3 for more detailed information.

Tree ring data can be obtained from a single tree-ring site or a network of several tree-ring sites in a region. The network of tree-ring chronologies is also used to verify the relationship

between tree growth and climate that is defined from the single tree-ring data (George, 2014); furthermore, networks can be used to map spatial patterns of effective climate events such as drought (Speer, 2010). In this study, both a single tree-ring site and a network of several tree-ring sites are applied for regional climate reconstruction. The longer and more climate-sensitive tree-ring data at KAR and KET sites are used to reconstruct air temperature and precipitation, respectively. Then, to verify their growth response to regional climate variability, tree-ring data of six sites are applied in a Principle Component Analysis to derive a network of tree-ring site chronologies.

Table 2.3: Sampling sites information.

Tree ring sites	Coordinates	Elevation (m)	Tree-line	Aspect	No of trees/cores
KAR*	46°39' / 91°26'	2748	Upper	North	21/32
KET*	46° 43' / 91° 31'	2603	Upper	West	23/46
GUR*	46° 48 / '91° 29'	2450	Upper	Northwest	13/26
YLT**	47° 05' / 91° 10'	2334	Lower	North	7/28
SHR**	46° 44' / 91° 28'	2478	Lower	West	9/36
KUD**	46° 36' / 91° 30'	2482	Lower	Northwest	4/16

KAR - Khargait, KET – Khets, GUR – Gurt, YLT – Yolt, SHR –Shiregt, KUD – Khudagt
*Samples taken with two replications in 2014 **Samples taken with four replications in 2013

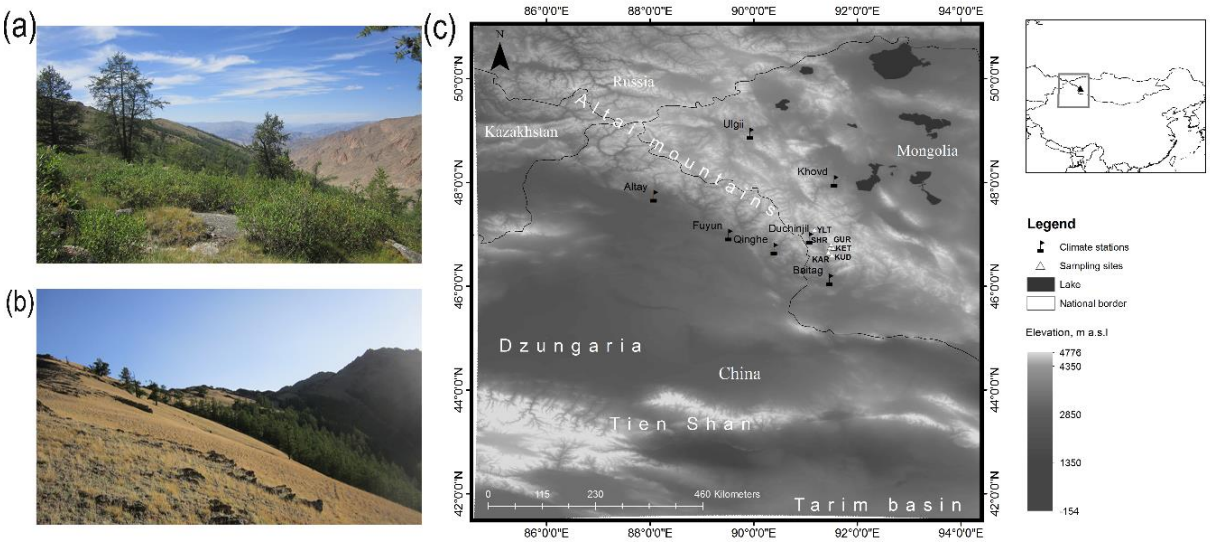

Figure 2.10: Photos from the sites Khargait (KAR) (a) and Khets (KET) (b). Map of the Altai-Dzungarian region in Central Asia (c). The black flags indicate the locations of the climate stations nearest to the six larch (*Larix sibirica*) sampling sites, which are shown as white triangles. The dark grey areas indicate lakes and the grey scale indicates elevation from low ranges (dark color) to high mountain ranges (white, see scale at the lower right).

Three sites, KAR, KET, and GUR, have rather steep slopes (25-33°) and revealed no indications of impacts by fire (scar) or insects (loss of needles) and only minimum human disturbances according to interviews with local officers and our site inspections. KAR is located on a north-facing slope and KET on a west-facing slope, which makes it more prone to westerly winds, more rainfall, and more radiation. The GUR site is on a northwest-facing

slope. The KAR site is characterized by large boulders covered with a thin soil layer and alpine shrubs (Figure 2.10a) while the KET and GUR sites have a well-developed soil layer with grasses and young trees (Figure 2.10b). During the field study, 32 cores were taken from 17 trees at KAR, 46 cores were taken from 23 trees at KET, and 13 cores were taken from 13 trees at GUR. Except for two trees, two cores were taken from each tree from opposite sides perpendicular to the slope direction.

The remaining three sites, YLT, SHR, and KUD, are on north-, west- and northwest-facing slopes, respectively. The SHR and KUD sites have steeper slopes (24°) than the YLT site (12°). All sites had a well-developed soil layer with young trees and some stumps caused by logging. Thus, tree-ring data of these sites need to be carefully examined to remove human disturbance and are only used in a network of tree-ring chronologies. Four cores were taken from each tree from all sites. The numbers of sampled trees and cores are listed in Table 2.3.

2.2.2 Climate dataset for past climate reconstruction

Very few climate stations with sufficiently long and complete records exist in the region. The climate station nearest to the tree-ring sampling sites, Duchinjil (1951 m a.s.l.), is located in a valley approx. 36 - 40 km away from the tree sampling sites and has an instrumental record starting in 1977. In addition to this short time series, observations from more distant climate stations in the southern Altai Mountains established between 1954 and 1963 (Figure 2.10c, Table 2.4) are also considered for climate reconstruction.

Regional monthly mean temperatures were derived by averaging the data from five stations, Baitag, Khovd, and Ulgii in Mongolia and Fuyun and Altay stations in China over their common period of 1963-2012. Based on both elevation and terrain characteristics, precipitation data were only used from the higher elevated and windward stations Duchinjil (1977-2012) in Mongolia and Qinghe (1958-2007) in China.

Table 2.4: Climate station locations, elevations, and timespans.

Climate stations	Latitude	Longitude	Elevation, m a.s.l	Timespan
Duchinjil*	46.92	91.08	1951	1977-2012
Baitag*	46.11	91.46	1186	1963-2012
Khovd**	48.01	91.56	1405	1937-2012
Ulgii**	48.93	89.93	1715	1959-2012
Qinghe***	46.71	90.40	1463	1958-2007
Altay****	47.73	88.03	737	1954-2012
Fuyun****	46.98	89.51	827	1961-2011

Obtained from the data sets *NAMHEM[5], **CRU[6], ***CNCDC[7], and ****GHCN[8]

[5] National Agency of Meteorology, Hydrology and Environmental Monitoring
[6] Climatic Research Unit
[7] China National Climate Data Center
[8] Global Historical Climatology Network

To verify the response of the tree-ring growth to regional climate variation on broad spatial scale, monthly mean gridded Climatic Research Unit data (CRU TS4.01; Harris and Jones, 2017) and monthly mean Self-Calibrating Palmer Drought Severity Index (scPDSI) data averaged over the area between 46°N to 47°N and 91°E to 92°E for the period 1963-2012, downloaded via the Climate Explorer website of the Royal Netherlands Meteorological Institute, were also used in the analysis.

2.2.3 Atmospheric circulation indices

Various large-scale atmospheric circulations influence the regional climate. The Altai-Dzungarian region is located at the junction between the North Atlantic climate system to the west and the Pacific climate system to the east (Zhang et al., 2018). In order to examine their mutual influences on the regional climate, we obtained the monthly and seasonal values of the North Atlantic Oscillation index (NAO, Jones et al*.,* 1997) over the period 1825-2012, the Arctic Oscillation index (AO, Thompson and Wallace, 2000) for the period 1899-2012, and the NINO3.4 index (Huang et al., 2017) for the period 1854-2012 from https://climexp.knmi.nl/ in February 2019.

2.2.3.1 North Atlantic Oscillation index

The NAO is a large-scale mode of natural climate variability, that plays an important role in the weather and climate of the North Atlantic basin, Europe, parts of northern America, the Mediterranean basin, and Eurasia (Pinto and Raible, 2012; Osborn, 2006). NAO phases cause distinctive changes in surface temperature, precipitation, and storm tracks over these regions (Figure 2.11; Pinto and Raible, 2012).

Measurements of the NAO index started in the early 1820s are generated from the monthly mean pressure data at stations on Gibraltar in southernmost Iberia and Reykjavik in south-western Iceland (Jones et al., 1997). The NAO index reflects the variation in the normalized atmospheric sea-level pressure difference between these two North Atlantic stations (Gibraltar minus Iceland) located near the center of the Azores High and the Icelandic Low (Jones et al., 1997; Ba´ez et al., 2013). The index is normalized monthly with the mean and standard deviation calculated from the reference period 1951-1980. This NOA index shows large interannual and interdecadal variability for the winter months from November to March (Jones et al., 1997; Osborn, 2006).

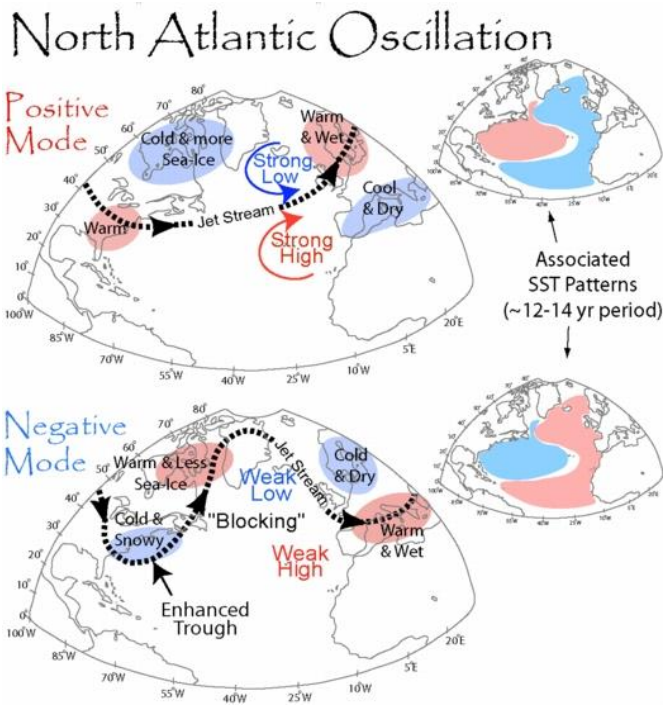

Figure 2.11: North Atlantic Oscillation phases. Positive and negative phases impact on the intensity and location of jet stream and zonal and meridional heat and moisture transport. SST: Sea surface temperature (source: http://www-personal.umich.edu/~auraell/precipitation/pages/NAO.html)

Generally, the NAO pattern is active all year and shifts in size and geographical location (Barnston and Livezey, 1987; Linderholm et al., 2013). The summer NAO moves westward and northward with respect to the winter position and has a smaller spatial extent (Barnston and Livezey, 1987; Portis et al., 2001). During the cold season, the magnitude and spatial coherence of atmospheric circulation variability are larger and the influence of circulation change on temperature and large-scale precipitation is greater than during the warm season (Osborn, 2006). Also, when horizontal temperature gradients are strong in the cold season, the effect of cloud cover variation is weak and the contribution of small-scale convective rainfall events are small (Osborn, 2006).

During a positive phase of NAO, the Azores High is stronger and the Iceland low is deeper. This atmospheric circulation leads to a stronger meridional pressure gradient over the North Atlantic, a more zonal flow regime, and stronger westerlies, which bring mild air from the Atlantic across the northern midlatitudes (Pinto and Raible, 2012). Thus, there are warmer and wetter conditions than average in northern Europe, the eastern United States, and parts of Scandinavia, whereas cooler and drier conditions are found over southern Europe, the Mediterranean, and North Africa (Ba´ez et al., 2013; Visbeck et al., 2001; Hurrell, 1995). The Northern Atlantic Ocean varies with the overlaying atmosphere (Visbeck et al., 2001). Thus, the strength of the NAO is related to the sea surface temperature (SST) and induces a tripole pattern in sea surface temperatures with a cold anomaly in Greenland and the Irminger Sea to Newfoundland (subpolar region) and a warm anomaly in the central North Atlantic (midlatitudes) and again a cold subtropical anomaly off the west African coast (Figure 2.11;

Pinto and Raible, 2012). The signs of this SST tripole pattern reverses during a negative NAO phase.

A negative NAO phase is characterized by a weakened Azores High and a shallow Iceland low leading to a reduced meridional pressure gradient and weaker westerlies over the North Atlantic and western Europe (Pinto and Raible, 2012). The negative NAO phase results in warmer and wetter than normal weather conditions in southern Europe but colder and drier conditions in northern Europe, associated with a blocking situation extending from Ural/eastern Europe to western/central Europe. This blocking might stay in place for several weeks, leading to stable weather conditions over central Europe (Pinto and Raible, 2012).

2.2.3.2 Arctic Oscillation index

The Arctic Oscillation Index (AO) is the difference in sea level pressure of the Arctic from northern mid-latitudes, Europe, and Asia (Rohman, 2014). We used the normalized monthly mean 1000hPA height anomalies (AO indices) poleward of 20° latitude for the Northern Hemisphere with the monthly AO index's standard deviation during the 1975-2000 period (Thompson and Wallace, 2000).

The regional manifestation of the AO in the North Atlantic is the NAO (Figure 2.12; Campos and Horn, 2018). Thus, AO and NAO are usually in sync, positive or negative (Greene, 2012). In 2012, unusual atmospheric conditions led to negative AO and positive NAO states, thus an odd combination of extreme cold and snowy weather across central and eastern Europe and Alaska but warm weather in the United States (Figure 2.12c, Greene, 2012).

The AO is related to the state of the northern hemisphere's climate, especially in winter, since its amplitude and meridional scale are more extensive during the cold season (He et al., 2017) compared to the warm season (Thompson and Wallace, 2000). In a positive AO phase, sea level pressure is low in the Arctic and high in the northern mid-latitudes, Europe, and Asia. Thus, strong winds circulate in the Arctic, which keeps colder air across the polar region. Westerlies bring warmer and wetter winter conditions to Asia but generate drought conditions in the Mediterranean (Thompson and Wallace, 2000; Rohman, 2014; He et al., 2017). In its negative phase, the pressure pattern is in reverse. Thus, the wind belt becomes weaker, and Arctic airmasses penetrate mid-latitudes; cold Arctic air comes to Asia, and strong westerlies push warm air and more precipitation into the Mediterranean (Rohman, 2014).

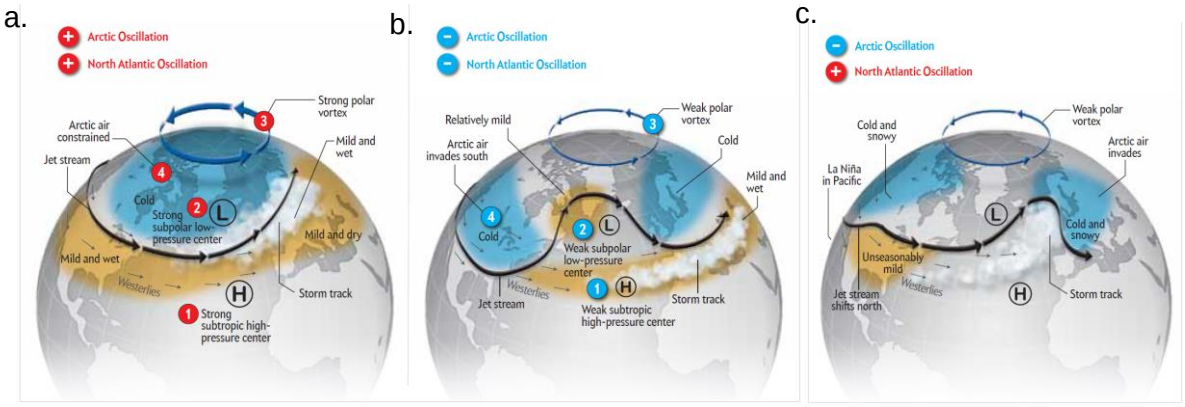

Figure 2.12: Different states of the Arctic Oscillation (AO) and the North Atlantic Oscillation (NAO). Positive AO and NAO states (a), negative AO and NAO states (b), positive AO and negative NAO states (c). The centers of high (circled H) and low (circled L) pressure systems over the Northern Atlantic indicate NAO phases. 1-subtropics, 2-subarctic, 3 -polar vortex, 4-cold Arctic air (Source: Greene, 2012).

2.2.3.3 NINO3.4 index or ENSO pattern

Several sea surface temperature indices are applied to monitor different regions of the tropical Pacific Ocean (Figure 2.13). All indices are sea surface temperature anomalies (SSTA) averaged across their corresponding Niño 1, 2, 3.4, and 4 regions. Ship tracks cross these regions and measure sea surface temperature (SST). The NINO3.4 index is commonly applied to define El Niño and La Niña events, but others help to characterize the features of each event (Trenberth, 2020). Measurement of the NINO3.4 anomaly has estimated by Huang et al. (2017), from January 1854, using the 2° x 2° gridded Extended Reconstructed Sea Surface Temperature data (Version 5) from the National Oceanic and Atmospheric Administration. The NINO3.4 anomaly is the area-averaged equatorial SSTs over a region bounded by 5N-5S and 170W-120W of the Pacific and normalized to the base period 1981-2010 (Huang et al., 2017). For details, see the metadata of monthly relative NINO3.4 at https://climexp.knmi.nl/.

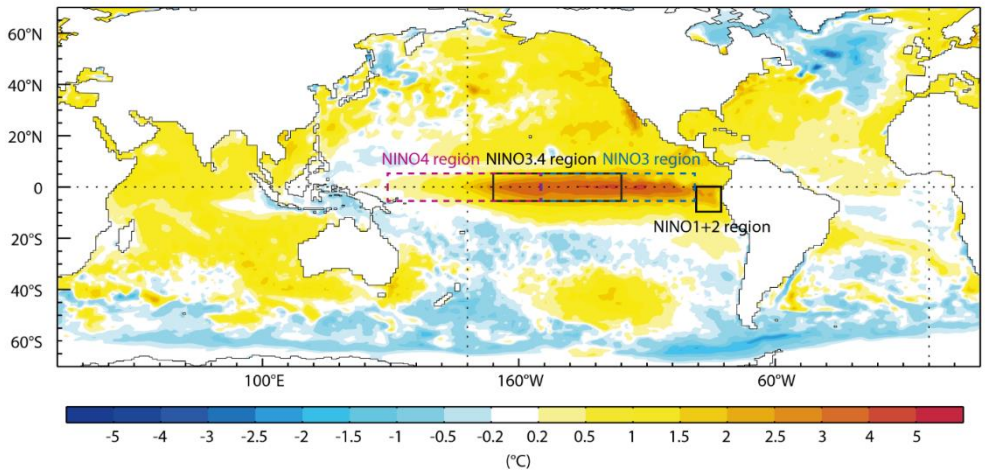

Figure 2.13: Niño 1, 2, 3.4 and 4 regions of the tropical Pacific Ocean and spatial structure of the El Niño at its peak in November 2015 (Source: Stockdale et al, 2017).

El Niño-Southern Oscillation (ENSO) is the most influential natural climate pattern operating in the world's largest ocean- the Pacific Ocean. There are opposite El Niño and La Niña phases. A warming of the surface waters in the central and eastern Pacific Ocean at the Peruvian coast is called El Niño (Rojas et al., 2014). In addition to the tropics, ENSO can affect temperature and precipitation across mid-latitudes by modifying the jet streams in winter (Lindsey, 2016). El Niño events affect wind and rainfall patterns globally (Rojas et al., 2014), as well as snow cover and surface temperatures over the Northern Hemisphere (Dagvadorj et al., 2014).

Trenberth (2020) explains that easterly trade winds weaken across the Pacific during El Niño. Thus, warm water in the eastern Pacific surges eastward along the equator and moistens the overlaying air. The warm and moist air rises into the atmosphere through convection. Thus, lower than normal surface air pressures develop over the central and eastern Pacific, along the west coast of South America, parts of South America near Uruguay, and southern parts of the United States in winter, producing heavy rains and flooding, whereas higher pressures develop over Australia, Indonesia, Southeast Asia, and the Philippines, bringing drier conditions (Trenberth, 2020).

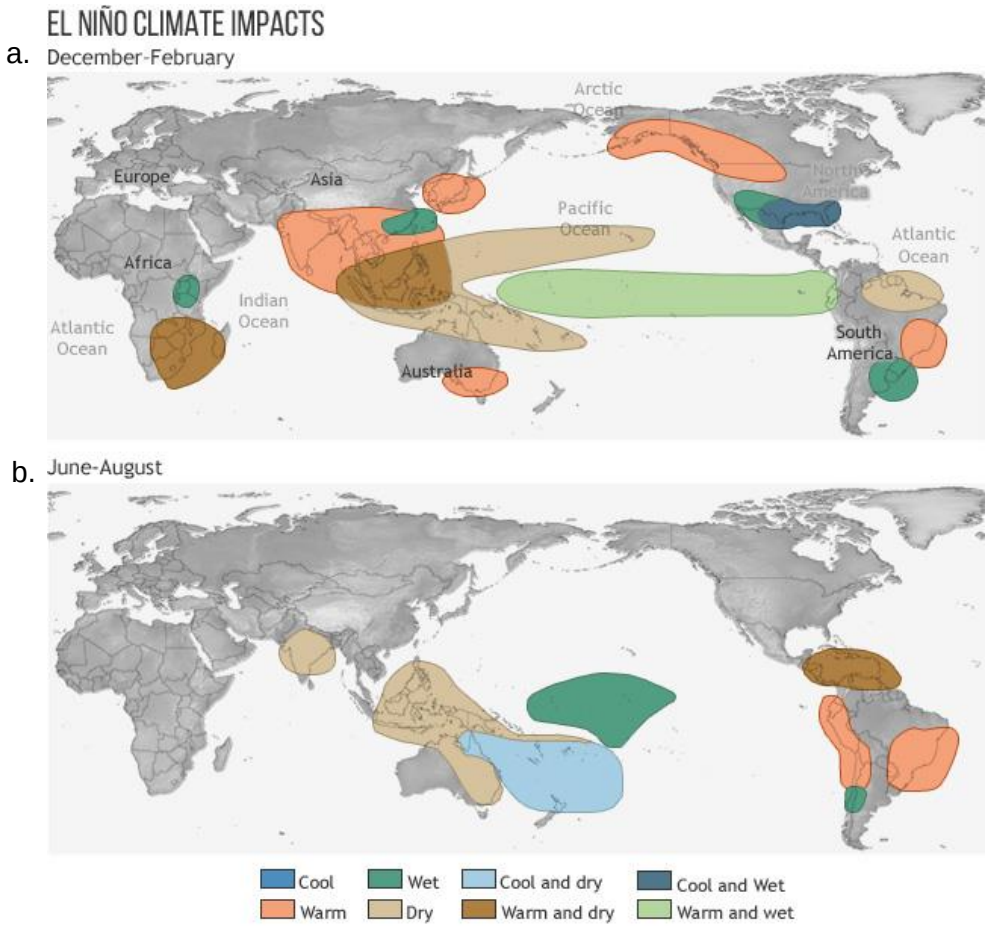

Figure 2.14: El Niño climate impacts: winter (a) summer (b) (Source: Lindsey, 2016).

The regional sea surface temperature becomes higher than normal during El Niño events (Figure 2.14), and lower than normal during La Niña events (Figure 2.15). Regions under dry conditions during El Niño events tend to become wet during La Nina events (Trenberth, 2020).

Rojas et al. (2014) found that the El Niño events of 2002/2003, 2004/2005, and 2006/07 produced droughts in Mongolia, and Dagvadorj et al. (2014) noted that the prolonged La Niña event of 1998/2001 brought 3 consecutive years with heavy-snow winters to Mongolia after the strong El Niño event of 1997/1998.

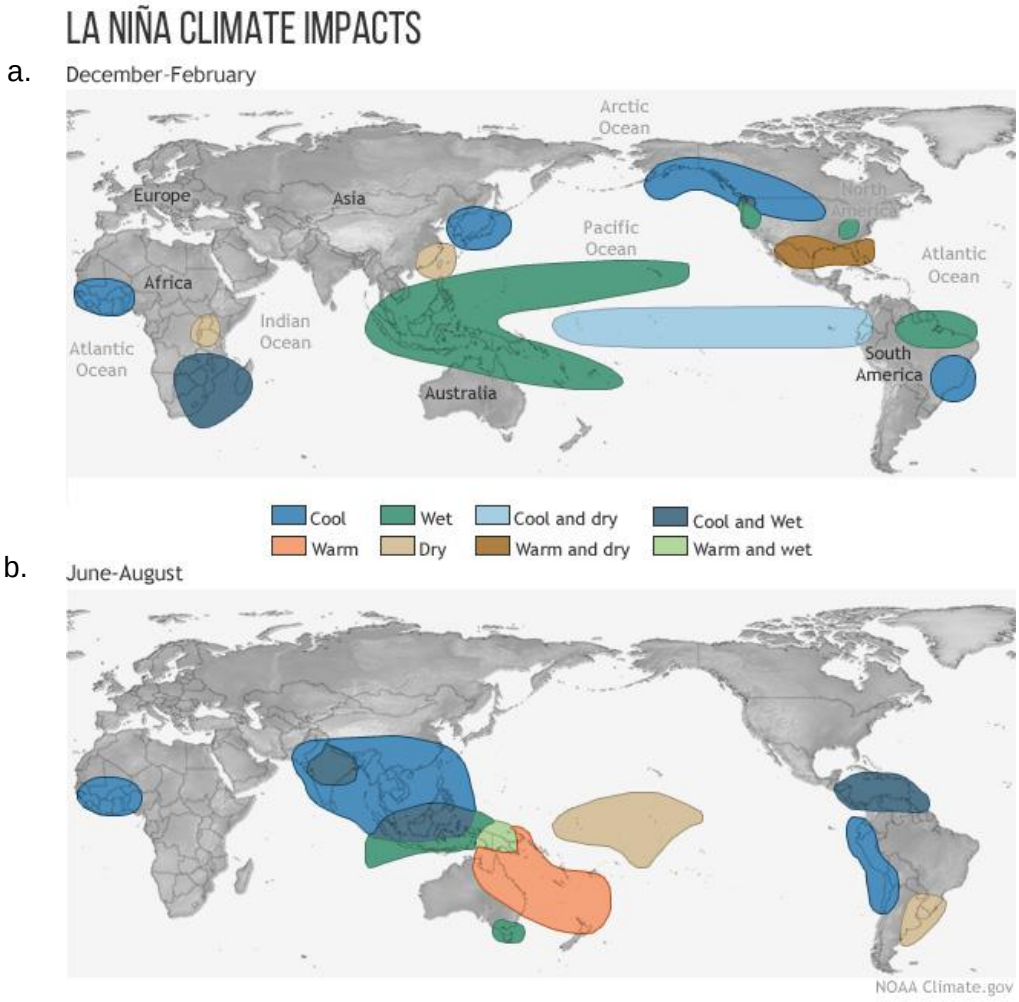

Figure 2.15: La Niña climate impacts: winter (a) summer (b) (Source: Lindsey, 2016).

In summary, El Niño leads to dry conditions in Mongolia but La Niña brings snowy winters.

2.2.4 Instrumental and gridded climate datasets

The Altai Mountains' climate stations are all located in the valley; thus, rain gauge observations might suffer from undercatch depending on slope direction, wind, and evaporation (Duethmann et al., 2013). Therefore, we used the Asian Precipitation-Highly-Resolved Observational Data Integration Towards Evaluation (APHRODITE) dataset (0.25ºx0.25º) in our climate impact study in addition to the station data since the APHRODITE has been shown to provide good estimates of temperature and precipitation amounts over high mountains and other data-scarce regions (Ji et al., 2020; Shen et al., 2018). The APHRODITE dataset consists of daily mean temperature and rain gauge–based daily precipitation accounting for the topographic effects (Yatagai et al., 2012).

APHRODITE precipitation data is an interpolated time series using datasets of the Global Historical Climatology Network (GHCN), National Climate Data Center (NCDC), Food and Agriculture Organization of the United Nations (FAO), Global Telecommunication System (GTS), and national institutes of hydrometeorology. Their spatial interpolation scheme considers the effect of mountain ranges by giving higher weights to gauges on windward sides and lower weights to rain gauges on leeward sides (Yatagai et al., 2012).

The APHRODITE dataset was evaluated by estimating the difference and Pearson's correlation coefficient between climate station data in the Bulgan catchment and their corresponding grid cell data. Moreover, areal climate input data was estimated at the mean elevation of the catchment from meteorological stations and the corresponding 25 grid cells of the APHRODITE dataset on daily time scales for hydrological simulations using the Thiessen polygon and annual lapse rates of temperature and precipitation. The observation period for the APHRODITE is longer than the whole observation period of stations in the southern Altai Mountains (Table 2.5). Precipitation and temperature of the APHRODITE cover the periods 1951-2015 and 1961-2015, respectively.

Table 2.5: Dataset information in hydrological study of the Bulgan catchment

No	Climate station	Lat	Lon	Elevation, m a.s.l	Period	Missing periods (%)
1	Baitag	46.09	91.55	1186	1963-2017	NA
2	Duchinjil	46.93	91.08	1951	1977-2017	NA
	Gauge stations					
1	Bulgan-Bulgan	46.93	91.08	1937	1984-2016	0.77
2	Bulgan-Baitag	46.12	91.56	1178	1984-2016	0.25
	APHRODITE (0.25ºx0.25º grids)					
1	Precipitation				1951-2015	NA
2	Temperature				1961-2015	NA

NA- Not available

2.2.5 Global and regional climate models

Dynamically and statistically downscaled outputs of two regional climate models (RCM) and their driving global climate models, HadGEM2-AO and CanESM2, are evaluated and corrected with observations in the Bulgan catchment to estimate the hydrological impact of future climate change under two Representative Concentration Pathway (RCP) scenarios, RCP4.5 and RCP8.5 (Figure 2.16 and Table 2.6). To avoid errors from model parameterization at a single grid cell (Demirel et al., 2013), averages of the corresponding 4 grids of GCMs and 12 grid cells of RCM covering the Bulgan catchment were transferred into a catchment average.

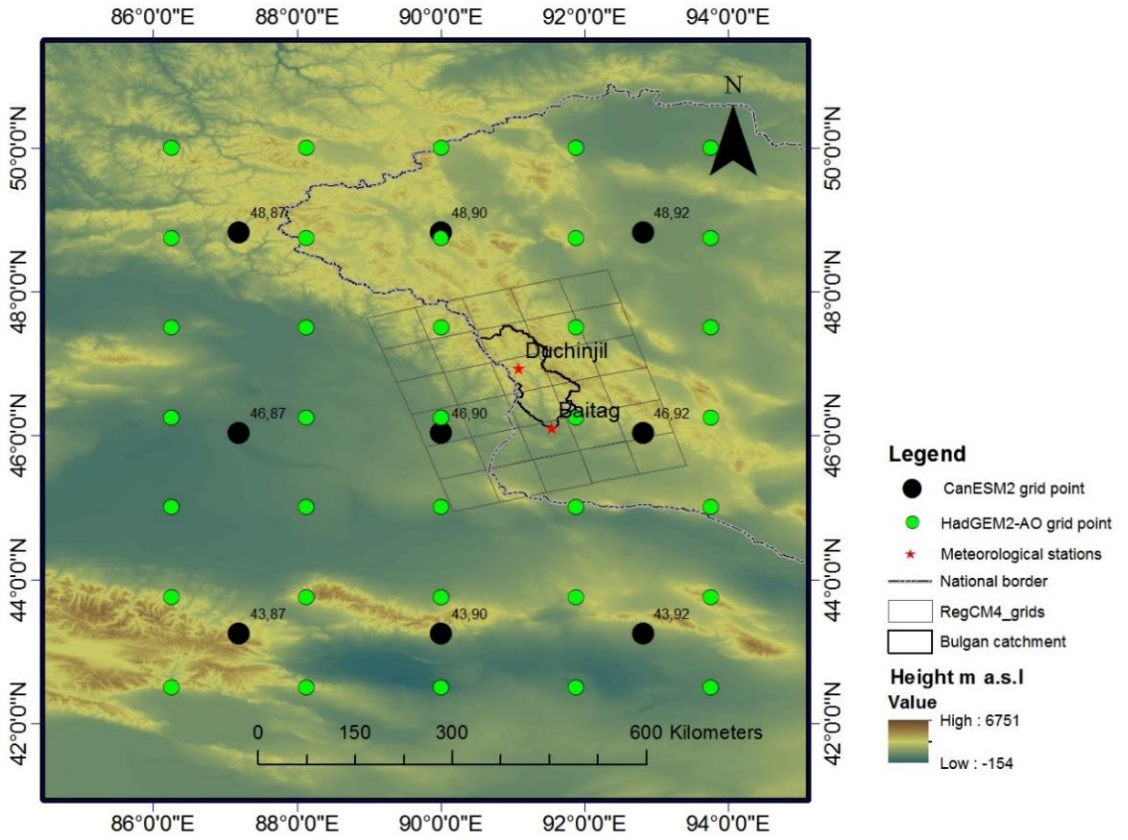

Figure 2.16: Spatial resolutions of the selected GCMs and RCMs in the Altai-Dzungarian region. The grids of the CanESM2 and HadGEM2-AO are marked by black and green dots, respectively. The grid cells of the RegCM4 are illustrated by black rectangles to display climate stations and Bulgan catchment transparently.

Table 2.6: Overview of GCMs and the corresponding RCM with different downscaling approaches

GCM	RCM	Downscaled approach of RCM
CanESM2 (311km x 311km) 365 days	SD_CanESM2	Statistically downscaled at two stations in Bulgan catchment using SDSM software - weather generator and linear regression
HadGEM2-AO (135kmx135km) 360 days	RegCM4 (50kmx50km)	Dynamical downscaled dataset of CORDEX- East Asia

The CanESM2[9] (second generation of the Earth System Model, 2.8°x 2.8°) is the fourth generation of the coupled global climate model (CGCM4) developed by the Canadian Centre for the Climate Modeling and Analysis of Environment Canada (Radojevic, 2014).

HadGEM2-AO (135km resolution), developed by Korean Meteorological Institute, shows good performance on global and East Asian climate variability. Although GCMs do not accurately show regional climate on a fine geographic or temporal scale, outputs from GCMs can be used to understand the range of uncertainty.

To fill the gap of GCMs accuracy, the dynamical downscaled regional climate model version 4 (RegCM4) with 18 vertical sigma levels over CORDEX East Asia was used in this study to represent regional characteristics and topography in future climate and runoff change assessment. The RegCM4 uses HadGEM2-AO as a boundary condition and is available from 1979 to 2050 with 50 km resolution (0.44˚ x 0.44˚) in RCP 8.5/4.5 (Oh et al., 2014).

CORDEX is an international collaborative project known as the Coordinated Regional Climate Downscaling Experiment established by the World Climate Research Program (WCRP), it provides a quality-controlled dataset of downscaled information for historical and future climate and changes (Park et al., 2016).

Using the SDSM software, grid cell data of the CanESM2 over the study area are evaluated using observations at Duchinjil and Baitag stations and statistically downscaled at the station level on the daily time scale.

[9] http://ccds-dscc.ec.gc.ca/ pred-canesm2

2.3 Methodology

2.3.1 Past climate reconstruction using tree ring proxy data

2.3.1.1 Cross-dating and Standardization

The tree cores sampled at each site were marked with calendar dates and visually cross-dated using so-called pointer years (isolated years with exceptionally narrow or wide rings). During cross-dating, the tree-ring width series were scanned for potential missing and false rings. By matching the tree-ring width patterns among the cores and by examining the ring structure (Fritts, 1976), mean chronologies based on common growth sequences of the trees were derived and compared to all cores from a site to detect missing, partial, and false rings formed e.g. under severe growth conditions.

The tree ring-widths were measured to the nearest 0.001mm with a Velmex measuring system and the MeasureJ2X software (Velmex, Inc., Bloomfield, NY, U.S.A). The measurement accuracy and the visual cross-dating among the individual tree chronologies at each site were checked by statistical cross-dating using COFECHAv6.06 (Grissino-Mayer, 2001), which calculates Pearson's correlation coefficients between segments of individual ring-width series and a master chronology consisting of all other series at the dated position and ten positions forward and backward. Flagged, i.e. potentially incorrectly dated segments, were re-examined and corrected when missing or false rings in that ring-width segment were found.

Standardized indices were calculated from the individual tree ring-width series by fitting a Friedman super smoother growth curve with alpha 5, and dividing each ring-width for a certain year by the value of the growth curve (Figure 2.17a, c). This data-adaptive smoothing technique (implemented in ARSTAN for Windows, version ARS41c_xp, Cook et al., 2006) preserves the low frequency variance (Friedman, 1984) and removes effects of aging and other non-climatic trends from the series (Cook, 1985). The standardized indices from the individual cores were then averaged to obtain the site chronology (Fritts, 1976).

The same detrending procedure was applied to all series. Some cores of the six sites came from lower-treeline trees, which contained logging effects from the past 50 years. These effects were most effectively removed by a Friedman super smoother curve with alpha 5. Although the latter is rather flexible and potentially removes longer-term (>100 yrs) trends, low-frequency variance was preserved as shown through the application of more conservative detrending procedures, which had very similar outcomes.

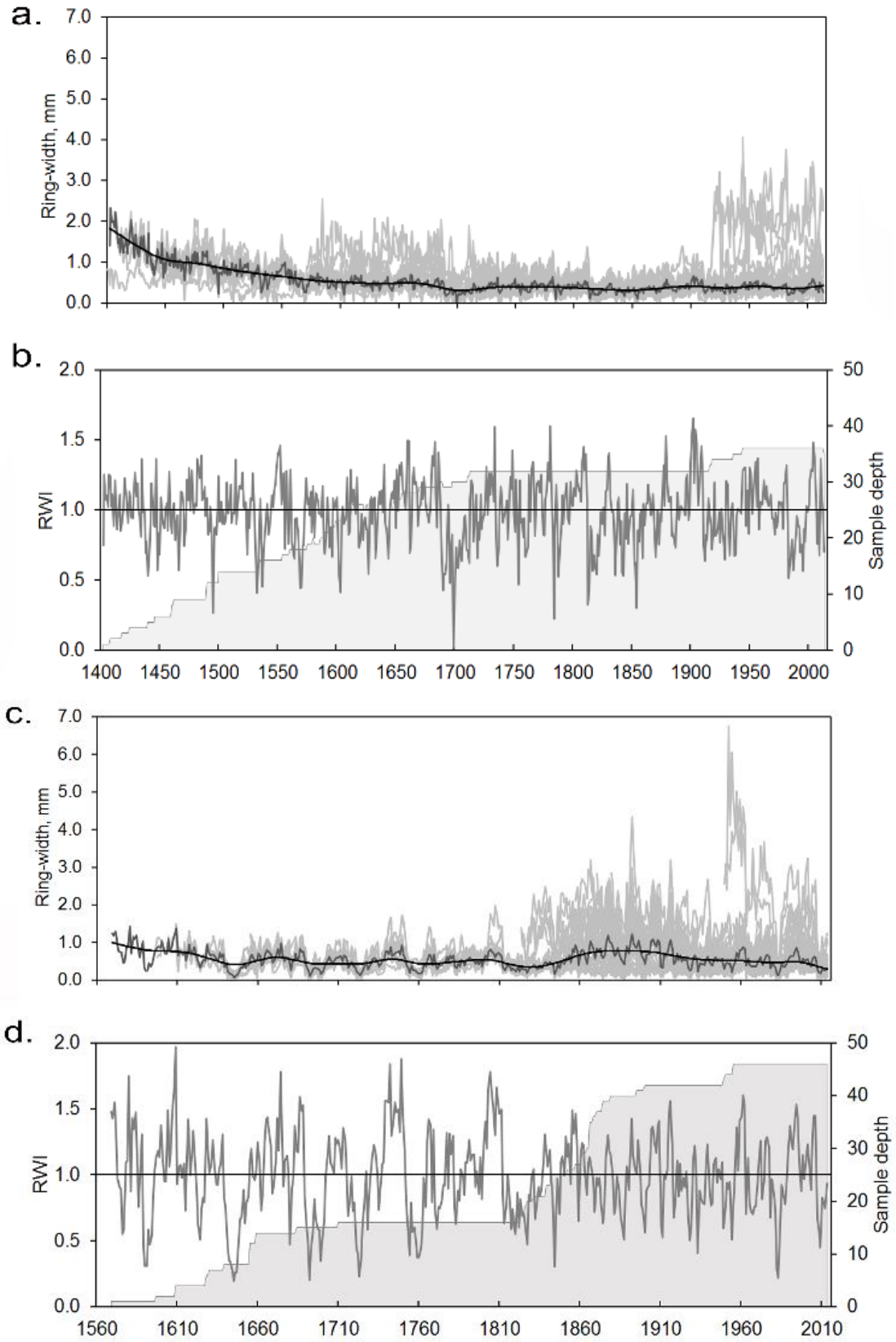

Figure 2.17: Mean *Larix sibirica* ring-width chronologies (dark grey) for the KAR (a) and KET (c) sites with a fitted Friedman super smoothing curve with an alpha of five (black line) and individual ring-width series (light grey lines). The mean standardized KAR and KET chronologies (Ring-Width Index; RWI) are shown in b and d, respectively, together with the sample depth.

The climate signal strength within a site chronology and its reliability are commonly described by its mean sensitivity, Expressed Population Signal (EPS), and the mean correlation between the individual tree-ring series ($\bar{r}$). The mean sensitivity is the relative difference between adjacent ring widths and indicates the range of the year-to-year variations in radial growth in response to climate (Fritts, 1976).

EPS quantifies the strength of the common signal in a given set of tree-ring series used for a chronology (Cook and Kairiukstis, 1990; Wigley et al., 1984) and is based on $\bar{r}$ and the sample size. Wigley et al. (1984) suggested 0.85 as a lower acceptable threshold for the EPS. $\bar{r}$ is a measure for the common growth signal or the common variance between all tree-ring width series. $\bar{r}$ and EPS were calculated with ARSTAN for all tree-ring series contributing to one chronology in 50-year intervals with 25 years overlap. The actual computation of the standardized chronologies, which are later used for the climate reconstruction are shown in Figure 2.17b, and 2.17d.

2.3.1.2 Climate-growth response analysis

Precipitation and temperature are growth controlling climate factors, since they affect soil moisture availability, tree transpiration and respiration, and photosynthesis (Fritts, 1966). Growth of Siberian larch in the Altai Mountains mainly occurs between April and September. Although cell division and lengthening ceases at the end of the growing season, thickening of the tracheid cell walls might continue depending on the weather conditions (Chen et al., 2012). Hence, correlations were tested between the site chronologies and both monthly and seasonal mean air temperature and precipitation sums. DendroClim2002 was used (Biondi and Waikul, 2004) to estimate the relations between monthly climate variables and tree ring widths for the time period of available instrumental and gridded climate data. DendroClim2002 uses 1000 bootstrapped samples to compute Pearson's correlation coefficients and their significance. Significances were tested at the $p<0.05$ level.

The standardized chronologies for all sites were correlated with the monthly mean temperatures and precipitation sums from the Duchinjil station, the monthly mean regional air temperature as estimated by the averaged longer time series of five climate stations including the Baitag, Khovd, and Ulgii in Mongolia, and the Fuyun and Altay in China, the monthly precipitation sums from the Qinghe station, monthly temperature means and precipitation sums from the CRU TS4.01 dataset, and the monthly mean scPDSI, the latter two averaged over the area from 46°N to 47°N and 91°E to 92°E. Correlations were determined for all months of a 18 months window starting May of the year prior to growth and October of the current year of growth. The monthly and seasonal climate data most significantly correlated with the site chronologies were selected for setting up transfer models for climate reconstructions.

2.3.1.3 Regression model development for summer air temperature and precipitation reconstruction

Transfer functions between the chronologies (predictor) and the climate parameters (predictand) were developed for the individual site chronologies using simple linear regression. If tree growth correlated with the climate conditions of both the previous and the current year, the site chronology and its lag by one year relative to the climate observations were considered as predictors. In addition, the first principal component of these predictors resulting from a Principal Component Analysis (PCA) of the complete time series was also used as predictor.

The reliability of the resulting transfer functions was assessed via calibration and verification statistics commonly used in dendrochronology, i.e. Pearson's correlation coefficient (r), Coefficient of Determination (R^2), Reduction of Error (RE), Coefficient of Efficiency (CE), Product Mean (PM) test, and first difference sign test (Cook et al., 1999; Weijers et al., 2010). r quantifies the association between tree rings and climate while the percentage of explained variance by the ring widths is given by R^2. RE and CE range between minus infinity and one with positive values close to one indicating good skill and negative values lower skill (Cook et al., 1999; Fritts, 1976; Weijers et al., 2010). The PM test (Fritts, 1976) takes into account both sign and magnitude of the actual and estimated departure from the mean value, while the non-parametric first difference sign test uses only the sign of change to quantify similarities between two series.

These calibration and verification statistics were calculated over separate periods while the full calibration periods, i.e. the complete overlapping periods between climate and tree-ring data, were used for the construction of the transfer functions. Besides the individual site chronologies, separate networks of regional tree-ring chronologies for temperature and precipitation were constructed from the first principal components of two or more individual site chronologies sensitive to the same climate condition over the overlapping periods and applied in the development of regional climate transfer functions to verify our climate reconstructions based on single-site chronologies.

2.3.2 Teleconnections between atmospheric indices and regional climate variability

To reveal the effect of large-scale atmospheric circulations on regional climate variability, the monthly and seasonal NAO, AO, and NINO3.4 indices were first spatially correlated with gridded data of CRU TS4.03 precipitation and temperature of the region using https://climexp.knmi.nl/, then correlated with estimated temperature and precipitation over the same period of 1960-2012. To specify the influence of the indices on the local climate of

the tree sampling sites in the southern Altai Mountains from regional teleconnections, all monthly indices were also correlated with the estimated and observed June-July temperature and June through December precipitation at the nearest Duchinjil station to the tree sampling sites for the whole observation period of 1977-2012.

Interannual variations of the ocean surface conditions are driven by wind-induced changes in the air-ocean energy fluxes, but interdecadal variations (~ 20 years) involve changes in the ocean circulation (Hurrel, 1995). Thus, all monthly and seasonal time series of the indices and the estimated temperature and precipitation are smoothed with a running 21-year averaging window in this study and correlated to find out their relationships at a low-frequency level, which suggest potential teleconnections of the atmospheric indices and possible mechanism.

Finally, we conducted a 25-year running correlation to reveal non-stationarities in the relationship between the significantly influencing monthly indices and the estimated temperature and precipitation over the Altai-Dzungarian region on the interannual time scale. Significance levels of the correlations were calculated based on the Fisher transform of r-values to normal Z values (Lenhard and Lenhard, 2014).

2.3.3 Trend analysis of observed climate and runoff change

2.3.3.1 Mann Kendall test and nonparametric Sen's slope

To quantify climate and hydrological change over the period of 1984-2015, the presence of monotonic increasing or decreasing trends in annual and seasonal temperature, precipitation, evapotranspiration, and river discharge time series are tested with the Mann-Kendall test. The slopes of the linear trends were estimated with the non-parametric Sen's slope, which is not affected by outliers or single data errors and a skewed distribution (Salmi et al., 2002).

The presence of statistically significant trends in time series was evaluated by the normal distributed and the two-tailed Z test at the 0.001, 0.01, 0.05, and 0.1 levels. Its positive/negative sign defines an upward (downward) trend (Salmi et al., 2002). Sen's non-parametric method is used to calculate a change per year or the true slope of the existing trends in the all-time series. Also, the 95% confidence intervals of the slopes are estimated. Since there is no measured evaporation data from the climate stations, we calculated reference evapotranspiration based on daily mean temperature time series as outlined in the next chapter 2.3.3.2.

2.3.3.2 Reference evapotranspiration estimation for semi-arid area

Reference evapotranspiration (ET_0), is the evapotranspiration rate from a well-watered grass-covered soil with a vegetation height of 0.12m and completely shaded ground by actively growing grass, a fixed surface resistance of 70sec/m, and an albedo of 0.23 (Allen et al 1998).

The Penman-Monteith approach (ET_0-PM) is recommended as the standard method for calculating the reference evapotranspiration by the FAO-56 guideline, but requires full climate data, including relative humidity and wind speed. For this data-limited region, we examined the performance of alternative ET_0 methods. Previous studies have suggested that the temperature-based modified Hargreaves-Samani as the best alternative to ET_0-PM for China that showed spatiotemporally the best accuracy and correlations to ET_0-PM among other methods in different subregions of mainland China (Berti et al., 2014; Peng et al., 2017).

In this study, we estimated evapotranspiration (ET_0) for the Duchinjil and Baitag stations using Penman-Monteith (ET_0-PM) (Juetten, 2015; Eq.1) as the reference value to evaluate the performance of the alternative temperature-based ET_0 methods for the southern Altai Mountains, the 1975 Hargreaves equation, Hargreaves-Samani and modified Hargreaves-Samani (Table 2.7). Mean absolute errors (MAE) and Nash-Sutcliffe efficiency coefficients (R_{eff}) are calculated for each alternative temperature-based ET_0 by comparing to ET_0- PM at daily time scale.

Table 2.7: FAO Penman-Monteith and temperature based empirical ET_0 methods

No	Abbreviation	Equation	Reference
1	FAO-56 Penman-Monteith (ET_0-PM)	$ET_0=\frac{\mathbf{0.408}\,\Delta\,(R_n-G)+\gamma\frac{900}{T+273}u_2\,(e_s-e_a)}{\Delta+\gamma(\mathbf{1}+\mathbf{0.34}\,u_2)}$ Eq.(1)	Allen et al.,1998
2	1975 Hargreaves (ET_0-H)	$ET_0=0.0135\ R_s\ (T_{mean}+17.8)$ Eq.(2)	Hargreaves and Allen, 2003
3	Hargreave-Samani (ET_0-HS)	$ET_0=0.0023\ (T_{mean}+17.8)\ (T_{max}-T_{min})^{0.5}R_a$ Eq.(3)	Hargreaves and Allen, 2003
4	Modified Hargreave-Samani (ET_0-MHS)	$ET_0=[0.00193\ R_a\ (T_{mean}+17.8)\ (T_{max}-T_{min})^{0.517}]\lambda$ Eq.(4)	Berti et. al. 2014

Eq. (1) of ET_0-PM reference evapotranspiration (mm/day) demands R_n the net radiation at the crop surface (MJ/m^2 day), G the soil heat flux density (MJ/m^2 day), T the mean daily air temperature at 2m height (˚C), u_2 the wind speed at 2m height (m/s), e_s the saturation vapor

pressure (kPa), e_a the actual vapor pressure (kPa), Δ the slope of the saturation vapor pressure curve with temperature (kPa/˚C), and γ the psychrometric constant (kPa/˚C).

In Eq. (2), R_s is the total solar radiation at the surface (mm/day) calculated from extraterrestrial radiation (R_a, MJ/m^2 day) by multiplying the conversion factor 0.408 from MJ/m^2 day into mm/day. In the FAO-50 guideline, this conversion factor is defined as the inverse of the latent heat of vaporization 1/λ=0.408 (Allen et al., 1998).

Eqs. (3) and (4) require only maximum (T_{max},˚C) and minimum (T_{min},˚C) temperatures and extraterrestrial radiation (R_a, MJ/m^2 day) for calculating reference evapotranspiration. λ is the latent heat of vaporization and varies slightly in the normal temperature range, so a single value of 2.45 MJ/kg is taken (Allen et al., 1998).

Daily extraterrestrial radiation (R_a, MJ/m^2 day) is extracted from the dataset with 0.5˚x0.5˚ grids of NASA Prediction of Worldwide Energy Resource (POWER) for the period of 1984-2018 (https://power.larc.nasa.gov/data-access-viewer/, 18 June 2019).

2.3.4 Hydrological impact assessment of climate variability and change

The hydrological impact of climate variability can be quantified as the percentage change in annual discharge in response to a change in annual precipitation and potential evapotranspiration (Ma et al., 2008). The equation of the water balance for a catchment:

$$P=ET+R+\Delta S$$

where P is precipitation, ET is evapotranspiration, R is surface runoff measured as river discharge, and ΔS is the change in catchment water storage. ΔS can be assumed to vanish for a sufficiently long period (Ma et al., 2008; Zhang et al., 2001).

Based on a water balance concept, some researchers have examined correlations between the seasonal variation of discharges and seasonal air temperature and precipitation sum to reveal the impact of climate change on river discharge in the high mountains of the Qinghai-Tibet Plateau (Fan and He, 2015), the Hengduan Mountains in southwest China (Ma et al., 2008), and the Qilian Mountains in northwest China (Wang et al.,2019).

River discharge is an output of the different catchment processes (Ma et al., 2008). Therefore, this study developed *Stepwise Regression Models* to assess the impact of climate change on the seasonal distribution of the Bulgan River runoff and run *a semi-distributed HBV-light model* to estimate changes in the water balance of the Bulgan catchment and to determine runoff sensitivity to climate change.

2.3.4.1 Stepwise linear regression

We developed Stepwise Linear Regression Models to determine the most influencing climate factors on the Bulgan River runoff. The areal mean precipitation and temperature of the Bulgan catchment are estimated using the Thiessen polygon. Also, measured discharge (m^3/s) at the hydrological stations is converted into surface runoff (mm). Then, we used the areal mean precipitation and temperature as predictors and the surface runoff of the catchment as predictand in the stepwise linear regression model.

The stepwise regression is performed using a combination of forward (step-up) selection and backward (step-down) elimination. The forward selection starts with the predictor best correlated with the predictand, then adds a potential second predictor based on the increase of explained variance and the significance of the F parameter (must be less or equal to 0.05 at each step, Urhausen, 2012). If the selected predictor becomes insignificant, the backward method removes those predictors from the regression with a probability of F of greater or equal to 0.10. For detail, please Wilks (2006) and Urhausen (2012).

Standardized Betas in the stepwise regression models are percentages of explained variations impact factors of those climate variables (or predictors) on the seasonal and annual runoff.

In addition, we used Stepwise Linear Regression to reveal important climate factors affecting regional evapotranspiration. In this case of the regression model development, reference evapotranspiration estimated by Penman-Monteith at the station is applied as a predictand, whereas maximum and minimum temperatures, precipitation, wind speed, relative humidity, and radiation are predictors.

2.3.4.2 HBV-light model

The HBV-light model is a conceptual rainfall-runoff model that simulates daily discharge based on daily rainfall and temperature, and monthly estimates of potential evapotranspiration. HBV-light is a semi-distributed model that uses subcatchments as hydrological units; moreover, elevation zones and land cover classification (forest, open, and lake) are described for each subcatchment (Bergström, 1992; Seibert, 2000; Seibert and Vis, 2012).

Based on the two hydrological stations along the Bulgan River, the catchment is divided into an upper and a lower subcatchment. The elevation of the Bulgan catchment ranges from 1185m to 4160m above sea level. The catchment area is divided into 15 elevation zones with 200m intervals. Areal mean temperature and precipitation are calculated for the mean

elevation of each subcatchment using the Thiessen polygon, then they are corrected from the mean elevation for each elevation zone assuming constant lapse rates.

The forested area is calculated using the Percent Tree Coverage Global map Version 1 from the Geospatial Information Authority of Japan, Chiba University (accessed on 12 May 2019, https://globalmaps.github.io/ptc.html). Glaciated areas are estimated using the glacier area of 2000 and 2001 created by Kamp (2012) in the database of Global Land Ice Measurements from Space (accessed 31 March 2019, http://www.glims.org/). Lake and Digital Elevation Model data are obtained from the WWF Mongolia database (accessed in January 2012, http://mongolia.panda.org/web_gis/).

HBV-light consists of four routines: snow, soil moisture, response, and routing (Figure 2.18). The snow and soil routines are performed separately for each elevation zone, whereas the response and routing routines are lumped for the catchment.

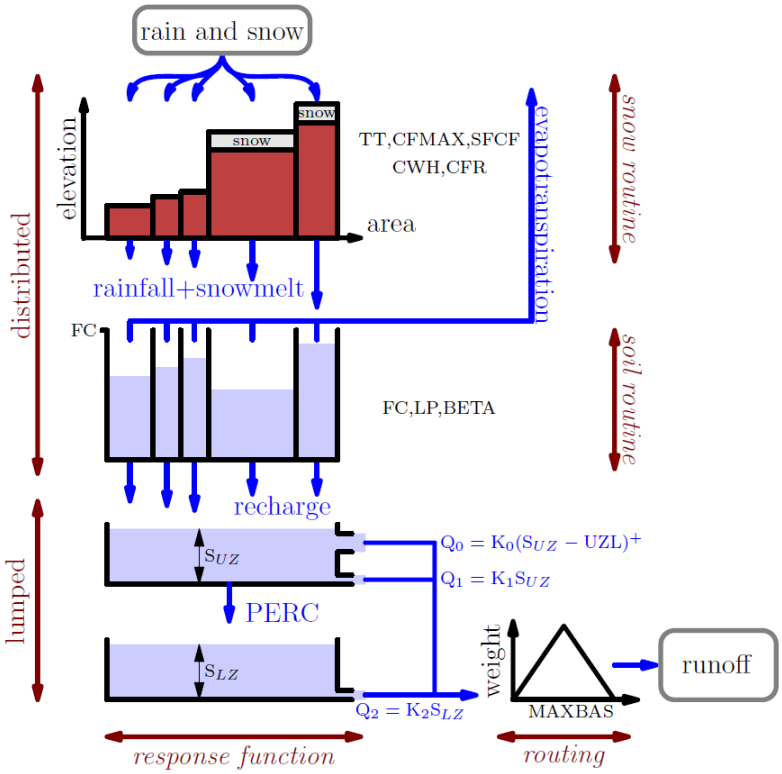

Figure 2.18: Schematic of the HBV-Light 4.0 model (Seibert, 2000). See description of the parameters in Table 2.8.

The 16 parameters of the four routines have a physical basis, but their values are derived by model calibration (Seibert, 2000). The snow routine controls snow accumulation and melt using temperature threshold values and the degree-day method (Bergström, 1992).

Groundwater recharge and actual evapotranspiration are computed in the soil moisture routine, and excess water from the soil moisture routine is transformed into a runoff by three linear reservoir equations in the response routine. Then the routing routine smooths the

runoff of the response routine by a triangular weighting function and generates total runoff (Bergström, 1992; Seibert, 2000; Seibert and Vis, 2012).

Rivers of the Altai Mountains are mainly fed by the meltwater of snow from April to June and glaciers from July to August (Davaa, 2015); furthermore, the rivers are sustained by seasonal thaws of permafrost from May to September (Sharkhuu, 2003). Thus, glacier routine and delay response function are added to the model structure. The glacier routine works between the snow routine and the soil routine and calculates the melting glacier and the modification of snow into ice using the degree-day method.

Seasonal thaw of the permafrost increases the deeper groundwater flow and alters the runoff temporarily through increasing hydrologic permeability with ice loss in soil pores and the release of water stored in frozen ground (Gruber et al., 2017). Thus, the “Delayed response” of deep groundwater with parameters DELAY and PART allows the representation of a temporal effect of the permafrost in the water distribution (Figure 2.19). The PART [0-1] parameter gives the fraction of the recharge to the Soil upper zone S_{UZ}, but the remaining recharge is evenly distributed to the subsequent period of DELAY [days] and the Soil lower zone S_{LZ} (Seibert, 2005).

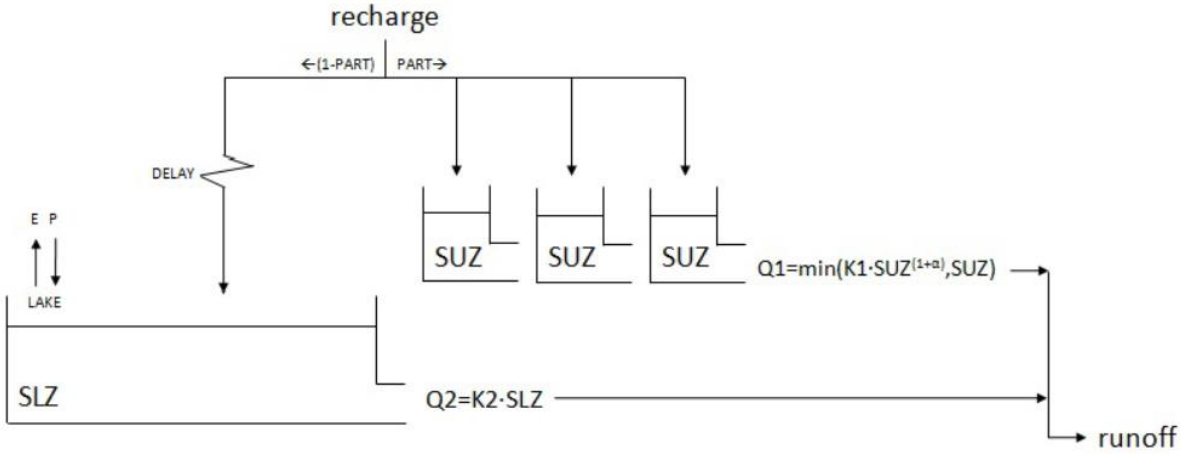

Figure 2.19: Schematic view of the Response routine with delay model (Seibert, 2005): recharge - Input from soil routine [mm/ Δt], DELAY - Period of delay for water added to the soil lower zone [Δt]; PART-Portion of the recharge added to the soil upper zone SUZ - Storage in soil upper zone [mm], SLZ - Storage in soil lower zone [mm], Ki - Recession coefficient [1/Δt]; Qi - Runoff component [mm/Δt], E - Evaporation from the lake P - Precipitation into the lake; and runoff = Total amount of generated runoff [mm/Δt]

2.3.4.2.1 Model calibration

As recommended in the manual of the HBV-light model (Siebert, 2005), the calibration period should cover a variety of hydrological events and 5 to 10 years; we chose a calibration period from 1985 to 2005 and a validation period from 2006 to 2015. One year of warm-up is required to evolve the appropriate values from the initial values based on meteorological conditions and parameters (Seibert and Vis, 2012). Thus, the first year (1984) of the time

series is applied as the warm-up period. Most parameters of the conceptual rainfall-runoff models are not measurable but estimated by calibration with observed runoff (Siebert, 2000).

The automatic model calibration GAP tool, Genetic Algorithm and Powell optimization, is used for simulation rather than time-consuming and subjective manual calibration. This tool first generates optimized parameter sets within a user-defined parameter range then the parameter sets are fine-tuned by Powell's quadratically convergent method (Siebert, 2000; Seibert and Vis, 2012). According to the default setting of the GAP optimization, we simulated 5000 model runs for the genetic algorithm and 1000 runs for local optimization by Powell's method. This calibration aims to simulate hydrographs well-fitting to observed hydrographs. In a range of default values of the GAP tool, parameters are optimized for the Bulgan catchment (Table 2.8).

Table 2.8: Range of calibrated parameters for the Bulgan catchment in GAP optimization

Parameters	Unit	Min	Max	Description	Source
Snow routine					
TT	ºC	-2	2	Threshold temperature	Zhang et al. (2004)
CFMAX	mm/ ºC *day	1	14	Snowmelt degree day function	Davaa (2015)
SP	-	0.1	1	Seasonal variability in degree day factor	-
SFCF	-	0.5	0.9	Snowfall correction factor to compensate snow measurement and evaporation	-
CFR	-	0.05	0.05	Freezing coefficient of refreezing water in snow	Default values
CWH	-	0.1	0.1	Water equivalent of snow	Default values
CFGlacier	-	1	5	Glacier correction factor	-
CFSlope	-	1	5	Slope correction factor	-
Soil moisture routine					
FC	mm	100	550	Maximum soil moisture storage (SM)	Default values
LP	-	0.3	1	Threshold of reduction of evaporation (SM/FC)	Default values
Beta	-	0.1	4	Relative contribution to runoff from rain or snow	Heerema (2013)
Glacier routine					
KSI	1/day	0.001	0.1	Snow to Ice conversion factor	-
KGmin	1/day	0.01	0.2	Minimum outflow coefficient	Default values
dKG	1/day	0.01	0.5	Maximum minus minimum outflow coefficient	Default values
AG	1/mm	0	1	Calibration parameter	Default values
Response routine					
Alpha	mm/day	0	1	Non-linearity coefficient	Default values
K1	1/day	0.01	0.1	Recession coefficient (upper box, lower outflow)	-
K2	1/day	0.00001	0.1	Recession coefficient (lower box)	Default values
PART	-	0	1	Portion of the recharge added to the soil upper zone	Default values
DELAY	day	0	50	Period of delay for water added to the soil lower zone	Default values
Routing routine					
MAXBAS	day	1	2.5	Length of triangular weighting function	Default values

The following absolute error (%) of the model output is used to compare model variants and select the appropriate one. *n* is number of time steps. $\boldsymbol{Q_s}$ and $\boldsymbol{Q_o}$ are simulated and observed discharges, respectively (Aghakouchak and Habib, 2010).

$$\left|\frac{\sum_{i=1}^{n} \boldsymbol{Q_s^i} - \sum_{i=1}^{n} \boldsymbol{Q_o^i}}{\sum_{i=1}^{n} \boldsymbol{Q_o^i}}\right| \times \mathbf{100}$$

2.3.4.2.2 Weighted fuzzy objective function

In this study, the most common objective functions of hydrological models are used for model performance evaluation. The Nash-Suffcliffe efficiency (R_{eff}; Eq1) indicates the goodness-of-fit of the simulated runoff, especially during high flow periods; while the logarithmic efficiency ($LogR_{eff}$; Eq2) emphasizes low flows (Siebert, 2005). The influence of low flow values is increased in the sensitivity of $\boldsymbol{LogR_{eff}}$ because the peaks are flattened through a logarithmic transformation of the runoff values (Krause et al., 2005). The Volume Error (*VE;* Eq3) defines the total volume difference and long-term water balance by calculating the closeness between the averages of the observed and simulated runoff (Reynolds et al., 2017).

Seibert (2000) suggested to evaluate the overall model performance by a fuzzy measure ($\boldsymbol{X}$; Eq4), a weighted combination of different objective functions. Parameter uncertainty can be reduced by the fuzzy measure ($\boldsymbol{X}$) because different parameter sets might perform well for only one objective function but not for other functions (Seibert, 1997). The values of the objective functions are transformed into fuzzy measures, then the highest values are obtained and joined to compute the best possible parameter sets (Seibert, 1999).

Goodness of fit was evaluated with weights of R_{eff}, $LogR_{eff}$ and *VE*, 0.7, 0.2, and 0.1, respectively.

$$\boldsymbol{R_{eff}} = \mathbf{1} - \frac{\sum(\boldsymbol{Q_{obs}} - \boldsymbol{Q_{sim}})^2}{\sum(\boldsymbol{Q_{obs}} - \overline{\boldsymbol{Q_{obs}}})^2} \qquad \text{(Eq 1)}$$

$$\boldsymbol{LogR_{eff}} = \mathbf{1} - \frac{\sum(\ln \boldsymbol{Q_{obs}} - \ln \boldsymbol{Q_{sim}})^2}{\sum(\ln \boldsymbol{Q_{obs}} - \overline{\ln \boldsymbol{Q_{obs}}})^2} \qquad \text{(Eq 2)}$$

$$\boldsymbol{VE} = \mathbf{1} - \frac{|\sum(\boldsymbol{Q_{obs}} - \boldsymbol{Q_{sim}})|}{\sum(\boldsymbol{Q_{obs}})} \qquad \text{(Eq 3)}$$

$$\boldsymbol{X} = \mathbf{0.7}\,\boldsymbol{R_{eff}} + \mathbf{0.2}\boldsymbol{LogR_{eff}} + \mathbf{0.1}\boldsymbol{VE} \qquad \text{(Eq 4)}$$

Here Q_{obs} and Q_{sim} are observed and simulated runoff, and $\overline{\mathbf{Qobs}}$ is the mean value of the observed runoff. The $\boldsymbol{R_{eff}}$, $\boldsymbol{LogR_{eff}}$, $\boldsymbol{VE}$ and $\boldsymbol{X}$ values range between $-\infty$ and 1. These statistic measures have 1 if the simulation and observation agree (Siebert, 2005) and 0 if the model does not perform better than the mean value of the observed runoff (Bergström, 1992).

2.3.4.2.3 Bias correction of measured precipitation at Tretyakov gauge

To improve hydrological simulations, we corrected precipitation measurements at two Tretyakov gauge stations along Bulgan River using an approach of the World Meteorological Organization solid precipitation measurement intercomparison project.

Both solid and liquid precipitation is measured by the Tretyakov gauge with a windshield, a manually operated instrument with a special measure-cup with 0.1mm resolution (Zhang et al., 2004). Zhang et al. (2004) applied the bias correction approach developed by the World Meteorological Organization solid precipitation measurement intercomparison project to 31 stations in Mongolia to improve the accuracy of precipitation measurements. The following equations are used in this bias correction method (Zhang et al., 2004; Khan and Koch, 2018):

$$\boldsymbol{P_c} = \boldsymbol{K} \times (\boldsymbol{P_m} + \Delta\boldsymbol{P_w} + \Delta\boldsymbol{P_e} + \Delta\boldsymbol{P_t}) \qquad \text{(Eq 1)}$$

$$\boldsymbol{K} = \boldsymbol{1/CR} \qquad \text{(Eq 2)}$$

where $\boldsymbol{P_c}$ is the corrected precipitation; $\boldsymbol{K}$, the adjustment coefficient of the wind-induced error; $\boldsymbol{P_m}$, the measured precipitation at gauge; $\Delta\boldsymbol{P_w}$, the wetting loss; $\Delta\boldsymbol{P_e}$, the evaporation loss; $\Delta\boldsymbol{P_t}$, the trace amount, and ***CR*** is the catch ratio (%).

The trace precipitation, $\Delta\boldsymbol{P_t}$ is less than the resolution of the Tretyakov gauge (<0.1mm) and corrected by the Institute of Meteorology and Hydrology before archiving gauge measurements (personal communication). The wetting loss $\Delta\boldsymbol{P_w}$ is evaporated precipitation from the surface of the inner wall of the gauge after precipitation events and from the container after emptying. The evaporation loss $\Delta\boldsymbol{P_e}$ is water loss by evaporation before measurement (Zhang et al., 2004).

As Zhang et al. (2004) suggested, we determined precipitation types based on daily mean temperature. If the daily temperature was below -2°C, snow was assumed but if above +2 °C it was rain. Mixed precipitation was assumed for air temperatures between -2°C and +2°C. The reference values of $\Delta\boldsymbol{P_w}$ and $\Delta\boldsymbol{P_e}$ for various precipitation types, suggested by Zhang et al. (2004) and Khan and Koch (2018), are shown in Table 2.9.

Table 2.9: Values for wetting and evaporation losses

Variable	Snow	Mixed	Rain
$\Delta\boldsymbol{P_w}$	0.15	0.15	0.20
$\Delta\boldsymbol{P_e}$	0.10	0.30	0.10

The catch ratio of the gauge is estimated for various precipitation types on daily time steps using the following equations (Zhang et al., 2004). $\boldsymbol{W_s}$ is wind speed (ms^{-1}) at gauge height $\boldsymbol{T_{min}}$ and $\boldsymbol{T_{max}}$ are daily maximum and minimum temperatures for various precipitation types. $\boldsymbol{CR}$ is daily catch ratio (%).

$$CR_{(snow)} = 103.10 - 8.67W_s + 0.30T_{max} \quad \text{(Eq 3)}$$

$$CR_{mixed} = 96.99 - 4.46W_s + 0.88T_{max} + 0.22T_{min} \quad \text{(Eq 4)}$$

$$CR_{(rain)} = 100 - 4.77W_s^{0.56} \quad \text{(Eq 5)}$$

2.3.4.2.4 Bias correction for gridded APHRODITE dataset

Using the Thiessen polygon approach, areal mean gridded precipitation and temperature for the Bulgan catchment are calculated from the corresponding 25 grids of the APHRODITE dataset on daily time scales. The bias of the areal mean gridded precipitation and temperature is adjusted by Linear Scaling and Cumulative Distribution Function Matching approaches.

a. Linear Scaling:

A scale factor for each month is estimated based on the ratio of the monthly areal mean observed data to monthly areal mean gridded data. Then, daily observations are multiplied by the scale factor of the corresponding month.

$$s = \frac{\mu(X_{obs}^{mth})}{\mu(X_{APHRO}^{mth})} \quad \text{(Eq 1)} \qquad X_c^{day} = X_{APHRO}^{day} \times s \quad \text{(Eq 2)}$$

where s is the scale factor; X_{obs}^{mth} and X_{APHRO}^{mth} are monthly observed and APHRODITE dataset, respectively; X_c^{day} and X_{APHRO}^{day} are the daily corrected and original APHRODITE data.

b. Cumulative Distribution Function Matching:

Based on the assumption that the observed and APHRODITE datasets have the same cumulative frequencies over a specific period, the APHRODITE data is matched to the equivalent observation data, and a transformation function is derived. The APHRODITE dataset is corrected based on the derived transformation function. For precipitation, the cumulative frequencies for wet day frequency are matched.

$$C_1(X_{APHRO}^{day}) = \int f_1(X_{APHRO}^{day}) \quad \text{(Eq 3)}$$

$$C_2(X_{obs}^{day}) = \int f_2(X_{obs}^{day}) \quad \text{(Eq 4)}$$

$$f_3(X_{APHRO}^{day}) = C_2^{-1}\left(C_1(X_{APHRO}^{day})\right) \quad \text{(Eq 5)}$$

$$X_c^{day} = f_3(X_{APHRO}^{day}) \quad \text{(Eq 6)}$$

where f_1 and f_2 are the probability of X_{APHRO}^{day} and X_{obs}^{day}; C_1 and C_2 are the cumulative frequency functions; f_3 is the transformation function of X_{APHRO}^{day} to X_{obs}^{day} at the same cumulative probability.

2.3.4.3 Runoff sensitivity to climate change

To test the runoff sensitivity of the optimized hydrological model to climate change, we developed different climate scenarios with temperature increases (+1ºC, +2ºC, +3ºC, +5ºC) and various scenarios of precipitation (±10%, ±20%).

The daily mean temperature increases by one degree, but daily precipitation increases or decreases by multiplying by the correction factors. Those constant changes keep the inter-annual variations from the original temperature and precipitation.

Altered climate input data of each climate scenario is applied to the HBV-Light model to simulate future runoff of that scenario. Changes in annual and seasonal runoff (%) under different scenarios are estimated for the validation period from 2006 to 2015.

2.3.5 Future climate and runoff change

In addition to dynamically downscaled data from the selected GCM and RCM, CanESM2 is statistically downscaled at climate stations in the Bulgan catchment using the Statistical DownScaling Model (SDSM) tool to assess near-future climate and runoff change in the Altai-Dzungarian region.

Performances of these climate models are evaluated and compared using the Taylor diagram. Systematic biases of the climate models are corrected by Distribution mapping. The corrected GCM and RCM data are applied to the optimized hydrological model for the Bulgan catchment to simulate runoff for the baseline (1985-2005) and the future period (2030-2050).

2.3.5.1 Statistical DownScaling Model - SDSM tool

CanESM2 is statistically downscaled to station level using the Statistical DownScaling Model (SDSM). The SDSM, a hybrid of a stochastic weather generator and multi-regression-based model, was used to downscale daily maximum and minimum temperature, and precipitation at the station level. This model generates daily weather at the site from large-scale atmospheric circulation indices and regional moisture variables by describing time-varying

parameters under unconditional (air temperature and wet day occurrence) or conditional (precipitation amount) downscaling processes (Wilby et al, 2014).

It has seven main steps: 1) quality control and data transformation, 2) screening of downscaling predictor variables, 3) model calibration, 4) weather generation from observed predictors of NCEP Reanalysis, 5) synthesis of observed and downscaled data, 6) generation of scenarios from climate model predictors and 7) statistical analysis. Regression-based downscaling is very sensitive to the predictor selection and statistical transfer function because it supposes that the model parameters are valid in the future (Wilby et al, 2002).

An ensemble of 26 daily predictors: NCEP/NCAR Reanalysis (1961-2005) and CanESM2 outputs for the historical period (1962-2005), and projections for both RCP4.5 and RCP8.5 (2006-2100) were downloaded from CCCMA's website[10] (Table 2.10). These predictors for both historical and future periods, except for wind direction, are normalized with the mean and standard deviations of the baseline period 1971-2000. The data is presented as a 128 x 64 grid cell covering the global domain as a T42 Gaussian grid and each cell is of a nearly uniform size of 2.8˚ x 2.8˚ (Radojevic, 2014).

Normalized variables of the nine grids over the catchment and observations at two meteorological stations are employed as predictors and predictands in the statistical downscaling, respectively (Figure 2.20). The airflow variables are derived from 3 x 3 arrays of pressure fields overlaying the target grid cell of the stations. Thus, the zonal wind component includes broader domain information than single-grid precipitation data (Crawford et al., 2007).

Table 2.10: List of NCEP predictors

Variables	Descriptions	Variables	Descriptions
temp	Mean temperature at 2m	*prcp*	Total precipitation
mslp	Mean sea level pressure	***_f*	Wind speed
p500	500 hpa geopotential height	***_u*	Zonal wind component
p850	850 hpa geopotential height	***_v*	Meridional wind component
shum	1000 hPa specific humidity	***_z*	Relative vorticity of true wind
s500	500 hPa specific humidity	***_th*	Wind direction
s850	850 hPa specific humidity	***_zh*	Divergence of True wind

** refers to different atmospheric levels: 1000 hPa height (p1), 850 hPa height (p8) and 500 hPa height (p5)

At the screening step, the strength of the relationship between NCEP predictors of each grid cell and the associated predictand is defined using an analysis of the monthly percentage of explained variance and the partial correlation. After filtering potential predictors with their capabilities to explain local climate variability, partial correlation coefficients are computed to

[10] http://ccds-dscc.ec.gc.ca/ pred-canesm2

explore the weights of the selected predictors in the regression equation. However, predictors, especially the same variable from different grids, are mutually correlated. Therefore, stepwise multiple forward and backward regressions are applied to add and eliminate variables by checking the significance of individual variables and selecting those with a high coefficient of determination (R^2), low mean square error (MSE), and low variance inflation factor (VIF) based on the F test (Wilks, 2005).

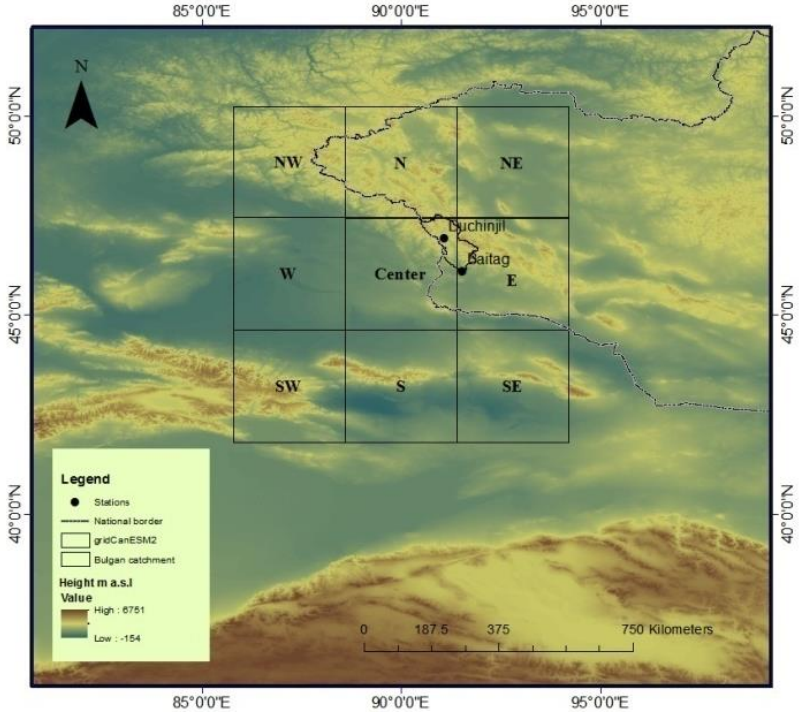

Figure 2.20: Nine grids of CanESM2 (2.81˚ x 2.81˚) over the Altai-Dzungarian region. Grids are named after directions from central grid. Duchinjil and Baitag meteorological stations used for statistical downscaling are marked by black dots.

Monthly regression models are established based on the selected predictors. The parameters of the regression models are optimized by the ordinary least square method. The regression model for precipitation downscaling is complicated since the occurrence and amount of precipitation must be specified as a condition. Thus, the "Event Threshold" of wet day occurrence was set as 0.3mm/day and the model was transformed with a natural log. For temperature downscaling, no transformation was applied since the temperature is an unconditional process. Using the stochastic component of the SDSM, 20 simulations are performed to produce an ensemble. Then the ensemble mean is compared to observation. The observation length of each station is divided into two independent sets for calibration (1977-1995) and validation (1996-2005).

Based on the monthly regression models, climate scenario outputs are generated based on climate model predictors for the historical period (1961-2005) and future scenarios (2006-2099) under RCP 4.5 and 8.5.

2.3.5.1.1 Delta statistics

As stated in the SDSM Manual (Wilby and Dawson, 2007), the following equations are used to calculate delta statistics of the statistically downscaled precipitation and maximum and minimum temperatures of CanESM2 at Duchinjil and Baitag stations over two periods: 2030-2050 (2040s) and 2080-2100 (2090s) under RCP4.5 and 8.5 scenarios comparing to a baseline period of 1985-2005 (1990s):

Percentage change for precipitation (%):

Δ2040s=$\frac{(P_{2040s}-P_{1990s})*100}{P_{1990s}}$; Δ2090s=$\frac{(P_{2090s}-P_{1990s})*100}{P_{1990s}}$

Absolute difference for temperature (°C):

Δ2040s=$T_{2040s}-T_{1990s}$; Δ2090s=$T_{2090s}-T_{1990s}$

2.3.5.2 Evaluation of global and regional climate models with Taylor Diagram

GCMs do not accurately show regional climate at fine-resolution geographic and temporal scales but can be used to help understand the uncertainty range of the climate projections. Most impact studies transfer gridded outputs of RCM into catchment average (Demirel et al., 2013) or use an average of four surrounding grid points to represent the climate over the station to avoid artificial errors from model parameterization at a single grid cell.

Regarding the complex terrain of the Altai Mountains, it is critical to check the topography accounting ability of climate models because there can be a systematic shift. Thus, simulated and observed climate time series are correlated for the whole study domain using the spatial Pearson correlation coefficient (r) as a simple measure of the similarity between simulated and observed climates over a baseline period of 1985-2005. It is found that the observed temperature and precipitation at stations better correlate with the outputs from the corresponding grid cell rather than neighboring grid cells for both the GCM and the RCM.

The Taylor diagram is a practical model evaluation tool used in climate studies. The following statistical relationships, including correlation (r), centered root mean square error (RMSE), and standard deviation (σ) between simulated and observed climate time series, are shown in the Taylor diagram (Taylor, 2001).

$$\boldsymbol{r} = \frac{\frac{1}{N}\sum_{n=1}^{N}(s_n-\bar{s})(o_n-\bar{o})}{\sigma_s\sigma_o} \qquad \text{Eq 1}$$

$$\boldsymbol{RMSE} = \left[\frac{1}{N}\sum_{n=1}^{N}\left((s_n-\bar{s})-(o_n-\bar{o})\right)^2\right]^{1/2} \qquad \text{Eq 2}$$

$$\boldsymbol{\sigma_s} = \left[\frac{\sum(s_n-\bar{s})^2}{n}\right]^{1/2} \qquad \text{Eq 3}$$

where $\bar{s}$ and $\bar{o}$ are the mean values and σ_s and σ_o are the standard deviations of s and o simulated and observed fields, respectively. The N is the number of discrete points in time or space.

Model accuracy is evaluated by its distance from the point denoted by the observation. r is shown by the angle (azimuth). At the observed value, the centered RMSE is equal to 0, and both ratios of standard deviations and the correlation coefficient are equal to 1 (Taylor, 2001).

2.3.5.3 Bias correction of GCM and RCM outputs

Due to limited process understanding and coarse spatial resolution, GCMs, and RCMs often present biased results; thus, it is essential to correct bias in RCMs and GCMs outputs before applying them in impact studies (Maraun et al., 2010).

Models have systematic and random errors, including too many drizzle days and untrue climate variability. Therefore, these model biases are quantified using statistical relationships between the modeled and observed climate series over the same baseline period. Then the bias correction is applied for future scenarios based on the assumption that the statistical relationship is applicable in the future.

Before bias correction, the modeled outputs are interpolated to the same Gregorian calendar. HadGEM2 and RegCM4 have a 360-day calendar, while CanESM2 has 365 days for a year. These different lengths of calendar days are converted into the same 365-day calendar with a leap year by adding days in January, March, May, July, August, October, and December, as stated in the post-processing approach by Dobor et al. (2015). Dry days are added to the precipitation time series, whereas averages of the previous and following days' temperatures are calculated for these days. For February, one or two days are removed from the 30 days of the month regarding the leap year. Raw GCM and RCM outputs are corrected by Distribution mapping.

2.3.5.3.1 Distribution mapping

This method matches the distribution function of the simulated climate variables to the distribution function of observations. This method corrects the mean and standard deviation of the climate model outputs, wet-day frequencies, and precipitation intensities (Teutschbein and Siebert, 2012).

Dynamic RCMs tend to simulate too many drizzle days with low precipitation due to the convection of moist air in a large area of the RCM grid size. It is recommended that this drizzle effect is eliminated from the model data before bias correction to avoid its influence on the modification factor (Willkofer et al., 2018). Furthermore, Kjellström et al. (2010) suggested 1.0mm day^{-1} as the best threshold to remove excess drizzle precipitation from

RCM data. Thus, we redefined days with less than 1.0 mm of precipitation to dry days before distribution mapping.

Cumulative distribution functions (CDF) are created as transfer functions for both observed and simulated daily climate variables within a month for the baseline period of 1985-2005. The value of the simulated precipitation/temperature is searched on the empirical CDF of the climate model data with its corresponding cumulative probability, then shifted to the value of precipitation/temperature of the same cumulative probability on the empirical CDF of observation (Teutschbein and Siebert, 2012).

For precipitation correction, the gamma CDF ($\boldsymbol{F_\gamma}$) and its inverse ($\boldsymbol{F_\gamma^{-1}}$) are applied as below:

$$\boldsymbol{P_{corr\_sim}(d) = F_\gamma^{-1}(F_\gamma(P_{sim}(d)|\alpha_{sim,month}, \beta_{sim,month})|\alpha_{obs,month}, \beta_{obs,month})}$$

$$\boldsymbol{P_{corr\_scen}(d) = F_\gamma^{-1}(F_\gamma(P_{scen}(d)|\alpha_{sim,month}, \beta_{sim,month})|\alpha_{obs,month}, \beta_{obs,month})}$$

where, $\boldsymbol{P_{corr\_sim}(d)}$ and $\boldsymbol{P_{corr\_scen}(d)}$ are the corrected daily values of the simulated precipitation for the baseline period of 1985-2005 ($\boldsymbol{P_{sim}}$) and for the future scenario ($\boldsymbol{P_{scen}}$) respectively. The $\boldsymbol{\alpha_{sim,month}}$ and $\boldsymbol{\beta_{sim,month}}$ are shape and scale parameters of the simulated precipitation CDF for the particular month, also $\boldsymbol{\alpha_{obs,month}}$ and $\boldsymbol{\beta_{obs,month}}$ are the parameters of the observed precipitation CDF for the same month.

For temperature, the following gaussian (normal) CDF ($\boldsymbol{F_N}$) and its inverse ($\boldsymbol{F_N^{-1}}$) are applied:

$$\boldsymbol{T_{corr\_sim}(d) = F_N^{-1}(F_N(T_{sim}(d)|\mu_{sim,month}, \sigma^2_{sim,month})|\mu_{obs,month}, \sigma^2_{obs,month})}$$

$$\boldsymbol{T_{corr\_scen}(d) = F_N^{-1}(F_N(T_{scen}(d)|\mu_{sim,month}, \sigma^2_{sim,month})|\mu_{obs,month}, \sigma^2_{obs,month})}$$

where, $\boldsymbol{T_{corr\_sim}(d)}$ and $\boldsymbol{T_{corr\_scen}(d)}$ are the corrected daily values of the simulated temperature for the baseline period of 1985-2005 (T_{sim}) and for the future scenario (T_{scen}), respectively. The $\mu_{sim,month}$ and $\sigma^2_{sim,month}$ are location and scale parameters of the simulated temperature CDF for the particular month; whereas $\mu_{obs,month}$ and $\sigma^2_{obs,month}$ are the parameters of the observed temperature CDF for the same month.

2.3.5.4 Future runoff simulation

The temperature and precipitation series of the GCMs and RCMs are applied to the optimized hydrological model as input to simulate runoff for the baseline period (1985-2005) and the future period (2030-2050) under RCP4.5 and 8.5 (Seibert 2003). The projected changes in seasonal runoff and high and low flows were analyzed by changes in monthly hydrographs and the exceedance probability curves of daily runoff (Teutschbein and Seibert, 2012).

CHAPTER 3. RESULTS AND DISCUSSION

“Meandering Bulgan River is the life-spring of my homeland…”

from “Bulgan River with Beavers” folk song

Photo: An upstream area of the Bulgan River, Oyunmunkh 2014

3.1 Past climate reconstruction

3.1.1 Site chronologies and climate-growth responses

A summary of the statistics of the site chronologies is shown in Table 3.1. After standardization, the first-order autocorrelations of the site chronologies decreased as expected. The EPS for six site chronologies remains above the threshold of 0.85 (Wigley et al., 1984) over their different chronology lengths. The running-mean correlation coefficients between the individual tree-ring series in a chronology ($\bar{r}$) for 50-year intervals with 25-year overlap ranges between 0.35 and 0.75.

Table 3.1: Summary of the statistics of the raw and standardized ring-width chronologies from all six sampling sites (*/** sampled in 2014/2013)

Tree ring sites	KAR*	KET*	GUR*	YLT**	SHR**	KUD**
Period, years	1402-2013, 612	1569-2013, 445	1648-2013, 366	1835-2012, 178	1815-2012, 198	1624-2012, 389
First-order autocorrelation						
Raw	0.89	0.77	0.81	0.92	0.88	0.70
Standardized	0.47	0.67	0.64	0.30	0.46	0.61
Average mean sensitivity[a]						
Raw	0.212	0.233	0.282	0.214	0.279	0.390
Standardized	0.206	0.228	0.253	0.201	0.269	0.287
EPS[b]	0.92-0.98	0.91-0.98	0.83-0.98	0.87-0.95	0.98-0.99	0.85-0.97
Rbar[c] ($\bar{r}$)	0.44-0.65	0.48-0.63	0.50-0.75	0.35-0.64	0.59-0.69	0.45-0.85
Period	1450-2013	1645-2013	1825-2013	1915-2012	1815-2012	1830-2012
Years with EPS>0.85 (number,percentage)	564/92%	369/83%	189/52%	98/55%	198/100%	183/47%

[a]Average mean sensitivity (Cook and Krusic, 2006); [b]Expressed population signal (Wigley et al., 1984)
[c]Mean correlation coefficient among all tree-ring series used in a chronology

Over the period 1835-2012, which is covered by all six site chronologies, upper and lower tree line chronologies obtained from northwest- and west-facing slope orientations each correlate significantly with each other (Table 3.2).

Table 3.2: Pearson's correlation coefficients between all six site chronologies over the common period 1835-2012

Site chronology	Aspect	Upper treeline			Lower treeline		
		KAR	KET	GUR	YLT	SHR	KUD
KAR /2748 m	N	1	0.263**	0.332**	0.170*	0.003	-0.003
KET/2603 m	W		1	**0.804****	0.203**	**0.559****	0.289**
GUR/2450 m	WN			1	0.275**	**0.428****	0.257**
YLT/ 2334 m	N				1	0.128	0.044
SHR/ 2478 m	W					1	**0.482****
KUD/ 2482 m	NW						1

**p<0.01 *p<0.05 Moderate correlation coefficients are marked in Bold

For instance, the KET upper-tree line chronology from a *west-facing slope* is relatively weakly correlated with the KAR chronology (also upper tree line but north-facing slope) ($r=0.26$ at $p<0.01$), whereas the KET chronology is strongly positively correlated with the GUR upper tree line chronology from a northwest-facing slope ($r=0.80$ at $p<0.01$). The KET chronology is also relatively strongly correlated with the SHR lower treeline chronology also obtained from a west-facing slope ($r=0.56$ at $p<0.01$).

This finding is in line with Fritts (1976), who sees slope orientation as an even more important site factor for growth response than elevation and latitude, because it more strongly affects the water and energy balance by controlling the amount of radiation received by the site, which in turn influences the allocation of moisture. Regardless of position (upper or lower tree line) and slope orientation, significant correlations among the site chronologies suggest one or more shared external growth-driving factors, like e.g. cooling, aerosols from volcano eruptions, and water stress.

The monthly climate data most significantly correlated with the site chronologies were selected for setting up transfer models for the reconstruction of climate based on the tree-ring widths. In the correlation analyses with the climate data, current year air temperatures (at KAR, YLT and KUD) and prior year precipitation sums (at KET, SHR, GUR, and YLT) were identified as the main drivers of radial growth.

As shown in Figure 3.1, the KAR chronology positively correlates with the regional station temperatures of the current year June ($r=0.61$, $p<0.01$), July ($r=0.29$, $p<0.05$), and the mean June-July ($r=0.55$, $p<0.01$) and the previous year June ($r=0.32$, $p<0.05$) over their common period (1963-2012) while the PC1 of YLT and KAR positively correlate with mean June temperatures ($r=0.57$, $p<0.01$). The KET chronology significantly correlates with the mean monthly precipitation sums at the Qinghe station for July ($r=0.38$, $p<0.05$), August ($r=0.40$, $p<0.05$), and November ($r=0.27$, $p<0.05$) of the previous year, whereas the PC1 of the KET, SHR, and GUR chronologies correlate with the precipitation sums for July ($r=0.32$, $p<0.05$), August ($r=0.37$, $p<0.05$), and November ($r=0.26$, $p<0.05$) of the previous year.

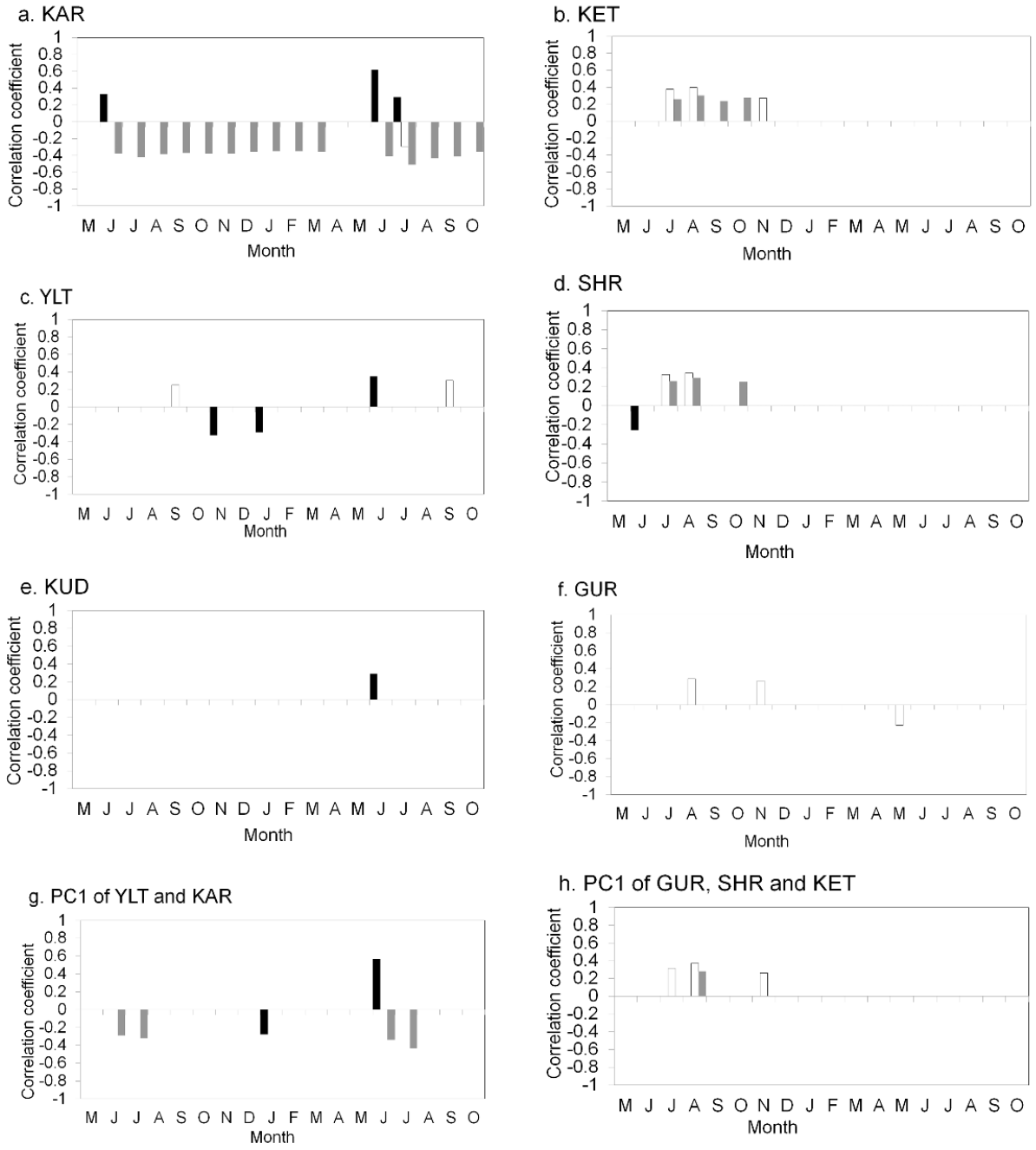

Figure 3.1: Pearson's correlation coefficients ($p<0.05$) between the tree-ring width chronologies of KAR (a), KET (b), YLT (c), SHR (d), KUD (e), GUR (f), the first principal component (PC1) of YLT and KAR (g), the PC1 of GUR, SHR and KET (h) and the monthly regional air temperature averaged from five climate stations (black columns) for the period 1963-2012, precipitation sums as measured at the Qinghe station (white columns) for the period 1958-2007, and the monthly scPDSI (grey columns) for the period 1963-2012 over an 18-month window from May of the year prior to growth to October of the year of growth.

Besides the significantly stronger correlations of the individual KAR and KET site chronologies with temperature and precipitation, respectively, both chronologies reach further back in time than those of the other sites and the regional chronologies of this study as well as previous reconstructions from the southern Altai Mountains. Hence, the KAR and KET chronologies are chosen for temperature and precipitation reconstructions

The KAR and KET chronologies are correlated with various climate datasets, as shown in Figure 3.2. The KAR chronology correlates positively with the mean monthly temperatures of June (r=0.66, p<0.01), July (r=0.40, p<0.01), and mean June-July (r=0.63, p<0.01) of the current year, and of June (r=0.38, p<0.01) and July (r=0.27, p<0.01) of the previous year of the gridded CRU TS4.01 time series over the period 1963-2012 (Figure 3.2a).

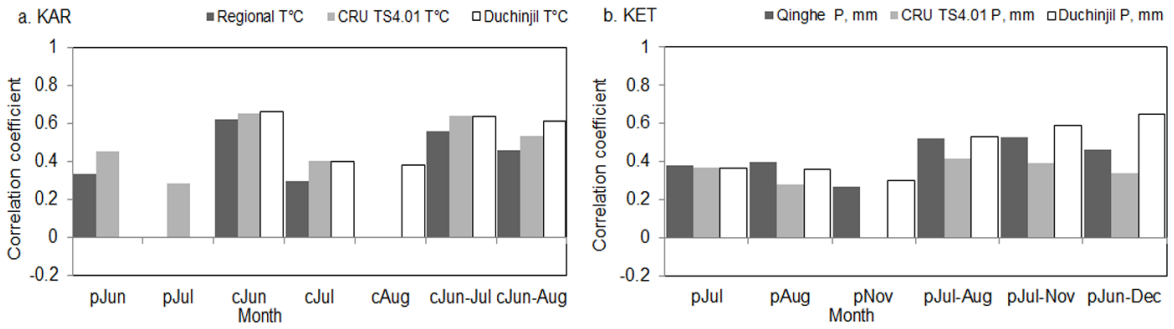

Figure 3.2: Significant (p<0.05) Pearson's correlation coefficients between the KAR chronology and the monthly and seasonal mean air temperatures of the regional temperature averaged over five stations, and the CRU TS4.01 (averaged over the grids of 91° E - 92°E and 41°N - 42°N) for the period 1963-2012, and the nearest station (Duchinjil) for the period 1977-2012 (a) and between KET and the monthly and seasonal precipitation sums as measured at the Qinghe station, the CRU TS4.01 (averaged over the grids of 91° E - 92°E and 41°N - 42°N), and the Duchinjil station over the period 1958-2007, 1958-2012 and 1977-2012, respectively (b). c: current year and p: year prior to growth

These results corroborate findings from previous studies in the Chinese southern Altai Mountains by Chen et al. (2012), Zhang et al. (2015), and Wang et al. (2013), who showed positive correlations of tree-ring widths with June-July air temperatures. They believe that the increased radial growth is caused both by higher photosynthetic rates and higher soil moisture levels due to increased snowmelt. The CRU TS4.01 temperatures for the period 1963-2012 were preferred over the Duchinjil station data because of the longer length of this time series. The CRU TS4.01 temperature data from before 1963 were not used due to too few stations in the region and the resultant low reliability of interpolations for that period.

The strongest correlations exist between the KET chronology and the precipitation sums (r=0.64, p<0.01) from June through December of the year prior to growth measured at the Duchinjil station for the period 1977-2012 (Figure 3.2b). Previous year monthly precipitation sums of July (r=0.37), August (r=0.36), and November (r=0.30) were also significantly correlated (p<0.05) with the KET chronology, as were those of July through November (r=0.58, p<0.01) and July through December (r=0.60, p<0.01).

These findings are largely in line with Chen et al. (2014), who found positive correlations between the radial growth of Siberian spruce in the Chinese southern Altai Mountains with July-August and December precipitation sums of the previous year in addition to May-July precipitation of the current year. According to Fritts (1974), the growth of arid-site conifers

during the current year might be enhanced by above-average precipitation in late summer and early autumn of the previous year due to its promotion of carbohydrate storage and bud formation. Winter precipitation, which mostly falls as snow from November to March in this area, increases soil moisture during the early growing season due to snowmelt and may thus also promote growth.

3.1.2 Temperature and precipitation sensitive tree-ring width networks

The KAR chronology is significantly correlated with mean June-July temperatures, while the KUD and YLT chronologies are correlated only with June temperatures (Figure 3.1). Four transfer function models of summer temperature were developed based on KAR, KUD and YLT chronologies, and a network (PC1) of these temperature-sensitive tree-ring widths for the June temperature of the gridded CRU TS4.01 dataset throughout 1963-2012 (Figure 3.3a).

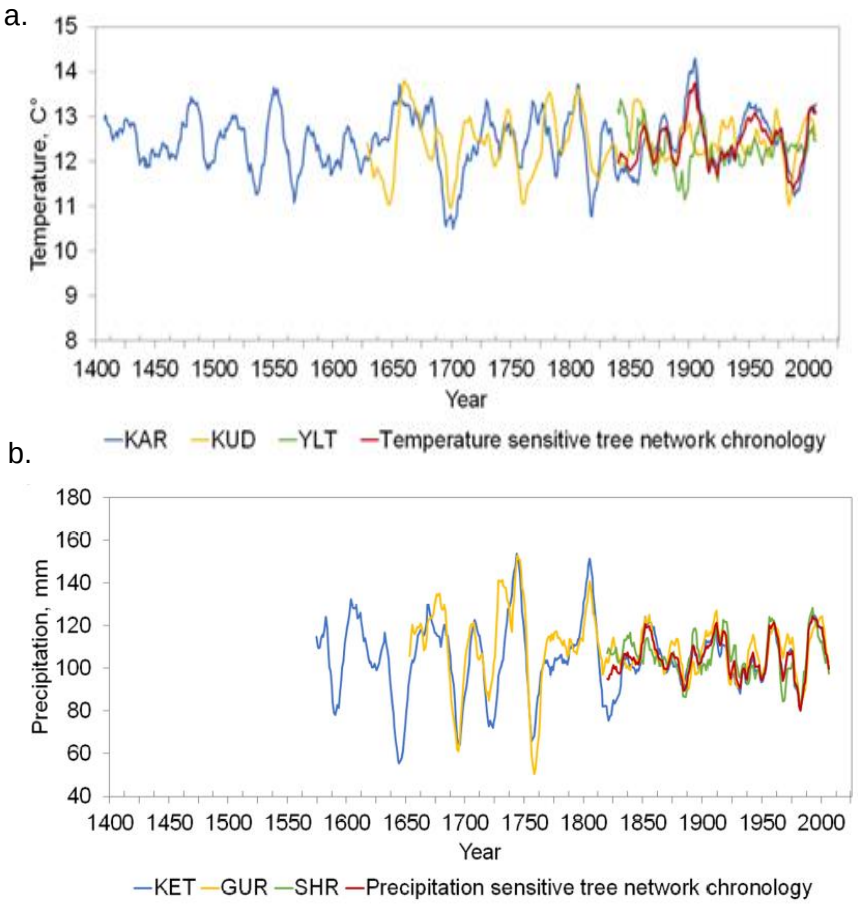

Figure 3.3: Reconstructed June temperature time series from the KAR, KUD, and YLT chronologies, and a network of these chronologies over their common period (a); reconstructed June-December precipitation sum time series from the KET, GUR, and SHR chronologies and a network of these chronologies (b) over their common period.

Model skill statistics were calculated for the calibration period from 1963 to 1986 and the verification period from 1987 to 2012. This was repeated with both periods interchanged. Validation statistics of the transfer function models are shown in Table 3.3.

The skills of the transfer functions derived from the KUD and YLT chronologies were poor, and their estimated June temperatures explained only 10.1% - 11.5% of the variance in observed temperature. That might be explained by their site characteristics, including their location at the lower tree line, which makes those sites more prone to human disturbances and less sensitive to temperature.

Table 3.3: Calibration and verification statistics of the June temperature reconstructions from the KAR, KUD, YLT and a network of these chronologies as calibrated with monthly mean temperatures from the CRU TS4.01 dataset (91°-92°E and 41°-42°N).

	Full calibration, 1963-2012	Calibration, 1963-1987	Verification, 1988-2012	Calibration, 1988-2012	Verification, 1963-1987
KAR					
r	0.650***	0.739***	0.603**	0.602**	0.737**
AdjR^2	0.397***	0.506***	-	0.335**	-
Explained variance	42.2%	54.6%	-	36.2%	-
RE	0.374	0.547	0.250	0.362	0.406
CE	-	0.547	-0.041	0.362	0.206
KUD					
r	0.318*	0.404*	0.066*	-	-
AdjR^2	0.082	0.127	-	-	-
Explained variance	10.1%	16.3%	-	-	-
RE	0.063	0.163	0.085	-	-
CE	-	0.163	-0.220	-	-
YLT					
r	0.340*	-	-	0.345*	0.317
AdjR^2	0.097	-	-	0.079	-
Explained variance	11.5%	-	-	11.9%	-
RE	0.079	-	-	0.119	0.123
CE	-	-	-	0.119	-0.105
A network of the chronologies					
r	0.633**	0.694***	0.589***	0.602**	0.614***
AdjR^2	0.376**	0.459***	-	0.334	-
Explained variance	40.16%	48.17%	-	36.29%	-
RE	0.351	0.482	0.345	0.363	0.367
CE	-	0.482	0.126	0.363	0.204

r - Pearson's correlation coefficient, R^2– Coefficient of Determination, AdjR^2 – Adjusted for degrees of freedom, RE- Reduction of Error statistic, CE- Coefficient of Efficiency *** p<0.001 **p<0.01 * p<0.05

Four transfer function models of precipitation were developed based on the KET, GUR, and SHR chronologies, a network of these chronologies, and the June-December precipitation sums observed at the Duchinjil station (Figure 3.3b). Transfer model skills are quite good except for the SHR chronology, which had negative values and thus little predictive skill (Table 3.4). The estimated precipitation via the transfer functions of the GUR and the network

chronology explained 26.9% and 34.7% of the variance in observed precipitation, respectively.

Table 3.4: Calibration and verification statistics of the June-December precipitation sum reconstructions from the KET, GUR, and SHR chronologies and a network of these chronologies as calibrated with the June-December precipitation sums observed at the Duchinjil station.

	Full calibration, 1977-2012	Calibration, 1977-1995	Verification, 1996-2012	Calibration, 1996-2012	Verification, 1977-1995
KET					
r	0.642***	0.711**	0.520**	0.520**	0.711**
AdjR^2	0.395***	0.477*	-	0.222**	-
Explained variance	41.3%	50.6%	-	27.1%	-
RE	0.379	0.506	0.231	0.271	0.458
CE	-	0.506	0.193	0.271	0.442
GUR					
r	0.519***	0.566**	0.448*	0.448*	0.566**
AdjR^2	0.248***	0.280	-	0.147	-
Explained variance	26.9%	32.01%	-	20.07%	-
RE	0.227	0.320	0.161	0.201	0.286
CE	-	0.320	0.119	0.201	0.265
SHR					
r	0.498**	0.615**	0.291	-	-
AdjR^2	0.226**	0.342**	-	-	-
Explained variance	24.8%	37.82%	-	-	-
RE	0.204	0.378	-0.038	-	-
CE	-	0.378	-0.078	-	-
A network of the chronologies					
r	0.589**	0.653**	0.468*	0.511*	0.666***
AdjR^2	0.327**	0.393**	-	0.209	-
Explained variance	34.69%	42.66%	-	26.16%	-
RE	0.308	0.427	0.187	0.262	0.404
CE	-	0.427	0.156	0.262	0.390

r - Pearson's correlation coefficient, R^2– Coefficient of Determination, AdjR^2 – Adjusted for degrees of freedom, RE- Reduction of Error statistic, CE- Coefficient of Efficiency *** p<0.001 **p<0.01 * p<0.05

The temperature and precipitation-sensitive networks prove that the single site chronologies, KAR and KET, can reconstruct regional temperature and precipitation variations over a long-time period. Therefore, we used KAR and KET chronologies in long-term climate reconstruction and analysis for this region.

3.1.3 Summer June-July temperature reconstruction

Based on the KAR chronology, a temperature transfer function was developed for June-July temperatures of the gridded CRU TS4.01 dataset over the period of 1963-2012. The first principal component from the PCA of the predictors - the KAR (t) and its lag (t+1) series - contained 79% of the total variance and was used in a linear regression model for the mean June-July temperature reconstruction. The skill statistics were calculated for the calibration period 1963-1986 and for the verification period 1987-2012, which was repeated with both periods interchanged.

The transfer function model verification statistics for the mean June-July temperature reconstruction (Table 3.5) indicated - with positive values of RE, significant PM values, and significant first-difference sign tests ($p<0.05$) - that the temperature reconstruction of this study adequately captures the high-frequency variation of the instrumental data. Therefore, the transfer function model from the KAR chronology calibrated over the whole period between 1963 and 2012 was used for reconstructing mean June-July temperatures over the period 1402-2012.

Table 3.5: Calibration and verification statistics for the transfer function model of the mean June-July temperature reconstruction from the KAR chronology and the monthly mean temperature averaged over CRU TS4.01 grids (91°E - 92°E; 41°N - 42°N)

	Full calibration (1963-2012)	Calibration (1963-1987)	Verification (1988-2012)	Calibration (1988-2012)	Verification (1963-1987)
r	0.631***	0.734***	0.603***	0.605***	0.733***
R^2	0.397**	0.539***		0.366**	
AdjR^2	0.371**	0.497		0.338**	
RE	0.347	0.539	0.238	0.366	0.356
CE		0.539	-0.183	0.366	-0.198
Sign test	-	18+/7-*	14+/11-	22+/3-***	16+/9-
Products means test		0.399**	0.597*	0.095	0.326**

r - Pearson's correlation coefficient, R^2– Coefficient of Determination, AdjR^2 – Adjusted for degrees of freedom, RE- Reduction of Error statistic, CE- Coefficient of Efficiency *** p<0.001 **p<0.01 * p<0.05

The reconstructed June-July temperature time series explained 39.7% of the year-to-year variance of the gridded CRU TS4.01 data over the period 1963-2012 and contained the same general positive trend as the instrument observations (Figure 3.4a).

This common trend between tree ring and instrumental temperature series might lead to partly spurious correlations. After removal of these linear trends from the KAR chronology and the mean June-July temperatures by taking the difference between the value in one year and the previous year, a moderate correlation ($r=0.49$, $p<0.01$) was still found between both detrended time series. However, it should be noted that such common trends may be causally linked and the removal of such trends from both the tree-ring and temperature series

might prevent the reconstruction of similar past trends based on the tree rings and lead to a false detection of divergence (Weijers et al., 2012).

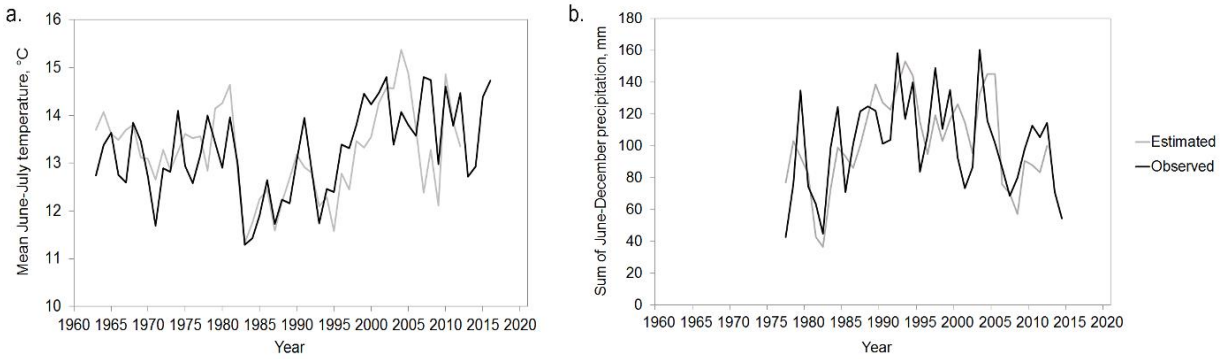

Figure 3.4: Mean June-July temperatures estimated from KAR ring-widths (grey line) and observed monthly mean air temperature (black line) averaged over the CRU TS4.01 grids over the sampling sites for the period 1963-2012 (r=0.63, p<0.01) (a); June-December precipitation sums as estimated from the KET ring-width chronology (grey line) and observed at the Duchinjil station (black line) over the period 1977-2012 (r=0.72, p<0.01) (b).

The spatial distribution of the correlation between reconstructed and gridded instrument-based CRU TS4.01 mean June-July temperatures for the period 1963-2012 (Figure 3.5a) demonstrates that our temperature reconstruction contains a clear regional signal, which covers the Altai Mountains and the western Sayan Mountains in northern Mongolia (r=0.5-0.6, p<0.1), the Mongolian Plateau (r=0.3-0.5, p<0.1), and the Dzungarian Basin (r=0.2-0.5 depending on the distance from the Altai Mountains, p<0.1). The strength of spatial correlation between the gridded and reconstructed temperatures decreases for the longer period (1950-2015) in Figure 3.5b due to the lack of long time series data from sparse climate stations in the southern Altai Mountains. Those stations were established between 1954 and 1963.

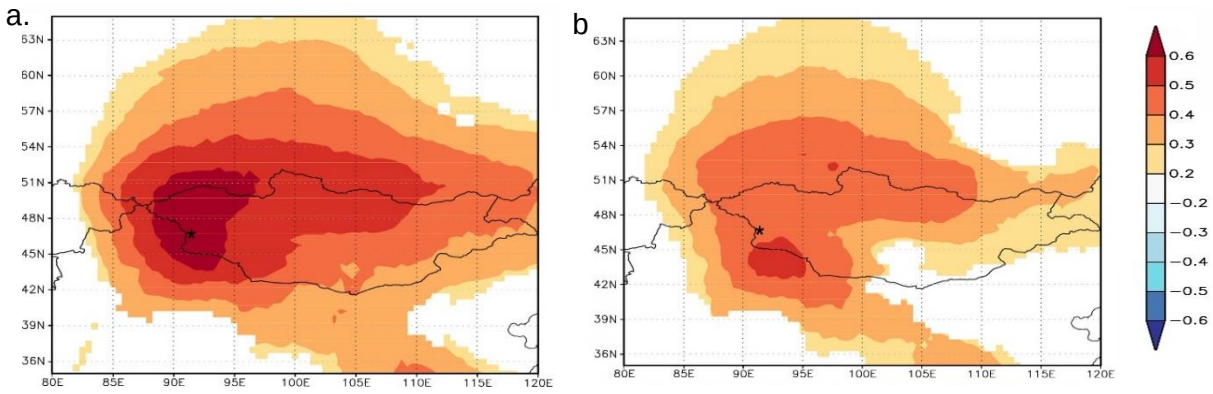

Figure 3.5: Maps showing the correlations between the gridded CRU TS4.01 (0.5°×0.5°) climate dataset and the reconstructed temperature as calculated with the KNMI climate explorer (http://climexp.knmi.nl). Gridded and reconstructed June-July temperatures (1963-2012) (a), gridded and reconstructed June-July temperatures (1950-2012) (b). The sampling site is marked with a black asterisk.

Long-term variation in summer temperature

According to the resulting 611-year June-July temperature reconstruction, over the period 1402-2012, mean summer temperatures in the region ranged from 9.3 to 16.0°C. The observed summer temperature variability is within the uncertainty range (+/-1 standard error of the prediction) of the reconstructed temperature over the common period (Figure 3.6).

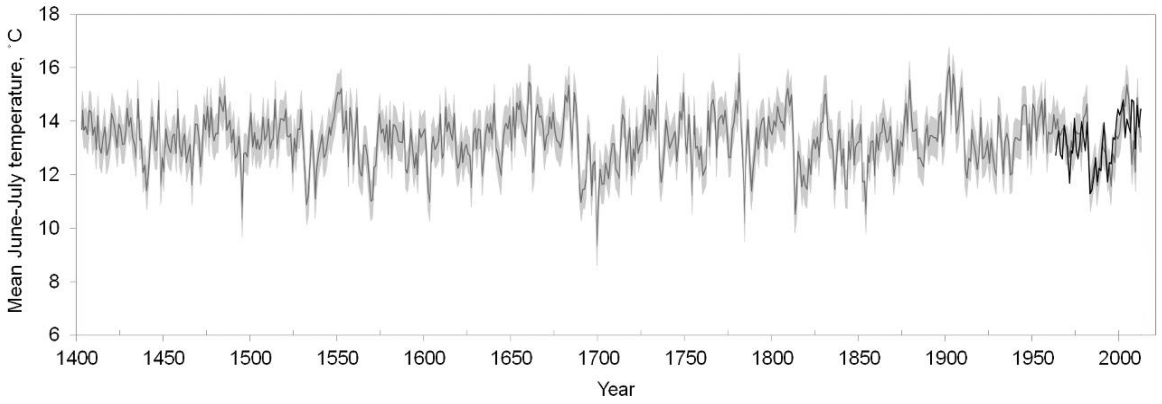

Figure 3.6: Mean June-July air temperature reconstruction based on the KAR tree ring-width chronology (thick grey line), its uncertainty (± 1 standard deviation of the prediction, grey area), and the temperature observations (CRU TS4.01) (black line).

In a graphical comparison with other tree ring-based reconstructed temperatures from the southern Altai from previous studies many similarities can be found (Figure 3.7).

All reconstructions lack the 20th century warming trend observed elsewhere over the northern hemisphere. Warm decades are suggested for the periods 1880-1910 and 1940-1975 and cold periods for 1490s, 1540s, 1680-1710, 1780s, 1810-1860, 1911-1939 and 1980s. These cold periods and the cooling in the 1930s are also revealed by a 750-year high resolution temperature reconstruction (1250-2000) from an ice-core oxygen isotope record from the Belukha glacier in the Siberian Altai and explained as periods of low solar activity (Eichler et al., 2009; Schwikowski et al., 2009). Moreover, periods of volcanic-induced cooling (Briffa et al., 1998; Eichler et al., 2009; Buentgen et al., 2016) and periods of low solar activity (Schwikowski et al., 2009) coincide with the observed periods with low temperatures in our reconstruction.

Most of the coldest summers took place during such periods of low solar activity and volcanic eruptions (Figure 3.7). Chen et al. (2012) explained the late 20th century cooling as a consequence of enhanced cloudiness and rainfall over the Altai Mountains and reduced growth of *Larix sibirica* at the tree line. The warm period in the 1950s and the cold period between 1983-1998 were also observed in tree-ring chronologies from mountainous areas in Nepal and China (Wang et al., 2013).

None of the temperature reconstructions from the Altai Mountains (this study and Panyushkina et al., 2005; Loader et al., 2010; Chen et al., 2012; Zhang et al., 2015, Buentgen et al., 2016) indicate a continuous 20th century warming trend as observed in the northern Mongolia reconstructions (Davi et al., 2015; D' Arrigo et al., 2000, 2001). Instead, a decrease in summer temperatures starting in the 1950s followed by a steep rise in the 1990s was observed. This warming till the 1950s and cooling afterwards till the 1990s was also revealed in mean June-July temperature-related tree growth series from upper tree-line sites in the Russian southeast Altai (Panyushkina et al., 2005) and in mean July-August temperature reconstructions from tree-ring oxygen and carbon isotopes of Siberian pine (*Pinus sibirica Du Tour*) from the central Russian Altai (Loader et al., 2010).

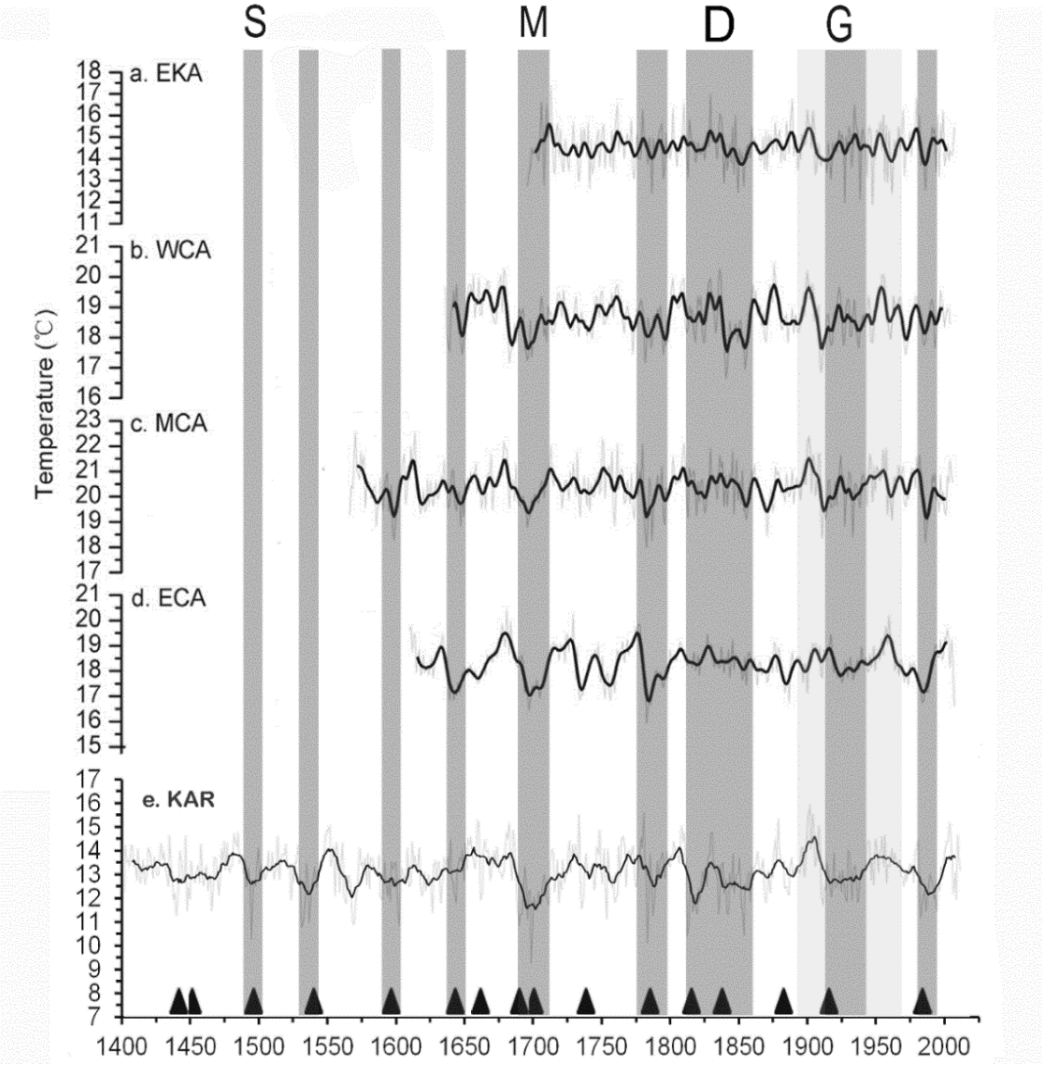

Figure 3.7: A graphical comparison of tree-ring based temperature reconstructions from the southern Altai. June temperatures for the eastern Kazakhstan Altai since 1698 (a), mean May-September temperatures for the western Chinese Altai since 1639 (b), June temperatures for the middle Chinese Altai since 1570 (c), mean June-July temperatures for the eastern Chinese Altai since 1613 (d), mean June-July temperatures for the southern Mongolian Altai since 1402 (e, this study). Thin grey lines and thick black lines show the reconstructed temperature and 13 year low pass filtered curve, respectively. (a)-(d) from Zhang et al. (2015). Dark and light grey bars show cold and warm periods. The cold periods of low solar activities are named by S = Spörer, M = Maunder, D = Dalton and G = Gleissberg minima (Schwikowski et al., 2009) and triangles indicate volcanic eruptions (Briffa et al., 1998; Eichler et al., 2009).

The temperature reconstruction from Siberian larch trees over the Chinese Altai Mountains from Chen et al. (2012) and in east Kazakhstan from Zhang et al. (2015) show similar patterns of change in mean June-July temperatures. This regional cooling from the 1950s to the 1990s contrasts with the area-weighted average of the past estimated temperature of all continents from the PAGES 2k Consortium (2013), which locates the warmest period in the late 20th century between 1971 and 2000. The past climate variability thus not only differs between continents but also between eastern and western Asia due to local factors like the Tibetan Plateau and the complex monsoon systems, which affect the stability of climatic teleconnections (Shi et al., 2015). This suggests, that the past temperature variability and change over the southern Altai and Dzungarian Basin region could differ from the mean Northern Hemisphere temperature pattern.

3.1.4 Precipitation reconstruction

A transfer function was developed based on the lagged (t+1) KET chronology and the June through December precipitation sum as observed at the Duchinjil station over the period 1977-2012 using simple linear regression. This model was first calibrated over the period 1977-1995 and verified over the period 1996-2012, which was repeated with interchanged periods. The reconstruction of June-December precipitation sums explains 41.3% of the variance in the instrumental data over the complete period (1977-2012).

The positive RE and CE values, and significant PM values suggest a high reliability of the transfer function model (Table 3.6). Consequently, June-December precipitation sums were reconstructed based on the KET chronology (t+1) for the period 1569-2012. The correlation between reconstructed and instrumental data over the whole common period is 0.64 ($p<0.01$) (Figure 3.4b).

Table 3.6: Calibration and verification statistics of the transfer function model for the June-December precipitation sum reconstruction from the KET tree-ring width chronology with observations from the Duchinjil station

	Full calibration (1977-2012)	Calibration (1977-1995)	Verification (1996-2012)	Calibration (1996-2012)	Verification (1977-1995)
r	0.642***	0.711**	0.520***	0.520**	0.711**
R^2	0.413***	0.506*		0.271**	
AdjR^2	0.395***	0.477*		0.222**	
RE	0.379	0.506	0.231	0.271	0.458
CE		0.506	0.193	0.271	0.442
Sign test		13+/6-	10+/7-	10+/7-	15+/4-
Products means test		680**	354	250***	392**

r - Pearson's correlation coefficient, R^2– Coefficient of Determination, AdjR^2 – Adjusted for degrees of freedom, RE- Reduction of Error statistic, CE- Coefficient of Efficiency *** $p<0.001$ **$p<0.01$ * $p<0.05$

The spatial distribution of the correlation between the reconstructed and the gridded instrument-based June-December precipitation sums from 1977 to 2012 (Figure 3.8a) shows a more local signal - compared to the mean June-July temperature reconstruction - with significant positive correlations over the southwestern and southern Altai Mountains (r=0.4-0.5, p<0.1) and the Dzungarian Basin (r=0.3-0.4, p<0.1). The strength of the spatial correlations between the chronologies and gridded precipitation data decreases for the longer period from 1950 to 2012 since the gridded dataset from a few stations in the 1950s might not represent the local climate enough (Figure 3.8b).

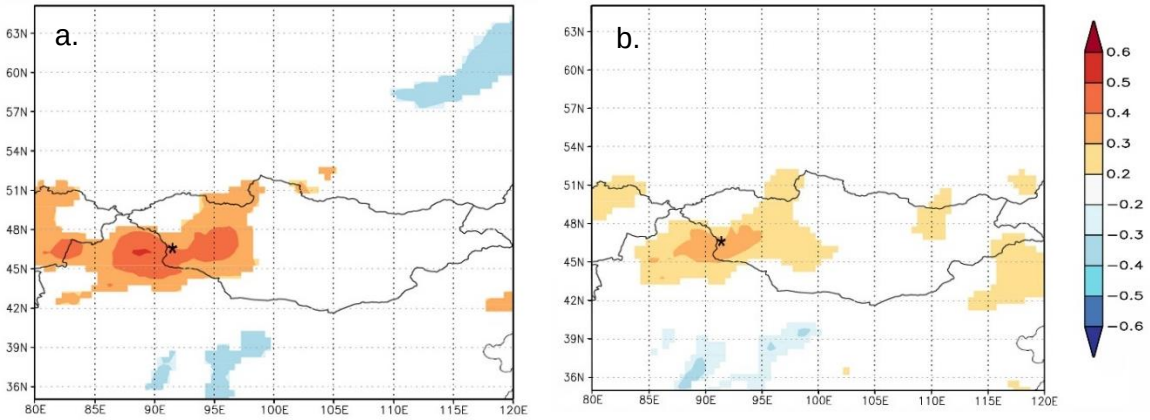

Figure 3.8: Maps showing the correlations between the gridded CRU TS4.01 (0.5°×0.5°) precipitation and the reconstructed precipitation as calculated with the KNMI climate explorer (http://climexp.knmi.nl). Gridded and reconstructed June to December precipitation sums (1977-2012) (a), gridded and reconstructed June to December precipitation sums (1950-2012) (b). The sampling site is marked with a black asterisk.

Long-term variation in regional precipitation

The reconstructed precipitation variability for the time period 1569 - 2012 shows recent wet maxima in the 1950s (1956 to 1962) and 1990s (1989-2005) after stable conditions between the 1830s and 1930s, which follow extreme wet and dry periods between the late 1600s to the early 1800s. The observed precipitation variability is within the uncertainty range (+/-1 standard error of the prediction) of the reconstructed precipitation over the common period (Figure 3.9).

In a graphical comparison with other precipitation reconstructions (Figure 3.10) from the northern and southern Altai Mountains, all reconstructions show similar wet (1915, 1956-1961, 1974-1976 and 1989-2006) and dry periods (1880-1885 and 1977-1985), although our sampling sites in the southern part of the Mongolian Altai Mountains are relatively dry due to the rain shadow probably caused by the central Mongolian Altai Mountains (Klinge et al., 2003) and the southern Chinese Altai Mountains. The differences in the high-frequency variation of the precipitation reconstructions might be explained by regional orographic

effects of the Altai Mountains on the storm tracks bringing moisture to this region (Davi et al., 2009).

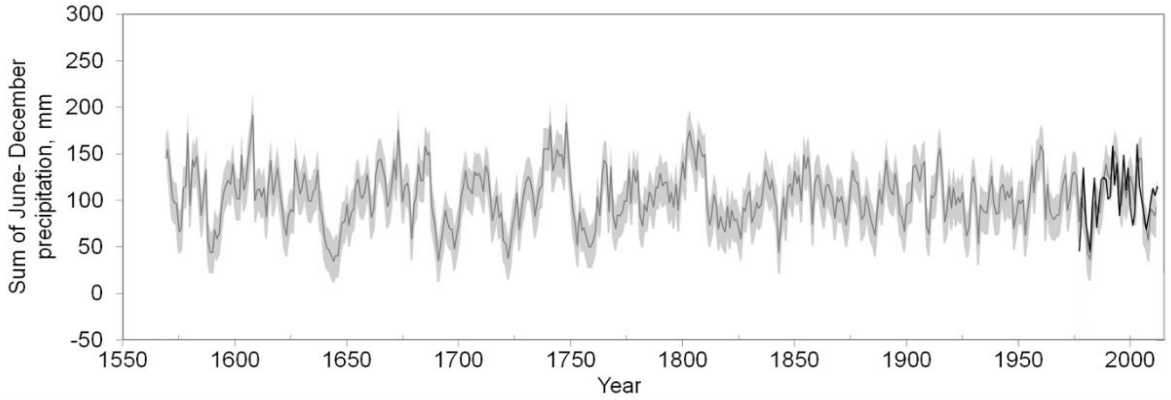

Figure 3.9: June-December precipitation sum reconstruction based on the KET tree ring-width chronology (thick grey line) and its uncertainty (± 1 standard deviation of the prediction, grey area), and the observations from the Duchinjil station (black line).

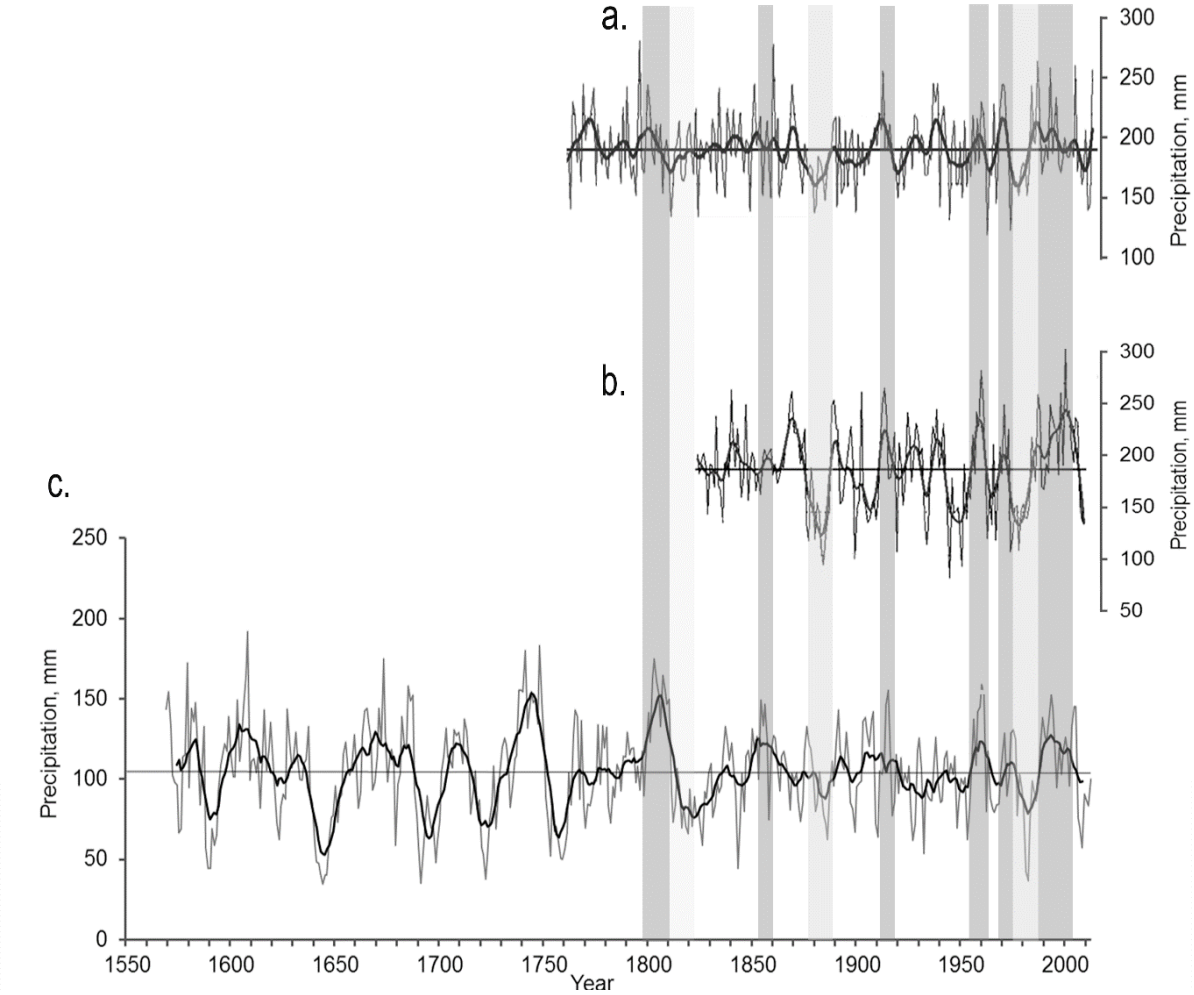

Figure 3.10: A graphical comparison of precipitation reconstructions from the southern Altai. Previous July to current June precipitation sums spanning 1760-2013 from the northwestern Chinese Altai (a) (Chen et al., 2015), July-June precipitation sums from Siberian spruce (Picea obavata) at a lower treeline spanning 1825 - 2009 for the southern Chinese Altai (b) (Chen et al 2014), June-December precipitation sums from Siberian larch (*Larix sibirica*) at the upper treeline spanning 1569 - 2012 for the southern Mongolian Altai (c) (this study). Thin grey lines and thick black lines show reconstructed precipitation sums and 10 year low pass filtered curves, respectively. Dark and light grey bars show wet and dry periods.

3.1.5 Long-term climatic variation and change

Climate variations were inferred for a 433-year period over the Altai-Dzungarian region from 20-year smoothed reconstructed temperature and precipitation series shown as standardized anomalies in Figure 3.11.

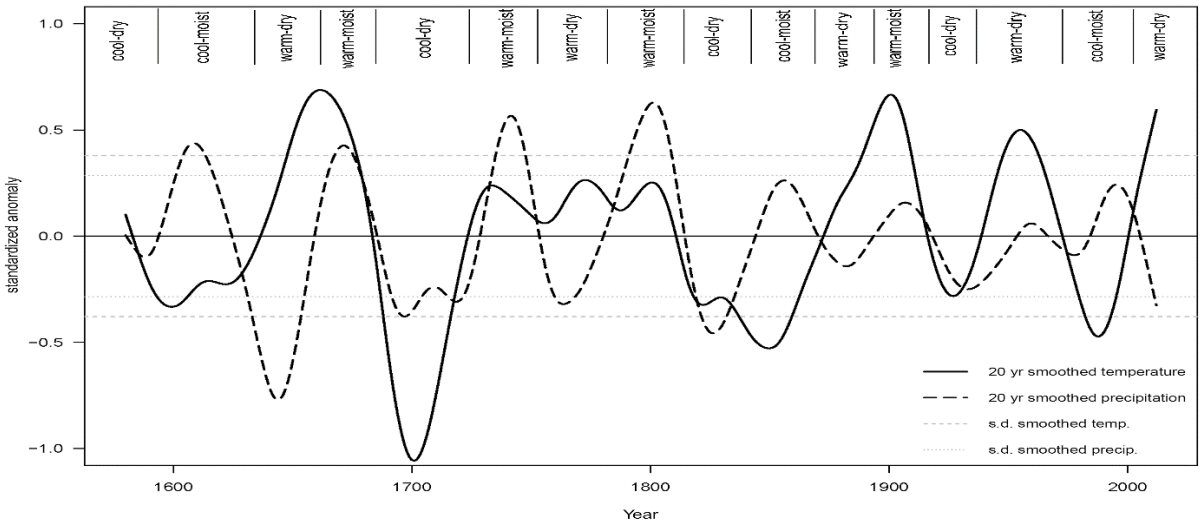

Figure 3.11: Inferred climate variation from the 20-year smoothed lines of the estimated temperature (solid line) and precipitation (dashed line) time series, expressed in standardized and normalized values. The horizontal dotted and thin grey lines indicate the range of one standard deviation for the 20-year smoothed precipitation (σ=±0.29) and temperature (σ=±0.37), respectively.

The inferred climate conditions were classified into cool-dry, cool-moist, warm-dry and warm-moist periods (Table 3.7). This classification suggests that cool-moist and cool-dry years have both decreased by about 8% since 1875, while warm-dry and warm-moist years have increased by about 14% and 2%, respectively. Thus, the more frequent warm-dry summers have replaced the cool/warm-moist and cool-dry episodes more common during the Little Ice Age (1580-1874). The extreme cool (1689-1691, 1705-1715, 1838-1859, 1983-1992), cool-dry (1692-1704, 1716), dry (1632-1647, 1717-1721, 1760-1768, 1820-1835), warm (1655-1664, 1889-1909, 1948-1962, 2008-2011) warm-dry (1648-1654, 2012), moist (1602-1616, 1677-1678, 1734-1749, 1789-1810) and warm-moist (1665-1676) periods are defined by the anomalies of the estimated temperature and precipitation above or below the +/- one standard deviation range of the whole record.

The cool-moist, cool-dry, warm-moist and warm-dry periods can be linked with different states of the general atmospheric circulation. The Little Ice Age period was cooler and wetter than the present climate condition in the Altai-Dzungarian region, which is supported by Putnam et al. (2016), who inferred wetter climate conditions during the LIA (which they defined as the period between 1150 and 1845) from geomorphological, biological, and historical evidence in the Tarim Basin, which neighbors the Dzungarian Basin. During that period, the northern hemisphere mountain glaciers expanded as a reaction to the lower

temperatures and descending snowlines. In parallel, the Tarim Basin became wetter with deeper snow packs over the high mountains due to increasing orographic precipitation as a result of a southward shift or a strengthening of the boreal Westerlies impinging the interior Asian desert belt. Moreover, the recent cool-moist period from 1985 to 2000 (Table 3.7) has been related to the Arctic Oscillation (this study, Robock, 1984, He et al., 2017).

Table 3.7: Inferred cool-dry, cool-moist, warm-dry and warm-moist periods over the Altai-Dzungarian region from the Little Ice Age (LIA) until present, based on estimated temperatures and precipitation sums.

Periods	1580-1874 (LIA)		1875-2012 (present)	
	DRY	MOIST	DRY	MOIST
COOL	1583-1593; 1625-1636; 1686-1723; 1815-1844; 1871-1872	1594-1624; 1684-1685; 1811-1814; 1845-1870	1919-1938; 1973-1984	1917-1918; 1985-2000
WARM	1581-1582; 1637-1659; 1724-1728; 1754-1780; 1873-1875	1580; 1660-1683; 1729-1753; 1781-1810	1875-1893; 1939-1953; 1967-1972; 2006-2012	1894-1916; 1954-1966; 2001-2005

The recent cooling could have been caused by volcanic aerosols of the El Chichón eruption (Volcanic Explosivity Index 5, 1982) in Southern Mexico, which impacted atmospheric wind patterns, including a positive phase of the Arctic Oscillation (Robock, 1984). However, no widespread volcanic-induced cooling was observed at this time due to the simultaneous warming ocean temperature caused by El Niño (Robock, 2002). During this recent cool-moist period, ice mass accumulation of the glaciers in the Russian Altai Mountains was observed, and Narozhniy and Zemtsov (2011) connected this phenomenon to increased annual precipitation by 8% - 10% especially in winter and spring (April-May) as a result of a strengthening of the zonal circulation over the Altai Mountains. This indicates that the positive AO interacting with El Niño could have reinforced the anomalous Westerlies in the midlatitudes (He et al., 2017).

3.2 Teleconnections of atmospheric indices to regional climate variation

3.2.1 Spatial correlations of the atmospheric indices with temperature and precipitation of CRU TS4.03 dataset (0.5°×0.5°)

The prominent NAO, AO, and NINO3.4 significantly correlated with monthly and seasonal temperature and precipitation over the Altai-Dzungarian region from 1960 to 2012 (Figure 3.12).

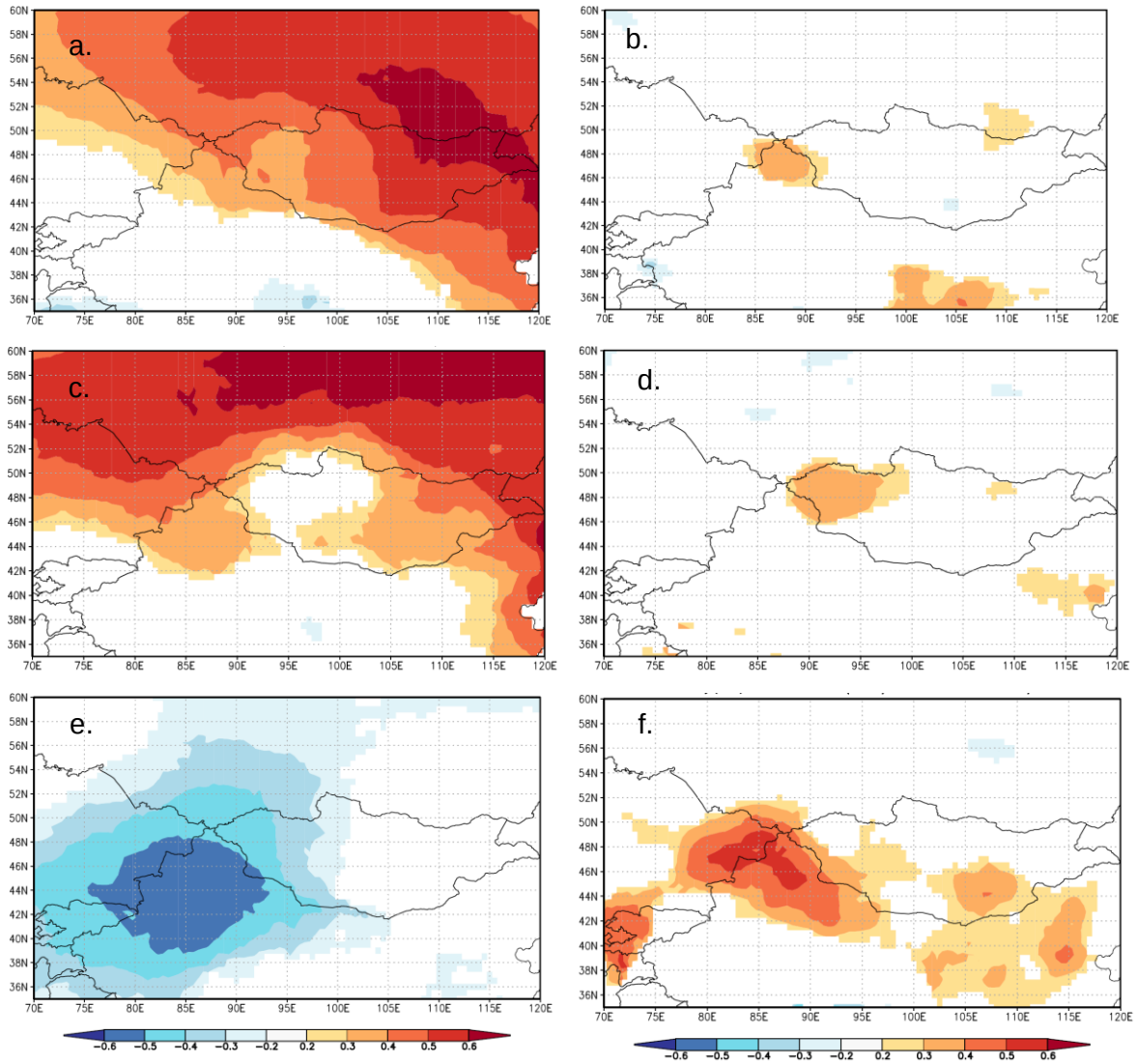

Figure 3.12: Maps showing the strongest interannual correlations of the NAO, AO, and NINO3.4 indices with the gridded temperature (left panel) and precipitation (right panel) of CRU TS4.03 (0.5°×0.5°) for the period of 1960-2012 at 0.1 significant level, as calculated with the KNMI climate explorer (http://climexp.knmi.nl). The mean February-March NAO index and mean February-March temperatures (a), the December NAO index of the previous year and current June precipitation (b), the mean January-May AO index and mean January-May temperature (c), the July AO index and August precipitation (d) the mean NINO3.4 index from May of the previous year through current March with current May temperatures (e) and current May precipitation (f).

A positive winter NAO and a positive winter through spring AO induced warm winter and spring temperatures (Figure 3.12a and c). The February-March NAO index positively

correlated with the February-March temperature (r=0.4, p<0.1, Figure 3.12a). Also, the mean January through May AO index positively correlated with the mean temperature of the same months (r=0.4, p<0.1, Figure 3.12c).

Furthermore, a positive early winter NAO (December) index and a positive summer AO index (July) yielded relatively higher early and late summer precipitation over the Altai-Dzungarian region, respectively. The preceding December NAO index correlated positively with the June precipitation (r=0.3, p<0.1, Figure 3.12b) but negatively with the June temperature (r=-0.3, p<0.1). Also, a positive summer NAO (July) induced a cool (r=-0.4, p<0.1) and wet (r=0.2, p<0.1) summer. Moreover, the July AO index positively correlated with August precipitation (r=0.3, p<0.1, Figure 3.12d).

Finally, a positive NINO3.4 brought cold and wet spring (May) to this region (Figure 3.12e and f). The mean NINO3.4 index of preceding May through current March negatively correlated with the current May temperature (r=-0.4 and -0.5, p<0.1) but positively correlated with the May precipitation (r=0.4 and 0.5, p<0.1). Also, the March-April NINO3.4 index negatively correlated with the mean July-August temperature (r=-0.3, p<0.1). These teleconnections confirm that a positive phase of the NAO index led to increased storm tracks in the Northern hemisphere from the 1960s to1990s (Hartmann et al., 2013) and a positive phase of the Arctic Oscillation brought warm and wet winter conditions over Mongolia in the 1980s due to a northward shift of the polar jet and an intensified westerly jet over the northern Tibetan Plateau (He et al., 2017).

3.2.2 Interannual and interdecadal correlations of the atmospheric indices with the estimated temperature and precipitation

The interannual correlations between the atmospheric indices and the estimated June-July temperature and June through December precipitation were tested for the same period of 1960-2012 as the interannual correlation with gridded observations in the previous subchapter. As expected, the positive winter NAO and AO indices induced cool and wet summers in the Altai-Dzungarian region (Table 3.8). The estimated June-July temperature correlated negatively with the preceding positive December NAO (r=-0.31), December AO (r=-0.32), and preceding April NINO3.4 (r=-0.29) at a 0.05 level. Moreover, the estimated June through December precipitation sum correlated positively with December AO (r=0.25) at a 0.1 level.

The interannual variation of the ocean surface conditions over the North Atlantic is controlled by wind-induced changes in the air-sea heat energy fluxes, while interdecadal variations reflect changes in the ocean circulation itself (Hurrel, 1995). Therefore, all monthly and seasonal time series of the indices and the estimated temperature and precipitation were

smoothed with a running 21-year averaging window over their common period of 1900-2012 and correlated on the interdecadal time scale (Figure 3.13).

Table 3.8: Correlation coefficients between the NAO, AO, and NINO3.4 indices and the estimated summer temperature and precipitation for the periods of 1960-2012

No	Atmospheric indices		Interannual correlation	
			June-July temperature	June-December precipitation
1	NAO	pOct	-	-0.33*
		pDec	-0.32*	-
2	AO	pOct	-0.29*	-
		pDec	-0.34*	0.25^{+}
		cJan	-0.29*	-
3	NINO3.4	pApr	-0.29*	-
		pMay	-0.26^{+}	-

p: previous year; *p<0.05; $^{+}$ p<0.1

On the interdecadal time scale, winter AO and spring NAO strongly correlated to summer temperature (Figure 3.13). The filtered estimated June-July temperature negatively correlated with NAO (-0.30 < r <-0.53) and AO (-0.57 < r <-0.72) from prior November throughout March, whereas positively correlated with April NAO (r=0.69) and April AO (r=0.49) (Figure 3.13ab). Moreover, the estimated temperature negatively correlated with autumn through winter NINO3.4 from prior August to January (-0.24 < r <-0.51) at a 0.001 level (Figure 3.13c).

Furthermore, the filtered estimated June through December precipitation negatively correlated with July NAO (r=-0.65) was strong. It was also positively correlated with the February-April NAO (0.28 < r <0.44) and prior December through March AO (0.23 < r <0.41) at 0.001 in Figure 3.13ab. Also, the estimated precipitation positively correlated with summer NINO3.4 (0.23 < r <0.32) at 0.001 (Figure 3.13c).

According to our findings, cool and wet summers over the Altai-Dzungarian region significantly correlated with positive winter NAO and AO indices for the period 1960-2012 on the interannual time scale; however, on longer and interdecadal time scales, those summers were more strongly correlated with spring and summer NAO indices than winter NAO indices. This difference might be related to the impact of changes in the oceans' heat storage and transport on climate (Hurrel, 1995; Visbeck et al., 2002) since large-scale horizontal and overturning ocean circulation takes several years to respond to large-scale changes in atmospheric forcing (Visbeck et al., 2002).

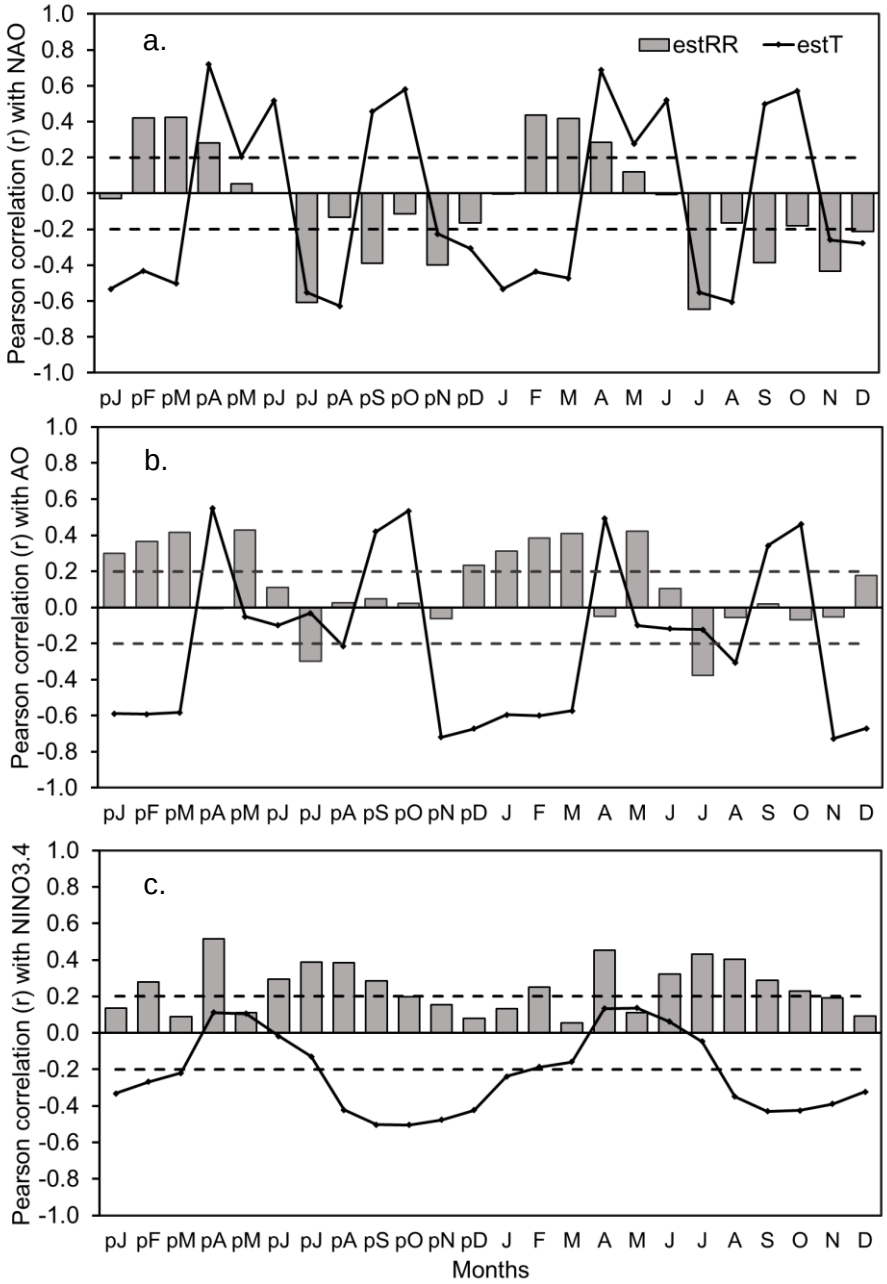

Figure 3.13: Monthly correlation coefficients of the 21-year smoothed estimated June-July temperature and June through December precipitation sum with atmospheric indices: NAO (a); AO (b) and NINO3.4 (c) from 1900 to 2012. The estimated temperature and precipitation are illustrated by a black line with markers, and grey columns respectively. Dashed lines show 95% confidence levels.

Early researchers investigated the most prominent NAO and AO patterns in winter rather than in other seasons (Portis et al., 2001; Hurrel, 1995; Gong and Ho, 2003; Osborn, 2006). Numerous studies proposed a remote and delayed influence of the winter NAO on climate over East Asia through its effect on the Asian jet or wave train patterns originating from the North Atlantic; however, any straightforward mechanism that allows a lag of several months for the North Atlantic or the Arctic signal to reach East Asia has not been suggested yet (Linderholm et al., 2011). A signal of the maximum positive or negative summer NAO event reaches east China in one week (Linderholm et al., 2011).

We found a direct connection between negative summer July NAO and warm and wet summers in the Altai-Dzungarian region. Some studies found the same strong negative correlations between a negative summer (July-September) NAO and warmer summer air temperatures over China and East Asia between 1979 and 2003 (Sun et al, 2008; Yuan and Sun, 2009).

Several studies demonstrated strong links between summer NAO (July-August) and summer climate (July-August) over northern Europe, and East Asia (Folland et al., 2009; Linderholm et al., 2011; Linderholm et al., 2013). They showed that variation of the summer NAO (SNAO) is associated with changes in the North Atlantic storm track. Negative (positive) SNAO is related to its southward (northward) movement over northwest Europe and East Asia. Thus, negative summer NAO brings warm and dry conditions over northwest Europe, northwest and central Mongolia, and northeast China but cooler and wetter conditions over southern Europe, the Mediterranean, and northwest China (Folland et al., 2009; Linderholm et al., 2011). More than half area of the Altai-Dzungarian region is in northwest China. Thus, their findings support our result that negative July SNAO induces wetter conditions over the Altai-Dzungarian region on the interdecadal scale.

In this study, winter AO shows high variations and significant correlations with the estimated summer temperature and precipitation on interannual and interdecadal time scales. Positive winter AO brings cool and wet summer conditions over the Altai-Dzungarian region. In a review of impacts of AO on the East Asian climate, He et al. (2017) accepts this inter-seasonal connection between preceding winter AO and summer precipitation over East Asia in addition to the impacts of AO on simultaneous winter East Asian climate through influences on the Siberian high, westerly winds, blocking frequency and Rossby waves. Winter AO impacts the East Asian summer climate via changes in soil moisture and sea surface temperature changes in the North Atlantic, the Indian, and North Pacific Oceans. The impacts then persists into the following summer (He et al., 2017).

Summer AO generally plays a vital role in anomalous summer weather in mid-latitudes of the Northern Hemisphere (Ogi et al., 2004). Summer AO has been found to be negatively correlated with the West Asian subtropical westerly jet position (WASWJ) and enhances westerlies over northwestern China (Linderholm at al., 2011; Zhao et al., 2014; Zhang and Zhou, 2015). However, in our study, the impact of summer July AO on regional precipitation over the Altai-Dzungarian region, while significant, is lower than the impact of winter AO. This could be explained by the smaller meridional scale of summer AO than winter AO due to the poleward shift of AO in summer.

The Altai-Dzungarian region in northern Xinjiang is located in a mid-latitude inland arid region, thus its rainfall variation depends on water vapor supply, modulated by the West Asian subtropical westerly jet, whereas in East Asia, the summer monsoon supplies sufficient water vapor and cold air from high latitudes participates in rainfall generation (Zhao et al., 2014). When WASWJ is located further south, anomalous southerlies prevail over Xinjiang, and southwest warm and moist air penetrates from low latitudes into the Xinjiang region (Zhao et al., 2014).

Numerous studies have also demonstrated that the Altai-Dzungarian region is influenced by southwesterly monsoonal airflow from the Mediterranean Sea, Black Sea, Caspian Sea, and Aral Sea (Iwao and Takahashi, 2006; Zhao et al., 2014; Zhang et al., 2018) in addition to midlatitude westerly and northwesterly airflow from the Atlantic Ocean during summer (Iwao and Takahashi, 2006; Bohner, 2006; Chen et al., 2015; Zhang et al., 2018).

In this study, we found that positive preceding autumn - early winter NINO3.4 induced cool summer temperatures and positive summer NINO3.4 led to high precipitation over the Altai-Dzungarian region on the interdecadal time scale. Similar cold and wet conditions in Xinjiang and the Dzungarian region were revealed during the El Nino years in research by Zhang and Zhou (2015). Also, Mariotti (2007) found that during warm ENSO events, strong southwesterly moisture flux reaches southwest central Asia, including Pamir and Tian Shan Mountain ranges next to the Altai-Dzungarian region, and across the Arabian Peninsula and tropical Africa over the period 1979-2000.

Winter ENSO can affect temperature and precipitation across middle latitudes by modifying the jet streams (Lindsey, 2016). The significant delayed impact of winter (December-February) NINO3.4 on summer (June-August) rainfall over north Xinjiang was found by Lu et al. (2019), who proposed that the ENSO-induced tropical Indian Ocean Sea surface temperature anomaly persists into the following spring and summer since the warm and wet air from the tropical Indian Ocean is transported into central Asia and converges with the cold air over north Xinjiang associated with the southward shift of subtropical westerly jet. However, this delayed impact of winter NINO3.4 on temperature and precipitation in our study area was observed in teleconnections on the interannual scale but not on the interdecadal scale. Thus, we checked teleconnections of the NAO, AO, and NINO3 indices with the estimated temperature and precipitation for the Altai-Dzungarian region with 25-year centered moving correlations.

3.2.3 Changes in teleconnection of NAO, AO, and NINO3.4 indices to the estimated temperature and precipitation

The 25-year centered moving correlations showed that our determined teleconnections were unstable on a long-time scale (Figure 3.14). These unstable connections were also found in teleconnections between summer NAO and middle East Asian air temperature (Sun et al., 2008; Yuan and Sun, 2009), spring NAO and East Asian Summer Monsoon (EASM) (Zuo et al., 2012), Spring AO and EASM (Gao et al., 2014; Chen et al., 2015), and NINO3.4 and drought in northwestern China (Yao et al., 2019).

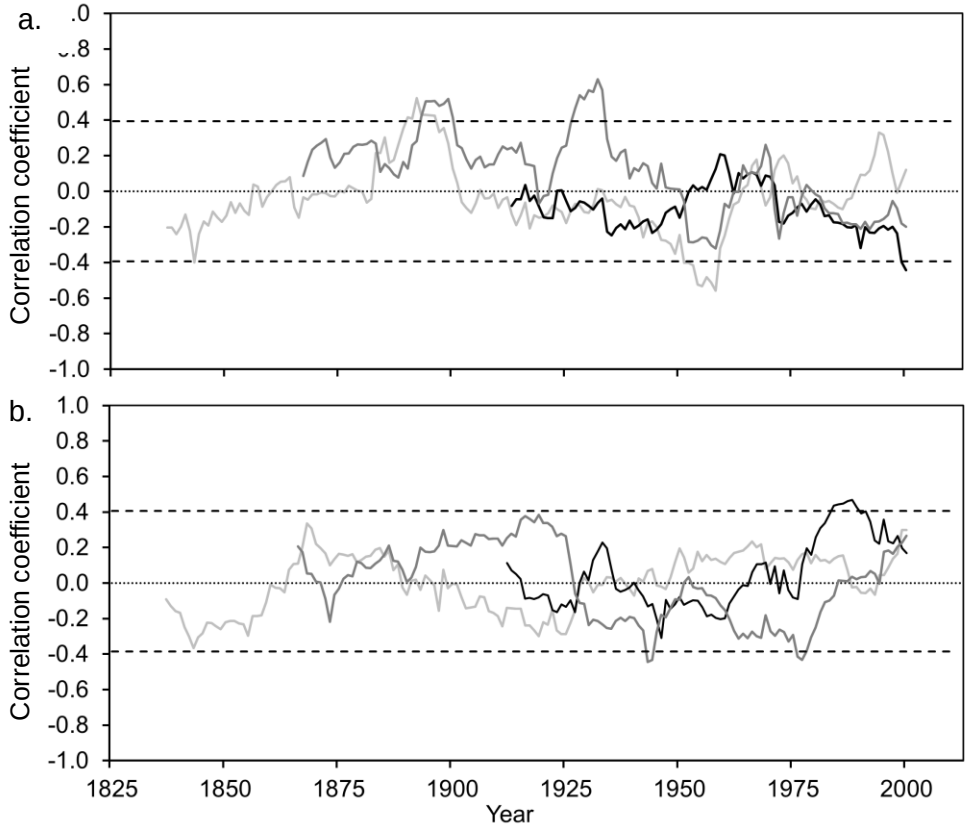

Figure 3.14. 25-year centered moving correlation coefficients between the estimated temperature and mean April-May NAO index (light grey), mean November through March AO (black) and mean April through June NINO3.4 index (grey) (a); and between the estimated precipitation and July NAO index (light grey), mean February-March AO (black) and July NINO3.4 index (grey) (b). Dashed lines show 95% confidence levels, computed by Fisher's z transform.

In Figure 3.14a, the running correlations between the April-May NAO and the estimated temperature showed a gradual change from significant negative correlations in the 1840s to low correlations close to zero, followed by positive and high correlations between 1880 and 1900 and afterward persistent negative low and high correlations till 1963. Later on, weak positive and very low negative correlation periods altered till the 1990s, and significant positive correlations occurred in the mid of 1990s. Mean November-March AO and the estimated temperature was correlated negatively between 1910 and 1950 but positively over

the period 1950-1970. The negative correlation strengthened from 1975 to 2000. The correlations between the mean April through June NINO 3.4 index and the estimated temperature were generally positive with different strengths till 1950, followed by significant negative correlations in the 1950s and weak positive correlations in the 1960s. After that, the correlation changed to negative and strengthened towards 2000.

In Figure 3.14b, the correlation of the estimated precipitation with July NAO was negative from the 1830s to 1860 and shifted to positive over the period the 1860s-1980s, followed by gradually strengthening negative correlations for the period 1900-1930. After low correlations close to zero in the 1930s-1940s and 1988-1995, persistent positive correlations were observed during 1948-1987 and 1996-2000, respectively. The negative correlations between the February-March AO and the estimated precipitation were observed in the 1910s-1920s and the 1940s-1960, altered by positive correlations in the 1930s, 1960s, and 1977-2000. The positive correlation between the July NINO3.4 and the estimated precipitation persisted relatively stable over the period 1875-1925 and gradually strengthened from the early 1900s to the 1920s. Despite low correlation in the early 1950s, moderate negative correlations occurred over the period 1925-1980, followed by very low positive correlation since the mid of 1990s.

During the recent cold period between 1976 and 1998, the estimated summer temperature correlated positively with negative April-May NAO, whereas it correlated negatively with positive November-March AO and April-June NINO3.4 (Figure 3.14a). During the wet period of 1987-2005, the June-December precipitation correlated positively with positive mean February-March AO and July NINO3.4 index. Interestingly, the negative correlation of the estimated precipitation with positive July NAO shifted to a positive correlation with negative July NAO in 1996 (Figure 3.14b). In the late 1970s, teleconnections of summer (July-September) NAO with middle East Asian air temperature and Northern Hemisphere land surface air temperature changed in sign from positive to negative and got stronger related to the shift of summer NAO mode from more westward in the period of 1951-1975 to more eastward from 1979 to 2003 (Sun et al., 2008; Yuan and Sun, 2009).

Also, the NINO3.4-drought connection in Xinjiang (northwestern China) significantly strengthened in 1997. Thus, the frequency of the drought increased in southern Xinjiang, whereas a wetting trend was detected in northwestern Xinjiang from 1997 to 2012, which could be associated with negative NINO3.4 with a delayed effect by 12 months and the transition of Atlantic Multidecadal Oscillation from negative into positive phase. These significant inflection points of the teleconnections in the 1970s and late 1990s coincided with the beginning and end of the recent cool-wet period in our study (Figure 3.11). Also, some studies suggested that a warming of sea surface temperatures over the North Atlantic and

the Indo-West Pacific Ocean led to changes in the position of westerly winds and increased their strength over the Altai-Dzungarian basin, bringing more rainfall over central Asia during the 1980s (Chen et al., 2014).

Overall, positive winter NAO and AO indices significantly correlated with both observed and estimated cool and wet summers over the Altai-Dzungarian region for the period 1960-2012 on the interannual time scale; however, those estimated summer temperature and precipitation correlated with spring and summer NAO indices stronger than winter NAO on the interdecadal time scale. Also, sign and strength of our determined interannual teleconnections were unstable on a long-time scale.

3.3 Hydrological impact of climate change in the southern Altai Mountains for 1984-2015

The Altai Mountains' climate stations are sparse and all located in the valley as illustrated in Figure 3.15; thus, rain gauge observations might suffer from undercatch depending on slope direction, wind, and evaporation (Duethmann et al., 2013). Therefore, we used the interpolated APHRODITE dataset (0.25ºx0.25º) in our climate impact study as an alternative dataset in addition to the station data since the APHRODITE has been shown to provide good estimates of temperature and precipitation amounts over high mountains, including the Himalayas (Ji et al., 2020) and Tianshan Mountains (Shen et al., 2018).

Although the APHRODITE dataset involved daily station data, the biases might come from the quality control and interpolation approach in mountain ranges (Yatagai et al., 2012; Yasutomi et al., 2011). We thus evaluated the climate data of the corresponding grid cells to Duchinjil and Baitag stations without height adjustment to keep the initial condition of the grid cell data in the analysis of linear trends in climate change. Later, the elevation difference of grid cells and stations is adjusted to the mean elevation of the Bulgan catchment; moreover, climate data is corrected with the lapse rate and evaluated before the hydrological simulation in Chapter 3.4.

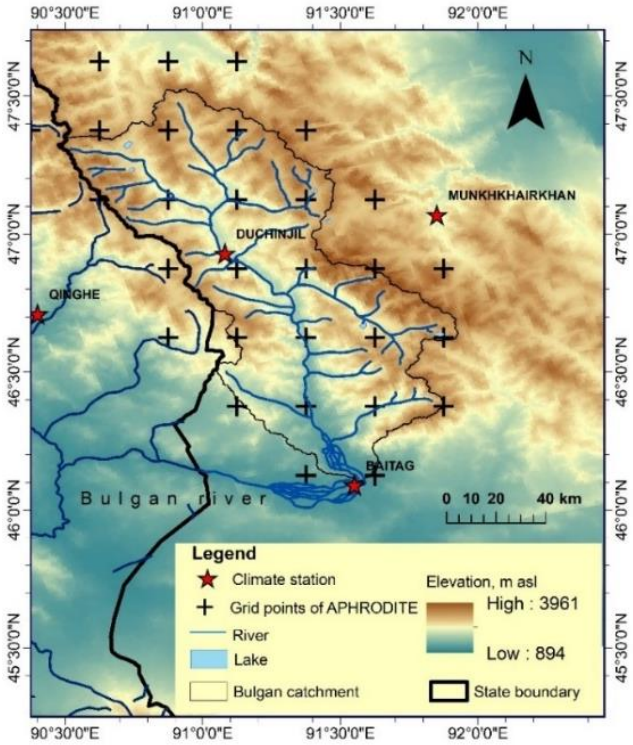

Figure 3.15: Locations of climate stations and the interpolated APHRODITE dataset grid cells (0.25ºx0.25º) overlayed the Bulgan catchment. The red stars indicate the location of the official climate stations close to and in the catchment. Black plus signs show the grid cell centers of APHRODITE.

The grid cell and station dataset and measured river discharges in the southern Altai Mountains have different timespans; thus, observed climate change and its hydrological impact were assessed for their overlapping period of 1984-2015 (Figure 3.16).

3.3.1 Evaluation of the APHRODITE dataset for the southern Altai Mountains

The APHRODITE dataset has the similar annual and seasonal variations to the observation at two stations (Figure 3.16-3.17); however, the APHRODITE underestimates observed precipitation at Duchinjil station in a mountain valley with high Pearson's correlations ($r=0.96$, $p<0.01$) but overestimates precipitation at Baitag station in a desert area ($r=0.86$, $p<0.01$) (Figure 3.18; Table 3.9-3.10). Besides, the numbers of rainy days at Duchinjil (66 days) and Baitag stations (38 days) are overestimated by the grid cells of APHRODITE as 169 and 173 days on average, respectively.

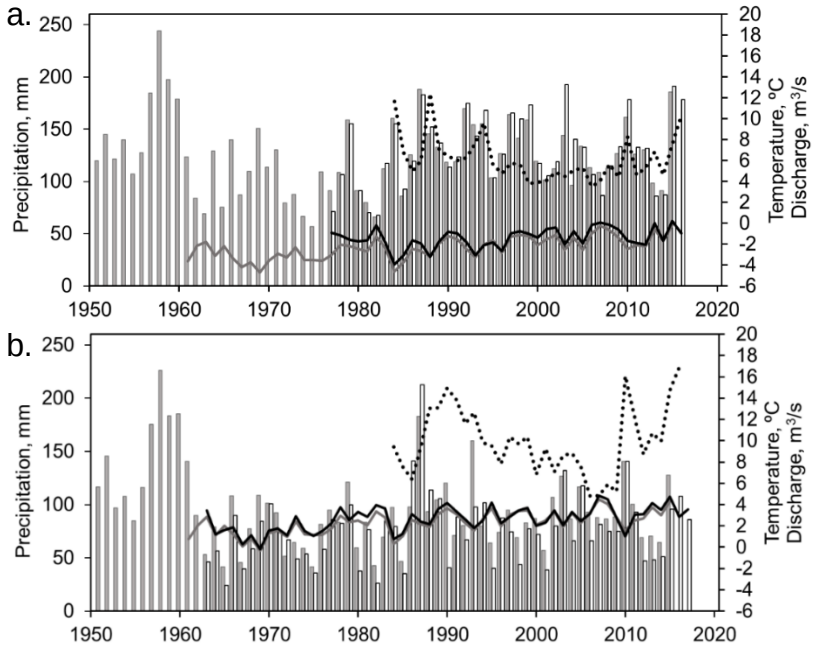

Figure 3.16: Long-term variability of annual mean temperature (ºC, solid lines), annual precipitation sum (mm, bars), and annual mean discharge (m^3/s, dotted lines) at Duchinjil, 1951m (a); and Baitag stations, 1186m (b). The station-based annual precipitation sums and the corresponding grid estimates of APHRODITE are shown by white and grey column bars, respectively. The temperatures of stations and the corresponding grid estimates of APHRODITE are illustrated by solid black and grey lines, respectively. The height of the grid cells corresponding to Duchjinjil and Baitag stations are 2390m and 1404m, respectively.

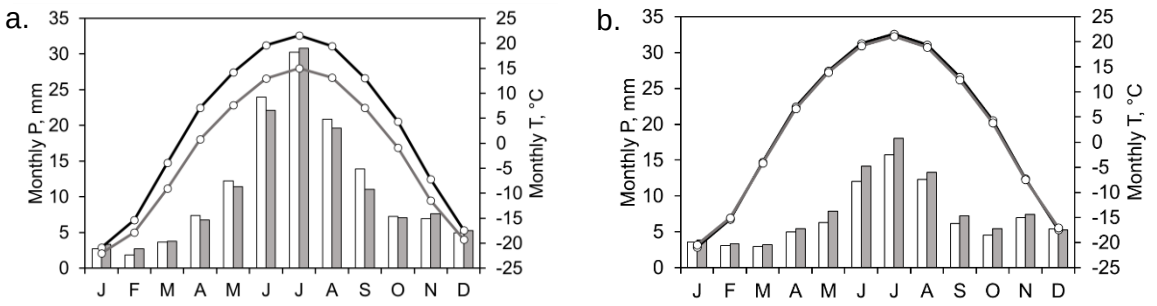

Figure 3.17: Monthly precipitation sum and mean temperature of the corresponding grid cells and Duchinjil (a) and Baitag (b) stations. The monthly precipitation sums of the stations and the grid cells are shown by white and grey column bars, respectively. The monthly temperatures of the stations and the grid cells are illustrated by solid black and grey lines with circles, respectively.

Extreme precipitation was underestimated at Baitag station; thus, summer precipitation had the largest difference in root mean square error (RMSE) and the lowest Pearson's correlation ($r=0.77$, $p<0.01$). Monthly temperatures at the grid cells significantly correlated with the monthly temperatures at both stations ($r=0.99$) at 0.01 (Table 3.11-3.12; Figure 3.18). However, the grid temperatures showed minus biases and were colder than monthly temperatures at the stations, except for positive bias in winter at Baitag.

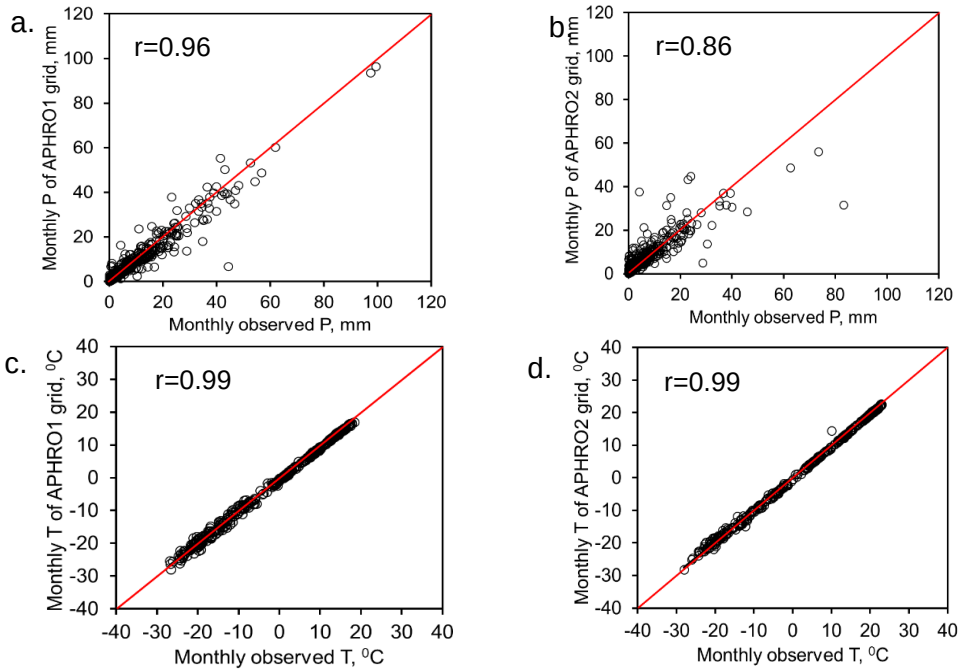

Figure 3.18: Relationships between monthly precipitation sum (P) and mean temperatures (T) of APHRO1 (2390m) and APHRO2 (1404m) grid cells and monthly observations at Duchinjil (a, c) and Baitag (b, d) stations from 1984 to 2015.

Table 3.9: Evaluation statistics of the annual and seasonal precipitation sums of grid cell APHRO1 corresponding to Duchinjil station from 1984 to 2015 on the monthly time scale

Periods	Precipitation sum		Monthly		
	Observation 1951m	APHRO1 2390m	Mean bias	RMSE	Corr (r)
Annual	136.0mm	132.0mm	-0.4mm	3.8mm	0.96
Winter	9.6mm	11.4mm	0.6mm	1.6mm	0.91
Spring	23.2mm	21.9mm	-0.4mm	2.7mm	0.94
Summer	75.1mm	72.6mm	-0.8mm	5.1mm	0.95
Autumn	28.1mm	25.7mm	-0.3mm	2.8mm	0.95

Table 3.10: Evaluation statistics of the annual and seasonal precipitation sums of grid cell APHRO2 corresponding to Baitag station from 1984 to 2015 on the monthly time scale

Periods	Precipitation sum		Monthly		
	Observation 1186m	APHRO2 1404m	Mean bias	RMSE	Corr (r)
Annual	84.0mm	95.0mm	0.9mm	5.1mm	0.86
Winter	12.0mm	12.4mm	0.1mm	1.4mm	0.96
Spring	14.2mm	16.5mm	0.8mm	2.8mm	0.93
Summer	40.0mm	45.5mm	1.8mm	9.5mm	0.77
Autumn	17.7mm	20.1mm	0.8mm	2.3mm	0.96

Table 3.11: Evaluation statistics of the annual and seasonal temperatures of grid cell APHRO1 corresponding to Duchinjil station from 1984 to 2015 on the monthly time scale

Periods	Temperature		Monthly		
	Observation 1951m	APHRO1 2390m	Mean bias	RMSE	Corr (r)
Annual	-1.5°C	-1.9°C	-0.5°C	+1.0°C	0.99
Winter	-19.6°C	-19.6°C	-0.1°C	+1.1°C	0.95
Spring	+0.3°C	-0.2°C	-0.5°C	+0.9°C	0.99
Summer	+14.6°C	+13.7°C	-0.9°C	+0.9°C	0.99
Autumn	-1.1°C	-1.7°C	-0.6°C	+0.9°C	0.99

Table 3.12: Evaluation statistics of the annual and seasonal temperatures of grid cell APHRO2 corresponding to Baitag station from 1984 to 2015 on the monthly time scale

Periods	Temperature		Monthly		
	Observation 1186m	APHRO2 1404m	Mean bias	RMSE	Corr (r)
Annual	+2.9°C	+2.7°C	-0.2°C	+0.7°C	0.99
Winter	-17.8°C	-17.5°C	+0.3°C	+1.0°C	0.98
Spring	+5.8°C	+5.5°C	-0.3°C	+0.7°C	0.99
Summer	+20.2°C	+19.7°C	-0.5°C	+0.5°C	0.99
Autumn	+3.4°C	+3.2°C	-0.4°C	+0.5°C	0.99

Among the precipitation products, the APHRODITE captures the spatial distribution and seasonal patterns of precipitation in the semi-arid Tianshan Mountains well although it underestimates precipitation (Shen et al., 2018). Moreover, the APRHODITE precipitation underestimates the amount of rainfall but overestimates the number of rainy days for the Tibetan Plateau (Ji et al., 2020).

Overall, the APHRODITE underestimates temperature and precipitation amount but overestimates the number of rainy days for the southern Altai Mountains as reported in the other mountainous regions.

3.3.2 Linear trends in temperature and precipitation changes for 1984-2015

The direction of the trendline and the degree of its slope in annual and seasonal temperature and precipitation of Duchinjil and Baitag stations and the corresponding grid cells varied in the long and short-time periods since a trend in the record is sensitive to the beginning and end dates. Generally, all seasonal temperatures of the stations and the grid cells slightly increased over their observation periods, 1977-2017 and 1961-2015, but moderately increased from 1984 to 2015 (Tables 3.13-3.14). Annual precipitation increased at both stations by 18%~31% (24mm) on average since the 1960s but decreased by 15%~24% (20mm) from 1984 to 2015.

During 1984-2015, spring (MAM), summer (JJA), autumn (SON), and annual mean temperatures at Duchinjil station in the mountainous area significantly increased by 2.7°C, 2.1°C, 1.8°C, and 2.1°C at 0.01 level, respectively (Table 3.13; Figure 3.19). Moreover,

spring, summer, and annual temperatures of Baitag station in the desert area significantly increased by 2.4°C ($p<0.05$), 1.8°C ($p<0.001$), and 1.4°C ($p<0.1$), respectively; but autumn temperature warmed by 1.2°C insignificantly (Table 3.14; Figure 3.20). Winter temperature insignificantly increased by 1.8°C at Duchinjil, but decreased by 0.3°C at Baitag from 1984 to 2015.

Between 1984 and 2015, no significant changes were detected in the seasonal and annual precipitation sums at both locations except for autumn precipitation (Figures 3.21-3.22). The autumn precipitation significantly decreased by 46% (-13mm) at Duchinjil in the mountain valley and 89% (-16mm) at Baitag in the desert area. Winter precipitation insignificantly increased by 21% (+2mm) at Duchinjil and 25% (+3mm) Baitag. Summer precipitation declined by 10% (-8mm) at Duchinjil but slightly increased by 4% (+2mm) at Baitag station. In contrast, spring precipitation increased by 12% (+3mm) at Duchinjil but decreased by 46% (-7mm) at Baitag.

Table 3.13: Observed trends (Sen's slope) in seasonal and annual temperatures and precipitation sums at Duchinjil station and its corresponding grid cell in the different periods.

Period	Duchinjil station				APHRO1 grid			
	1977-2017		1984-2015		1961-2015	1951-2015	1984-2015	
	T	P	T	P	T	P	T	P
	°C/ decade	mm/ decade	°C/ decade	mm/ decade	°C/ decade	mm/ decade	°C/ decade	mm/ decade
Annual	+0.3^{+}	+6.3	+0.7**	-6.5	+0.4***	+0.8	+0.6**	-8.5
DJF	+0.0	+1.8*	+0.6	+0.7	+0.5**	-1.4*	+0.0	+1.3
MAM	+0.4*	+1.4	+0.9**	+0.9	+0.3*	-0.7	+0.8**	+0.5
JJA	+0.5***	+2.7	+0.7***	-2.6	+0.4***	+3.2*	+0.7***	-2.4
SON	+0.3	-0.5	+0.6*	-4.5^{+}	+0.5***	-1.0^{+}	+0.7*	-4.3**

+ p=0.1 * p=0.05 ** p=0.01 *** p=0.001

Table 3.14: Observed trends (Sen's slope) in seasonal and annual precipitation sums, and temperature at Baitag station and its corresponding grid cell of APHRODITE in the different periods.

Period	Baitag station				APHRO2 grid			
	1963-2017		1984-2015		1961-2015	1951-2015	1984-2015	
	T	P	T	P	T	P	T	P
	°C/ decade	mm/ decade	°C/ decade	mm/ decade	°C/ decade	mm/ decade	°C/ decade	mm/ decade
Annual	+0.4***	+4.4^{+}	+0.4^{+}	-6.8	+0.4***	-2.5	+0.4*	-1.1
DJF	+0.2	+0.8	-0.1	+1.0	+0.4^{+}	-1.2*	+0.2	+0.1
MAM	+0.4**	+0.7	+0.8*	-2.2	+0.3**	-1.3^{+}	+0.8**	-0.9
JJA	+0.3***	+2.6^{+}	+0.6***	+0.6	+0.4***	+0.7	+0.6***	+1.5
SON	+0.5**	-0.2	+0.4	-5.3*	+0.6***	-1.4*	+0.4	-4.0^{+}

+ p=0.1 * p=0.05 ** p=0.01 *** p=0.001

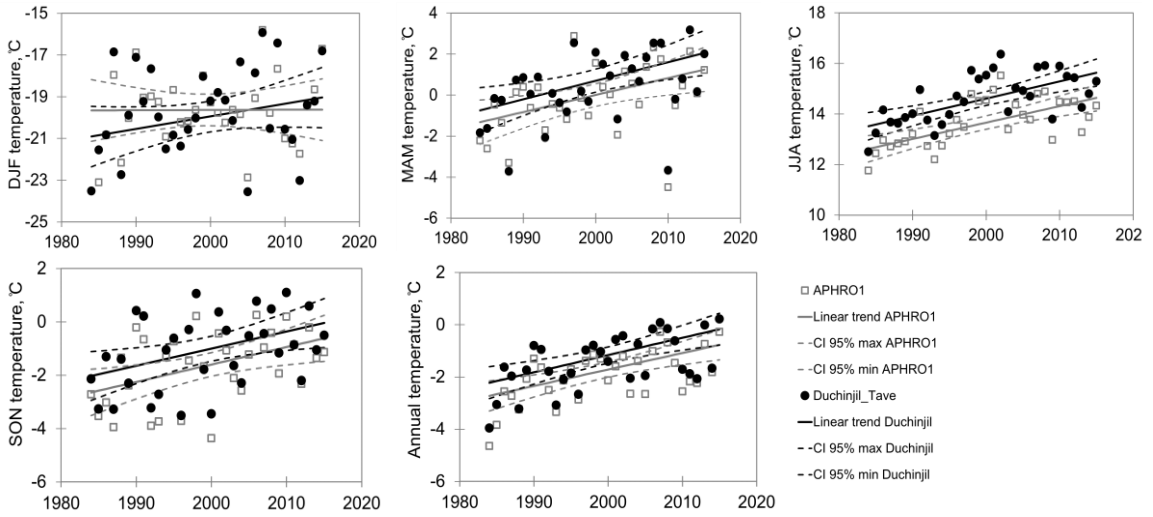

Figure 3.19: Linear trends (non-parametric Sen's slope) in annual and seasonal temperatures of Duchinjil station (1951m a.s.l) and the corresponding APHRO1 grid cell (2390m a.s.l) from 1984 to 2015. Dashed lines show 95% confidence levels.

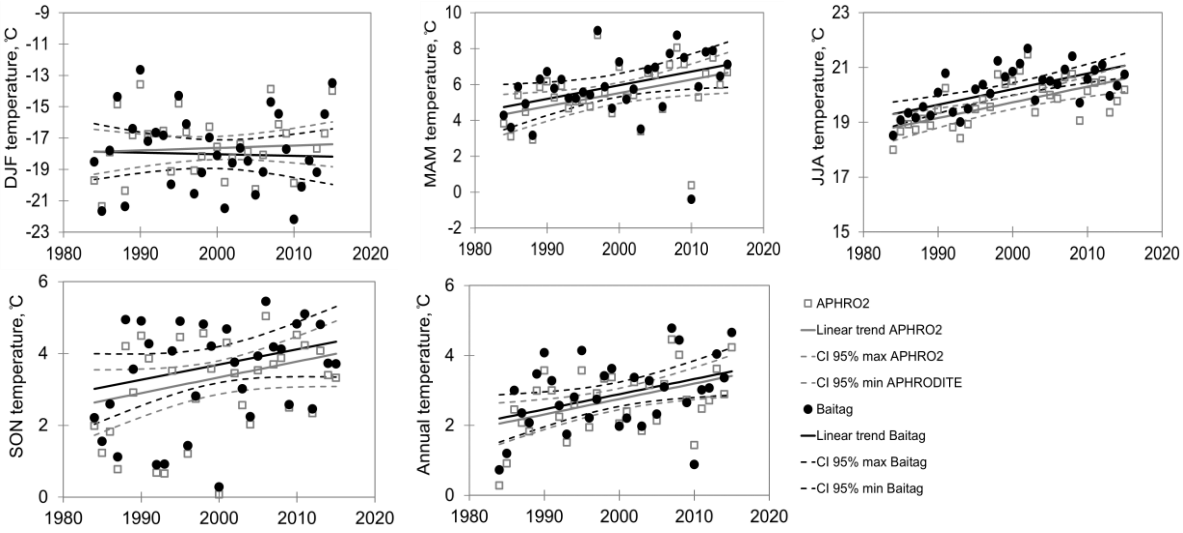

Figure 3.20: Linear trends (non-parametric Sen's slope) in annual and seasonal temperatures of Baitag station (1186m a.s.l) and the corresponding APHRO2 grid cell (1404m a.s.l) for 1984-2015.

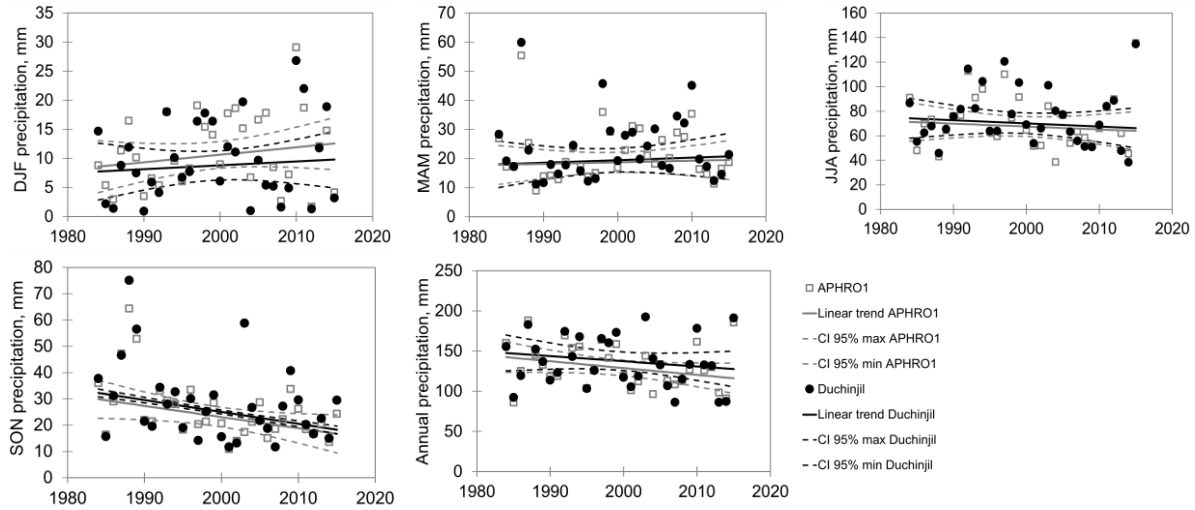

Figure 3.21: Linear trends (non-parametric Sen's slope) in annual and seasonal precipitation of Duchinjil station (1951m a.s.l) and the corresponding APHRO1 grid cell (2390m a.s.l) from 1984 to 2015. Dashed lines show 95% confidence levels.

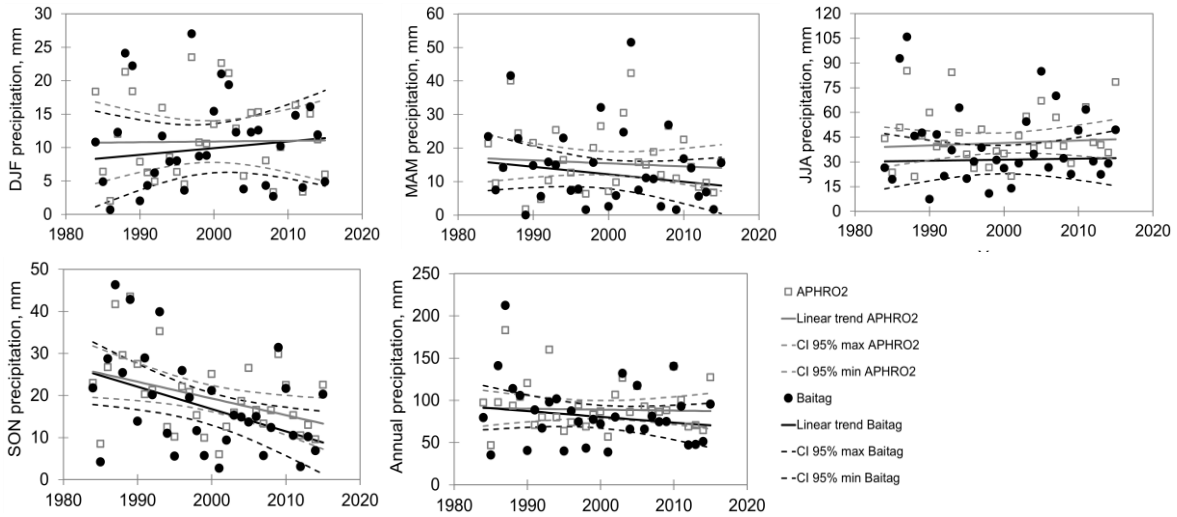

Figure 3.22. Linear trends (non-parametric Sen's slope) in annual and seasonal precipitation sums of Baitag station (1186m a.s.l) and the corresponding APHRO2 grid cell (1404 m a.s.l) from 1984 to 2015. Dashed lines show 95% confidence levels

Taken together, in the southern Altai Mountains air temperature significantly increased by +2°C on average but annual precipitation insignificantly decreased by 15%~24% over the period 1984-2015. Seasonally, precipitation significantly decreased in autumn but increased in winter. The APHRODITE grids showed the same direction of trends but slightly different degree of slopes from station data.

3.3.3 Seasonal and annual evapotranspiration changes

3.3.3.1 Evaluation of temperature-based evapotranspiration methods for semi-arid area

Since the gridded APHRODITE dataset has only daily mean air temperature, affordable and appropriate temperature-based reference evapotranspiration methods are explored for the southern Altai Mountains. Based on the reference evapotranspiration estimation over China by Peng et al. (2017), the empirical temperature-based 1975 Hargreaves equation (H), Hargreaves-Samani (HS), and modified Hargreaves-Samani (MHS) methods were evaluated by comparing with a reference evapotranspiration calculated at Duchinjil and Baitag stations using the Penman-Monteith (PM) method (Table 3.15-3.16; Figure 3.23).

Among those empirical methods, the 1975 Hargreave equation results in the lowest Mean Absolute Error (MAE) and the best performance of the Nash-Sutcliffe efficiency coefficient (R_{eff}) on the daily time scale (Table 3.16).

Table 3.15: Annual and seasonal ET_0 estimates of Penman-Monteith and temperature-based ET methods

Seasons	Duchinjil ET_0 (mean±stdev), mm				Baitag ET_0 (mean±stdev), mm			
	PM	H	HS	MHS	PM	H	HS	MHS
Annual	757±42	691±41	432±32	379±28	825±73	845±43	568±34	499±42
Winter	20±3.7	6.2±3.1	3.6±1.9	3.2±1.7	25.4±8.7	11±5.6	7±3.8	6.1±3.4
Spring	227±20	194±24	121±17.3	106±15	269±34	251±27	168±21	148±18
Summer	390±21	372±19	232±15.5	203±14	419±31	436±20	291±15.4	256±14
Autumn	120±11	119±10.6	77.2±8.7	67±7.7	112±15.3	147±21	101±11	89 ±9.5

Table 3.16: The evaluation statistics of the daily ET estimates by temperature-based ET methods with the reference ET_0 using Penman-Monteith

No	ET methods	Duchinjil				Baitag			
		Mean	Std	R_{eff}	MAE	Mean	Std	R_{eff}	MAE
1	FAO Penman-Monteith (PM)	2.07	1.76			2.24	1.94		
2	1985 Hargreave-Samani (HS)	1.18	1.17	0.78	0.90	1.55	1.45	0.87	0.74
3	Modified Hargreave-Samani (MHS)	1.04	1.03	0.71	1.04	1.37	1.28	0.81	0.90
4	1975 Hargreave (H)	1.89	1.78	0.97	0.33	2.31	2.07	0.95	0.48

Related to the seasonal distribution of solar radiation and air temperature, a high ET_0 occurs from May to August, while a low ET_0 occurs in December and January. The 1975 Hargreaves equation underestimated ET_0 sums for a year and winter through summer months at Duchinjil station but overestimated ET_0 sums for a year and summer through autumn months at Baitag station (Figure 3.23).

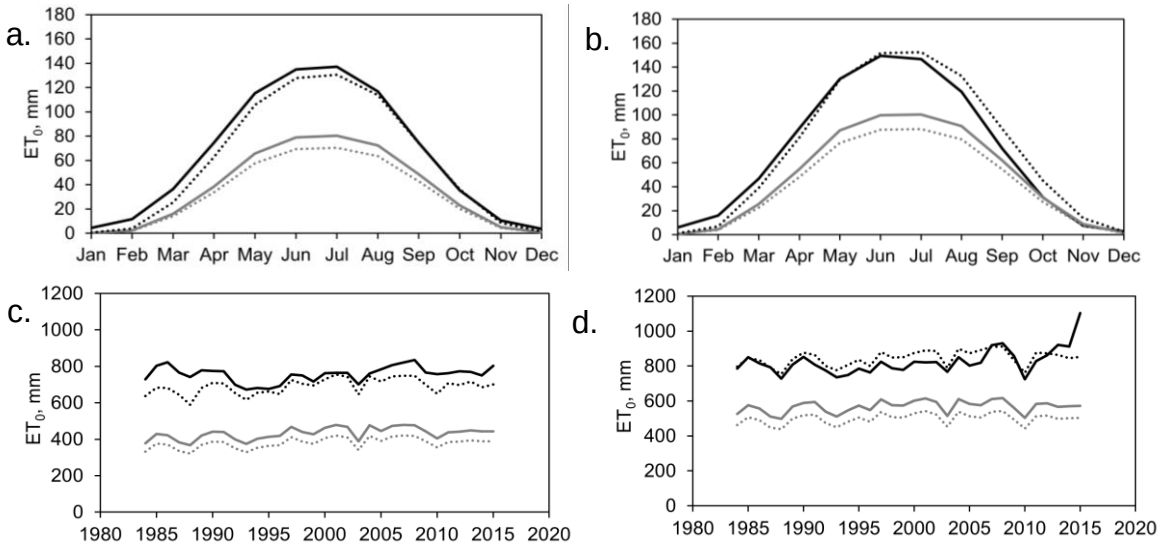

Figure 3.23. Annual and monthly ET_0 sums estimated by Penman Monteith (PM as a reference evapotranspiration), 1975 Hargreave (H), 1985 Hargreave-Samani (HS), and Modified Hargreave-Samani (MHS) at Duchinjil (a, c) and at Baitag (b, d) stations over the period of 1984-2015 are shown in black line (PM), black dotted line (H), grey line (HS) and grey dotted line (MHS), respectively.

1975 Hargreave equation is applied to estimate daily ET_0 for the stations and the corresponding APHRODITE grid cells to reveal observed changes in evapotranspiration over the southern Altai Mountains from 1984 to 2015.

3.3.3.2 Linear trends in seasonal and annual evapotranspiration sums

The annual and seasonal ET_0 of stations and the corresponding grid cells illustrated increasing trends over time (Figure 3.24-3.25).

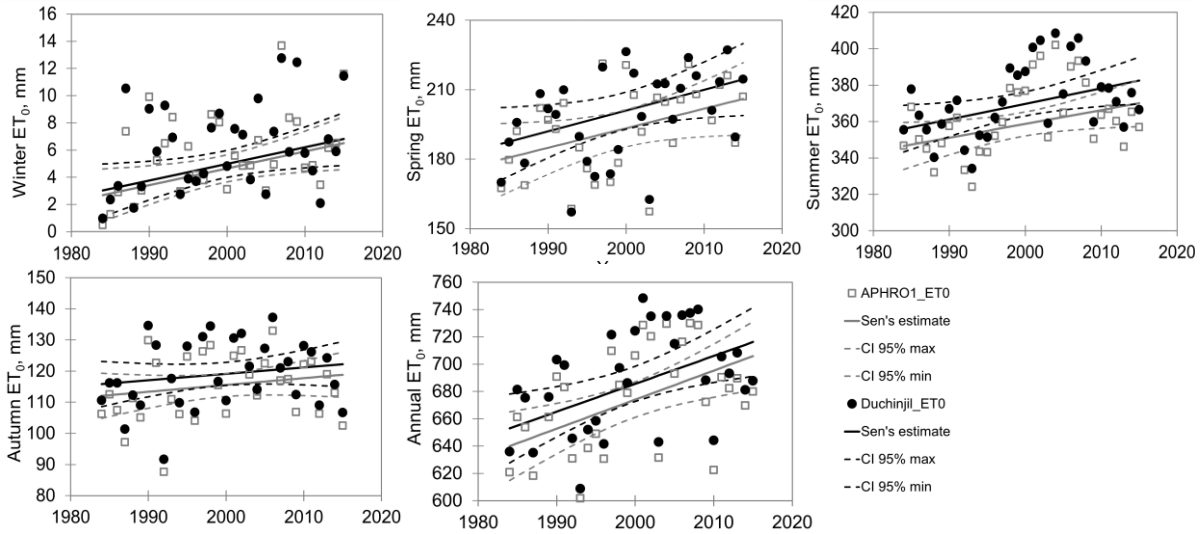

Figure 3.24: Linear trends in annual and seasonal evapotranspiration sums observed at Duchinjil station (1950m a.s.l) and the corresponding grid cell from 1984 to 2015. Dashed lines show 95% confidence levels.

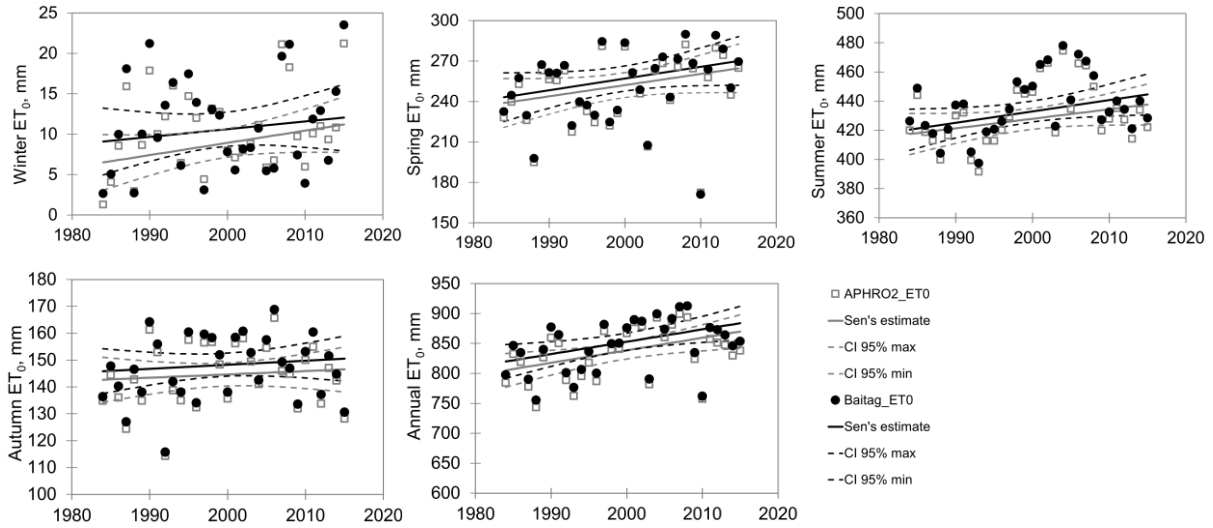

Figure 3.25. Linear trends in annual and seasonal evapotranspiration sum (ET_0) observed at Baitag station (1186m a.s.l) and the corresponding grid cell from 1984 to 2015. Dashed lines show 95% confidence levels.

Summer ET_0 in the Altai Mountains moderately increased and reached peak values in mid of the 2000s, which coincided with drought years from 2000 to 2002 and 2007 in Mongolia (Nandintsetseg and Shinoda, 2013), then declined. At Baitag station, the minimum spring and annual ET_0 sums were recorded in the abnormally heavy snowy and extremely cold winter of 2009-2010 (Figure 3.25). That might be related to unusual frost days in the southern Altai Mountains from December 2009 to March 2010 (Middleton et al., 2014). Moreover, the snow was deeper (>33cm) with a greater extent in the desert area than that in the high mountains from January to March of 2010; furthermore, snow cover stayed until the end of April 2010 since many days of April had lower temperatures than zero (Middleton et al., 2014).

Between 1984 and 2015, annual ET_0 increased significantly by 9% (60 mm) in the southern Altai Mountains at 0.05 (Table 3.17). Seasonally, ET_0 rose significantly by 10% in spring and by 6% in summer on average. In particular, ET_0 of March, April, and July increased at Duchinjil by 34%, 17%, and 9%, respectively. Winter ET_0 rose by 20% at Duchinjil and 8% at Baitag. Although autumn ET_0 increased insignificantly, November ET_0 significantly increased by 12% at Duchinjil station and APHRO1 grid cell.

Table 3.17: Observed trends (Sen's slope) in monthly, seasonal, and annual evapotranspiration at Duchinjil and Baitag stations and their corresponding grid cells of APHRODITE from 1984 to 2015.

Period	Duchinjil	APHRO1	Baitag	APHRO2
	ET_0, mm/ decade	ET_0, mm/ decade	ET_0, mm/ decade	ET_0, mm/ decade
Annual	+20.4*	+21.3*	+20.6*	+20.8+
Winter (DJF)	+1.2+	+1.2*	+0.9	+1.5
Spring (MAM)	+8.9*	+8.4*	+8.7*	+8.3*
Summer (JJA)	+8.5*	+7.6*	+7.8*	+6.5+
Autumn (SON)	+2.0	+2.2	+1.5	+1.2

+ p=0.1 * p=0.05 ** p=0.01

Briefly, among three temperature-based equations, the 1975 Hargreaves equation was found as a viable alternative to the Penman-Monteith method to estimate ET_0 over the semi-arid Altai-Dzungarian region. Seasonal and annual ET_0 sums increased over the southern Altai Mountains of Mongolia from 1984 to 2015. This result supports previous findings that the reference ET_0 significantly increased over the whole territory of Mongolia (Yu et al., 2016) and in the semi-arid northwestern China or the Dzungarian region (Wei and Wang, 2013). These studies concluded that the upward trend of the reference ET_0 is related to the continuous increase in air temperature since the 1970s.

3.3.3.3 Important climate factors in intensification of evapotranspiration over the southern Altai Mountains

To identify driving factors, we calculated reference evapotranspiration (ET_0) at Duchijil and Baitag stations by the Penman-Monteith approach as a predictand and developed stepwise linear regression models on seasonal and annual scales. The maximum and minimum temperatures, precipitation, wind speed, relative humidity, and radiation are used as predictors in the models. Although maximum temperature, wind speed, relative humidity, and radiation explained 88% to 98% of the variations in the evapotranspiration over the southern Altai Mountains, wind speed and the maximum temperature more positively correlated with ET_0 at both stations (Table 3.18).

Table 3.18: Statistics of the stepwise linear regressions for seasonal and annual Penman-Monteith ET_0 estimates at different altitudes ($p<0.001$)

Duchinjil station in high mountains, 1951m						Baitag station in desert area, 1186m				
Periods	R	Exp. var (%)	SE	Predictors	Std Beta	R	Exp. var (%)	SE	Predictors	Std Beta
Winter	0.94	88	1.3	Wind, m/s	0.70	0.94	88	3.0	Wind, m/s	0.80
				Tmax, ℃	0.65				Tmax, ℃	0.28
									Radiation	0.19
Spring	0.98	95	4.3	Tmax, ℃	0.62	0.99	97	5.6	Tmax, ℃	0.36
				RH, %	-0.22				RH, %	-0.32
				Wind, m/s	0.29				Wind, m/s	0.33
				Radiation	0.30				Radiation	0.26
Summer	0.99	98	3.4	Wind, m/s	0.68	0.98	96	6.1	Wind, m/s	0.76
				Tmax, ℃	0.53				Tmax, ℃	0.38
				RH, %	-0.18				RH, %	-0.29
				Radiation	0.33				Radiation	0.25
Autumn	0.96	91	3.3	Wind, m/s	0.83	0.94	88	5.4	Wind, m/s	0.98
				Tmax, ℃	0.51				Tmax, ℃	0.20
				RH, %	-0.25				Radiation	0.17
Annual	0.95	90	13.7	Wind, m/s	0.61	0.95	91	23.4	Wind, m/s	0.67
				Tmax, ℃	0.54				Radiation	0.29
				Radiation	0.30				RH, %	-0.28
				RH, %	-0.19					

Unit of radiation - MJ/m^2; R- Pearson's correlation; Exp.var - Explained variance (R^2, %); SE - Std. Error of the Estimate; p value – significance level; Std Beta - Standardized Beta shows impact of predictor; $p<0.05$

The impact of the temperature on ET_0 seemed higher in the mountains than in the desert, whereas the effect of the wind speed on ET_0 appeared high in the desert. Besides moderate warming between 1984 and 2015, the wind speed increased at Baitag station by 1.2m/s ($p<0.001$) in winter, 0.3m/s ($p<0.1$) in spring, and 0.3m/s ($p<0.01$) on an annual scale, but insignificantly rose by 0.1m/s in summer and autumn. In contrast, wind speed insignificantly decreased at Duchinjil station by 0.5m/s on average.

Overall, an increase in wind speed and temperature might intensify the evapotranspiration over the semi-arid southern Altai mountains since increasing wind speed effects largely on the evapotranspiration by replacing water vapor over the evaporating surface with dry air (Allen et al., 1998). The dryness of the air and the amount of solar radiation leads to high ET_0 demand (Allen et al., 1998). Our findings are consistent with previous studies (Huang et al., 2015; Yu et al., 2016). Huang et al. (2015) found that ET_0 over China correlated positively with sunshine hours, maximum temperature, and wind speed but negatively with relative humidity during 1960-2013. Also, Yu et al. (2016) revealed positive correlations of air temperature, wind speed, and sunshine hours but negative correlations of relative humidity and precipitation with ET_0 estimated using Penman-Monteith over Mongolia for the period 1980-2006. The Yu et al. (2016) study also found that ET_0 was also affected by land surface characteristics including vegetation and elevation.

3.3.4 Annual and seasonal runoff changes in the Bulgan catchment

Rivers of the Altai Mountains are temperature-dependent and fed by rain and snowmelt, ice and glacier melt; thus, they have low flows in the cold season and high flows in the warm season (Davaa, 2015).

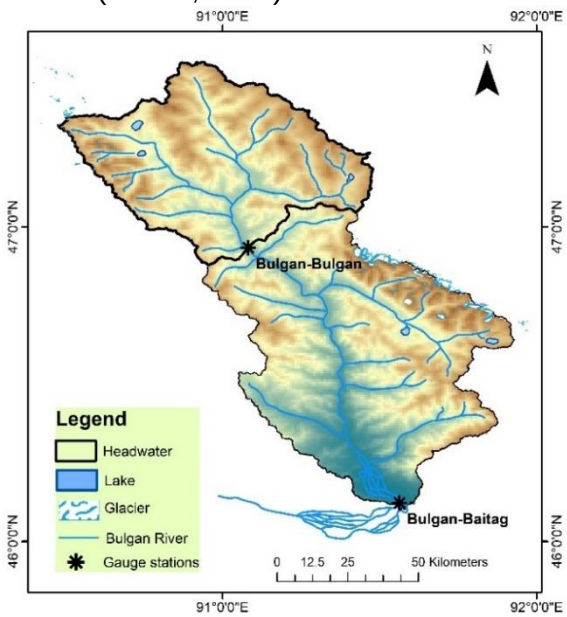

Based on runoff components, previous studies suggested four periods in hydrological regime of the rivers in the southern Altai Mountains (Davaa, 2015; Zhang et al., 2017). Therefore, we evaluated changes in hydrological regime of Bulgan River by estimating linear trends in runoff changes at the upstream and downstream gauge stations in the different runoff component-based periods since the runoff contributors were varied under climate change (Figure 3.26).

Figure 3.26: Location of gauge stations along the Bulgan River.

3.3.4.1 Hydrological regime of Bulgan River

The peak flow of the snowmelt period from April through June dominates in the natural regime of the Bulgan River; moreover, groundwater contribution in the downstream runoff is higher than the upstream runoff (Table 3.19).

Table 3.19: The upstream and downstream runoff distributions (%) of the Bulgan River in different runoff component-based periods.

Runoff component-based periods	*Upstream runoff, %*	*Downstream runoff, %*
A. Snowmelt period of April-May-June (snowmelt 60%, rainfall 40%)	48	34
B. Glacier melt and rainfall period of July-August (glacier 13%, rainfall 87%)	31	27
C. Mixed contribution period of September-October (groundwater 50%, rainfall 30%, snowmelt 20%)	14	15
D. Groundwater recharge period of November through next March (groundwater 100%)	12	24
Total	100	100

High flow rates up to 10% but low flow rates above 70% of the exceedance probability (percent of time). Medium flow ranges between 10% and 70% (Eslamian, 2014; Figure 3.27a). The slope of the FDC is steep for the highly varied upstream runoff due to more rainfall and snowmelt runoff contribution in the high mountains; however, the slope of the flow duration curve (FDC) is flat for the downstream discharge of Bulgan River as more groundwater sustains a low flow in cold season (Figure 3.27a).

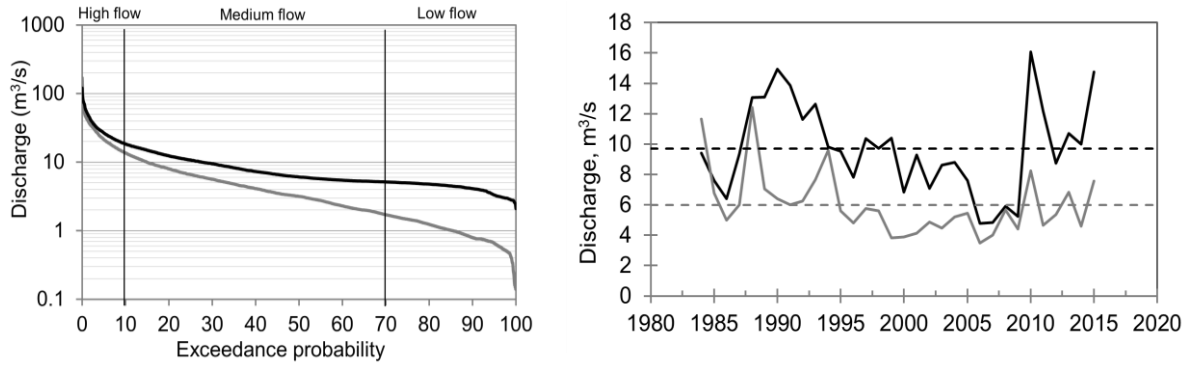

Figure 3.27: Flow duration curves of the upstream (grey line) and downstream (black line) discharges on a daily time scale (a). Year-to-year variation of the upstream and downstream discharges and their long-term means (grey and black dashed lines) throughout 1984-2015 (b) The vertical axis of the left figure is on a logarithmic scale to show all data on a single chart.

As shown in Figure 3.27b, The Bulgan River has shown strong decadal fluctuations with a high flow from 1988 to 1995, followed by a persistent low flow from 1996 to 2009, then a high flow from 2010 to 2015 again. The coefficients of variation of the upstream and the downstream discharges are 34% and 29% over the period 1984-2015, respectively.

According to the year-to-year variations of the upstream and downstream discharges for 1984-2015, the highest and the lowest values were observed as 12.4m^3/s in 1988 and 3.5m^3/s in 2006 at the upstream Bulgan-Bulgan station (1937m a.s.l). Also, the highest value of 16m^3/s and the lowest value of 4.8m^3/s were recorded in 2010 and 2006 at the downstream Bulgan-Baitag station (1178m a.s.l). The long-term means of the upstream and the downstream discharges are 6.0±2.1m^3/s and 9.5 ± 2.7m^3/s, respectively.

On daily time scales, at the upstream hydrological station, the maximum discharge of 170m^3/s was observed on 26-27 July 1994, whereas the minimum value of 0.14m^3/s occurred in February-March 1992. At the downstream station, the peak discharge of 120m^3/s was recorded on 3 June 1987, whereas the lowest value of 2.1m^3/s occurred on 31 December 2006.

3.3.4.2 Changes in timing and amounts of the seasonal and annual runoffs

We analyzed linear trends in runoff variations of the Bulgan catchment in different runoff component-based periods, identified by previous studies (Zhang et al., 2017; Davaa, 2015). From 1984 to 2015, runoff at the upstream Bulgan-Bulgan gauge significantly increased by 87% (6mm) in the cold season from November to March but decreased by 57% (28.2mm) in the warm season from April to August, especially summer discharge declined by 60% (21.6mm). The runoff at the downstream Bulgan-Baitag gauge insignificantly decreased in all seasons, in particular the summer discharge declined by 32% (6mm) (Table 3.20; Figure 3.28).

Table 3.20: Linear trends in river runoff changes at the upstream Bulgan-Bulgan and the downstream Bulgan-Baitag gauges during seasonal and specified periods over the period 1984-2015.

Seasons	Bulgan-Bulgan	Bulgan-Baitag	Runoff component-based periods	Bulgan-Bulgan	Bulgan-Baitag
	mm decade	mm decade		mm decade	mm decade
Winter (DJF)	+1.3***	-0.2	Snowmelt (AMJ)	-4.8*	-1.0
Spring (MAM)	-1.3	-0.2	Rainfall & glacier (JA)	-4.4**	-1.3
Summer (JJA)	-7.2*	-2.0	Rain, snowmelt & groundwater (SO)	-0.2	+0.1
Autumn (SON)	+0.3	+0.0	Groundwater/ Cold season (NDJFM)	+2.0***	-0.1
Annual	-7.3*	-2.7	High flow/Warm season (AMJJA)	-9.4**	-2.2

+ p=0.1 * p=0.05 ** p=0.01 *** p=0.001 Significant trends are marked in Bold.

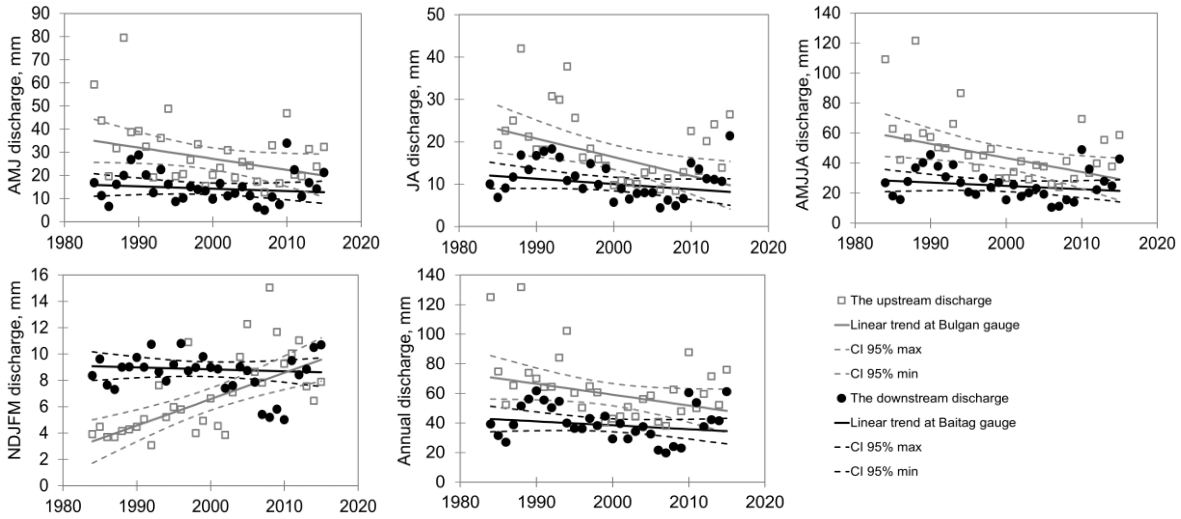

Figure 3.28: Linear trends (non-parametric Sen's slope) in discharge changes annually and in runoff component-based periods from 1984 to 2015. The upstream discharge at Bulgan gauge and the downstream discharge at Baitag gauge are illustrated by grey squares and black circles, respectively. Dashed lines show 95% confidence levels of the trendlines.

The flow duration curve (FDC) is sensitive to the vertical distribution of the soil moisture within the catchment but not to the timing of hydrologic events (Yilmaz et al., 2008). Therefore, we compared flow duration curves (FDC) of the upstream and downstream discharges in two different periods: glacier recession period from 1984 to 2000 and glacier stagnation period from 2001 to 2015 (see Chapter 2.1.4). During the stagnation period, the slope of the FDC of the upstream discharge altered from steep to flat as a result of a decrease in short period high flows and an increase in low flow. However, at the downstream discharge station, both high and low flows slightly reduced over the recent period of 2001 to 2015 (Figure 3.29).

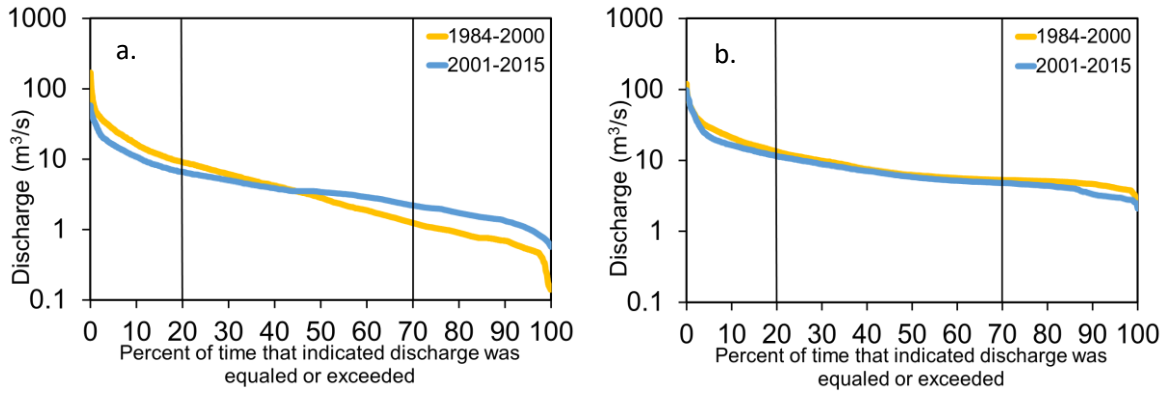

Figure 3.29: Flow duration curves of daily discharges at the upstream (a) and the downstream gauges (b) in the periods 1984-2000 and 2001-2015. The vertical axis is on a logarithmic scale to show all data on a single chart. Separation of High, Medium and Low flows are highlighted by the vertical thick lines.

The steep slope of the FDC indicates a fast response of the catchment as a result of small soil storage capacity and a large amount of overland flow, whereas a flat slope is related to the slow and sustained response of groundwater flow (Yilmaz et al., 2008).

The same significant increases in river discharge during the cold season were also reported in high-latitude permafrost regions (Liljedahl et al., 2017) and high mountain permafrost regions in the past decades (Wang et al., 2019, Wang et al., 2017). These studies suggested different reasons for this upward trend in winter discharge, including an increase in glacier-derived aquifer recharge (Liljedahl et al., 2017), an increase in groundwater recharge to baseflow (Wang et al., 2019), and a delay in water recharge from summer rainfall due to expansion of the soil storage capacity as a result of permafrost degradation (Wang et al., 2017). Also, Kong and Pang (2012) found that discharges in autumn and winter in northwestern China have increased since 1990 due to increased precipitation and groundwater contribution into the Urumqi River rather than glacier melt. Thus, like in other high mountain permafrost regions, the groundwater capacity of the Bulgan catchment might have enlarged and brought an increase in the low flow of the upstream discharge in recent decades.

Furthermore, Wang (2019) determined an important role of the freezing temperature in controlling winter discharge by reducing the hydraulic conductivity and active water content of the aquifer in the cold region. In Canada, the Albany catchment conductivity decreased by half when air temperature accumulated to -172°C from winter start. Thus, climate warming in cold region significantly increases baseflow in winter through increasing hydraulic conductivity (Wang, 2019). Wang (2019) also suggested that the change in baseflow might have influenced river ice formation and breakup. We found that from 1984 to 2010 ice break-up of the Bulgan River started 17 days earlier ($p<0.05$) and freeze-up was delayed by 16 days at the upstream gauge (Figure 3.30a). However, at the downstream gauge, the ice break-up was insignificantly delayed by 8 days and the freeze-up date was significantly delayed by 20 days at 0.01 (Figure 3.30b).

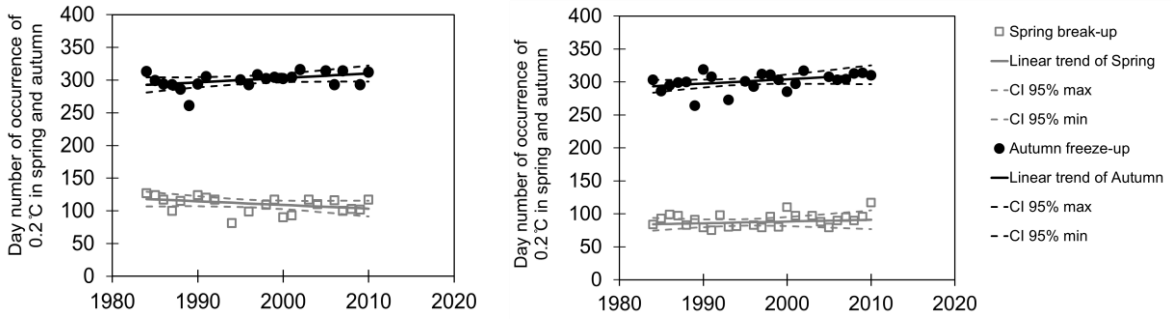

Figure 3.30: Linear trends (non-parametric Sen's slope) in river ice formation and breakup changes at the upstream Bulgan-Bulgan gauge (a) and the downstream Bulgan-Baitag gauge (b) 1984 to 2010

In addition, between 1984 and 2007, the maximum water temperature also increased by 0.45°C per decade ($p<0.01$) at the upstream gauge and by 2.3°C ($p<0.01$) per decade at the downstream gauge. Similarly, monthly mean water temperatures increased at both gauges. Overall, the shortened cold season and increased groundwater recharge due to permafrost degradation might have led to increasing baseflow of the Bulgan River in winter like in other high mountain permafrost regions.

3.3.5 Relationship between climate and seasonal runoff change

Regarding observed changes in the seasonal runoff of the Bulgan River, the most influencing climate factors on Bulgan River were determined using Stepwise Linear Regression Models using seasonal temperatures and precipitation from January of the previous year to December of the current year as predictors.

Interestingly, the upward trend in the upstream discharge during winter (DJF) was driven by July temperature ($\beta=0.52$), whereas the downward trend during the warm season (AMJJA) was triggered by November precipitation ($\beta=0.59$) and summer temperature (JJA, $\beta=-0.35$) of the previous year and August precipitation ($\beta=-0.35$) (Table 3.21). Furthermore, 40% of the variation in snowmelt runoff from April through June at the upstream area was explained by June temperature ($\beta=-0.39$) and November precipitation ($\beta=0.38$) of the previous year, whereas 58% of the variation in glacier melt fed runoff of July to August was explained by November precipitation ($\beta=0.47$) of the previous year and June through August temperature ($\beta= -0.55$) of the current year.

At the downstream discharge, 54% of the variation in snowmelt runoff from April through June was explained by only precipitation sum from September of the previous year through February of the current year ($\beta=0.74$). 44% of the variation in glacier melt runoff of July to August was explained by a positive correlation with June through August precipitation sum ($\beta=0.48$) of the current year but a negative correlation with both precipitation ($\beta=-0.46$) and temperature ($\beta=-0.32$) for April of the current year. Furthermore, 41% of the variation in river flow from April through August was explained by accumulated snow from September of the previous year through February of the current year ($\beta=0.64$).

Table 3.21: Statistics of stepwise linear regression for seasonal and annual river discharges

	Upstream discharge						Downstream discharge					
Periods	R	Exp. var (%)	SE	p value	Predictors	Std Beta	R	Exp. var (%)	SE	p value	Predictors	Std Beta
Winter, DJF	0.52	27	1.6	0.003	pJuly_T	0.52	-					
Spring, MAM	0.56	31	4.8	0.006	pSept_P pNov_T	0.36 -0.37	0.83	69	2.4	<0.001	pSep_P pDec_P cMay_P	0.77 0.41 -046
Summer, JJA	0.74	55	13.1	<0.001	pNov_P cMay_T	0.53 -0.45	0.65	43	6.4	<0.001	pSONDJF_P cJun_P	0.52 0.40
Autumn, SON	0.45	20	2.2	0.011	cJJA_P	0.45	0.57	33	2.1	0.004	pNov_P pOct_T	0.55 0.38
Snowmelt period, AMJ	0.64	40	10.6	0.001	pNov_P pJun_T	0.38 -0.39	0.74	54	4.6	<0.001	pSONDJF_P	0.74
Rainfall and glacier melt period, JA	0.76	58	5.6	<0.001	cJJA_T pNov_P	-0.55 0.47	0.66	44	3.4	0.001	cJJA_P cApr_P cApr_T	0.48 -0.46 -0.32
SO	0.65	42	1.7	0.002	JJA_P Apr_P Sept_P	0.40 -0.32 0.31	0.45	20	1.8	0.012	cMAM_T	-0.45
Groundwater/ Cold season, NDJFM	0.49	24	2.7	0.005	pJuly_T	0.49	-					
High flow/Warm season, AMJJA	0.78	61	13.1	<0.001	pNov_P pJJA_T cAug_P	0.59 -0.35 -0.35	0.64	41	8	<0.001	pSONDJF_P	0.64
Water year	0.75	55	13.6	<0.001	pNov_P cAug_P	0.76 -0.46	0.58	33	10.1	0.001	pSONDJF_P	0.58

R- Pearson's correlation; Explained variance (R^2, %); SE - Std. Error of the Estimate; p value – significance level; Std Beta - Standardized Beta shows impact of predictor; p<0.05; c: current year; p: previous year; NA – Not available

Taken together, snow accumulated from late autumn through winter and summer temperature are important factors in runoff variation. In other words, more accumulated snow and June rainfall generate more river flow, while little snowfall and high summer temperature cause prolonged low flow. These results also suggest that the warming of summer temperature by +2.1°C in the southern Altai Mountains increased winter discharge by 87% in the upstream area but the significant decrease in autumn precipitation of 46% reduced both annual upstream and downstream discharges by 34% and 20% from 1984 to 2015.

3.4 Hydrological modeling of Bulgan catchment

Simulating the water balance of the Bulgan catchment by rainfall-runoff HBV-Light model, the hydrological impact of climate variability was quantified as the percentage change in annual discharge in response to a change in annual precipitation and potential evapotranspiration.

The equation of the water balance for a catchment (Ma et al., 2008):

$$P=ET+R+\Delta S$$

where P is precipitation, ET is evapotranspiration, R is surface runoff measured as river discharge, and ΔS is the change in catchment water storage.

3.4.1 Climate input data preparation

Based on two hydrological stations along the Bulgan River, the catchment is divided into upper and lower subcatchments as a hydrological unit (Figure 3.31). The elevation of the Bulgan catchment ranges from 1185m to 4160m above sea level (a.s.l). The catchment area is divided into 15 elevation zones with 200m intervals. The elevation zone from 2300 to 2900 dominates in the Bulgan catchment.

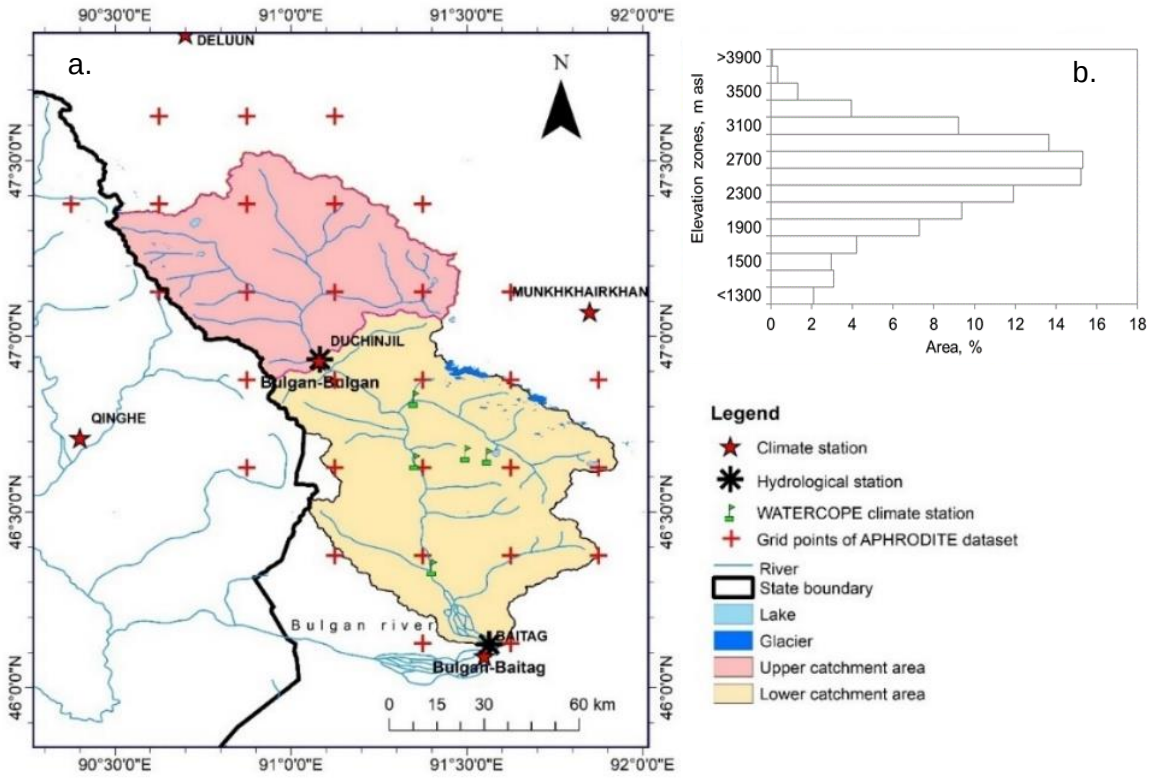

Figure 3.31: Climate stations and grid points of the APHRODITE dataset (0.25ºx0.25º, http://www.chikyu.ac.jp/precip/) overlaying the Bulgan catchment (a). Elevation zones of the whole catchment (b). The red stars and black asterisks indicate the locations of the official climate stations in and closest to the catchment and the Bulgan-Bulgan and Bulgan-Baitag hydrological stations, respectively. The climate stations of the WATERCOPE project are set up at different heights and illustrated by green flags.

Regarding high elevations, the upper subcatchment in the mountains is colder and has higher precipitation than the lower subcatchment, which is in a transition area between the mountain and the desert. The lower subcatchment has higher evapotranspiration but lower runoff due to a larger catchment area than the upper catchment (Table 3.22).

Table 3.22: Climate characteristics of the Bulgan catchment.

Catchment	Elevation (m a.s.l)	Annual Temperature, °C			Annual precipitation, mm			Annual potential evapotranspiration, mm			Annual runoff, mm
		Mean	Max	Min	Mean	Max	Min	Mean	Max	Min	Mean
Upper subcatchment	2787	-7.1	-5.4	-9.6	215	305	137	518	565	442	65
Lower subcatchment	2399	-4.7	-3.0	-7.1	167	282	97	570	617	496	40
Whole catchment	2552	-5.6	-3.9	-8.1	184	290	113	546	591	473	40

For hydrological simulation, areal climate input data was estimated at the mean elevation of the catchment from meteorological stations and the corresponding 25 grid cells of the APHRODITE dataset on daily time scales using Thiessen polygon and annual lapse rates of temperature and precipitation.

Based on four WATERCOPE project stations and two official climate stations in the Bulgan catchment, we found that the annual lapse rates of the air temperature, precipitation, and evapotranspiration in the southern Altai Mountains to be -0.67ºC, 7%, and -3% per 100m, respectively (Annex A). Annual lapse rates of the interpolated temperature, precipitation, and evapotranspiration of APHRODITE grid cells overlaying the Bulgan catchment are -0.42ºC, 2.3%, and -2% per 100 m, respectively (Annex B). Despite of different lapse rates between the station and gridded climate input data, we applied the same height increments of temperature and precipitation in the catchment settings of HBV-Light 4.0 model, as -0.67ºC and 7% based on the climate station lapse rates.

3.4.1.1 Bias correction of the measured precipitation at Tretyakov rain gauges

Precipitation undercatch at gauge stations over Mongolia, especially in forest and steppe zones, was between 17 and 42% due to biases from wind-induced undercatch, wetting, and evaporation losses (Zhang et al., 2004). Therefore, we corrected the systematic biases of the measured precipitation at Duchinjil and Baitag gauges using the bias correction technique for the Tretyakov rain gauges. The total catch ratio for different precipitation types at both gauges was 92% on average (Table 3.23).

Table 3.23: Estimated catch ratios (CR) for various precipitation types at gauges on the daily scale.

Stations	CRsnow (%)	CRmixed (%)	CRrain (%)	CRtotal (%)	K=100/CR
Duchinjil	88	90	94	92	1.10
Baitag	86	93	97	92	1.10

At Duchinjil station, precipitation loss from wind, wetting, and evaporation was 32%, 30%, and 39% on average, respectively. Moreover, wind-induced bias ranged between 31% and 59% during mixed and solid precipitation from November to April but between 25% and 28% from May to October. Also, wetting loss varied from 23% to 41% throughout the year. Evaporation loss is between 43% and 45% from May to October and 18% and 37% from November to April (Figure 3.32a).

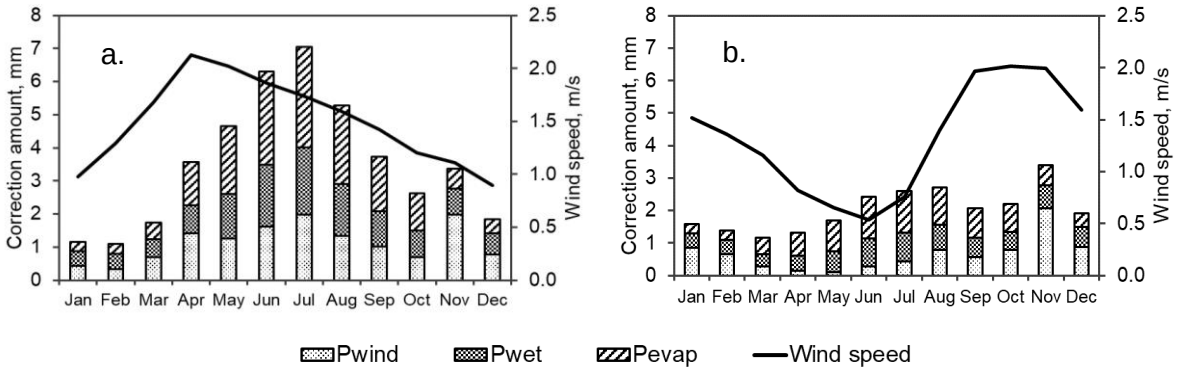

Figure 3.32: Monthly mean correction amounts for precipitation loss from wind, wetting, and evaporation, and monthly mean wind speed at Duchinjil (a) and Baitag stations (b) from 1984 to 2015.

At Baitag station, precipitation loss from wind, wetting, and evaporation was 34%, 32%, and 40% on average, respectively. Wind-induced bias varied between 36% and 61% during mixed and solid precipitation fall from October to February but between 7% and 28% during the warm period from March to September. Moreover, wetting bias was high between 31% and 37% during the warm period from March to July and low in the range of 20 and 29% during the cold period. Furthermore, evaporation bias was high at more than 50%, especially in the late spring and early summer months but low between 19% and 22% during cold months from November to February (Figure 3.32b).

Overall, the wind-induced bias was higher than the wetting and evaporation bias in the measured precipitation at both gauges in the Bulgan catchment; moreover, the evaporation loss in the spring was very high to 58% at the Baitag gauge in the desert. After adjusting gauge precipitation measurements from 1984 to 2016, annual precipitation sums rose by 23% and 21% at Duchinjil and Baitag, respectively.

3.4.1.2 Bias correction of the gridded precipitation and temperature

Recent studies preferred spatial representatives of bias correction to the limited information of gauge point data (Koutsouris et al., 2017; Ji et al., 2020). They applied bias correction to the catchment or different climate zone averages of the gridded precipitation and temperature, where each grid was weighted based on an areal coverage of the catchment or climate zone (Teutschbein and Seibert, 2012; Koutsouris et al., 2017; Ji et al., 2020).

Thus, we used Thiessen polygons to regionalize climate stations and grid cells data on the Bulgan catchment scale and calculated the areal mean precipitation and temperature at the mean elevations of the Bulgan catchment and subcatchments from stations and grids at different elevations by correcting with the corresponding lapse rates.

The gridded APHRODITE dataset underestimated the precipitation amount and overestimated the number of rainy days for the Bulgan catchment on the daily and monthly time scales; however, it overestimated the areal mean temperature and evapotranspiration (Table 3.24 and Figure 3.33). These biases were corrected by Linear Scaling (LS) and Cumulative Distribution Function Matching (CDF) approaches. The upper subcatchment had larger mean biases and root mean square errors (RMSE) in the areal means of the gridded precipitation and temperature than the lower subcatchment.

Table 3.24: Statistics of the areal original and adjusted APHRODITE datasets for the upper and lower subcatchments on the daily time scale

Daily data	Upper subcatchment								
	Precipitation, mm			Temperature, ºC			Evapotranspiration, mm		
	Mean bias	RMSE	Corr (r)	Mean bias	RMSE	Corr (r)	Mean bias	RMSE	Corr (r)
APHRO	-0.21	1.58	0.86	3.32	3.85	0.99	0.25	0.39	0.99
APHRO_LS	0.0	1.30	0.87	0.0	1.68	0.99	0.0	0.10	0.99
APHRO_CDF	0.0	1.17	0.89	0.0	1.68	0.99	0.0	0.09	0.99
	Lower subcatchment								
APHRO	-0.13	1.08	0.90	3.30	3.58	0.99	0.25	0.41	0.99
APHRO_LS	0.0	0.87	0.90	0.0	1.05	0.99	0.0	0.18	0.99
APHRO_CDF	0.0	0.80	0.91	0.0	1.05	0.99	0.0	0.17	0.99

The correlation coefficients (Corr) of the areal mean precipitation for the upper and lower subcatchments were 0.86 and 0.90, respectively; whereas, the correlation coefficients of temperature and evapotranspiration were 0.99 for both subcatchments. Compared to the observed (obs) and the corrected gauge precipitation (Pcor), the mean of the original gridded precipitation (APHRO) was lower, and its dispersion was more compacted to low values on the monthly time scale (Figure 3.33a, b).

Both LS and CDF methods corrected the mean of the APHRO precipitation; moreover, CDF adjusted the standard deviation, wet-day frequency, and intensity of the APHRO precipitation. Thus, the adjusted APHRO precipitation based on CDF (APHRO_CDF) had higher extremes and outliers and a more spread interquartile range than the adjusted APHRO precipitation by LS (APHRO_LS); therefore, the difference in maximum and extreme values of the adjusted precipitation APHRO_LS and APHRO_CDF might result in various runoffs for the Bulgan catchment. The monthly original APHRO temperature and evapotranspiration had higher means and more spread interquartile ranges than observation, and these biases were corrected well by LS and CDF (Figure 3.33c-f).

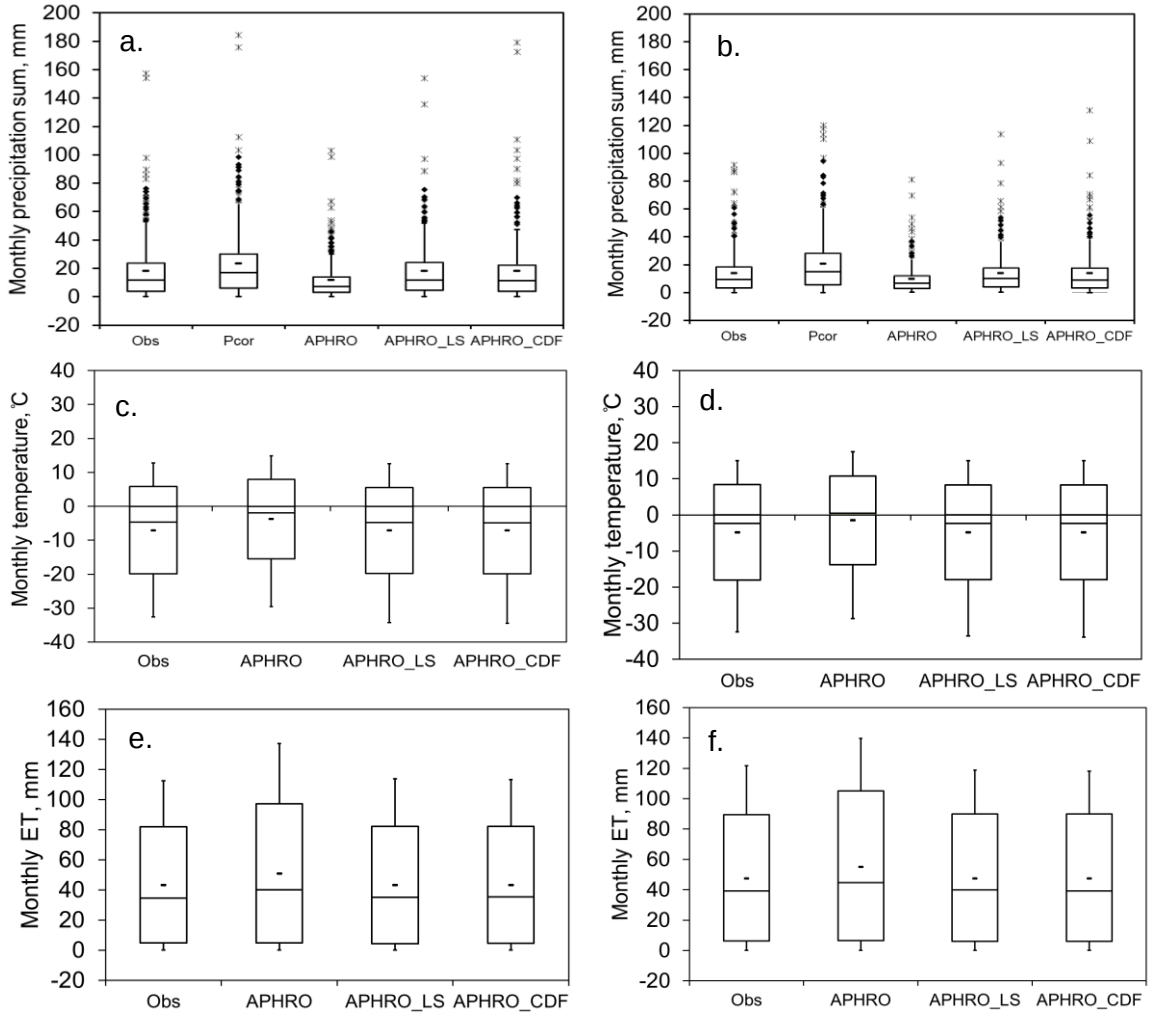

Figure 3.33: The characteristics of the areal mean observed and gridded APHRODITE data for the upper (left panel) and lower subcatchments (right panel) from 1984 to 2015. The observed and bias-corrected gauge precipitation, and the original APHRODITE (APHRO) and bias corrected gridded precipitation (a, b), temperature (c, d), and evapotranspiration (e, f) by linear scaling (APHRO_LS) and Cumulative Distribution Function (APHRO_CDF) are compared, also extreme and outlier values are illustrated by asterisks and rhombus, respectively. Mean values are marked by minus in the boxes.

The boxplots of the adjusted temperature and evapotranspiration by LS and CDF appeared the same. Also, gridded dataset was evaluated based on their hydrological simulation performance for the Bulgan catchment in next Chapter.

3.4.2 Semi-distributed and lumped HBV-light model performance

The HBV-light model was warmed up for the first year of 1984 until the model reached its natural state and the effect of the initial condition was not visible. After calibration from 1985 to 2005 (21 years), covering wet and dry years, we validated the simulated runoff for the recent period 2006-2015 (10 years). The goodness of model best fit was evaluated by fuzzy measure (X) of weighted model efficiency (R_{eff}), efficiency for low flow ($LogR_{eff}$), and volume error (VE) (See Chapter 2.3.4.2 for details). Also, we rated our model performance according to the following evaluation categories (Table 3.25).

Table 3.25: Rating of the model performance (Moriasi et al., 2007).

Values	Performance rating	Values	Performance rating
$0.75 < R_{eff} \leq 1.00$	Very good	$0.50 < R_{eff} \leq 0.65$	Satisfactory
$0.65 < R_{eff} \leq 0.75$	Good	$R_{eff} \leq 0.50$	Unsatisfactory

3.4.2.1 Model calibration (1985-2005)

The calibration aims to simulate a good shape of hydrograph fitting to the observed hydrograph. We simulated 5000 model runs for the genetic algorithm and 1000 runs for local optimization by Powell's method; then calibrated them ten times. The parameter set with the highest fuzzy measure (X) from the ten calibration results was determined as the optimal parameter set for the model validation. We analyzed the performance of all models with their optimized parameter sets.

In addition to the hydrological simulation with observed station data (OBS), we evaluated the adjusted gauge precipitation (OBS_Pc), original APHRO precipitation (P_{APHRO}) and two corrected APHRO precipitation (P_{APHRO_LS}, P_{APHRO_CDF}) based on LS and CDF matching, also raw APHRO precipitation and temperature together, and their bias-corrected data based on linear scaling (APHRO_LS) and CDF matching (APHRO_CDF) methods.

Over the calibration period 1985-2005, the fuzzy measure (X) of the model performance varied in a range from 0.65 to 0.70 (close to 1.0 is a perfect fit) for a lumped model and in the range from 0.56 to 0.66 for a semi-distributed model for the Bulgan catchment (Table 3.25). Furthermore, the model efficiency (R_{eff}) was more satisfactory for the lumped model than the semi-distributed model since R_{eff} varied from 0.59 to 0.66 for the Bulgan catchment and from 0.55 to 0.64 for the subcatchments, except 0.47 when the original precipitation and temperature of APHRODITE dataset (APHRO) was used for the upper subcatchment.

Moreover, the efficiency for low flow ($LogR_{eff}$) was good (0.68 to 0.72) for the Bulgan catchment and satisfactory for the upper (0.47 to 0.61) and lower (0.58 to 0.64) subcatchments (Table 3.26). The total volume difference (VE) of the models (close to 1.0 is

a perfect fit) explains the closeness between the long-term averages of the observed and simulated runoff. The VE was 1.0 for the Bulgan catchment but ranged between 0.91 and 1.0 for the subcatchments.

Table 3.26: Performance of the semi-distributed and lumped models for the Bulgan catchment with different datasets during the calibration period 1985-2005.

COEFs	A. Semi-distributed model performance							
	OBS	*OBS_Pc*	P_{APHRO}	P_{APHRO_LS}	P_{APHRO_CDF}	APHRO	APHRO _LS	APHRO _CDF
Fuzzy measure (X)	*0.63*	*0.66*	*0.62*	*0.65*	*0.63*	0.56	0.62	0.60
Upper subcatchment (2787m asl)								
Reff	*0.57*	*0.64*	*0.56*	*0.62*	*0.60*	0.47	0.58	0.55
LogReff	*0.58*	*0.61*	*0.59*	*0.58*	*0.58*	0.54	0.53	0.47
VE	*1.00*	*0.99*	*1.00*	*0.98*	*1.00*	1.00	0.99	1.00
Mean difference	*-0.19*	*-0.84*	*-0.02*	*-0.06*	*-0.03*	0.03	-0.32	0.00
Lower subcatchment (2399m asl)								
Reff	*0.60*	*0.61*	*0.59*	*0.63*	*0.59*	0.54	0.59	0.56
LogReff	*0.62*	*0.64*	*0.63*	*0.64*	*0.63*	0.58	0.61	0.64
VE	*0.91*	*0.93*	*0.93*	*0.93*	*0.93*	0.94	0.96	0.95
Mean difference	*3.51*	*3.08*	*2.95*	*2.29*	*2.87*	2.42	1.72	2.01
B. Lumped model performance								
Bulgan catchment (2552m asl)								
Fuzzy (X)	*0.68*	*0.69*	*0.69*	*0.70*	*0.67*	0.65	0.69	0.65
Reff	*0.62*	*0.63*	*0.64*	*0.66*	*0.61*	0.59	0.64	0.60
LogReff	*0.72*	*0.72*	*0.72*	*0.72*	*0.69*	0.70	0.71	0.68
VE	*1.00*	*1.00*	*1.00*	*1.00*	*1.00*	1.00	1.00	099
Mean difference	*0.00*	*0.00*	*-0.01*	*0.00*	*0.00*	0.00	0.00	0.40

Runoff simulation of the HBV-Light model is sensitive to various precipitation inputs. Of all input datasets, the model efficiency of the adjusted gauge precipitation (OBS_Pc) and the adjusted APHRO precipitation by linear scaling (P_{APHRO_LS}) was higher for the Bulgan catchment and its subcatchments than other input datasets.

According to the comparison of the observed and simulated weekly total discharges, all models underestimated high flows for the Bulgan catchment and its subcatchments but overestimated low flows for the upper subcatchment (Figure 3.34). Moreover, for the Bulgan catchment and the lower subcatchment, the models underestimated the recession curves and low flows during the wet years of 1985-1995 but overestimated the recession curves during the dry years 2000 and 2002.

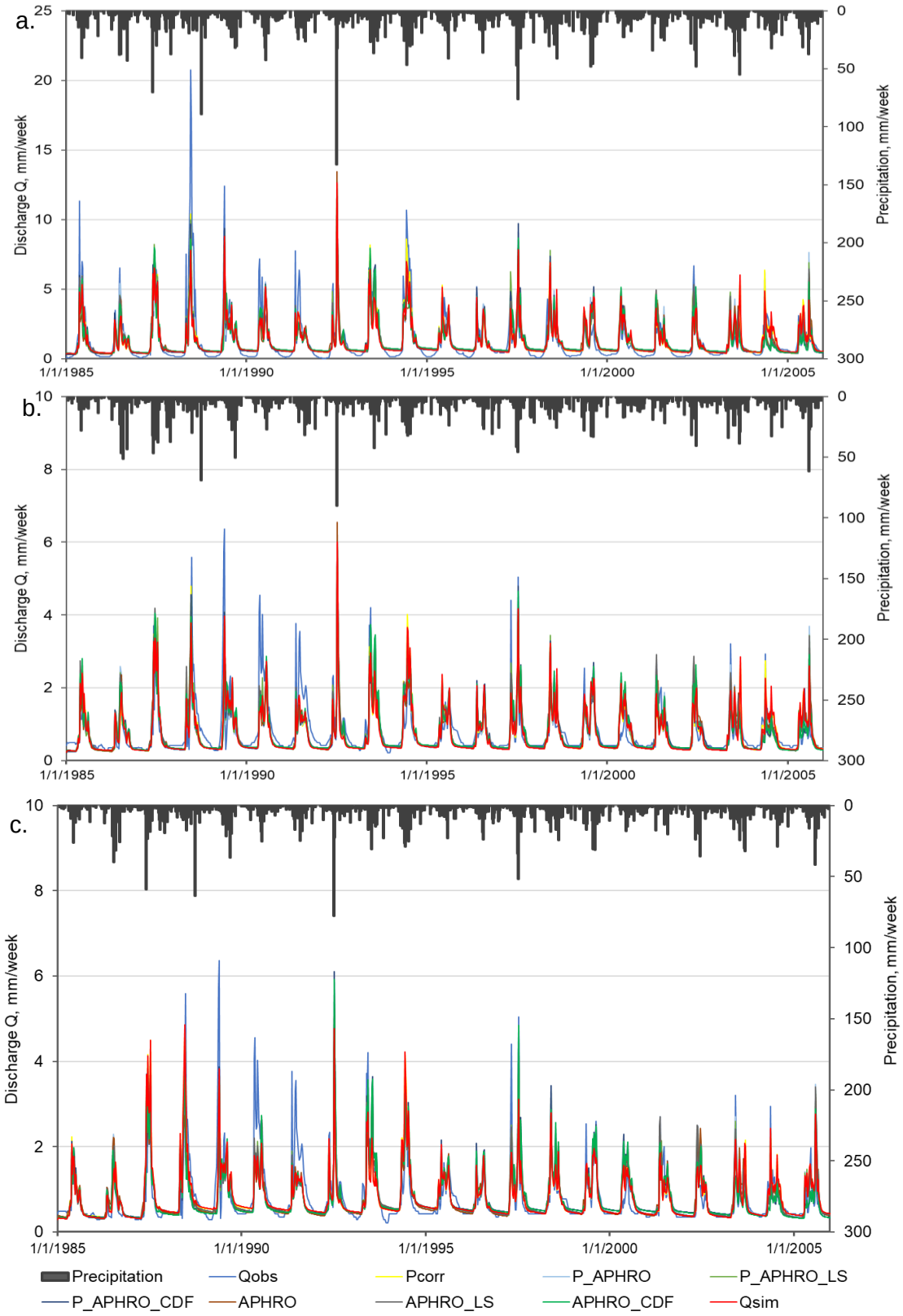

Figure 3.34: Weekly precipitation sums and the observed and simulated weekly total discharges for the upper (a) and lower (b) subcatchments and Bulgan catchment (c) over the calibration period 1985-2005.

According to the exceedance probability curves of the observed and simulated daily runoff from 1985 to 2005, the high flow was underestimated by all models for the Bulgan catchment and the upper and lower subcatchments (Figure 3.35a, c, and d). Peak flow (<10%) was produced better by the adjusted gauge precipitation (Pcorr) and the adjusted APHRODITE dataset by CDF matching (P_APHRO_CDF and APHRO_CDF) than others (Figure 3.35b, d, and f). All models considerably overestimated the medium and low flow sections of the exceedance probability curve (>50%) for the upper subcatchment and slightly underestimated for the lower subcatchment, whereas they were well simulated for the Bulgan catchment.

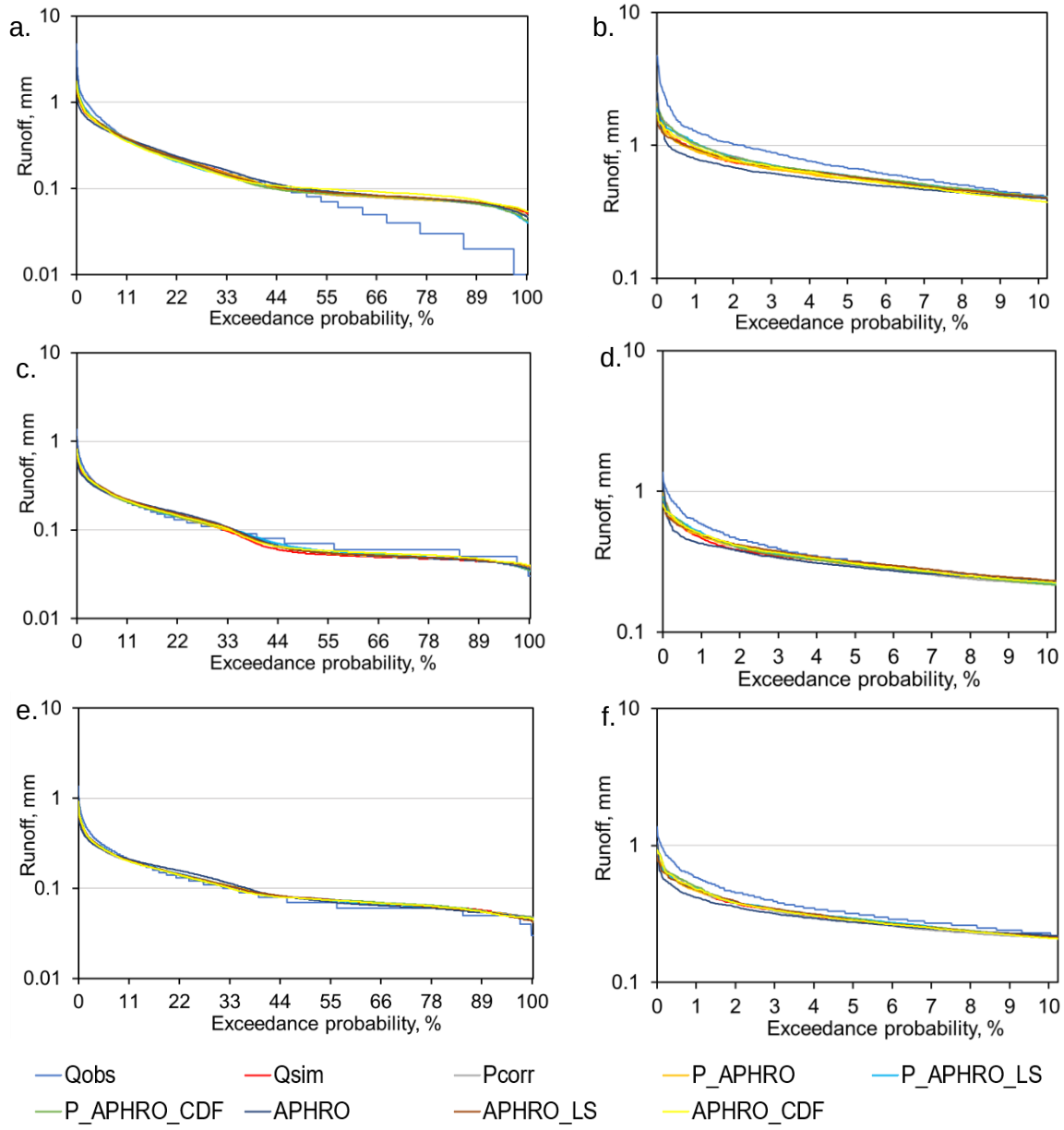

Figure 3.35: The exceedance probabilities of the observed and simulated daily runoff at the upper (a, b) and the lower subcatchments (c, d), and Bulgan catchment (e, f) from 1985 to 2005.

3.4.2.2 Model validation (2006-2015)

For the validation period, the model efficiency (R_{eff}) ranged from 0.51 to 0.62 for the Bulgan catchment; moreover, it varied from 0.44 to 0.61 and from 0.56 to 0.62 for the upper and lower subcatchments, respectively. According to the rating of the model performance (Moriasi et al., 2007), it was satisfactory even if R_{eff} got worse in the validation period than in the calibration period (Table 3.27).

The efficiency of the low flow ($LogR_{eff}$) varied in the range of 0.61-0.68 for the upper subcatchment, whereas it ranged from 0.51 to 0.56 and from 0.55 to 0.59 for the lower subcatchment and the Bulgan catchment, respectively. Likewise, the VE also declined to 0.78 for the Bulgan catchment and 0.80 for the subcatchments.

The optimized parameter set of the adjusted gauge precipitation (OBS_Pc) during the calibration resulted in the best model performance for the Bulgan catchment and its subcatchments as well. Although the adjusted APHRODITE precipitation by linear scaling (P_{APHRO_LS}) produced the poor model performance for high flow of the upper subcatchment during the validation period due to underestimation of mountain precipitation, P_{APHRO_LS} simulated low flow better than other datasets. Also, the parameter sets of P_{APHRO_LS} and APHRO_LS still simulated runoff well for the Bulgan catchment and the lower subcatchment with smaller mean difference and closer VE to 1.0 than P_{APHRO_CDF} and APHRO_CDF.

Table 3.27: Performance of the semi-distributed and lumped models for the Bulgan catchment with different datasets during the validation period 2006-2015.

COEFs	A. Semi-distributed model performance							
	OBS	*OBS_Pc*	P_{APHRO}	P_{APHRO_LS}	P_{APHRO_CDF}	APHRO	APHRO_LS	APHRO_CDF
Upper subcatchment								
Reff	*0.61*	*0.60*	*0.56*	*0.44*	*0.50*	0.59	0.60	0.54
LogReff	*0.62*	*0.61*	*0.67*	*0.68*	*0.64*	0.65	0.67	0.63
VE	*0.85*	*0.84*	*0.95*	*0.97*	*0.83*	0.92	0.99	0.81
Mean difference	*8.72*	*9.51*	*-2.72*	*-2.04*	*10.1*	-4.48	-0.86	11.0
Lower subcatchment								
Reff	*0.62*	*0.62*	*0.56*	*0.57*	*0.57*	0.58	0.59	0.58
LogReff	*0.51*	*0.55*	*0.56*	*0.56*	*0.55*	0.56	0.56	0.56
VE	*0.80*	*0.80*	*0.95*	*0.92*	*0.82*	0.98	0.96	0.83
Mean difference	*7.68*	*7.6*	*2.01*	*2.96*	*7.01*	0.76	1.71	6.73
B. Lumped model performance								
Whole catchment (2552m asl)								
Reff	*0.61*	*0.62*	*0.57*	*0.57*	*0.51*	0.57	0.57	0.51
LogReff	*0.58*	*0.60*	*0.57*	*0.57*	*0.55*	0.57	0.57	0.56
VE	*0.88*	*0.87*	*1.00*	*0.97*	*0.78*	0.99	0.97	0.78
Mean difference	*4.46*	*5.0*	*0.02*	*1.25*	*8.68*	0.20	1.06	8.41

All models overestimated high flow during the dry years of 2006-2007 and underestimated peak flow during the wet years 2013-2014 for the upper subcatchment (Figure 3.36a). Also, the high and low flows of the Bulgan catchment and the lower subcatchment were overestimated for the dry period of 2006-2009 but underestimated during the wet period of 2010-2015 (Figure 3.36b and c). All models could not simulate the observed increase in winter flow since 2006.

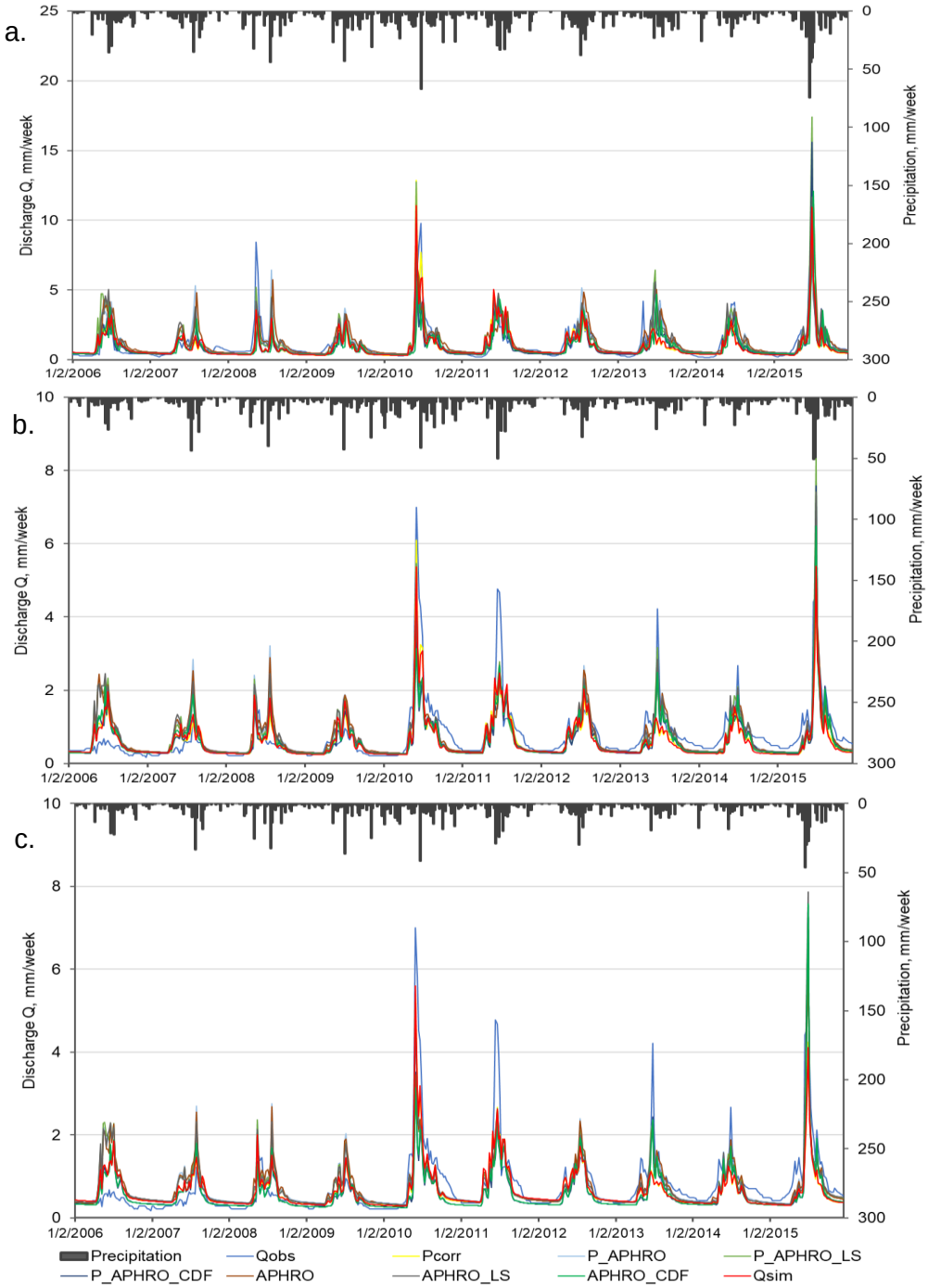

Figure 3.36: Weekly precipitation sums and the observed and simulated weekly total discharges for the upper subcatchment (a), the lower subcatchment (b) and whole catchment (c) for the validation period 2006-2015.

Over the validation period 2006-2015, Qsim, Pcorr, P_{APHRO_CDF}, and APHRO _CDF underestimated high and mid flow sections (<66%) of the exceedance probability curves for the Bulgan catchment and the subcatchments, whereas the P_{APHRO}, P_{APHRO_LS}, and APHRO_LS simulated well the mid flow section from 10 to 40%, then underestimated the mid flow section from 40 to 70% for the Bulgan catchment and its subcatchments (Figure 3.37a-f). In other words, the exceedance probability curves of the runoff simulation for the validation period were split up to two groups according to the applied mean-based and distribution-based bias correction methods to precipitation.

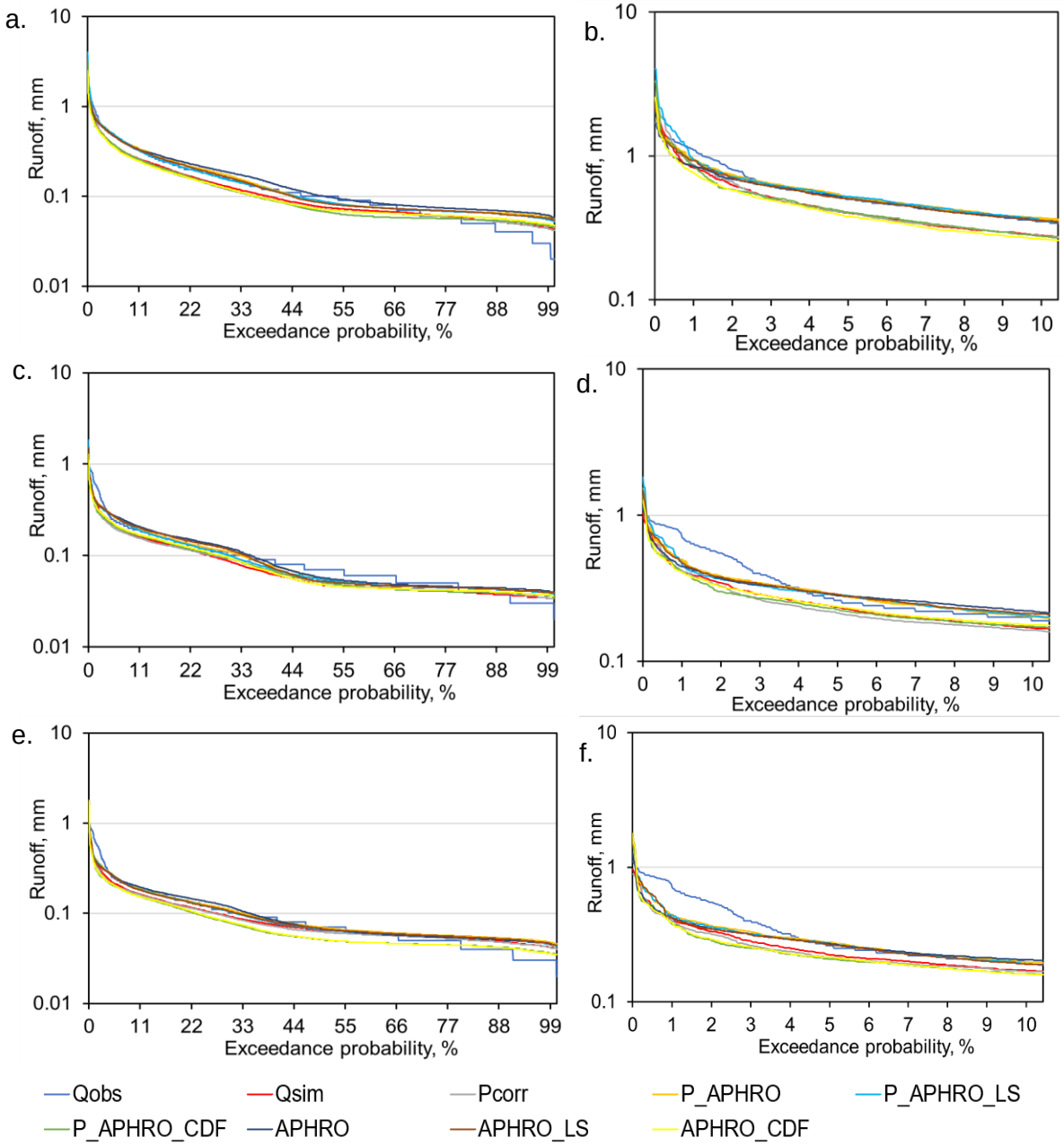

Figure 3.37. The exceedance probabilities of the observed and simulated daily runoff for the upper (a, b) and the lower (c, d) subcatchments and Bulgan catchment (e, f) for the validation period 2006-2015.

The CDF corrected most of the statistical characteristics of the gridded data to observed precipitation; thus, the adjusted gridded data by CDF has similar variations to the observation. In contrast, LS changed the monthly mean values of the gridded data with the same correction factors and left the variability of the gridded data. According to the exceedance probability curves of high flow (<10%), peak flows (1-4%) were underestimated by all simulations for the Bulgan and its subcatchments (Figure 3.37b, d, f).

In summary, hydrological performance was good for the Bulgan catchment and slightly improved by the adjusted gauge precipitation with an increase in the total precipitation amount. Observed precipitation could not represent the complex terrain precipitation and underestimated runoff. The alternative gridded APHRODITE dataset satisfactory simulated Bulgan catchment runoff in the semi-arid southern Altai Mountains even if it underestimated the amount of precipitation and overestimated temperature for the high mountains. Moreover, Linear scaling performed better model efficiency for the Bulgan catchment and its subcatchments than CDF approach. All models underestimated high flow during wet years but overestimated low flow during dry years; moreover, they could not simulate the observed increase in winter flow that has occurred since 2006.

3.4.3 The simulated water balance of the Bulgan catchment

The simulated water balances of the Bulgan catchment for the calibration and the validation periods are shown in Figure 3.38a-b. An increase in total precipitation inputs resulted in different water storages due to distinct optimized model parameters.

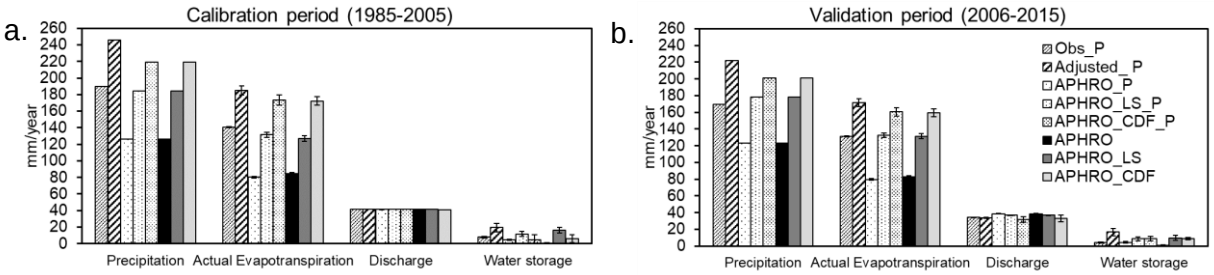

Figure 3.38: Simulated water balances for the calibration (a) and the validation (b) periods.

Moreover, all models simulated the same decreasing trends in the discharges In response to a decrease in precipitation and a slight increase in potential evapotranspiration for the Bulgan catchment (Figure 3.39).

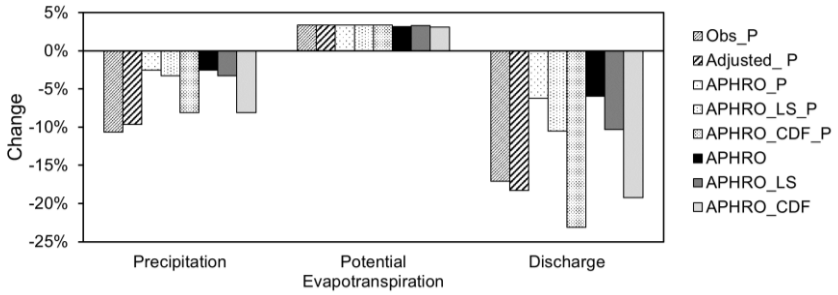

Figure 3.39: Change in water balance components of all models for the calibration and the validation periods.

In the case of the simulated water balance with station data (Obs_P), the annual precipitation sum decreased by 11%, but potential evapotranspiration increased by 4%; thus, the efficiency of the precipitation over the Bulgan catchment decreased, and river runoff declined by 17%. Moreover, water storage in the catchment decreased by 38% (Table 3.28).

Table 3.28: The simulated water balances (mm/year±stdev) of the Bulgan catchment for the calibration and the validation periods and change.

Water balance components (P=ET+R +ΔS)	Calibration period 1985-2005	Validation period 2006-2015	Change %
Precipitation (obsP), mm/y	190	169	-11%
Potential evapotranspiration, mm/y	541	560	4%
Actual evapotranspiration (ET_{act}), mm/y	143±0.8	131±0.7	-8%
Simulated discharge ($Q_{sim)}$, mm/y	41	34±0.4	-17%
Storage, mm/y ($\Delta S=P- ET_{act} - Q_{sim}$)	8±0.8	4±0.6	-38%
Efficiency of the precipitation (*Q/P)*	*22%*	*20%*	-2%

Over the whole period of 1985-2015, the simulated annual subsurface flow declined at a rate of 2.1mm or 15% ($p<0.5$) per decade, and base flows decreased at the rate of 3.5mm or 15% ($p<0.001$) per decade (Figure 3.40a). Moreover, contributions of rain and snow to the annual runoff decreased by 2.5mm (12%) and 2.8mm (17%) per decade at 0.01 level, respectively. In contrast, glacier input in the runoff recharge significantly increased by 0.4mm (26%) per decade at 0.5 (Figure 3.40b). However, the model did not simulate the increasing baseflow of the Bulgan River in winter like in other high mountain permafrost regions.

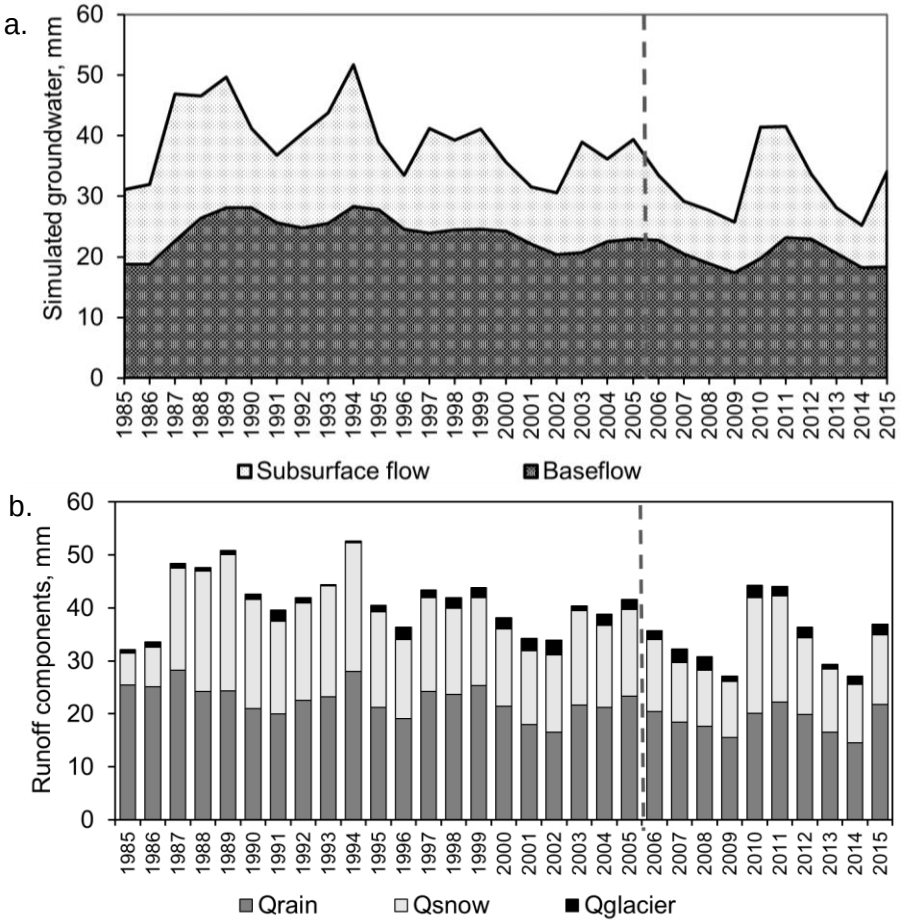

Figure 3.40: Year to year variation of simulated groundwater (a) and runoff components (b) for the Bulgan catchment over the period 1985-2015

3.4.4 Yearly model performance

The model efficiency of all model performances for the Bulgan catchment and subcatchments was checked for each year of the calibration and validation periods. Model efficiency was generally good for the wet years of 1985-1994 and 2010-2015 but poor for the dry years of 2000 and 2006-2007 (Figure 3.41, Table 3.29). The R_{eff} reached -30.0 in 2006; thus, 2006 is removed from the figure to show the other R_{eff} distribution clearly.

Different climate inputs with the same model structure generated various runoff for each year. The maximum R_{eff} ranged between 0.83 and 0.94 the years 1992, 1993, 1996 and 2002 of the calibration period but ranged between 0.52 and 0.88 the years 2010-2015 of the validation period. The minimum Reff was estimated for the years 1999, 2000, 2003 and 2005 ($-1.87<R_{eff}<-0.21$) of the calibration period and the years 2006 and 2007 ($-30.0<Reff<0.22$) for the validation period.

All models performed poorly for the same years 2000, 2006, and 2007. These years coincided with the consecutive dry years in the mid of 2000s; especially in the southern Altai Mountains, local herders and farmers faced challenges with droughts in 1997, 2000, 2003, 2005, and 2007 (own study). Thus, the poor model performance for the drought years might be assigned to the quality of discharge data. Moreover, the quality of precipitation data at two gauges in the Bulgan catchment might be not enough to identify precipitation characteristics of the complex terrain with a 7588 km^2 area.

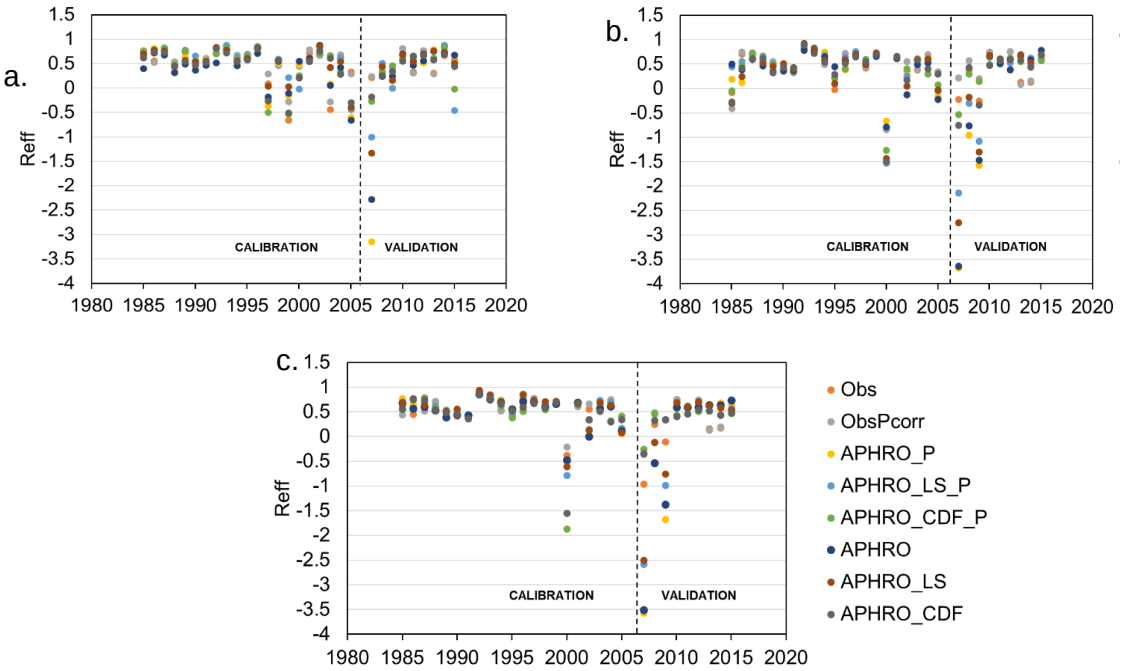

Figure 3.41: Year to year model performance for the upper (a) and the lower (b) subcatchments and Bulgan catchment (c) over the period of 1985-2015.

Table 3.29: Maximum and minimum model efficiency (Reff) of the hydrological model with different climate datasets.

	Calibration period				Validation period			
Model types	MAX Reff	Year	MIN Reff	Year	MAX Reff	Year	MIN Reff	Year
Upper subcatchment								
Observed	0.86	1993	-0.66	1999	0.81	2010	0.22	2007
ObsPcorrected	0.87	1993	-0.28	2003	0.81	2010	0.24	2007
APHRO_P	0.84	2002	-0.60	2005	0.85	2014	-3.14	2007
APHRO_LS_P	0.88	1993	-0.44	2005	0.88	2014	-1.00	2007
APHRO_CDF_P	0.84	1996	-0.53	1999	0.83	2014	-0.27	2007
APHRO	0.88	2002	-0.66	2005	0.76	2013	-2.28	2007
APHRO_LS	0.85	2002	-0.39	2005	0.76	2013	-1.33	2007
APHRO_CDF	0.81	1996	-0.51	1999	0.69	2014	-0.18	2007
Lower subcatchment								
Observed	0.81	1992	-0.82	2000	0.73	2010	-8.29	2006
ObsPcorrected	0.87	1992	-0.84	2000	0.76	2012	-7.38	2006
APHRO_P	0.87	1992	-0.66	2000	0.68	2015	-25.46	2006
APHRO_LS_P	0.91	1992	-1.53	2000	0.70	2013	-26.65	2006
APHRO_CDF_P	0.85	1992	-1.26	2000	0.63	2012	-1.58	2006
APHRO	0.79	1992	-0.79	2000	0.79	2015	-27.9	2006
APHRO_LS	0.93	1992	-1.43	2000	0.75	2015	-30.0	2006
APHRO_CDF	0.90	1992	-1.49	2000	0.69	2015	-11.73	2006
Bulgan catchment								
Observed	0.89	1992	-0.38	2000	0.75	2010	-10.7	2006
ObsPcorrected	0.90	1992	-0.21	2000	0.75	2010	-9.39	2006
APHRO_P	0.89	1992	-0.51	2000	0.68	2010	-27.57	2006
APHRO_LS_P	0.93	1992	-0.78	2000	0.69	2010	-4.01	2006
APHRO_CDF_P	0.86	1992	-1.87	2000	0.52	2013	-7.31	2006
APHRO	0.86	1992	-0.47	2000	0.73	2015	-25.5	2006
APHRO_LS	0.94	1992	-0.61	2000	0.71	2012	-4.08	2006
APHRO_CDF	0.86	1992	-1.55	2000	0.54	2012	-7.79	2006

3.4.5 Uncertainties in hydrological simulation

Hydrological model performance depends on conceptualizing parameters, model structure and initial condition, input and calibration data (Moges et al., 2021). Thus, many sets of parameters that produced good results in runoff simulation during calibration might give different results during validation because of the errors in climate variables and model structure, and the interaction of the model parameters (Seibert, 1997).

The range of the 100 hydrological predictions with automatically calibrated and optimized 100 parameter sets for the Bulgan catchment was narrow. All simulations underestimated high and low flows for the wet periods 1989-1993 and 2010-2015 and overestimated for the dry period 2006-2008 (Figure 3.42). The uncertainty range of the simulated runoff is broad for the high flow in the warm period and narrow for the low flow (Figure 3.43).

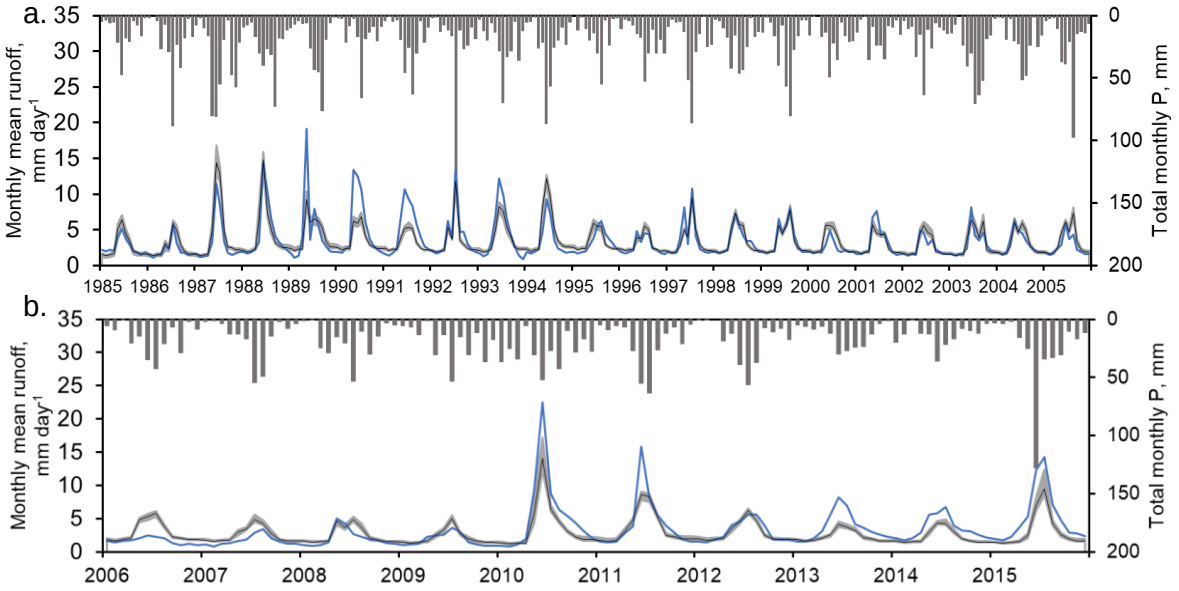

Figure 3.42: Range of 100 hydrological predictions for the monthly mean runoff of the Bulgan catchment for the calibration (a) and validation periods (b). Grey shadow illustrates the range between maximum and minimum values of the 100 simulations. Black line shows an average of the simulated monthly mean runoffs in absolute values (mm/day). The blue line is observed monthly mean runoff. The grey column is total monthly precipitation.

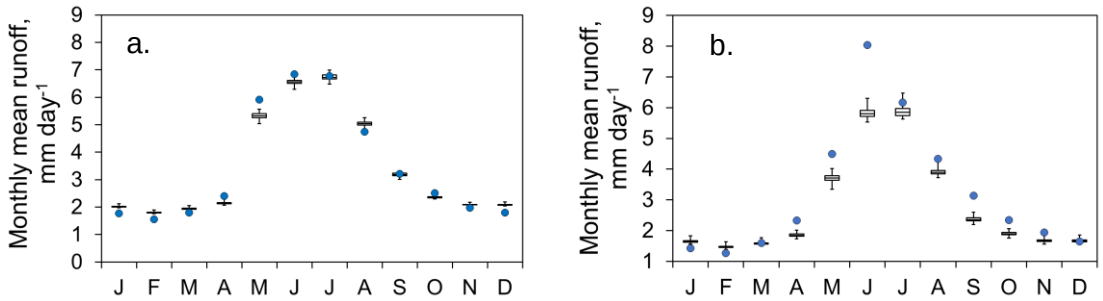

Figure 3.43: Boxplots of the 100 simulated monthly mean runoffs for the calibration period 1985-2005 (a) and validation period 2006-2015 (b). The boxplots show median, 25 and 75 quartiles, and extreme values of the 100 simulated runoffs. Blue dots are the monthly mean measured runoffs (mm.day^{-1}).

Snowmelt runoff from April through June was underestimated throughout the whole period. Recession curve of the simulated hydrograph was close to the observed hydrograph during calibration but decreased largely during the validation due to (Figure 3.43b). Thus, uncertainties in input and discharge data must be examined first.

3.4.5.1 Uncertainty in discharge measurement

In Mongolia, the water level is measured by a gauge man twice a day and the relationship with discharge is regularly checked since the condition of the natural river is not stable. Thus, a stage-discharge relationship varies each year (Heerema, 2013). According to the stage-discharge relationships at the outlet of Bulgan catchment, baseflows and peaks were skeptical for the wet years 1986-1988 and for the dry years 2000 and 2006 (Figure 3.44).

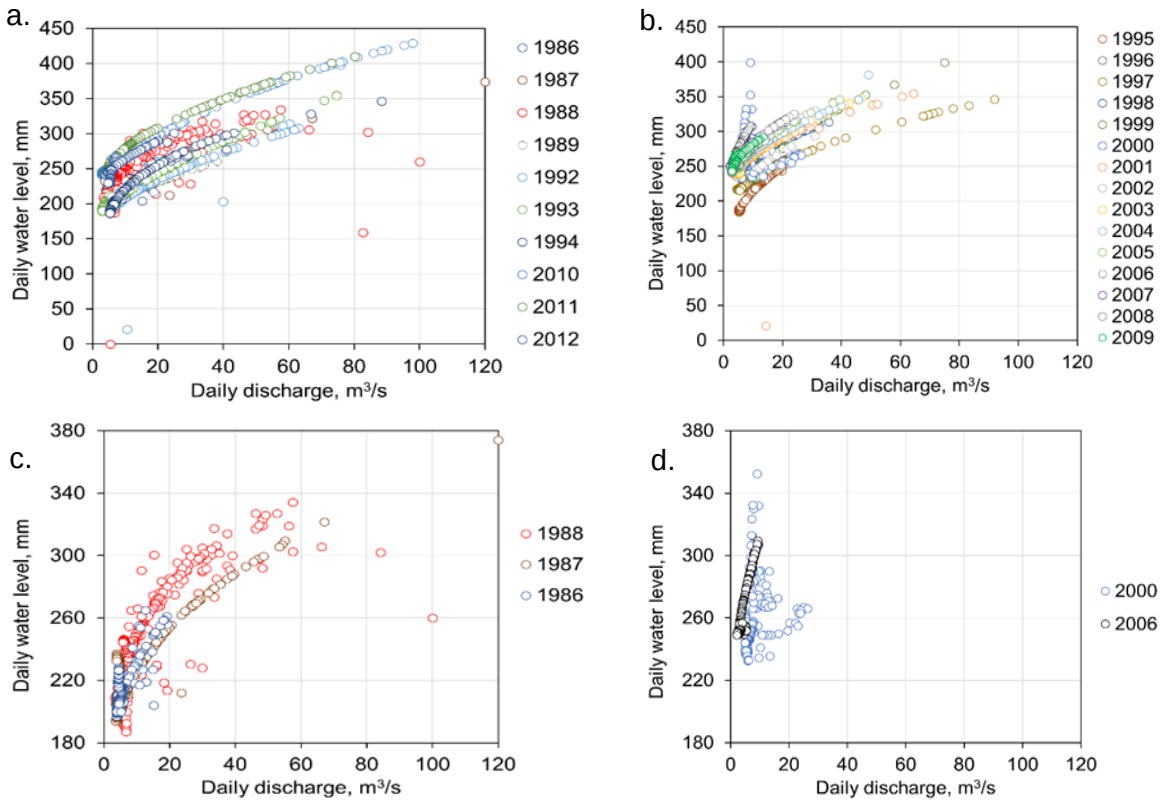

Figure 3.44: Rating curves at the outlet of the Bulgan catchment showing the stage-discharge relationships for the wet years (a) and dry years (b) and their skeptical years (c, d).

These biases might have caused our poor model performance in 2000, 2006, and 2007 (Table 3.29). On the other hand, our runoff prediction for the dry years might have showed potential biases in the discharge measurements that might be caused by human observation and data processing error, measurement error, non-stationary river cross-section, the influence of backwater, and assumptions of the form of the rating curve.

3.4.5.2 Uncertainty in precipitation data

Precipitation is vital in hydrological simulation. The gauge and gridded precipitation data for the same area have different characteristics. The APHRODITE has many small rainfall events but underestimates the total amount of rainfall. Thus, the negative bias of the APHRODITE precipitation was adjusted by LS and CDF (Figure 3.45). These precipitation data resulted in different hydrographs for the Bulgan catchment (Figure 3.46).

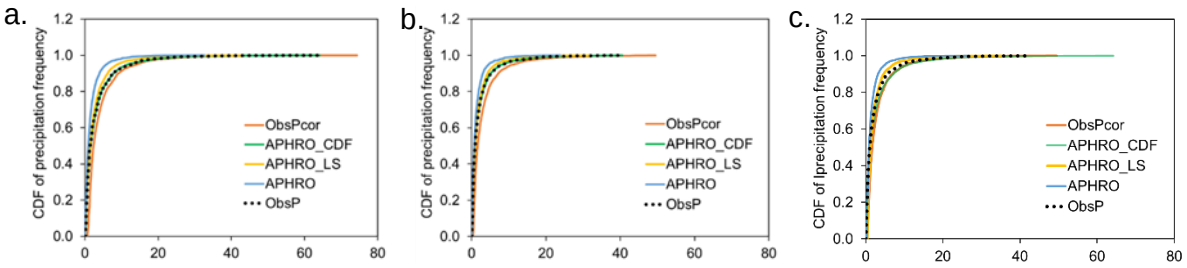

Figure 3.45: CDF curves of the daily observed and adjusted areal precipitation (mm) at the upper (a) and the lower subcatchments (b) and whole catchment (c) for 1984-2015.

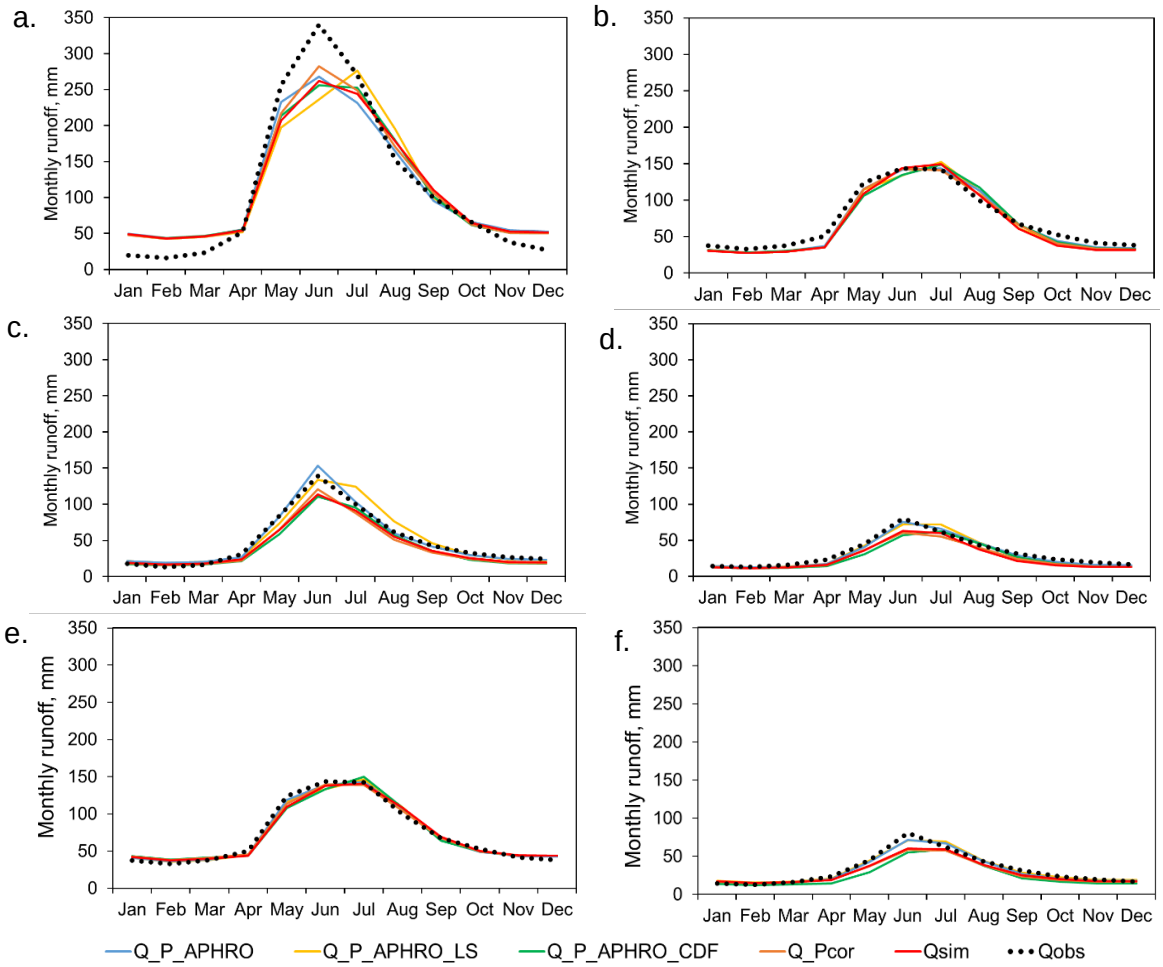

Figure 3.46: Simulated and observed hydrographs for the upper (a-b) and lower (c-d) subcatchments and Bulgan catchment (e-f) during the calibration period 1985–2005 (left panel) and validation period 2006–2015 (right panel).

During the calibration period, runoff simulations for the upper and lower subcatchments driven by these precipitation data underestimated the high flow from snowmelt and rainfall but overestimated base flow for the cold period for the upper catchment (Figures 3.46a and c). Except for simulations by APHRO and APHRO_LS precipitation, the simulated runoffs underestimated the high flow for the lower subcatchment, whereas all simulated runoff fitted the measured runoff for the whole catchment (Figure 3.46e).

During the validation period, all simulated runoff matched the observed runoff for the upper subcatchment (Figure 3.46b). For the lower subcatchment and Bulgan catchment, APHRO and APHRO_LS precipitation simulated monthly high flows from May to July better than other precipitation on average despite their low precipitation amount but a large number of wet days. Because the overestimated high flow by APHRO and APHRO_LS precipitation during the dry years 2006-2009 compensated for the underestimated increasing winter flow during the wet years 2010-2015 (Figure 3.36b-c).

3.4.5.3 Uncertainty in model structure

To represent Bulgan catchment characteristics, we added glacier and a delayed response function to the standard model structure. The delayed response function was applied to conceptualize the seasonal thaw of the permafrost, which increased deeper groundwater flow and altered temporal runoff (Gruber et al., 2017).

Three model structures with either glacier or delayed response or their combination were tested for the Bulgan catchment. The efficiency of the model structure with glaciers was good for low flow ($LogR_{eff}$=0.62) but was satisfactory for high flow (R_{eff}=0.51). The delayed response function improved model efficiency for low ($LogR_{eff}$=0.71) and high flow (R_{eff}=0.61), especially the high flow for May and June was well fitted. Furthermore, the model structure with a combination of delay response and glacier simulated high and low flow better than other models and performed the highest fuzzy measure of 0.69 and the lowest absolute error of 7.6% (Table 3.30 and Figure 3.47).

Furthermore, the conceptualizing permafrost conditions of the Bulgan catchment help us predict low flow in winter and improve the unsatisfactory performance of the SWAT model simulated for the water use efficiency of the irrigated area at the downstream area of the Bulgan catchment (Jordan, 2016).

The delayed response routine does not support dynamic changes in glacier areas in HBV Light4.0 (Seibert, 2005). That might increase uncertainty related to model structure.

Table 3.30: Performance of three model structures for the Bulgan catchment

	Glacier		*Delayed response function*		*Glacier+ Delayed response function*	
	1985-2005	*2006-2015*	*1985-2005*	*2006-2015*	*1985-2005*	*2006-2015*
Fuzzy measure (X)	*0.58*		*0.67*		*0.69*	
R^2	*0.52*	*0.60*	*0.62*	*0.66*	*0.63*	*0.66*
Reff	*0.51*	*0.58*	*0.62*	*0.61*	*0.62*	*0.62*
LogReff	*0.62*	*0.45*	*0.71*	*0.56*	*0.72*	*0.60*
VE	*0.98*	*0.90*	*1.00*	*0.87*	*1.00*	*0.87*
Mean difference	*0.68*	*4.03*	*0.00*	*5.18*	*0.00*	*5.00*
Absolute error, %	*16.3*		*9.1*		*7.6*	

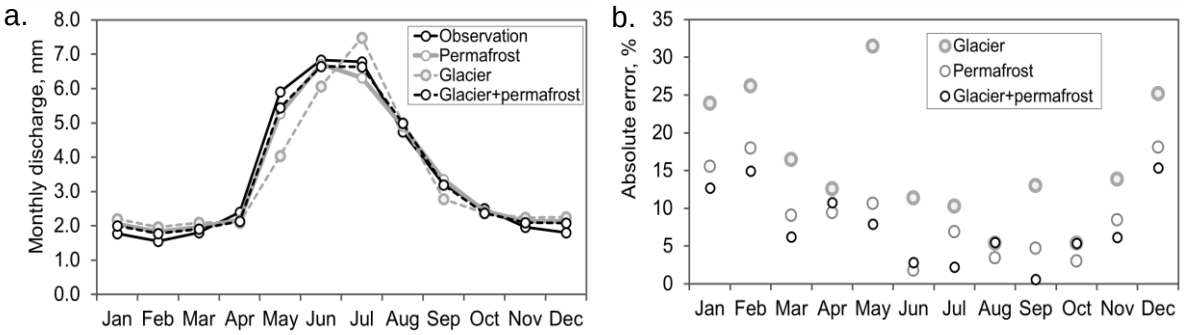

Figure 3.47: Comparison of the observed hydrograph to the simulated hydrographs by three model structures (a) and Absolute Errors of monthly simulated discharges (b) for the calibration period of 1985-2005.

Previous studies have successfully conceptualized permafrost conditions in hydrological simulation in different ways. To predict high flow in summer and low flow in winter, Heerema (2013) added soil threshold temperature-based freezing and melting functions and ice storage into the soil and response routines of the HBV model and improved overall model performance up to 0.65 for the neighboring Buyant catchment in the Altai Mountains. Council et al. (1999) adjusted the field capacity to vary with permafrost conditions to represent the seasonal thawing of the active layer in the soil and the evapotranspiration routine of the HBV model. Also, several studies on the Qinghai-Tibet Plateau ran hydrological models coupled with different freeze-thaw modules and simulated complex permafrost groundwater models. Please see more details in a review of permafrost modeling by Gao et al. (2021).

3.4.5.4 Parameter uncertainty

The 100 optimized parameter sets were obtained by calibrating the model 100 times with GAP after 500,000 simulations to evaluate parameter uncertainty as suggested by Teutschbein and Seibert (2012). Some parameters influence the model efficiency of low flow (LogReff), and others impact the model efficiency of high flow (Reff). Thus, the fuzzy measure (X), the combination of Reff, LogReff, and VE, was used for the model evaluation to reduce parametric uncertainty in the hydrological simulation (Seibert, 1997).

These 100 calibrated models had fuzzy measures (X) between 0.66 and 0.69, which were plotted against one parameter (Figure 3.48).

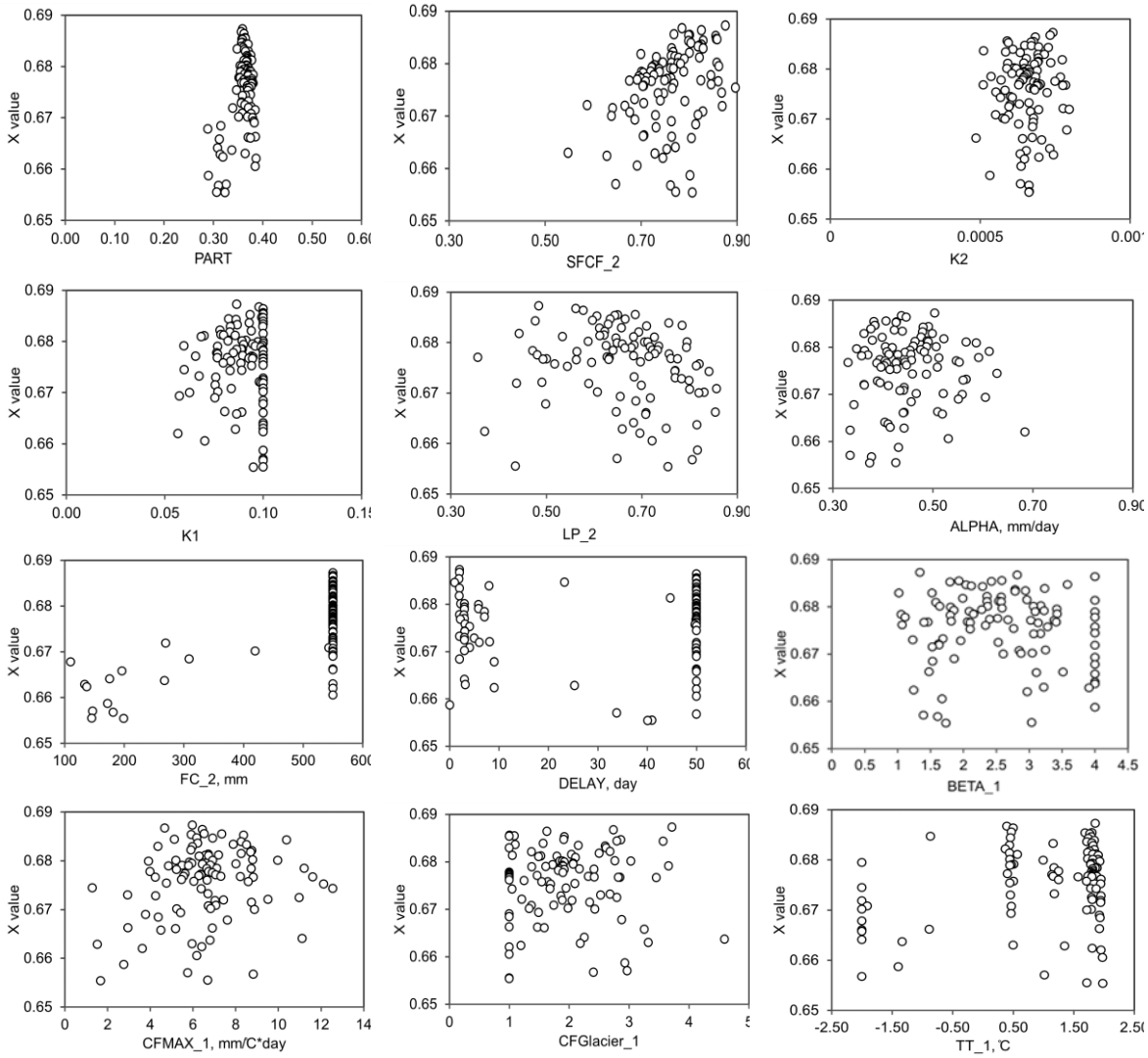

Figure 3.48: The scatter plots of model goodness and some parameters of the best 100 calibrations.

To avoid over-parameterization during model calibration, the insensitive parameters CFR and CWH are fixed to 0.05 and 0.1 (Seibert, 2000). For a well-defined parameter, the fuzzy measure decreased when the parameter value deviated from its optimal value, for instance PART, SFCF, LP and ALPHA showed peaks in our calibrations; whereas for a not well-defined parameter, the fuzzy measure was good in broad range of parameter value simulations. On the other hand, parameters can compensate each other in the simulation, thus different values for one parameter could perform well (Seibert, 1997).

We estimated ranges and standard deviations of the parameter values to show uncertainty range of the parameters (Figure 3.49). The confined PART, SFCF, K2 and K1 parameters resulted in smaller uncertainty than the dispersed TT, CFSlope, FC and CFMAX parameters. Also, parameter uncertainty might be different for each vegetation zone. For the Bulgan catchment, hydrological simulation is more sensitive to parameters for non-forested area than forested area.

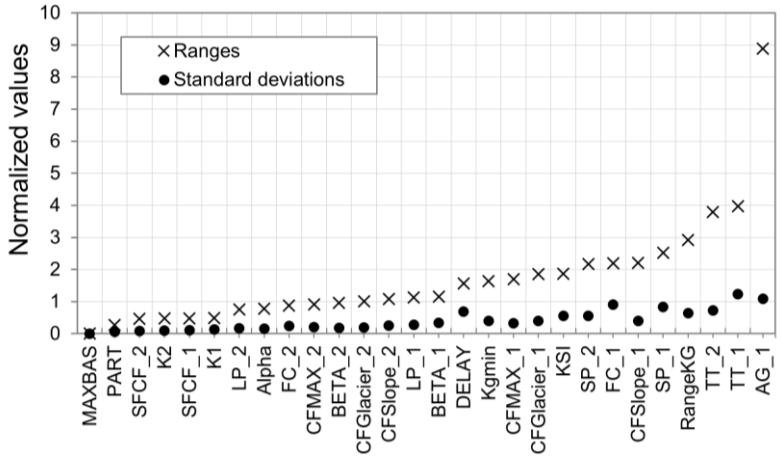

Figure 3.49: Comparison of parameters variation of the 100 best-calibrated models. Ranges and standard deviations of these parameters are normalized by the corresponding mean values. Parameters for forested area (1) and non-forested area (2).

In summary, limited precipitation data of two rain gauges and error in discharge measurement for the wet years 1986-1988 and for the dry years 2000 and 2006 impacted our model performance. Although the performance of the model structure with a combination of delay response and the glacier was good for the Bulgan catchment, our optimized model might lack the physical process representation of the regional hydrological regime under changing climate over time due to a lack of temperature adjustment in the soil box of the HBV-Light model and constant fractions of glacier area at the specified elevation zones over the whole simulation period.

All models could not simulate high and low flows during the wet period 1990-1993, which might be related to the highest acceleration of glacier recession from 1990 to 2000. Also, underestimation of monthly runoff throughout the year over the validation period 2006-2015 might be assigned to the model structure since the model could not represent deeper infiltration of surface water and deepening groundwater flow circulation with complete thawing of the permafrost over time. Based on the 100 optimized parameter sets, some parameters for non-forested areas were well-defined, but most parameters for the forested areas had a broad range of uncertainty. Furthermore, the uncertainty range of the 100 runoff simulations for the Bulgan catchment was narrow due to the combination of three objective functions.

3.5 Runoff sensitivity to climate change

For each climate scenario, climate input data was altered and applied to the optimized model for the Bulgan catchment to predict runoff. Compared to the reference runoff from 1985 to 2005, the predicted runoff was more sensitive to changes in precipitation than the air temperature. An increase in daily precipitation by 10% amplified the annual runoff by 22%, whereas daily temperature warming by +1°C reduced the annual runoff by 6% (Table 3.31). Moreover, the potential evapotranspiration increased along with warming temperature and brought drier conditions. When air temperature increased by +5°C but precipitation dropped by 20%, evapotranspiration intensified by 20.3%, and the runoff of the Bulgan river declined by 41%.

Table 3.31: Annual runoff sensitivity (%) to changes in temperature and precipitation.

ΔT, °C	ΔET, %	ΔP, %				
		-20%	-10%	0	+10%	+20%
0	0	-37	-20		+22	+46
+1°C	+3.9	-41	-25	-6	+14	+36
+2°C	+8.0	-42	-28	-11	+8	+29
+3°C	+12.0	-43	-29	-14	+4	+24
+5°C	+20.3	-41	-30	-16	0	+17

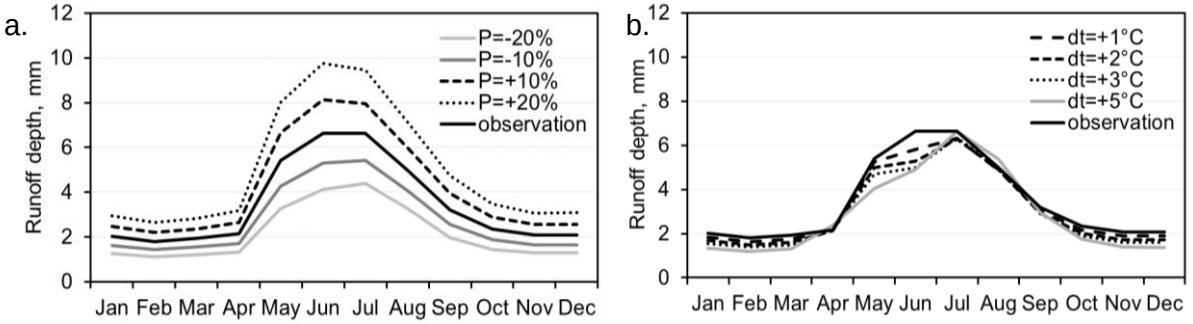

Figure 3.50: Runoff sensitivity of Bulgan River to changes in precipitation (a) and temperature (b).

When precipitation decreased by 10% and 20%, runoff declined for all months, mainly in June; thus, peak flow transferred to July (Figure 3.50a). Also, an increase in precipitation by 10% and 20% led to a rise in runoff in all months, predominantly in the warm period from May through August. When the temperature increased by +1°C, +2°C, +3°C, and +5°C, the runoff decreased significantly during the snowmelt period from May to June and the cold period from October to March; in contrast, the glacier melt runoff slightly increased in August (Figure 3.50b). The same high variation of runoff with changes in precipitation was found in the most river basins of Mongolia (Batima, 2006). The glacierized area of the Bulgan catchment is 0.13%, thus our finding contradicts the sensitivity of the glacier dominated (78%) Koxkar river runoff in the western Tianshan Mountain, which was more sensitive to changes in temperature than precipitation (Xu et al., 2017).

3.6 Future climate and runoff change in the Bulgan catchment

General Circulation Models (GCM) are used to help understand the uncertainty range of the climate projections, whereas Regional Climate Models (RCM) accurately show regional climate at fine-resolution geographic and temporal scales. Statistical downscaling (SD) of GCM is computationally cheaper than dynamical downscaling (DD) if there is no RCM data for the interested region.

The performance of the SD and DD depends on region, season, climate variable, spatial and temporal scales, thus sometimes SD performs better than DD (Teutschbein et al., 2011).

In addition to dynamically downscaled RegCM4 for East Asia from HadGEM2-AO, we used SDSM tool to downscale CanESM2 statistically at two stations in the Bulgan catchment. Then future climate and runoff changes for the Bulgan catchment were predicted based on both dynamically and statistically downscaled RCMs (RegCM4 and SD-CanESM2) and their driving GCMs (HadGEM2-AO and CanESM2) in this chapter.

3.6.1 Statistical downscaling of CanESM2 projections

3.6.1.1 Evaluation of the statistical downscaling SDSM model for the Bulgan catchment

In statistically downscaling daily precipitation of the General Circulation Model at the station level, grid cell choice and predictor variable selection significantly influence the downscaled output (Crawford et al., 2007). This is critically important for the impact study because the land-sea mask of GCM grids mismatch the real land surface spatially. Also, Crawford et al (2007) emphasized the importance of space and time substitution to reflect real atmospheric processes in the downscaling.

To find the optimal one grid cell for reflecting the local precipitation regime, the corresponding nine grid cell predictors of the NCEP Re-analysis dataset over the Altai-Dzungarian region were correlated with the observed precipitation at the stations on monthly time scales. Based on the highest explained variances and explanatory powers of predictors in monthly precipitation sums, we found the overlaying center and east grid cells of the NCEP Re-analysis were the optimum grids cells for Duchinjil and Baitag stations to statistically downscale daily precipitation of CanESM2 (2.81˚ x 2.81˚), respectively (Figure 3.51, Table 3.32).

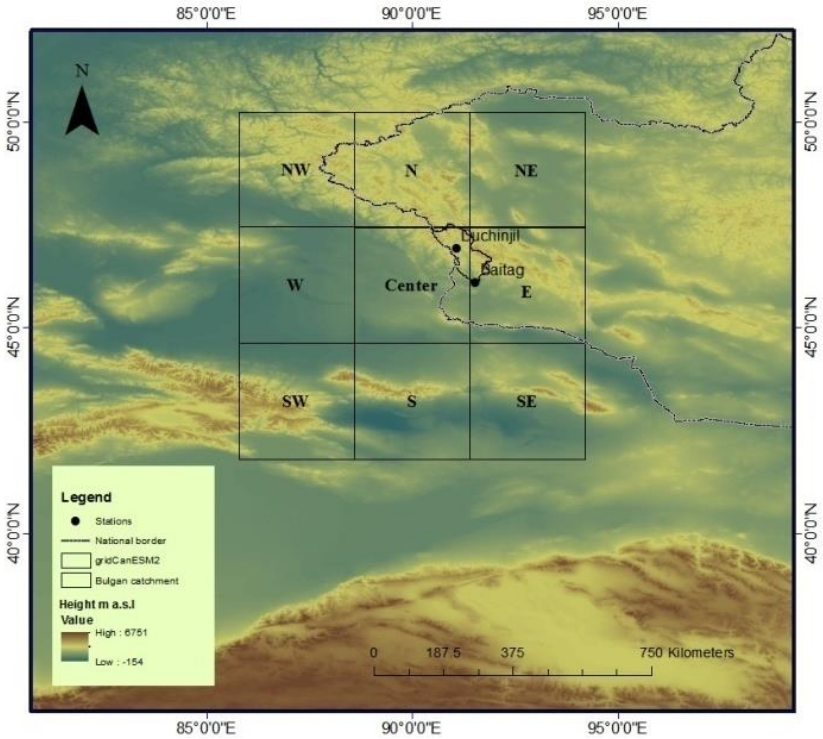

Figure 3.51: Nine grids of NCEP Re-analysis and CanESM2 (2.81˚ x 2.81˚) over the Altai-Dzungarian region. Duchinjil and Baitag stations are marked by black dots. Grid names: NW – northwest, W – west, SW – southwest, N- north, S – south, NE – northeast, E- east, and SE – southeast.

At each grid cell of NCEP reanalysis, the candidate predictor variables of large-scale atmospheric circulation patterns and moisture contents at the surface, 850hPa and 500hPa levels were used in the investigation of their statistical relationships with the measured precipitation using the SDSM downscaling tool. Furthermore, we correlated predictors from the same, previous, and subsequent day of the grid cell with the predictand precipitation to consider time substitution since NCEP reanalysis data (1200h GMT) and precipitation measurement (0100h and 1300h GMT) at the Southern Altai Mountains did not coincide. Predictors from the previous and the same day showed higher R^2 and r than predictors from the subsequent day.

Some studies have noted that three to six predictors were appropriate in statistical downscaling (Crawford et al., 2007). Thus, the top five and six predictors for downscaling precipitation at Duchinjil and Baitag stations were determined by screening potential predictors as shortlisted in Table 3.32. The combination of the airflow strength, zonal velocity and vorticity of the same day, and specific humidity of the previous day at 500hPa level and precipitation of the corresponding grid cells significantly explained observed precipitation regimes at Duchinjil and Baitag stations. The secondary airflow variables were derived from 3x3 arrays of the pressure fields, for instance, zonal velocity included information from a larger domain than the specific humidity of the overlaying single target grid cell (Crawford et al., 2007).

Specific humidity at 500hPa and precipitation were prominent predictors of precipitation at Duchinjil during winter, spring, and summer and were the leading variables at Baitag during

winter and autumn. Also, at both stations, airflow strength, zonal velocity, and the specific humidity at 500hPa were prominent during autumn. Vorticity at 500hPa was one of the leading factors for precipitation at Duchinjil in the summer months but at Baitag in the spring months. Also, the meridional velocity at 500hPa influences spring and summer precipitation regimes at Baitag.

Furthermore, the vorticity and geopotential height at 500hPa, and 2m temperature of the corresponding central grid cells of NCEP Reanalysis were the prominent variables in predicting maximum and minimum temperatures. Mean sea level pressure was a leading predictor in all seasonal temperatures of Duchinjil station in the valley of the southern Altai Mountain (Table 3.32).

Table 3.32: List of selected predictors and their annual partial correlation coefficients with predictands

	Duchinjil		Baitag	
Predictands	NCEP predictors	Partial r p<0.01	NCEP predictors	Partial r p<0.01
Precipitation				
	p5_fC	0.108	*p5_fE*	0.126
	p5_uC	-0.118	*p5_uE*	-0.134
	p5_zC	0.125	*p5_zE*	0.101
	prcpC	0.147	*prcpE*	0.125
	s500_prevC	0.270	*s500_prevE*	0.090
			p5_vE	0.170
Maximum temperature				
	mslpC	-0.294	*p5_z_prevE*	0.237
	p500C	0.571	*p500_prevE*	0.413
	temp_prevC	0.552	*tempE*	0.811
Minimum temperature				
	mslp_prevC	-0.200	*p5_z_prevE*	0.136
	p5_zC	0.190	*p500_prevE*	0.264
	p500C	0.364	*temp_prevE*	0.854
	temp_prevC	0.463		

Variable and grid box names are denoted by characters 1-4 and 5-10, respectively. prev – previous day
p5 – pressure fields at 500hPa, f- airflow strength, u-zonal velocity, v-meridional velocity z-vorticity, prcp-precipitation, p500-geopotential height at 500hPa, mslp- mean sea level pressure, temp – temperature. Grid names: C – Center, E- East

Our developed SDSM models for the Bulgan catchment in the southern Altai Mountains had good prediction skills for daily maximum and minimum temperatures at both stations (R^2=0.95-0.96 p<0.01) but relatively low skill for predicting precipitation at Duchinjil station in the valley of the mountains (R^2=0.56, p<0.001) during the validation period of 1996-2005 (Table 3.33; Figure 3.52). Moreover, precipitation for the Baitag station at the edge of the Dzungarian desert area was not simulated well (R^2=0.24, p<0.001).

Table 3.33: Statistics of simulated precipitation and temperature by the statistical downscaling model (SDSM) for the calibration (1977-1995) and validation (1996-2005) periods.

Periods	Monthly P_{total}			Daily T_{max}			Daily T_{min}		
	R^2	r	RMSE	R^2	r	RMSE	R^2	r	RMSE
	Duchinjil station								
Calibration	0.67	0.82	7.4	0.96	0.98	2.7	0.95	0.97	3.0
Validation	0.56	0.75	8.7	0.96	0.98	3.0	0.95	0.98	3.0
	Baitag station								
Calibration	0.27	0.52	9.2	0.96	0.98	3.1	0.96	0.98	3.0
Validation	0.24	0.49	9.0	0.96	0.98	2.9	0.96	0.98	3.1

R^2- Coefficient of determination, r – correlation coefficient, RMSE – Root Mean Square Error.

The same poor model skill was found in previous studies in other desert areas (Xu et al., 2016; Wang et al., 2019). Xu et al. (2016) found the same low skill of the NCEP predictors-based SDSM model (R^2=0.15) in the simulation of the precipitation for the Kaidu River basin on the northeastern edge of the Taklimakan Desert, northwest China.

Also, Wang et al. (2019) developed a precipitation model based on ERA-40 Reanalysis data (2°x2°) for northwest China and found low model simulation efficiency (R^2<0.5) at the climate stations in the Gobi Desert region but good (R^2>0.6) at the stations in the mountainous region of the Heihe River basin in the Qilian Mountains. These low model skills in generating precipitation for the arid area might be related to the spatial and temporal extreme natural variability of the desert climate; moreover, precipitation frequency might be too low in the desert area to develop statistical relationships between the predictors and predictand (Wang et al., 2019).

The established monthly regression models from the prominent predictors of the selected NCEP grid cell were used to downscale daily precipitation and temperature from the same predictors of the corresponding CanESM2 grid cell at the station level for the historical period (1961-2005) and future scenarios (2006-2100) under RCP 4.5 and 8.5 (Figure 3.52-3.53).

Although our NCEP-based SDSM model well-estimated spring precipitation for May, downscaled CanESM2 (SD_CanESM2) overestimated precipitation for May but underestimated summer precipitation from June through August at Duchinjil (Figure 3.52a). At Baitag station, SD_CanESM2 generally overestimated precipitation during the warm season (Figure 3.52b). Moreover, our developed SDSM model from NCEP predictors simulated monthly maximum and minimum temperatures well, but statistically downscaled temperatures from CanESM2 predictors slightly underestimated spring temperatures at both stations during the validation period (Figure 3.53).

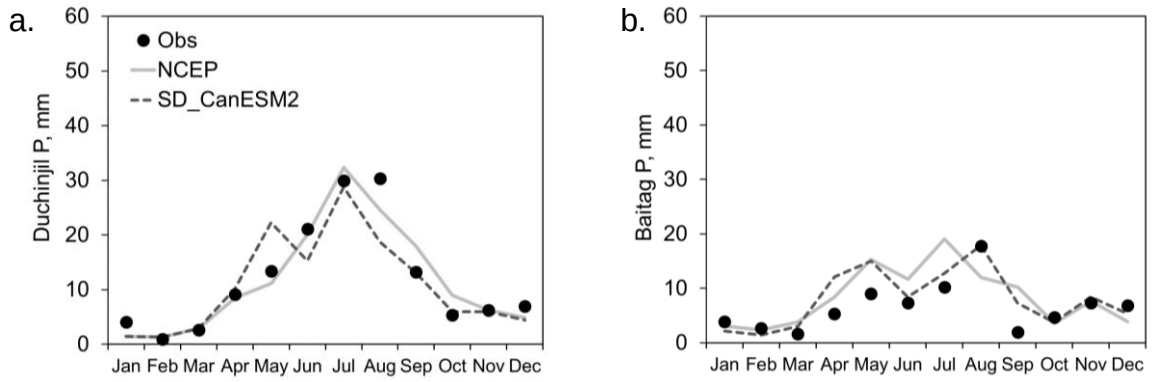

Figure 3.52: Comparison of observed monthly precipitation sums and the statistically downscaled precipitation sums from NCEP and CanESM2 predictors (SD_CanESM2) at Duchinjil (a) and Baitag stations (b) over the validation period from 1996 to 2005.

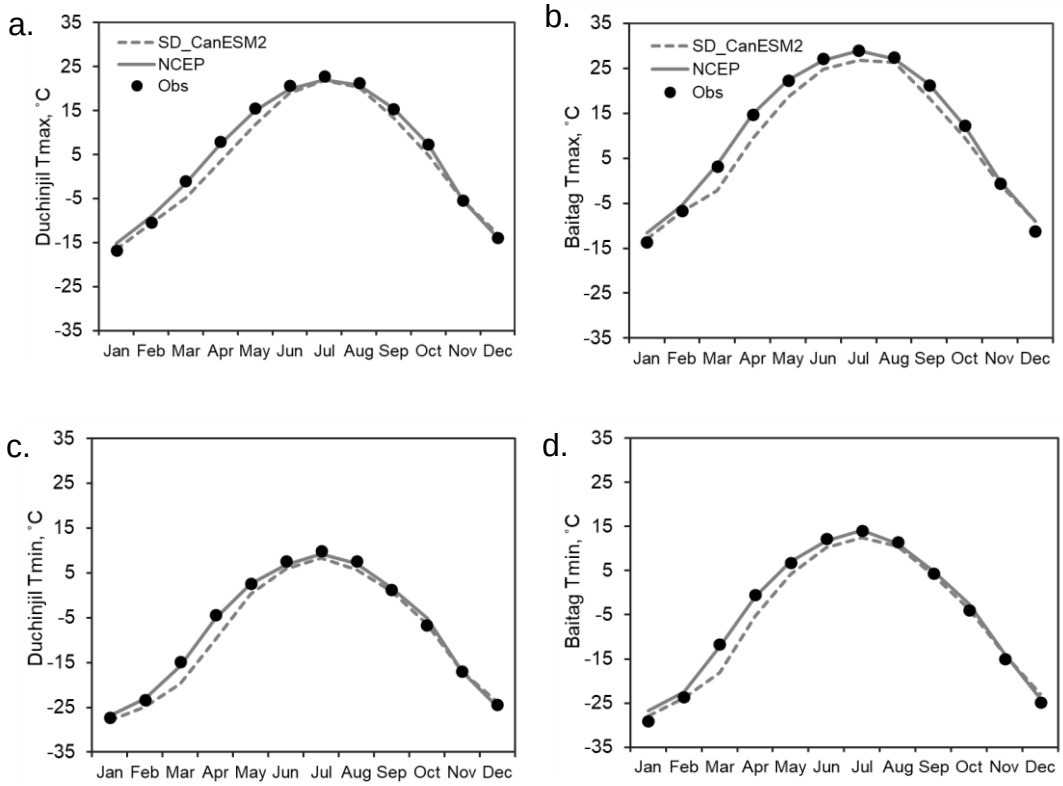

Figure 3.53: Maximum (a-b) and minimum (c-d) observed temperatures and the statistically downscaled temperatures from NCEP and CanESM2 predictors (SD_CanESM2) at Duchinjil (left panel) and Baitag stations (right panel) over the validation period from 1996 to 2005.

In summary, the prediction skill of our SDSM model for precipitation was satisfactory for the mountainous area but poor for the desert area due to low rainfall frequency and extreme climate conditions in the Dzungarian Desert. However, statistically downscaled maximum and minimum temperatures of CanESM2 at the two stations give a better representation of the local temperature regime except for underestimated temperatures for spring months.

3.6.1.2 Climate change projections of statistically downscaled CanESM2 in near and far future under RCP 4.5 and 8.5 scenarios

Under RCP4.5 and 8.5 scenarios, we calculated delta changes in statistically downscaled precipitation and maximum and minimum temperatures from the CanESM2 at Duchinjil and Baitag stations for near and far future periods: 2030-2050 and 2080-2100 (Table 3.34).

The statistically downscaled CanESM2 (SD_CanESM2) projected to increase annual total precipitation at Duchinjil station in the southern Altai Mountains by 27% in the 2040s and 41% in the 2090s under RCP4.5; whereas, SD_CanESM2 predicted to increase annual total precipitation at Baitag station in the semi-desert area by 33% in the 2040s and 35% in the 2090s under RCP4.5 (Table 3.34). Moreover, annual total precipitation was projected to increase by 110% at Duchinjil and by 145% at Baitag in the 2090s under RCP8.5.

Table 3.34: Projected changes in precipitation of SD_CanESM2 at Duchinjil and Baitag stations in the 2040s and the 2090s compared to the baseline period of 1985-2005 under RCP4.5 and 8.5 scenarios.

Seasons	Percentage change in precipitation							
	2040s (2030-2050)				2090s (2080-2100)			
	Duchinjil		Baitag		Duchinjil		Baitag	
	RCP4.5	RCP8.5	RCP4.5	RCP8.5	RCP4.5	RCP8.5	RCP4.5	RCP8.5
Winter	5%	89%	42%	22%	17%	125%	21%	310%
Spring	-10%	16%	-10%	12%	25%	79%	31%	113%
Summer	26%	31%	37%	34%	36%	94%	23%	87%
Autumn	80%	99%	84%	70%	79%	187%	77%	249%
Annual	27%	44%	33%	33%	41%	110%	35%	145%

Precipitation was predicted to increase more in autumn than in other seasons (Figure 3.54). In contrast, spring precipitation was projected to decrease by 10% at both stations in the 2040s then increase by 25-31% in the 2090s under RCP4.5. The extreme increase in winter precipitation at Baitag in the 2090s under RCP8.5 might be related to the relatively poor prediction skills of our developed regression model for the desert area.

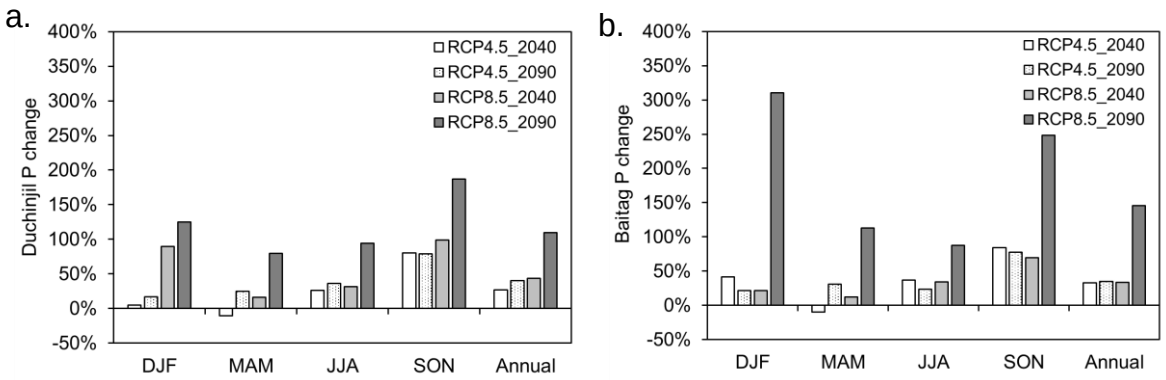

Figure 3.54: Projected percentage change (%) in precipitation of SD_CanESM2 at Duchinjil (a) and Baitag (b) in the 2040s and the 2090s compared to the baseline period under RCP4.5 and 8.5.

Annual maximum temperature will increase by +3.2°C in the 2040s and +4.1°C in 2090s at Duchinjil under RCP4.5; moreover, maximum temperature will warm more intensively in spring than summer at both stations by the 2040s and the 2090s under RCP4.5 and 8.5 scenarios (Table 3.35; Figure 3.55).

Table 3.35: Projected changes in maximum temperatures (°C) of SD_CanESM2 at Duchinjil and Baitag stations in the 2040s and the 2090s compared to the baseline period of 1985-2005 under RCP4.5 and 8.5 scenarios.

Seasons	Absolute difference of maximum temperatures (°C)							
	2040s (2030-2050)				2090s (2080-2100)			
	Duchinjil		Baitag		Duchinjil		Baitag	
	RCP4.5	RCP8.5	RCP4.5	RCP8.5	RCP4.5	RCP8.5	RCP4.5	RCP8.5
Winter	+2.7	+3.4	+2.7	+3.6	+3.8	+6.5	+4.1	+7.3
Spring	+4.0	+4.5	+4.6	+5.1	+4.6	+8.4	+5.3	+9.5
Summer	+3.5	+4.2	+2.9	+3.4	+4.6	+8.5	+3.8	+6.9
Autumn	+2.5	+3.4	+3.4	+4.6	+3.5	+6.9	+4.7	+9.0
Annual	+3.2	+3.9	+3.4	+4.2	+4.1	+7.6	+4.5	+8.2

Under RCP8.5 scenario, the maximum temperature was predicted to increase extremely at both stations by +8.0°C on average in the 2090s.

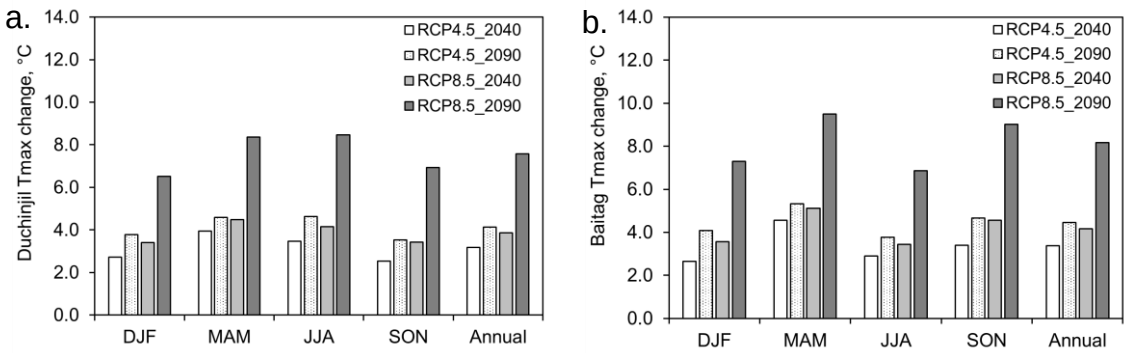

Figure 3.55: Projected changes in maximum temperatures (℃) of SD_CanESM2 at Duchinjil (a) and Baitag (b) in the 2040s and the 2090s compared to the baseline period under RCP4.5 and 8.5.

Furthermore, annual minimum temperature will increase less by +0.5°C than maximum temperatures at both stations in the 2040s and 2090s under RCP4.5 and 8.5 (Table 3.36).

Table 3.36: Projected changes in minimum temperatures (°C) of SD_CanESM2 at Duchinjil and Baitag stations in the 2040s and the 2090s compared to the baseline period of 1985-2005 under RCP4.5 and 8.5 scenarios.

Seasons	Absolute difference in minimum temperature (°C)							
	2040s (2030-2050)				2090s (2080-2100)			
	Duchinjil		Baitag		Duchinjil		Baitag	
	RCP4.5	RCP8.5	RCP4.5	RCP8.5	RCP4.5	RCP8.5	RCP4.5	RCP8.5
Winter	+2.7	+3.3	+3.3	+4.4	+3.7	+6.3	+5.0	+8.5
Spring	+3.9	+4.4	+4.3	+4.8	+4.5	+8.0	+5.1	+9.0
Summer	+2.2	+2.6	+2.2	+2.6	+2.9	+5.2	+2.8	+5.1
Autumn	+1.8	+2.3	+2.3	+3.0	+2.6	+5.1	+3.3	+6.4
Annual	+2.6	+3.2	+3.0	+3.7	+3.4	+6.1	+4.0	+7.2

The annual minimum temperature was projected to increase by +2.6°C in the 2040s and +3.4°C in 2090s at Duchinjil under RCP4.5;

More intensive warming of the minimum temperature was predicted in spring for both stations as well as the maximum temperature in spring. Also, extensive warming of the minimum temperature was projected for all seasons at both stations under RCP8.5 (Figure 3.56).

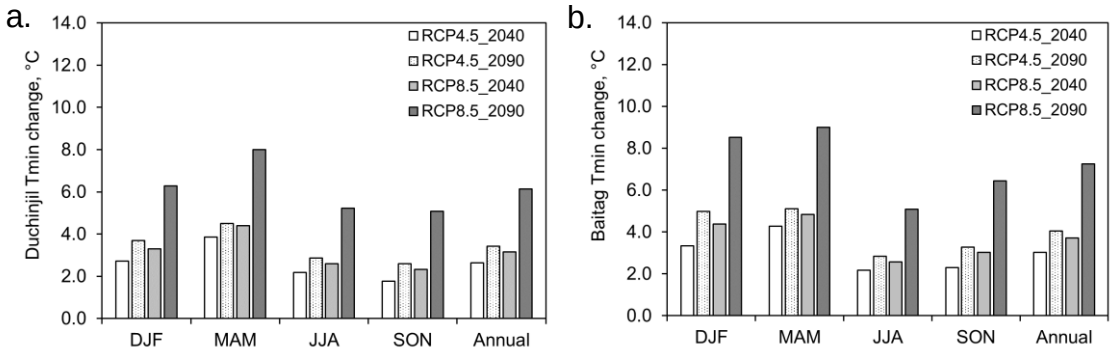

Figure 3.56: Projected changes in minimum temperatures (℃) of SD_CanESM2 at Duchinjil (a) and Baitag (b) in the 2040s and the 2090s compared to the baseline period under RCP4.5 and 8.5.

Overall, spring will be warmer and autumn will be wetter than other seasons at both stations in the 2040s and the 2090s under RCP4.5 and 8.5. Satisfactory downscaled precipitation and temperature of CanESM2 at Duchinjil station were used in a hydrological impact study of climate change on the Bulgan catchment in the next Chapter 3.6.2.

3.6.2 Projected climate change for the Bulgan catchment in the 2040s and the 2090s

A single GCM/RCM is not reliable for the prediction of future climate; thus, the ensemble mean of several GCM/RCMs is suggested due to model bias and inter-model variability (Teutschbein and Seibert, 2010). Thus, we estimated projected changes in seasonal temperatures and precipitation sums for the Bulgan catchment in the 2040s and the 2090s using the mean of two GCMs (HadGEM2-AO and CanESM2) and the mean of the dynamical and statistical downscaled RCMs (RegCM4 and SD_CanESM2) under RCP4.5 and RCP8.5 (Figure 3.57).

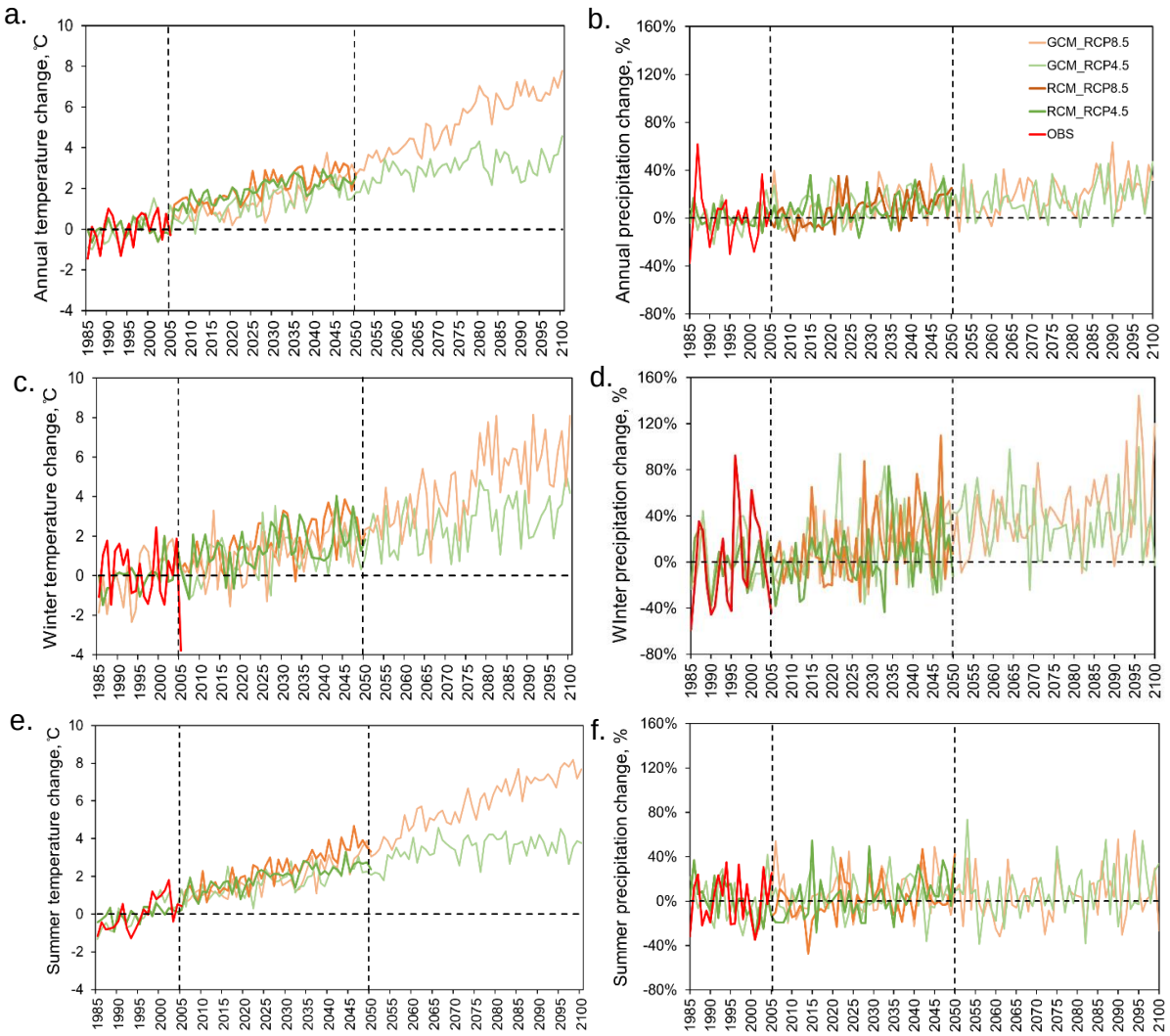

Figure 3.57: Projected changes in the annual (a, b), winter (c, d), and summer (e, f) temperature (left panel, °C) and precipitation (right panel, %) relative to the baseline period of 1985-2005. The red line marks the observed change in areal mean temperature and precipitation for the Bulgan catchment. Dark green and orange lines mark the mean changes of the dynamical and statistical downscaled temperature and precipitation of RCMs (RegCM4 and SD_CanESM2) by 2050 under RCP4.5 and 8.5, respectively. Light green and orange lines show mean changes in temperature and precipitation of two GCMs (HadGEM2-AO and CanESM2) by 2100 under RCP 4.5 and RCP8.5, respectively.

The mean of GCMs projects that annual temperature will increase by +1.8°C from 2030 to 2050 and +3.3°C from 2080 to 2100 under RCP4.5 compared to the baseline period from 1985 to 2005; moreover, the temperature will increase by +2.3°C from 2030 to 2050 and +6.6°C from 2080 to 2100 under RCP8.5 (Table 3.37). Also, the mean of RCMs projects that annual temperature will warm by +2.3°C under RCP4.5 and +2.9°C under RCP8.5 from 2030 to 2050.

Table 3.37: Seasonal temperature and precipitation changes in the near future (2030-2050) and far future (2080-2100) periods under RCP 4.5 and 8.5 compared to the baseline period 1985-2005.

Seasons	2040s (2030-2050)								2090s (2080-2100)			
	GCMs mean				RCMs mean				GCMs mean			
	RCP4.5		RCP8.5		RCP4.5		RCP8.5		RCP4.5		RCP8.5	
	T, ˚C	P, %	T, ˚C	P, %	T, ˚C	P, %	T, ˚C	P, %	T, ˚C	P, %	T, ˚C	P, %
Winter	+1.4	+21	+1.8	+32	+1.9	+11	+2.4	+27	+3.2	+30	+6.0	+51
Spring	+1.9	+15	+2.3	+21	+2.8	+3	+3.3	+20	+2.9	+22	+6.9	+32
Summer	+2.2	+6	+2.6	+8	+2.4	+9	+3.2	+5	+3.7	+13	+7.2	+9
Autumn	+1.9	+21	+2.5	+22	+2.4	+26	+2.6	+20	+3.1	+3	+6.3	+52
Annual	+1.8	+13	+2.3	+16	+2.3	+12	+2.9	+14	+3.3	+21	+6.6	+26

The GCMs projected an increase of 13% and 16% in annual precipitation by the 2040s, then 21% and 26% by the 2090s under RCP4.5 and 8.5, respectively. Similarly, RCMs project an increase of 12% and 14% in annual precipitation in the 2040s under RCP4.5 and 8.5. In the projections of GCMs, the winter precipitation will vastly rise by 21% and 32% in the 2040s and by 30% and 51% in the 2090s under RCP4.5 and RCP8.5, respectively; whereas, summer precipitation will slightly increase by 6% and 8% in the 2040s and by 13% and 9% in the 2090s under RCP4.5 and RCP8.5, respectively (Table 3.37, Figure 3.58).

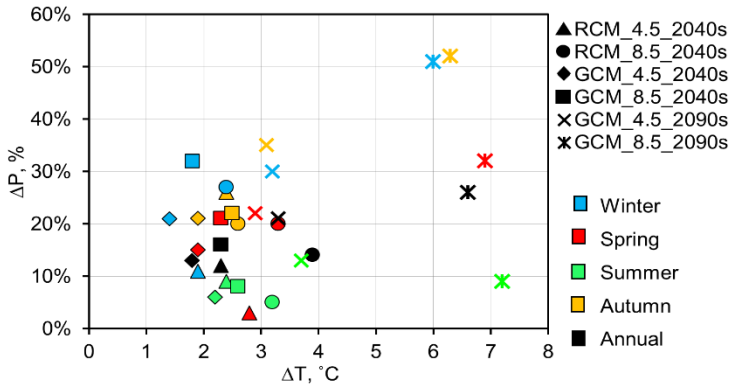

Figure 3.58: Projected changes in annual and seasonal temperatures (℃) and precipitation sums (%) in the 2040s and the 2090s under RCP4.5 and RCP8.5 compared to the baseline period of 1985-2005.

By the 2040s, GCMs projected intensive warming by +2.2°C and +2.6°C in summer temperature and by +1.3°C and +1.8°C in winter temperature under RCP4.5 and RCP8.5, respectively. However, RCMs anticipated a more significant warming of temperature in spring by +2.8°C and +3.3°C in the 2040s under RCP4.5 and RCP8.5, respectively. In

general, the temperature change was projected to be higher under RCP 8.5 than these under RCP 4.5 for both regional and global climate models (Table 3.37, Figure 3.58).

In the far future from 2080 to 2100, precipitation is projected to increase by +51% in autumn and by a similar amount in winter; whereas, summer precipitation is projected to increase by +9% accompanied by intensive warming (+7.2°C) (Figure 3.58).

Overall, projections for annual and seasonal temperature and precipitation tend to increase in the Bulgan catchment in the 2040s and the 2090s but at different rates. Generally, precipitation is projected to increase by a higher percentage in winter and autumn than in summer. On the contrary, accompanied by the high rate of warming, summer precipitation is only projected to increase by a low percentage in the future.

3.6.3 Hydrological impact of the projected climate change on the Bulgan catchment in the 2040s

Raw climate model outputs simulate surface runoff in unrealistic scales (Wörner et al., 2019). Thus, for a hydrological impact study, systematic errors and uncertainties in GCMs and RCMs should be post-processed with a convenient approach to changing climate conditions (Teutschbein and Seibert, 2010).

3.6.3.1 Post processing of General and Regional Climate Models

Over the Bulgan catchment, raw CanESM2 and HadGEM2-AO overestimated precipitation for spring but underestimated precipitation for autumn (Figure 3.59a, c). Dynamically downscaled RegCM4 overestimated precipitation through the year, whereas statistically downscaled SD-CanESM2 underestimated precipitation through the year, except for the spring months of April and May. GCMs reproduced warmer temperatures for the Bulgan catchment throughout the year, except in March (Figure 3.59b, d). Monthly temperatures were estimated quite well by RegCM4 except for the overestimation of temperatures for winter and summer months. We corrected these biases in the GCMs and RCMs by distribution mapping approach. The SD_CanESM2 is already post-processed data at the station level from GCM, thus it was not corrected.

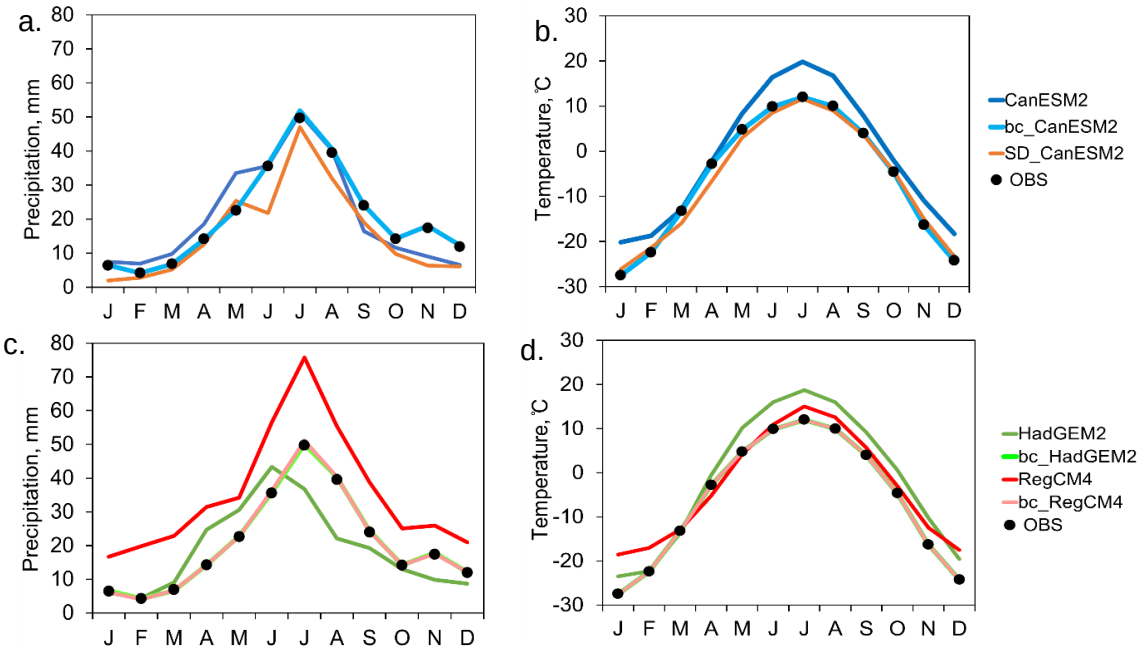

Figure 3.59: Monthly precipitation sums (left panel: a, c) and monthly mean temperatures (right panel: b, d) of the raw and bias-corrected (bc) GCMs and RCMs in the baseline period of 1985-2005. Observations are marked by black dots. SD is an abbreviation of the statistical downscaling.

Compared to the station data, the GCMs and RCMs had too many drizzle days with low precipitation. Thus, we eliminated excess drizzle precipitation from these climate model data with threshold 1.0mm day^{-1}, then corrected daily precipitation sums of all models by distribution mapping approach based on their ability to reproduce the Cumulative Distribution Function (CDF) of the observed precipitation over the baseline period of 1985-2005 (Figure

3.60a, c). The distribution mapping increased the amount of precipitation on wet days. Furthermore, the CDFs of the bias corrected temperatures shifted to the left and fitted the CDF of the colder observed temperature (Figure 3.60b, d).

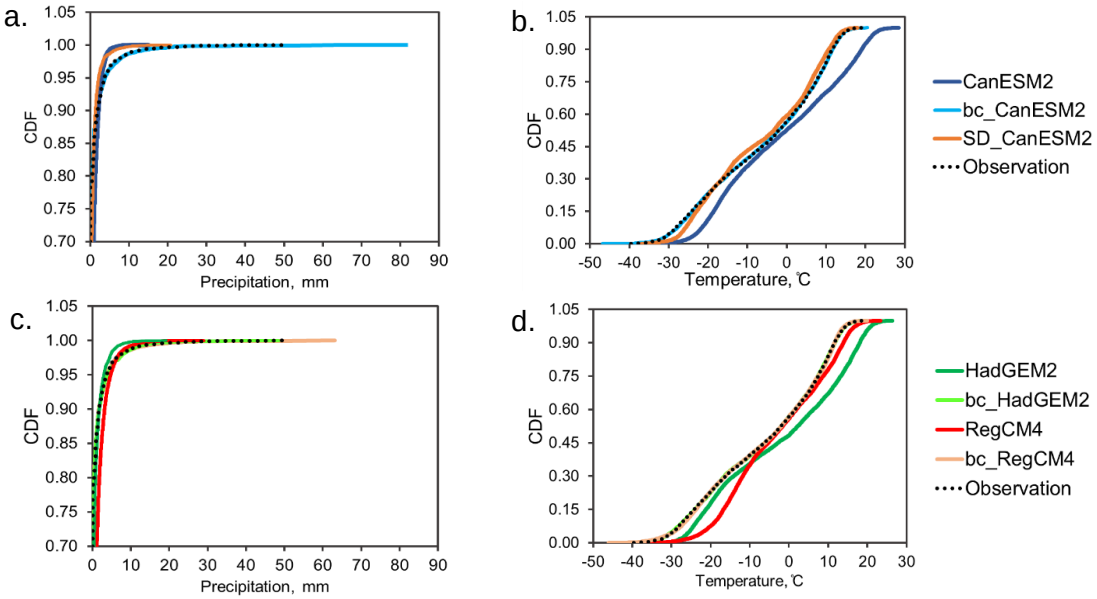

Figure 3.60: Raw and bias-corrected cumulative distributions of the simulated precipitation on wet days (left panel: a, c) and daily temperatures of GCMs and RCMs (right panel: b, d) from 1985 to 2005.

The Taylor diagram summarizes the standard deviation, the centered Root Mean Square Error (RMSE), and the correlations of raw and bias-corrected model outputs with observation in Figure 3.61.

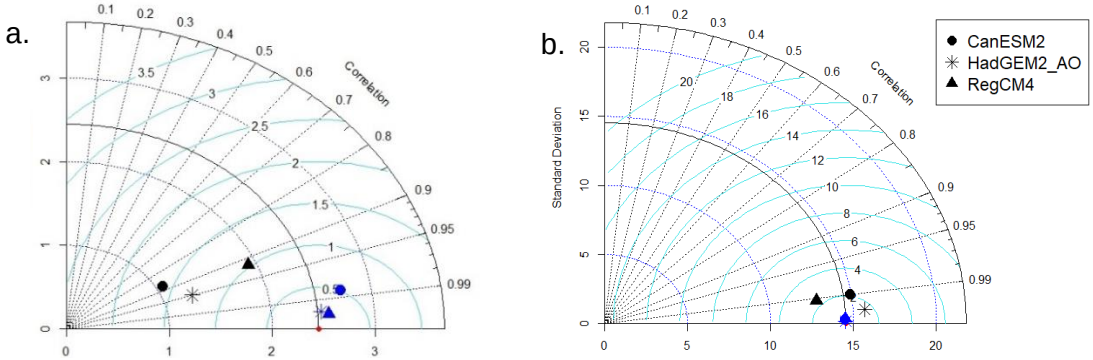

Figure 3.61: Taylor diagrams of the raw and bias-corrected daily precipitation (a) and temperature (b) of GCMs and RCMs over the baseline period of 1985-2005. The light blue contour is the centered RMSE. The red point on the x-axis is the observed value as a reference. Raw GCMs and RCMs are shown by black colored marks and the corresponding bias-corrected models are illustrated by blue colored marks.

In the Taylor diagram, raw CanESM2 precipitation resulted in the lowest correlation coefficient (r=0.88, p<0.001, stdev=1.06) and the largest RMSE (1.60), whereas raw HadGEM2-AO showed the highest correlation coefficient (r=0.95, stdev=1.29, RMSE=1.29). Raw RegCM4 had the lowest RMSE (1.06) and good correlation (r=0.92) with observation. After post-processing, correlations of modeled precipitation with observation were significantly improved (r=0.98-1.00) at 0.01 level and their RMSE ranged from 0.22 to 0.50.

For temperature, the correlation coefficients of the original model outputs were 0.99 at 0.001 and approached 1 after bias correction. Furthermore, the RMSEs of raw CanESM2 and HadGEM2-AO were considerably reduced from 2.1 and 1.5 to 0.26 and 0.16, respectively. Also, the RMSEs of raw RegCM4 decreased from 2.4 to 0.4.

Raw CanESM2 and HadGEM2 overestimated the high flows of summer months and underestimated baseflow during the cold season for the reference period of 1985-2005. Also, raw RegCM4 greatly overestimated runoff through the year; whereas, SD_CanESM2 underestimated runoff through the year (Figure 3.62a, c). After post-processing GCMs and RCMs, these biases in the simulated runoff were also corrected and fitted to the observed runoff better (See Annex C).

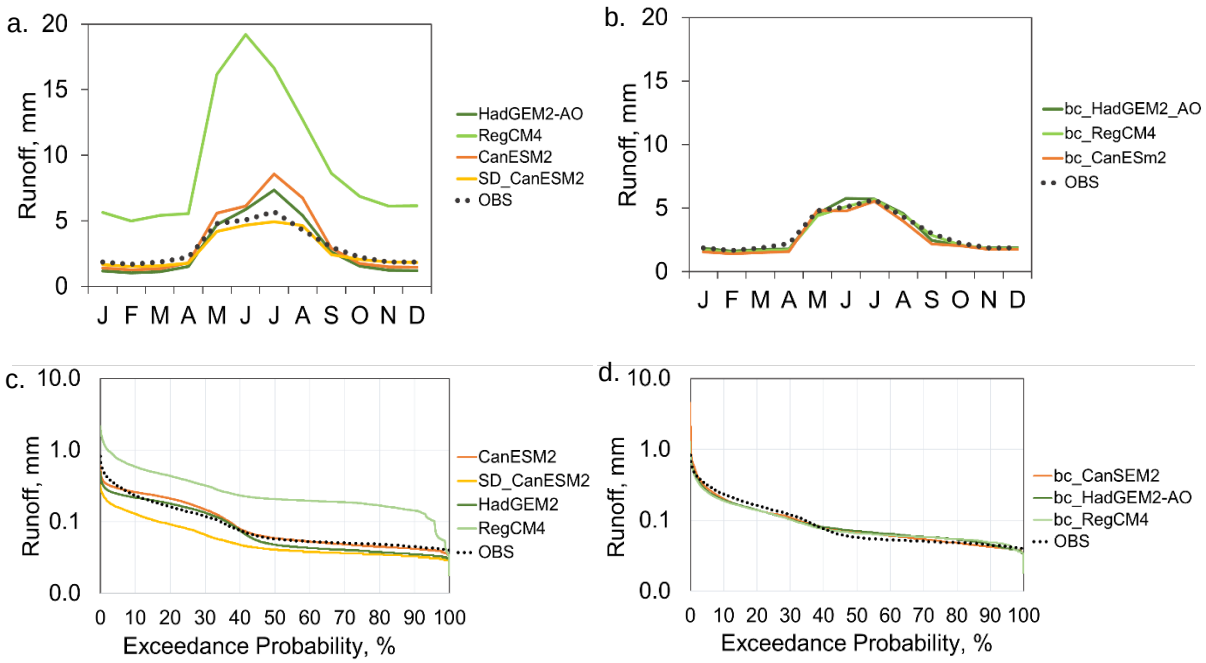

Figure 3.62. Observed and simulated hydrological regimes of Bulgan catchment using raw (left panel) and bias-corrected (right panel) GCM and RCM outputs over the period of 1985-2005: seasonal distribution of Q_{50} median (a-b) and the exceedance probability curves of daily runoffs (c-d). bc: bias-corrected.

On the monthly time scale, mean absolute error (MAE) in the simulated runoffs by raw CanESM2 (0.33), HadGEM2-AO (0.14), and RegCM4 (6.47) reduced in the simulated runoffs by bias-corrected CanESM2 (0.30) HadGEM2-AO (0.05) and RegCM4 (0.13). Also, MAE in the simulated runoff by SD_CanESM was 0.28. Furthermore, the exceedance probability curves of the simulated runoffs with the bias-corrected GCMs and RCM showed a slight underestimation of high flow (<30%) except peak flow (<3%). Also, they slightly overestimated mid-flow (40-70%) for the observed runoff (Figure 3.58c).

As a consequence of correcting biases in the climate model outputs by considering local climate variability in the Bulgan catchment from 1985 to 2005, previous projected changes in precipitation and temperature by raw climate model outputs as presented in Chapter 3.6.2

generally altered into a higher increase in seasonal precipitation, except for a decrease in winter precipitation from the GCM and in the spring precipitation from the RCM under RCP4.5. However, no difference was observed in warming rates in the projected seasonal temperatures between raw and bias-corrected outputs (Figure 3.63).

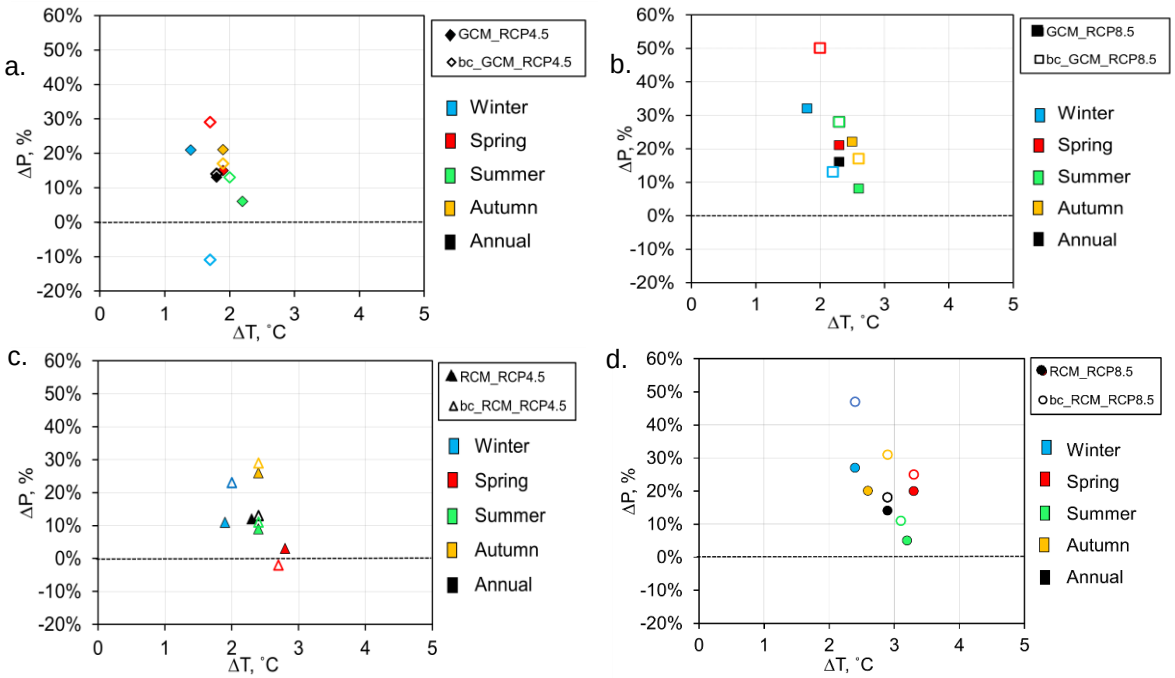

Figure 3.63: The difference in the projected changes in annual and seasonal temperatures (℃) and precipitation sums (%) by the means of raw and bias-corrected GCMs (a-b) and RCMs (c-d) from 2030 to 2050 under RCP4.5 (left panel) and RCP8.5 (right panel).

Overall, raw GCMs and RCMs simulated warmer temperatures and higher precipitation for the Bulgan catchment with more drizzle days than observed climate conditions. These biases were significantly corrected using the distribution mapping approach. After post-processing, the temperature was projected to increase in all seasons; whereas, a higher increase in precipitation was generally projected for the Bulgan catchment, except for a decrease in the winter by the GCM and spring by the RCM.

3.6.3.2 Projected climate and runoff change on Bulgan catchment in near future

Compared to the baseline period from 1985 to 2005, GCMs project an increase of 14% and 28% in annual precipitation from 2030 to 2050 under RCP4.5 and 8.5, respectively. Similarly, RCMs project an increase of 13% and 18% in annual precipitation in the 2040s under RCP4.5 and 8.5.

By the 2040s, GCMs projected the highest increase of +29% and 50% in precipitation during spring under RCP4.5 and RCP8.5, respectively. In contrast, winter precipitation was likely to decrease by -11% in under RCP4.5 but slightly increase by +13% under RCP8.5. Contrary to the projections of the GCM, RCMs projected a high increase of +23% and +47% in winter

precipitation under RCP4.5 and RCP8.5, respectively. Also, in spring, precipitation was projected to slightly decrease by -2% under RCP4.5 but increase by +25% under RCP8.5. Moreover, precipitation is projected to increase by a low amount of +11% in summer but to increase by +29% in autumn and by the same amount in winter under RCP4.5 (Figure 3.64).

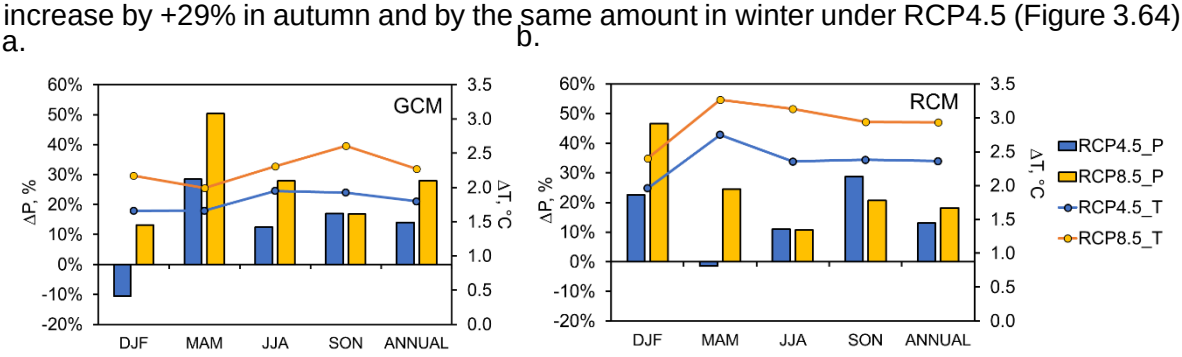

Figure 3.64: Projected precipitation and temperature changes in the near future period of 2030-2050 by raw and bias-corrected GCMs (a) and RCMs(b) under RCP4.5 (blue color) and RCP8.5 (orange color) scenarios.

GCMs project that annual temperature will increase by +1.8°C under RCP4.5 and +2.3°C under RCP8.5 from 2030 to 2050. RCMs also projects that annual temperature will warm by +2.4°C under RCP4.5 and +2.9°C under RCP8.5. By the 2040s, GCMs projected warming by +2.0°C in summer under RCP4.5 but more intensive warming by +2.6°C in autumn under RCP8.5. Also, RCMs project a more significant warming of temperature in spring by +2.7°C and +3.3°C in the 2040s under RCP4.5 and RCP8.5, respectively.

GCMs projected increasing trends in runoffs for all seasons from 2030 to 2050, characterized by a low increase in summer runoff; whereas, RCMs projected the lowest increase in autumn runoff (Figure 3.65, Table 3.38).

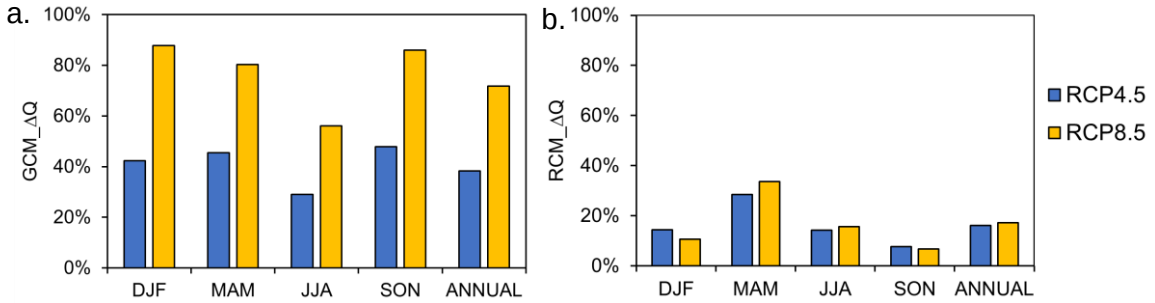

Figure 3.65: Projected seasonal runoff changes (%) in near future period of 2030-2050 by bias-corrected GCMs (a) and RCMs(b) under RCP4.5 (blue color) and RCP8.5 (orange color) scenarios.

Increasing trends in the simulated runoffs for the Bulgan catchment might be related to increasing trends in the projected precipitation since the hydrological regime of Bulgan River was more sensitive to precipitation changes (See Chapter 3.5). The lowest increasing trend in summer runoff by GCMs, particularly in June (Figure 3.66) can be explained by intensive warming trends in spring and summer as the sensitivity analysis of the Bulgan River to climate change showed that an increase in temperature resulted in a large decrease in June flow but an increase in high flow for August (See Chapter 3.5).

Table 3.38: Seasonal runoff changes in the near future (2030-2050) under RCP 4.5 and 8.5 compared to the baseline period 1985-2005.

	GCM mean		RCM mean	
Seasons	RCP4.5	RCP8.5	RCP4.5	RCP8.5
Winter	42%	88%	14%	11%
Spring	46%	80%	28%	34%
Summer	29%	56%	14%	16%
Autumn	48%	86%	8%	7%
Annual	38%	72%	16%	17%

RCMs project a larger increase in spring runoff related to earlier snowmelt with the strongest warming in spring and a high percent increase of precipitation in autumn and winter. In addition, RCMs projected more intensive warming than GCMs, thus the effect of temperature on runoff simulation might be more pronounced. Also, more precipitation projected in summer by RCM resulted in more runoff projection for summer than autumn since the summer runoff of Bulgan River is largely influenced by summer precipitation (See Chapter 3.3). According to the shaded areas between the 25th and 75th percentiles of the simulated monthly discharges, Bulgan River has a larger variation in spring and summer than in autumn and winter (Figure 3.66). By the 2040s, GCMs and RCMs project an increase in runoff through the year, characterized by the highest increase in the spring months of April and May, but the lowest increase in June. SD_CanESM also projected the highest decrease in June but the largest increase in September under RCM4.5 (Figure 3.66).

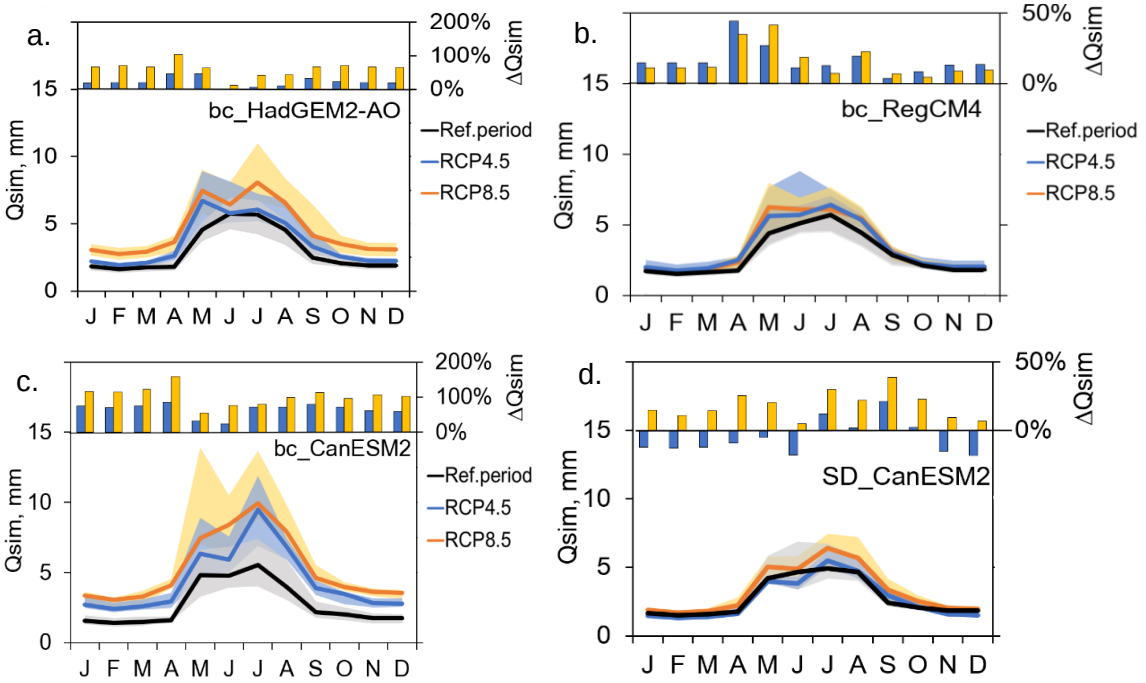

Figure 3.66. Comparison of the projected monthly median runoffs (Q_{sim}, mm) and their changes (%) by raw (left panel) and bias-corrected (right panel) GCMs and RCMs for the period of 2030-2050 under RCP4.5 and RCP8.5 scenarios compared to the reference period of 1985-2005. Shaded bands show a range between the 25th and 75th percentiles of the corresponding simulated runoffs for the reference period and RCPs. The blue and orange columns show projected changes in the monthly mean runoffs under RCP4.5 and RCP8.5, respectively.

CanESM2 and HadGEM2-AO projected a high increase of 70% and 20%, respectively, in low flow during the cold season under the RCP4.5 scenario. Bias-corrected RegCM4 projected a low increase of 13% in the low flow of the Bulgan River; whereas, SD-CanESM2 projected a minor decrease of 12% in the low flow (Figure 3.67).

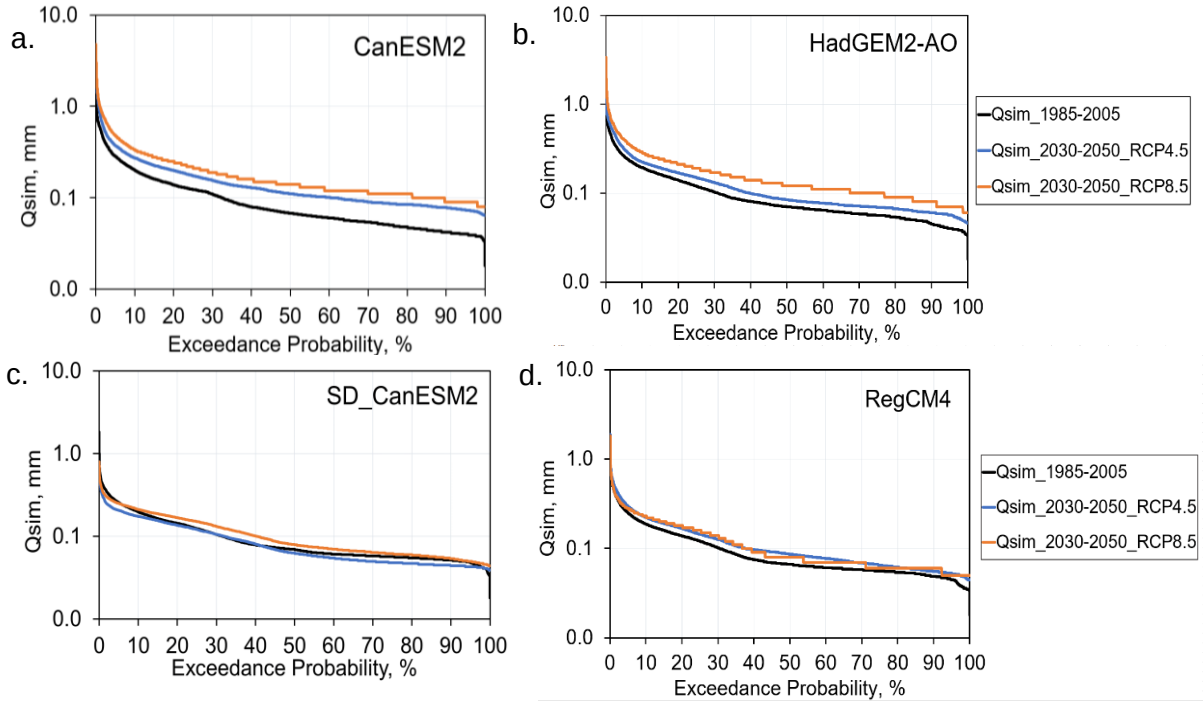

Figure 3.67. Exceedance probability curves of the simulated runoffs in the reference period of 1985-2005 (black line) and the near future period of 2030-2050 under RCP4.5 (blue line) and RCP8.5 (orange line) scenarios: GCMs (upper panel): CanESM2 (a) and HadGEM2-AO (b), and the corresponding RCMs (lower panel): SD_CanESM2 (c) and RegCM4 (d).

Despite the different runoff projections, the ensemble mean of the projected monthly runoffs by GCMs and RCMs shows that runoff will increase in the period 2030-2050 under RCP4.5 and RCP8.5 scenarios as a result of an increase in precipitation. However, the seasonal distribution of the runoff through a year will be altered due to warming. Peak flow in June might shift to May due to earlier snow melt in April and May (Figure 3.68a-b). Also, the shortened cold season might increase baseflow due to permafrost degradation.

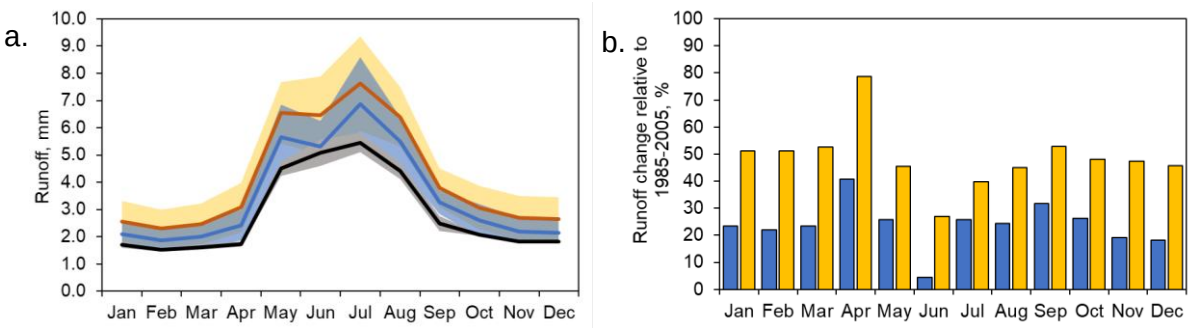

Figure 3.68. The ensemble mean of the projected monthly runoffs by GCMs and RCMs (a) and its change (b) in the period 2030-2050 under RCP4 and RCP8.5 scenarios compared to the baseline period of 1985-2005. The black line marks the ensemble mean runoff for the baseline period. Thick blue and orange lines are the projected monthly mean runoffs under RCP4.5 and RCP8.5, respectively. The corresponding shaded bands show the confidence intervals (95%) of the runoff projections (a). The blue and orange columns show projected changes in the monthly mean runoff under RCP4.5 and RCP8.5, respectively (b).

Like our GCMs projections, another 12 GCMs projected an increase in precipitation and accelerated warming in the Altai Mountains for RCP4.5 and 8.5 during 2006-2100, resulting in the starting projected loss of entire glaciers by 2050s and disappearing of most glaciers by 2100 (Zhang et al., 2016). Also, previous studies on the hydrological impact of climate change in the Altai Mountains using RCMs (HadGEM3, SUN-MM5 and RegCM4) (Luo et al., 2019), and in the Kaidu watershed of northwest China using the statistically downscaled HadCM3 (Ma et al., 2013) supported our findings of the largest increase in spring runoff but a decrease or the smallest increase in summer runoff in the region.

Based on ensemble mean projection of three RCMs, Lou et al. (2019) found a decreasing trend in summer precipitation with the highest warming for the catchments in the northwestern Altai Mountains, but the mean of our dynamical and statistical downscaling RCMs projected a slight increasing trend in summer precipitation and the highest warming in spring temperature in the southern Altai Mountains. Different future climate projections for catchments in the northern and southern Altai Mountains might be acceptable since a drying trend in the northern Altai but a wetting trend in the southern Altai were observed during the period 1966-2015. This period was characterized by an increasing contribution of west zonal and southern meridional circulation over this complex terrain (Zhang et al., 2018).

In summary, CanESM2 was statistically downscaled at Duchinjil and Baitag stations using the SDSM tool. The prediction skill of the statistical model for precipitation was satisfactory for Duchinjil station in the mountainous area but poor for Baitag in the desert area due to low rainfall frequency and extreme climate conditions in the Dzungarian Desert. Thus, statistically downscaled CanESM2 at Duchinjil station (SD-CanESM2), CanESM2 and HadGEM2-AO, and RegCM4 outputs were further used in the estimation of future climate and runoff change in the Bulgan catchment in the southern Altai Mountains. After post-processing, climate model outputs better represented local climate variability and were applied to the optimized HBV model.

By the 2040s, spring runoff will increase in April and May due to earlier snow melt as a result of warmer spring and more precipitation in cold season but summer runoff will decrease in June because of less rainfall in summer.

3.6.4 Comparison of future climate change to past climate variation

Combining reconstructed and projected climate time-series data for the Altai-Dzungarian Region allows us to analyze the regional climate variations and change from the Little Ice Age to the mid of the 21st century. It must be kept in mind, however, that these reconstructed and projected climate changes have uncertainties e.g. related to assumptions on tree growth response, observation errors, climate model uncertainties and RCP scenarios.

Although the ensemble mean of the projected June-July temperatures derived from bias-corrected GCMs and RCMs increases continuously from 1985 to 2050 (Figure 3.69a), the projected change in the summer temperature (+2.96±0.79°C) in the 2040s under RCP4.5 is likely to be the same as the reconstructed temperature (+2.94±0.96°C) in the beginning of the 1900s while the impact of the former on the water resources can be larger. Moreover, the projected summer temperature increase from the RCP8.5 (+3.62±0.8°C) is significantly higher, and the June-December precipitation sum is projected to increase in the 2040s compared to the dry period after Little Ice Age (Figure 3.69b).

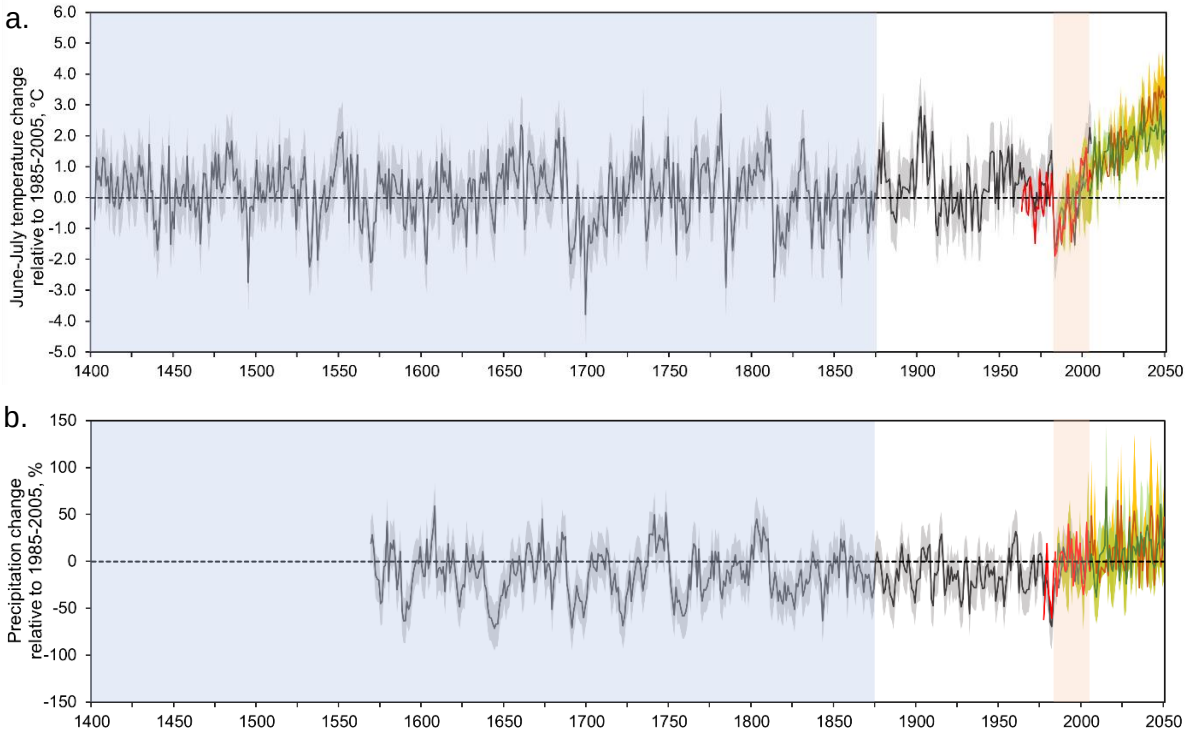

Figure 3.69. Long-term variation and changes in the estimated mean June-July temperature (a) and June-December precipitation sum (b) for the Altai-Dzungarian region from the Little Ice Age (blue-shaded area,1400-1875) until 2050 relative to 1985-2005 period (pink-shaded bar). The thick black lines marks mean June-July air temperature reconstruction (a) and the June-December precipitation sum reconstruction (b). The grey-shaded band shows the uncertainty range of the reconstructions (± 1 stdev). The red line marks observed temperature of CRU TS4.01 (a) and precipitation at Duchinjil station (b). The thick green line marks the ensemble mean of the projected June-July temperature (a) and June-December precipitation sum (b) obtained from bias-corrected GCM and RCM runs under the RCP4.5 scenario. The thick orange line shows the ensemble mean of the projected June-July temperature (a) and June-December precipitation sum (b) under the RCP8.5 scenario. The corresponding shaded bands show the confidence intervals (95%) of the ensemble mean temperature and precipitation sum under the RCP4.5 and RCP8.5 scenarios.

CHAPTER 4. CONCLUSION AND RECOMMENDATION

"The Bulgan with Beavers is my homeland, a beautiful place like a beaver's fur

Meandering Bulgan River is the life-spring of my homeland…"

from "Bulgan River with Beavers" folk song

Photo: A downstream area of the Bulgan River valley, Oyunmunkh 2014

4.1 Conclusion

During the 20th-century warming of the Northern-Hemisphere, volcano eruption and AO caused a late 20th-century cool and wet period in the Altai-Dzungarian region and also other mountainous areas of Central Asia. The subsequent warm years since the 1980s have accelerated the regional hydrological cycle and enhanced glacier recession in the Altai Mountains. The shortening of the freezing period resulted in permafrost degradation and a thickening of the active layer, which increased the water storage capacity. Accordingly, the winter baseflow has increased in this high-latitude permafrost region since the 1990s, and warm winters shortened the duration of the snow cover in the southern Altai Mountains since 1977. These impacts of climate change on the water resources might threaten agriculture and livelihood security in the Altai-Dzungarian region in the future.

Thus, this thesis evaluated long-term climate variability and change over the semi-arid Altai-Dzungarian region from the past to the future and including its hydrological impacts on the Bulgan catchment. The main conclusions are summarized according to the research questions as follows.

A. Climate variations over the Altai-Dzungarian region during and after the Little Ice Age

The long-term climate change and variation over the Altai-Dzungarian region was reconstructed for 611 years for temperature and for 444 years for precipitation from tree-ring proxies collected in the southern Altai Mountains. The temperature reconstruction shows cooler periods related to volcanic and low solar activities during the Little Ice Age, followed by a warming period interrupted by two short cold periods to the 20th century. The precipitation reconstruction shows alternating extreme wet and dry conditions during the Little Ice Age (1580-1874), followed by more stable conditions until a late 20th-century wetting. The precipitation variability is related to the pattern and strength of westerly winds governed by the Arctic (AO) and North Atlantic Oscillation (NAO). Although this region has warmed since 1875, a positive AO phase might have caused a late 20th-century cool and wet period by strengthening westerly winds in addition to volcanic-induced cooling over the Altai-Dzungarian region. The reconstructed summer temperature and precipitation variations for the Altai-Dzungarian region are significantly correlated with NAO, AO, and the El Niño-Southern Oscillation (here quantified by the NINO3.4 index). On the interannual time scale, prominent positive winter NAO and AO indices resulted in cool-wet summers in the Altai-Dzungarian region for the period 1960-2012 due to the northward shift of the polar jet and intensified westerlies. However, the signs and strengths in the interannual teleconnections between these global climate drivers and the regional climate have changed over the longer time scales from 1900 to 2012. On the interdecadal time scale, the identified cool and wet summers are more strongly and negatively correlated with the spring and summer NAO than

the winter NAO for the 1900-2012 period due to interdecadal changes in the oceans' heat storage and transport. But winter AO was still a prominent climate driver in summer temperature and precipitation on the interdecadal time scale.

B. Hydrological impact of observed climate change in the Bulgan catchment in the Altai-Dzungarian region between 1984 and 2015

The accumulated snow amount, summer rainfall, and summer temperature significantly influence the hydrological regime of the Bulgan River. Thus, a decrease in precipitation during summer and autumn and an intensive warming in summer resulted in a significant decline in annual discharge but an increase in winter flow for the period 1984-2015 due to permafrost degradation and an expansion of the soil storage capacity. The increase in baseflow might have shortened the period between river ice formation and break-up.

Compared to the period 1985-2005, a decrease in total precipitation and an increase in potential evapotranspiration reduced the water storage of the Bulgan catchment in the period 2006-2015. Also, the groundwater contribution to the annual runoff increased.

C. Projected climate and runoff changes for the Bulgan catchment for the period 2030-2050

The runoff of the Bulgan catchment is more sensitive to changes in precipitation than changes in temperature. An increase in the daily precipitation sums amplifies the annual runoff; whereas a warming temperature changes the seasonal distribution of runoff throughout the year.

Under the RCP4.5 and RCP8.5 scenarios, total precipitation and annual temperature are projected to increase in the period 2030-2050 compared to the baseline period 1985-2005. The GCMs projected an intensive warming in summer and autumn and the highest increase in precipitation during spring. However, RCMs projected a high increase in winter precipitation and more significant warming in spring in the 2040s. Despite these different climate projections, spring runoff is projected to increase due to an earlier snow melt in April and May but to decrease in June in the period 2030-2050. On the long timescale, the projected change in summer temperature in the 2040s is the same as the reconstructed temperature change in the early 1900s. However, the impact of the consecutive warming on the water resources since 1985 might be more severe than the short warming period in the 1900s.

Overall, NAO, AO, volcano eruption, and solar activity impact climate variation in the Altai-Dzungarian region. After a late 20th-century cool and wet period caused by AO and volcanic eruption, the subsequent warming years have changed the regional hydrological regime of the Bulgan catchment. In response to the projected increase in precipitation in the 2040s,

runoff of the Bulgan River is projected to increase; however, the seasonal water allocation will be altered into a high runoff in spring but a low runoff in summer. Therefore, the intensified agriculture along the Bulgan River might face challenges related to water shortage and heat stress during the growing season in the future.

4.2 Recommendation

The interpolated APHRODITE dataset was found as a valuable data source for this data-limited mountainous region despite its underestimation of air temperature and precipitation amounts in the southern Altai Mountains. After correcting these biases, this dataset simulated satisfactorily the runoff of the Bulgan catchment. In a further study, a good regionalization approach of precipitation data at the station to the catchment scale should be selected to improve its model efficiency of the hydrological simulation.

Moreover, the seasonal thawing of permafrost and glaciers are vital for the hydrological simulation of the Bulgan River in the southern Altai Mountains. Thus, our attempt to conceptualize the permafrost condition with a delayed response function and glacier variant to the standard model structure of the HBV model improved the baseflow simulation. Although model efficiency was good (0.69) with a low absolute error of 7.6%, the high flows of the Bulgan River in wet years were underestimated and low flows in dry years were overestimated. Besides, the observed upward trend in winter flow since 2006 was not simulated most probably due to a lack of data on glacier area change and the rather simple conceptualization of the permafrost degradation. In a future study, the conceptualization of permafrost in the hydrological model should be improved to better simulate the seasonal runoff change as groundwater recharge has increased in the winter baseflow of the Bulgan River.

The uncertainty of the hydrological simulation for the Bulgan catchment might have also originated from limited precipitation measurements in this complex terrain, errors in discharge measurement for the extreme years, the lack of glacier and permafrost data, and model structure and parameter deficiencies. Therefore, data availability and accuracy should be considered in the simulation period to reduce uncertainty in future runoff simulations.

The statistical downscaling of precipitation from CanESM2 for the southern Altai Mountains was satisfactory but poor for the desert area due to low rainfall frequency and extreme climate. The maximum and minimum temperatures were downscaled well. In future research, HadGEM2 can be statistically downscaled at the station level by the SDSM tool and compared with its dynamically downscaled RCM (RegCM4) simulations in order to select a more appropriate downscaling for the hydrological impact study of climate change in this semi-arid region.

REFERENCES

Adler, C., P. Wester, I. Bhatt, C. Huggel, G.E. Insarov, M.D. Morecroft, V. Muccione, and A. Prakash, 2022: Cross-Chapter Paper 5: Mountains. In: *Climate Change 2022: Impacts, Adaptation, and Vulnerability. Contribution of Working Group II to the Sixth Assessment Report of the Intergovernmental Panel on Climate Change* [H.-O. Pörtner, D.C. Roberts, M. Tignor, E.S. Poloczanska, K. Mintenbeck, A. Alegría, M. Craig, S. Langsdorf, S. Löschke, V. Möller, A. Okem, B. Rama (eds.)]. Cambridge University Press. In Press.

Aghakouchak, A. and Habib, E. (2010) Application of a Conceptual Hydrologic Model in Teaching Hydrologic Processes*. Int. J. Engng Ed. Vol.* 26. 4. 963-973

Allen, R.G., Pereira, L.S., Raes, D. and Smith, M. (1998) Crop evapotranspiration-Guidelines for computing crop water requirements-FAO Irrigation and drainage paper 56. *FAO*, *Rome* 300, D05109

D' Arrigo, R., Jacoby, G., Pederson, N., Frank, D., Buckley, B., Nachin, B., Mijiddorj, R. and Dugarjav, Ch. (2000) Mongolian tree-rings, temperature sensitivity and reconstructions of Northern Hemisphere temperature. *The Holocene* 10 (6), 669-672.

D' Arrigo, R., Jacoby, G., Pederson, N., Frank, D., Buckley, B., Nachin, B., Mijiddorj, R. and Dugarjav, Ch. (2001) 1738 years of Mongolian temperature variability inferred from a tree-ring width chronology of Siberian Pine. *Geophysical Research Letters* 28 (3), 543-546

Ba´ez, J.C., Gimeno, L., Go´mez-Gesteira, M., Ferri-Ya´n˜ ez, F. and Real, R. (2013) Combined Effects of the North Atlantic Oscillation and the Arctic Oscillation on Sea Surface Temperature in the Albora´n Sea. PLoS ONE 8(4), doi:10.1371/journal.pone.0062201

Barnston, A.G. and Livezey, R.E. (1987) Classification, seasonality and persistence of low-frequency atmospheric circulation patterns. Monthly Weather Review 115, 1083–1126

Batjargal, Z., 2018. Mongolia Third National Communication. The United Nations Framework Convention on Climate Change. Ulaanbaatar. Mongolia

Batima, P. 2006. Climate change vulnerability and adaptation in the Livestock Sector of Mongolia. AIACC. Project No.AS06. The International START Secretariat. Washington DC.USA

Bayartaa, N., Goldammer, G. and Uibrig, H. (2007) Fire situation in Mongolia, International Forest Fire News: 36, 46–66. ISSN 1029-0864.

Bergström, S. (1992) The HBV Model: Its Structure and Applications, ¨Swedish Meteorological and Hydrological Institute (SMHI), Hydrology, Norrkoping, 35 pp.

Berhanu, B., Seleshi, Y., Demisse, S.S, and Melesse, A.M. (2015) Flow Regime Classification and Hydrological Characterization: A Case Study of Ethiopian Rivers. *Water* 7, 3149-3165.

Berti, A., Tardivo, G., Chiaudani, A., Rech, F. & Borin, M. Assessing reference vapotranspiration by the Hargreaves method in north-eastern Italy. Agr Water Manage 140, 20–25, doi:10.1016/j.agwat.2014.03.015 (2014).

Biondi, F. and Waikul, K. (2004) DENDROCLIM2002: a C++ program for statistical calibration of climate signals in tree-ring chronologies. *Computer & Geosciences* 30, 301-311.

Bladé, I., Liebmann, B., Fortuny, D. and van Oldenborgh, G. J. (2012) Observed and simulated impacts of the summer NAO in Europe: Implications for projected drying in the Mediterranean region. *Climate Dyn.,* 39, 709–727, https://doi.org/10.1007/s00382-011-1195-x.

Bohner, J. (2006) General climatic controls and topoclimatic variations in Central and High Asia. *Boreas* 35, 279-295. doi 10.1080/03009480500456073.

Braeuning, A. and Mantwill, B. (2004) Summer temperature and summer monsoon history on the Tibetan Plateau during the last 400 years recorded by tree rings. *Geophysical Research Letters* 31, doi:10.1029/2004GL020793.

Briffa, K., Jones, P., Schweingruber, F. and Osborn, T. (1998) Influence of volcanic eruptions on Northern Hemisphere summer temperature over the past 600 years, *Nature* 393, 450–455.

Buentgen ,U., Myglan, V.S., Ljungqvist, C.F., McCormick, M., Di Cosmo, N., Sigl, M., Jungclaus, J., Wagner, S., Krusic, P.J., Esper, J., Kaplan, J.O., de Vaan, M.A.C., Luterbacher, J., Wacker, L., Tegel, W. and Kirdyanov, A.V. (2016) Cooling and societal change during the Late Antique Little Ice Age from 536 to around 660 AD. *Nature Geoscience* 9, 231-236. doi: 10.1038/ngeo2652.

Campos, C. and Horn, M. (2018) The Physical System of the Arctic Ocean and Subarctic Seas in a Changing Climate. In: Jungblut S., Liebich V., Bode M. (eds) YOUMARES 8 – Oceans Across Boundaries: Learning from each other. Springer, Cham, doi:10.1007/978-3-319-93284-2_3

Cook, E.R. (1985) *A time series analysis approach to Tree ring standardization.* The University of Arizona. Arizona.

Cook, E.R. and Kairiukstis, L.A. (1990) *Methods of Dendrochronology*. Applications in the Environmental Sciences. Kluwer Academic Press, Dordrecht.

Cook, E.R., Meko, D.M., Stahle, D.W. and Cleaveland, M.K. (1999) Drought Reconstruction for the Continental United States. *Journal of Climate* 12, 1145-1162.

Cook, E.R. and Krusic, P.J. 2006. *Program ARSTAN*. A Tree-Ring Standardization Program Based on Detrending and Autoregressive Time Series Modeling, with Interactive Graphics. Tree-Ring Laboratory. Lamont Doherty Earth Observatory of Columbia University. Palisades. New York.

Chen, F., Yuan, Y., Zhang, T. and Shang, H. (2015) Precipitation reconstruction for the northwestern Chinese Altay since 1760 indicates the drought signals of northern part of Inner Asia. *International Journal of Biometeorology*. doi: 10.1007/s00484-015-1043-5.

Chen, F., Yuan,, Y.J., Wei, W.S. and Zhang, T.W. (2014) Precipitation reconstruction for the southern Altay Mountains (China) from tree rings of Siberian spruce, reveals recent wetting trend. *Dendrochronologia* 32, 266-272.

Chen, F., Yuan, Y.J., Chen, F.H., Wei, W.S., Yu, S.L., Chen, X.J., Fan, Z.A., Zhang, R.B., Zhang, T.W., Shang, H.M. and Qin, L. (2013) A 426-year drought history for Western Tian Shan, Central Asia inferred from tree-rings and its linkages to the North Atlantic and Indo-West Pacific Oceans. *The Holocene* 23, 1095-1104.

Chen, F., Yuan, Y.J., Wei, W.S., Fan, Z.A., Zhang, T.W., Shanh, H.M., Zhang, R.B., Yu, S.L., Ji, C.R. and Qin, Li. (2012) Climate response of ring width and maximum latewood density of Larix sibirica in the Altay mountain reveals recent warming trend. *Annals of Forest Science*. doi:10.1007/s13595-013-0187-2.

Chen, S., Chen, W. and Wu, R. (2015) An Interdecadal Change in the Relationship between Boreal Spring Arctic Oscillation and the East Asian Summer Monsoon around

the Early 1970s. *Journal of Climate* 28, 1527-1542. doi: 10.1175/JCLI-D-14-00409.1

Crawford, T., Betts, N, and Favis-Mortlock, D. (2007). GCM grid-box choice and predictor selection associated with statistical downscaling of daily precipitation over Northern Ireland. *Climate Research* 34, 145-160. 10.3354/cr034145.

Davaa, G. (2015) Surface water regime and resources of Mongolia. Information and Research Institute of Meteorology, Hydrology and Environment. Ulaanbaatar. ADMON printing. ISBN 978-99973-0-767-5

Dagvadorj, D., Batjargal, Z. and Natsagdorj, L. (2014) *Mongolia second assessment report on climate change - 2014*. Ministry of Environment and Green Development of Mongolia. Ulaanbaatar, Mongolia.

Dashtseren, A., Ishikawa, M., Iijima, Y. and Jambaljav, Y. (2014) Temperature regimes of the active layer and seasonally frozen ground under a forest-steppe mosaic, Mongolia. Permafrost and Periglacial Processes 25:295–306.doi:10.1002/ppp.1824.

Davi, N.K., Jacoby, G.C., D' Arrigo R., Baatarbileg, N., Li, J. and Curtis, A.E. (2009) A tree-ring-based drought index reconstruction for far-western Mongolia: 1565-2004, *International Journal of Climatology* 29, 1508-1514. doi:10.1002/joc.1798.

Davi, N.K., D' Arrigo, R., Jacoby, G.C., Cook, E.R., Anchukaitis, K.J., Nachin, B., Rao, M.P. and Leland, C. (2015) A long-term context (931-2005 C.E.) for rapid warming over Central Asia. *Quaternary Science Reviews* 121, 89-97. doi:10.1016/j.quascirev.2015.05.020.

Demirel, M.C., Booij, M.J. and Hoekstra, A.Y., 2013. Impacts of climate change on the seasonality of low flows in 134 catchments in the River Rhine basin using an ensemble of bias-corrected regional climate simulations. *Hydrology and Earth System Sciences*, 17(10), pp.4241-4257.

Dobor, L., Barcza, Z., Hlásny, T., Havasi, Á., Horváth, F., Ittzés, P. and Bartholy, J., 2015. Bridging the gap between climate models and impact studies: The FORESEE Database. *Geoscience data journal,* 2(1), pp.1-11.

Dulamsuren, Ch. and Khishigjargal, M. (2012) Opposing growth trends created by external disturbance in larch forests of the Mongolian Altai. *Exploration into the Biological Resources of Mongolia (Halle/Saale) 12*, 353–363.

Eichler, A., Olivier, S., Henderson, K., Laube, A., Beer, J., Papina, T., Gäggeler, H.W. and Schwikowski, M. (2009) Temperature response in the Altai region lags solar forcing. *Geophysical Research Letters* 36, L01808, doi:10.1029/2008GL035930.

Estilow, T.W., Young, A.H. and Robinson, D.A. (2015) A long-term Northern Hemisphere snow cover extent data record for climate studies and monitoring. *Earth System Science Data* 7, 137-142, doi:10.5194/essd-7-137-2015.

Eslamian, S. (2014) Handbook of Engineering Hydrology: Environmental hydrology and water management. CRC Press. 978-1-4665-5250-0

Fan, H. and He, D. (2015) Temperature and precipitation variability and its effect on streamflow in the upstream regions of the Lancang-Mekong and Nu-Salween Rivers. Journal of Hydrometeorology 16, 2248-2263, doi: 10.1175/JHM-D-14-0238.1

Folland, C.K., Knight, J., Linderholm, H.W., Fereday, D., Ineson, S. and Hurrell, J.W. (2009) The Summer North Atlantic Oscillation: Past, present, and future. *J. Clim.*, 22, 1082– 1103, doi:10.1175/2008JCLI2459.1.

Fritts, H.C. (1966) Growth-Rings of Trees: Their correlation with climate. *Journal of Science*: 973-979. doi: 10.1126/science.154.3752.973.

Fritts, H.C. (1974) Relationships of Ring Widths in Arid-Site Conifers to Variations in Monthly Temperature and Precipitation. *Ecological Monographs* 44, 411–440. doi: 10.2307/1942448.

Fritts, H.C. (1976) *Tree rings and Climate*. Academic Press. London. 582 pp

Friedman, J.H. (1984) A variable span smoother, Tech. Rep. LCS5, Department of Statistics, Stanford University. Stanford, California.

Gao, H., Wang, J., Yang, Y., Pan, X., Ding, Y. and Duan, Z. (2021) Permafrost Hydrology of the Qinghai-Tibet Plateau: A Review of Processes and Modeling. *Front. Earth Sci*. 8:576838. doi: 10.3389/feart.2020.576838

Gao, M.N., Yang, J., Gong, D.Y. and Kim, S.J. (2014) Unstable relationship between spring Arctic Oscillation and East Asian summer monsoon. *Int. J. Climatol 34 (7),* 2522-2528

George, S.S. (2014) The global network of tree-ring widths and its applications to paleoclimatology. *Science Highlights: Annual Recorders of the Past*, PAGES Magazine 22, 16-17

Grissino-Mayer, H.D. (2001) Evaluating crossdating accuracy: A manual and tutorial for the computer program COFECHA. *Tree-Ring Research* 57 (2), 205-221.

Gruber, S., Fleiner, R., Guegan, E., Panday, P., Schmid. M.O., Stumm, D., Wester, P., Zhang, Y. and Zhao. L. (2017) Review article: Inferrinf permafrost and permafrost thaw in the mountains of the Hindu Kush Himalaya region. *The Cryosphere* 11, 81-99, doi:10.5194/tc-11-81-2017

Gong, D.Y. and Ho, C.H. (2002) The Siberian High and climate change over middle to high latitude Asia. *Theoretical and Applied Climatology* 72, 1-9.

Gong, D. Y. and Ho, C. H. (2003) Arctic Oscillation signals in the East Asian summer monsoon. *J. Geophys. Res.,* 108(D2): 4066, doi: 10.1029/2002JD002193

Grünewald, T., Bu¨hler, Y., Lehning, M. (2014) Elevation dependency of mountain snow depth. Cryosphere 8, 2381e2394. https://doi:10.5194/tc-8-2381-2014.

Hargreaves, G.H. and Samani, Z. A. (1985) Reference crop evapotranspiration from temperature. *Appl Eng Agric* 1, 96–99.

Hargreaves, G.H. and Allen, R.G. (2003) History and Evaluation of Hargreaves Evapotranspiration Equation. Journal of Irrigation and Drainage Engineering, 129, 53-63. https://doi.org/10.1061/(ASCE)0733-9437(2003)129:1(53)

Harris, I.C. and Jones, P.D. (2017) *CRU TS4.01: Climatic Research Unit (CRU) Time-Series (TS) Version 4.01 of High-Resolution Gridded Data of Month-by-month Variation in Climate (Jan. 1901- Dec. 2016)*. Centre for Environmental Data Analysis, University of East Anglia Climatic Research Unit; *04 December 2017*. doi:10.5285/58a8802721c94c66ae45c3baa4d814d0

Hartmann, D.L., Klein Tank, A.M.G., Rusticucci, M., Alexander, L.V., Brönnimann, S., Charabi, Y.A.R., Dentener, F.J., Dlugokencky, E.J., Easterling, D.R., Kaplan, A., Soden, B.J., Thorne, P.W., Wild, M. and Zhai, P. (2013). Observations: Atmosphere and surface. In *Climate Change 2013 the Physical Science Basis: Working Group I Contribution to the Fifth Assessment Report of the Intergovernmental Panel on Climate Change* (pp. 159-254). Cambridge University Press. https://doi.org/10.1017/CBO9781107415324.008

He, S., Gao, Y., Li, F., Wang, H. and He, Y. (2017) Impact of Arctic Oscillation on the East asian climate: A review. *Earth Science Reviews* 164, 48-62

Heerema, K (2013) Hydrological modeling of a Mongolian river basin under current and changed climate conditions using permafrost conceptualizations. Master thesis, University of Twente

Huang, B., Thorne, P.W., Banzon, V.F., Boyer, T., Chepurin, G., Lawrimore, J.H., Menne, M.J., Smith, T.M., Vose, R.S. and Zhang, H.M. (2017) Extended Reconstructed Sea Surface Temperatures Version 5 (ERSSTv5): Upgrades, Validations, and Intercomparisons. *Journal of Climate,* doi.org/10.1175/JCLI-D-16-0836.1

Huang, H., Han, Y., Cao, M., Song, J., Xiao, H., Cheng, W. (2015) Spatiotemporal Characteristics of Evapotranspiration Paradox and Impact Factors in China in the Period of 1960–2013. *Advances in Meteorology*, https://doi.org/10.1155/2015/519207

Hurrell, J.W. (1995) Decadal trends in the North Atlantic Oscillation: Regional temperatures and precipitation. *Science* 269, 676

Iwao, K. and Takahashi, M. (2006) Interannual change in summer time precipitation over northeast Asia. *Geophysical Research Letter* 33, L16703. doi:10.1029/2006/GL027119

IPCC, 2013: Summary for Policymakers. In: Climate Change 2013: The Physical Science Basis. Contribution of Working Group I to the Fifth Assessment Report of the Intergovernmental Panel on Climate Change [Stocker, T.F., D. Qin, G.-K. Plattner, M. Tignor, S.K. Allen, J. Boschung, A. Nauels, Y. Xia, V. Bex and P.M. Midgley (eds.)]. Cambridge University Press, Cambridge, United Kingdom and New York, NY, USA

IRIMHE (2021) http://119.40.97.103/climateservice/index.php?menuitem=2&product=49 (accessed in January 2022)

Jambaljav. Ya (2017) Changes in Permafrost of Mongolia. Ulaanbaatar. ISBN: 978-99962-1-035-8

Jeong, J.H., Ou, T., Linderholm, H.W., Kim, B.M., Kim, S.J., Kug, J.S. and Chen, D. (2011) Recent recovery of the Siberian High intensity, *Journal of Geophysical Research* 116, D23102. doi:10.1029/2011JD015904

Ji, X., Li, Yu., Luo, X., He, D., Guo, R., Wang, J., Bai, Y., Yue, C and Liu, Chi (2020) Evaluation of bias correction methods for APHRODITE data to improve hydrologic simulation in a large Himalayan basin, *Atmospheric Research*, Volume 242, https://doi.org/10.1016/j.atmosres.2020.104964.

Jones, P.D., Jónsson, T. and Wheeler, D. (1997) Extension to the North Atlantic Oscillation using early instrumental pressure observations from Gibraltar and South-West Iceland. *Int. J. Climatol*. 17, 1433-1450 doi.org/10.1002/(SICI)1097-0088

Jordan, G. (2016) Water use efficiency and management of agro-pastoral landuse systems in the Mongolian -Chinese Altay. Dissertation. University of Kassel. Witzenhausen

Ju, J., Lü, J., Cao, J. and Ren, J. (2005) Possible impacts of the Arctic Oscillation on the interdecadal variation of summer monsoon rainfall in East Asia. *Advances in Atmospheric Sciences*. 22, 39-48

Juetten, T. (2015) ETo Calculation Spreadsheet according to Penman-Monteith (FAO 56), University of Bonn

Kamp, U., Krumwiede, B., McManigal, K., Pan, C., Walther, M. and Avirmed, D. (2013) The Glaciers of Mongolia. Institute of Arctic and Alpine Research (INSTAAR) Occasional Papers. 61. 48 pp

Kamp Ulrich (submitter) and Pan Caleb (analyst(s)), (2012) GLIMS Glacier Database. Boulder, CO. National Snow and Ice Data Center. http://dx.doi.org/10.7265/N5V98602

Kharuk, V.I., Im, S.T. & Soldatov, V.V. (2020) Siberian silkmoth outbreaks surpassed geoclimatic barrier in Siberian Mountains. J. Mt. Sci. 17, 1891–1900. https://doi.org/10.1007/s11629-020-5989-3

Khalzan, P., Sakai, A. and Fujita, K. (2022) Mass Balance of Four Mongolian Glaciers: In-situ Measurements, Long-Term Reconstruction and Sensitivity Analysis. *Front. Earth Sci.* 9:785306. doi: 10.3389/feart.2021.785306

Khan, A.J. and Koch, M. (2018) Correction and Informed Regionalization of Precipitation Data in a High Mountainous Region (Upper Indus Basin) and Its Effect on SWAT-Modelled Discharge" Water 10, no. 11: 1557. https://doi.org/10.3390/w10111557

Kharuk, V.I., Demidko, D.A., Fedotova, E.V., Dvinskaya, M.L. and Budnik, U.A. (2016) Spatial and temporal dynamics of Siberian silk moth large-scale outbreak in dark-needle coniferous tree stands in Altai. *Contemporary Problems of Ecology* 9, 711–720

Klinge, M., Böhner, J. and Lehmkuhl F. (2003) Climate patterns, snow- and timberlines in the Altai Mountains, Central Asia, Erdkunde, 57, 296–308

Koutsouris, A.J.; Seibert, J.; Lyon, S.W. (2017) Utilization of Global Precipitation Datasets in Data Limited Regions: A Case Study of Kilombero Valley, Tanzania. *Atmosphere, 8, 246.* https://doi.org/10.3390/atmos8120246

Kjellström, E., Boberg, F., Castro, M., Christensen, J.H., Nikulin, G., Sánchez E. (2010) Daily and monthly temperature and precipitation statistics as performance indicators for regional climate models. *Clim. Res.,* 44 (2-3), pp. 135-150

Kong, Y. and Pang, Z. (2012) Evaluating the sensitivity of glacier rivers to climate change based on hydrograph separation of discharge. *J. Hydrol.* doi:10.1016/j.jhydrol.2012.02.029

Kurzrock, F., Buerkert, A., Byambaa, O., Goenster, S., Jin, L., Ohlwein, Ch., Simmer, C. and Simon, T. (2017) Dynamical downscaling with COSMO and COSMO-CLM in the Sino-Mongolian Altai region. *Meteorol Atmos Phys* 129, 211–228 doi:10.1007/s00703-016-0487-4

Krause, P., Boyle, D. P., and Bäse, F. (2005) Comparison of different efficiency criteria for hydrological model assessment, *Adv. Geosci.*, 5, 89–97, https://doi.org/10.5194/adgeo-5-89-2005

Krumweide, S.B. (2010) Mapping glacier variation from 1990 to 2006 in the Central Mongolian Altai. Master thesis. The University of Montana, Missoula Montana

Krumwiede B.S., Kamp U., Leonard G.J., Kargel J.S., Dashtseren A., Walther M. (2014) Recent Glacier Changes in the Mongolian Altai Mountains: Case Studies from Munkhkhairkhan and Tavan Bogd. In: Kargel J., Leonard G., Bishop M., Kääb A., Raup B. (eds) Global Land Ice Measurements from Space. Springer Praxis Books. Springer, Berlin, Heidelberg. https://doi.org/10.1007/978-3-540-79818-7_22

Lenhard, W. and Lenhard, A. (2014). Hypothesis Tests for Comparing Correlations. available: https://www.psychometrica.de/correlation.html. Bibergau (Germany): Psychometrica. DOI: 10.13140/RG.2.1.2954.1367

Liljedahl, A.K, Gädeke, A., O'Neel, S., Gatesman, T.A. and Douglas, T.A. (2017) Glacierized headwater streams as aquifer recharge corridors, subarctic Alaska, *Geophys. Res. Lett* 44, 6876–6885, doi:10.1002/2017GL073834

Linderholm, H. W., T. Ou, J.-H. Jeong, C. K. Folland, D. Gong, H. Liu, Y. Liu, and D. Chen (2011), Interannual teleconnections between the summer North Atlantic Oscillation and the East Asian summer monsoon,*J. Geophys. Res.,*116, D13107, doi:10.1029/2010JD015235

Lindsey, R. (2016) Global impacts of El nino and La nina. Climate news. NOAA. www.climate.gov

Loader, N.J., Helle, G., Los, S.O., Lehmkuhl, F. and Schleser, G.H. (2010) Twentieth-century summer temperature variability in the southern Altai Mountains: A carbon and oxygen isotope study of tree rings. *The Holocene* 20 (7), 1149-1156. doi:10.1177/0959683610369507

Lu, B., Li, H., Wu, J., Zhang, T., Liu, J., Liu, B., Chen, Y. and Baishan, J. (2019) Impact of El Niño and Southern Oscillation on the summer precipitation over Northwest China. Atmos Sci Lett. doi.org/10.1002/asl.928

Luo, M., Liu, T., Meng, F., Duan, Y., Bao, A., Xing, W. and Frankl, A. (2019) Identifying climate change impacts on water resources in Xinjiang, China, *Science of The Total Environment,* Volume 676, p613-626, https://doi.org/10.1016/j.scitotenv.2019.04.297

Ma, Z., Kang, Sh., Zhang, L., Tong, L. and Su, X. (2008) Analysis of impacts of climate variability and human activity on streamflow for a river basin in arid region of northwest China*. Journal of Hydrology* 352, 239-249

Ma, Y., Huang, Y., Chen, X., Li, Y. and Bao, A. (2013) Modelling Snowmelt Runoff under Climate Change Scenarios in an Ungauged Mountainous Watershed, Northwest China, Mathematical Problems in Engineering. Volume 2013, https://doi.org/10.1155/2013/808565

Maraun, D., Wetterhall, F., Ireson, A.M., Chandler, R.E., Kendon, E.J., Widmann, M., Brienen, S., Rust, H.W., Sauter, T., Themeßl, M. and Venema, V.K.C., 2010. Precipitation downscaling under climate change: Recent developments to bridge the gap between dynamical models and the end user. *Reviews of geophysics,* 48(3)

Mariotti, A. (2007) How ENSO impacts precipitation in southwest central Asia, *Geophys. Res. Lett*., 34, L16706, doi:10.1029/2007GL030078

Middleton, N., Rueff, H., Sternberg, T., Batbuyan, B., and Thomas, D. (2015) Explaining spatial variations in climate hazard impacts in western Mongolia, *Landscape Ecol*, 30:91-107, DOI 10.1007/s10980-014-0091-2

Mirzabaev, A., L.C. Stringer, T.A. Benjaminsen, P. Gonzalez, R. Harris, M. Jafari, N. Stevens, C.M. Tirado, and S. Zakieldeen, 2022: *Cross-Chapter Paper 3: Deserts, Semi-Arid Areas and Desertification. In: Climate Change 2022: Impacts, Adaptation, and Vulnerability. Contribution of Working Group II to the Sixth Assessment Report of the Intergovernmental Panel on Climate Change* [H.-O. Pörtner, D.C. Roberts, M. Tignor, E.S. Poloczanska, K. Mintenbeck, A. Alegría, M. Craig, S. Langsdorf, S. Löschke, V. Möller, A. Okem, B. Rama (eds.)]. Cambridge University Press. In Press

Moges, E., Demissie, Y., Larsen, L., Yassin, F. (2021) Review: Sources of Hydrological Model Uncertainties and Advances in Their Analysis. *Water*, 13, 28. https://doi.org/10.3390/w13010028

Moriasi, D.N., Arnold, J.G., Van Liew, M.W., Bingner, R.L., Harmel, R.D. and Veith, T.L. (2007) Model Evaluation Guidelines for Systematic Quantification of Accuracy in Watershed Simulations. *American Society of Agricultural and Biological Engineers*, 50, 885-900

Munkhbat, B. (2010) Snow cover variability of Mongolia, Master thesis. National University of Mongolia

Narozhniy, Y.K. and Zemtsov, V.A. (2011) Current state of the Altai glaciers (Russia) and trends over the period of instrumental observation 1952-2008. *Ambio* 40, 575-588. Doi 10.1001/s13280-011-0166-0

Nandintsetseg, B. and Shinoda, M. (2013) Assessment of drought frequency, duration, and severity and its impact on pasture production in Mongolia. *Nat Hazards* 66, 995–1008. https://doi.org/10.1007/s11069-012-0527-4

Pan, X. D., Zhang, L., & Huang, C. L. (2020). Future climate projection in Northwest China with RegCM4.6. *Earth and Space Science*, 7, https://doi.org/10.1029/2019EA000819

Pan, C.G., Kamp, U., Munkhjargal, M., Halvorson, S.J., Dashtseren, A. and Walther, M. (2019) An Estimated Contribution of Glacier Runoff to Mongolia's Upper Khovd River Basin in the Altai Mountains. *Mountain Research and Development* 39(2), https://doi.org/10.1659/MRD-JOURNAL-D-18-00059.1

Pan, C.G., Pope, A., Kamp, U., Dashtseren, A., Walther, M. and Syromyatina, M.V. (2018) Glacier recession in the Altai Mountains of Mongolia in 1990–2016, Geografiska Annaler: Series A, Physical Geography, 100:2, 185-203, doi: 10.1080/04353676.2017.1407560

PAGES 2k Consortium. (2013) Continental-scale temperature variability during the past two millennia. *Nature Geoscience* 6(5), 339-346. doi: 10.1038/NGEO1797

Panyushkina, I.P., Ovtchinnikov, D.V. and Adamenko, M.F. (2005) Mixed response of decadal variability in larch tree-ring chronologies from upper tree-lines of the Russian Altai. *Tree-ring research* 61 (1), 33-42

Park, C., Min, S. K., Lee, D., Cha, D. H., Suh, M. S., Kang, H. S., ... & Kwon, W. T. (2016). Evaluation of multiple regional climate models for summer climate extremes over East Asia. Climate Dynamics, 46(7), 2469-2486

Peng, L., Li, Y. and Feng, H. (2017). The best alternative for estimating reference crop evapotranspiration in different sub-regions of mainland China, Scientific reports. 7: 5458 DOI:10.1038/s41598-017-05660-y

Polyakova, E.I., Journel, A. G., Polyakov, I. V. and Bhatt, U. S. (2006). Changing relationship between the North Atlantic Oscillation and key North Atlantic climate parameters, Geophys. Res. Lett.,33, L03711, doi:10.1029/2005GL024573

Pörtner, H.-O., Roberts, D.C., Adams, H., Adelekan, I., Adler, C., Adrian, R., Aldunce, P., Ali, E., Ara Begum, R.... Ibrahim, Z. Z. (2022) Technical Summary. In: Climate Change 2022: Impacts, Adaptation, and Vulnerability. Contribution of Working Group II to the Sixth Assessment Report of the Intergovernmental Panel on Climate Change. Cambridge University Press, Cambridge, UK and New York, NY, USA, pp. 37-118, doi:10.1017/9781009325844.002

Portis, D.H., Walsh, J.E., Hamly, M.E. and Lamb, P.J. (2001). Seasonality of the North Atlantic Oscillation. *J. Clim.*, 14, 2069– 2078

Pinto, J.G. and Raible, C.C. (2012) Past and recent changes in the North Atlantic oscillation. *Clim Change* 3, 79-90. doi:10.1001/wcc.150

Putnam, A.E, Putnam, D.E., Andreu-Hayles, L., Cook, E.R., Palmer, J.G., Clark, E.H., Wang, Ch., Chen, F…Broecker, W.S. (2016) Little Ice Age wetting of Interior Asian deserts and the rise of the Mongol Empire. *Quaternary Science Reviews* 131, 33-50. doi:10.1016/j.quascirev.2015.10.033

Purevdagva, Kh. (2014). Snow measurement of Bulgan catchment, the southern Altai mountains. Field survey report of WATERCOPE project. Ulaanbaatar

Radojevic M (2014) The ensemble of daily predictor variables developed from the CanESM2 CMIP5 experiments. Canadian Centre for Climate Modelling and Analysis (CCCma), Canada

Reynolds, J.E., Halldin, S., Xu, C.Y., Seibert, J. and Kauffeldt, A. (2017) Sub-daily runoff predictions using parameters calibrated on the basis of data with a daily temporal resolution, Journal of Hydrology, Volume 550, 399-411, https://doi.org/10.1016/j.jhydrol.2017.05.012

Robock, A. (1984) Climate model simulations of the effects of the El Chichon eruption. *Geofisica Internacional* 23, 403-414

Robock, A. (2002) Volcanic Eruption, El Chichon. *Encyclopedia of Global Environmental Change:* Volume 1: 736. ISBN 0-471-97796-9

Rohman, J. (2014) Global climate influencer Arctic Oscillation. TransRe. New York

Rojas, O., Li, Ya. and Cumani, R. (2014) Understanding the drought impact of El Nino on the global agricultural areas: An assessment using FAO's Agricultural Stress Index. Food and Agriculture Organization of the United Nations, Rome, ISBN 978-92-5-108671-1

Salmi, T., Määttä, A., Anttila, Pia., Ruoho-Airola, T. and Amnell, T. (2002) Detecting trends of annual values of atmospheric pollutants by the Mann-Kendall test and Sen's slope estimates- the Excel template application MAKESENS. Air Quality: 31, Air Quality Research. Finnish Meteorological Institute. Helsinki, Finland. ISBN 951-697-563-1

Schwikowski, M., Eichler, A., Kalugin, I., Ovtchinnikov, D. and Papina, T. (2009) Past climate variability in the Altai. *Pages News* 17 (1), 44-45

Shen, Y.-J., Shen, Y., Fink, M., Kralisch, S., & Brenning, A. (2018). Unraveling the hydrology of the glacierized Kaidu Basin by integrating multisource data in the Tianshan Mountains, Northwestern China. Water Resources Research, 54, 557–580. Doi:10.1002/2017WR021806

Sheppard, P.R. (2010) Dendroclimatology: extracting climate from trees. *WIREs Climate change* 1, 343-352. DOI: 10.1002/wcc.42

Shi, F., Ge, Q., Yang, B., Li, J., Yang, F., Ljungqvist, F.Ch., Solomina, O., Nakatsuka, T., Wang, N., Zhao, S., Xu, Ch., Fang, K., Sano, M., Chu, G., Fan, Z., Gaire, N.P. and Zafar, M.U. (2015) A multi-proxy reconstruction of spatial and temporal variations in Asian summer temperatures over the last millennium. *Climate change* 131 (4), 663. doi:10.1007/s10584-015-1413-3

Shi, Y., Shen, Y., Kang, E., Li, D. and Ding, Y. (2006) Recent and future climate change in northwest China. *Climate change* 80, 379. doi:10.1007/s10584-006-9121-7

Seibert, J (1997) Estimation of Parameter uncertainty in the HBV model, *Nordic Hydrology* 28 (4/5), 247-262

Seibert, J. (2000) Multi-criteria calibration of a conceptual runoff model using a genetic algorithm, *Hydrol. Earth Syst. Sci.,* 4, 215–224, doi:10.5194/hess-4-215-2000

Seibert, J. (2005) HBV light version 2. User's manual. Stockholm University

Seibert, J and Vis, M.J.P. (2012) Teaching hydrological modeling with a user-friendly catchment-runoff-model software package. *Hydrol. Earth Syst. Sci* 16, 3315-3325, doi:10.5194/hess-16-3315-2012

Speer, J.H. (2010) Fundamentals of tree-ring research. Tucson, University of Arizona Press

Stockdale, T., Balmaseda, M. and Ferranti, L. (2017) The 2015/2016 El Nino and beyond. European Centre for Medium-Range Weather Forecas. www.ecmwf.int

Sun, J. and Wang, H. (2012) Changes of the connection between the summer North Atlantic Oscillation and the East Asian summer rainfall. *Journal of Geophysical Research* 117, doi: 10.1029/2012JD017482

Sun, J., Wang, H. and Yuan, W. (2008) Decadal variations of the relationship between the summer North Atlantic Oscillation and middle East Asian air temperature. *Journal of Geophysical Research* 113, doi:10.1029/2007JD009626

Taylor, K. E. (2001). Summarizing multiple aspects of model performance in a single diagram. Journal of Geophysical Research: Atmospheres, 106(D7), 7183–7192. https://doi.org/10.1029/2000JD900719

Thompson, D.W.J. and Wallace, J.M. (2000) Annular modes in the extratropical circulation. Part I: Month-to-month variability, J. Clim., 13, 1000–1016, doi:10.1175/1520-0442(2000)013<1000:AMITEC>2.0.CO;2

Trenberth, K.E., and. Paolino, D. A, (1980) The Northern Hemisphere sea level pressure data set: Trends, errors and discontinuities. Mon. Wea. Rev., 108, 855–872

Trenberth, Kevin & National Center for Atmospheric Research Staff (Eds). Last modified 21 Jan 2020. "The Climate Data Guide: Nino SST Indices (Nino 1+2, 3, 3.4, 4; ONI and TNI)." Retrieved from https://climatedataguide.ucar.edu/climate-data/nino-sst-indices-nino-12-3-34-4-oni-and-tni

Teutschbein, C.and Seibert, J. (2010) Regional climate models for hydrological impact studies at the catchment scale: a review of recent modeling strategies. Geography Compass 4(7), 834-860. https://doi.org/10.1111/j.1749-8198.2010.00357.x

Teutschbein, C., Wetterhall, F. and Seibert, J. (2011) Evaluation of different downscaling techniques for hydrological climate-change impact studies at the catchment scale. Clim Dyn 37, 2087–2105 https://doi.org/10.1007/s00382-010-0979-8

Teutschbein, C. and Seibert, J. (2012) Bias correction of regional climate model simulations for hydrological climate-change impact studies: Review and evaluation of different methods. Journal of Hydrology 456: 12-29

Obu, J., Westermann, S., Kääb, A., and Bartsch, A. (2018) Ground Temperature Map, 2000-2016, Northern Hemisphere Permafrost. Alfred Wegener Institute, Helmholtz Centre for Polar and Marine Research, Bremerhaven, PANGAEA, https://doi.org/10.1594/PANGAEA.888600

Obu, J., Westermann, S., Bartsch, A., Berdnikov, N., Christiansen, H. H., Dashtseren, A., Delaloy, R., Elberling, B., Etzelmüller, B., Kholodov, A. et al. (2019) Northern Hemispherepermafrost map based on TTOP modelling for 2000–2016 at 1km2 scale. Earth-Science Reviews 193:299–316. doi:10.1016/j.earscirev.2019.04.023

Odgarav, J and Munkhbat, B (2012) Estimation of snow cover change in the Bulgan catchment using satellite data, Scientific booklet of the Institute of Hydrology and Meterology №33

Osborn, T. (2006) Recent variations in the winter North Atlantic Oscillation. *Weather* 61, 353-355

Osborn, T. (2017) North Atlantic Oscillation Index. Climatic Research Unit, University of East Anglia. https://crudata.uea.ac.uk/cru/data/nao/viz.htm (accessed in Janruay 2020)

Ogi, M., Yamazaki, K. and Tachibana, Y. (2004) The summertime annular mode in the Northern Hemisphere and its linkage to the winter mode *J. Geophys. Res*. 109, D20114

Oh, S.-G., Park, J.-H., Lee S.-H., and Suh M.-S. (2014) Assessment of the RegCM4 over East Asia and future precipitation change adapted to the RCP scenarios,J. Geophys. Res. Atmos., 119, 2913–2927, doi:10.1002/2013JD020693

Umbanhowar, C.E., Shinneman, A.L.C., Tserenkhand, G., Hammon, E.R., Lor, P. and Nail, K. (2009) Regional fire historu based on charcoal analysis of sediments from nine lakes in westerm Mongolia. *The Holocene* 19 (4), 611-624

Urhausen, S. (2012) Recent and future climate conditions and their impact on viticulture at the Upper Moselle region. Dissertation. University of Bonn

Visbeck, M.H., Hurrel, J.W., Polvani, L. and Cullen, H.M. (2001) The North Atlantic Ocsillation: past, present, and future. PNAS 98:12876-12877

Wang, K., Zhang, T. and Yang, D (2021). Permafrost dynamics and their hydrologic impacts over the Russian Arctic drainage basin, Advances in Climate Change Research, Volume 12, Issue 4, 2021, pages 482-498, ISSN 1674-9278, https://doi.org/10.1016/j.accre.2021.03.014

Wang, S. (2019). Freezing temperature controls winter water discharge for cold region watershed. *Water Resources Research*, Volume 55, 12, 10493-1047, https://doi.org/10.1029/2019WR026030

Wang, R., Cheng, Q., Liu, L., Yan, C., and Huang, G. (2019). Multi-model projections of climate change in different RCP scenarios in an arid inland region, Northwest China. *Water*, 11(2), 347

Wang, X., Chen, R., Han, Ch., Yang, Y., Lui, J., Lui, Zh. and Song, Ya. (2019) Changes in river discharge in typical mountain permafrost, northern China. *Quaternary International* 519, 32-41 https://doi.org/10.1016/j.quaint.2018.11.010

Wang, X., Chen, R. and Yang, Y. (2017) Effect of permafrost degradation on hydrological regime in the source regions of the Yangtze and Yellow Rivers, China. *Water* 9, doi:10.3390/w9110897

Wang, H., Chen, F., Yuan, Y., Yu, S., Shang, H. and Zhang, T. (2013) Temperature signals in tree-ring width chronology of alpine treeline conifers from the Baishui River Nature Reserve China. *Terrestrial, Atmospheric and Oceanic Sciences* 24, 887-898, doi:10.3319/TAO.2013.06.18.01(A)

Weijers, S., Broekman, R. and Rozema, J. (2010) Dendrochronology in the High Arctic: July air temperatures reconstructed from annual shoot length growth of the circumarctic dwarf shrub Cassiopetetragona. *Quaternary Science Reviews* 29, 3831–3842. doi:10.1016/j.quascirev.2010.09.003

Weijers, S., Alsos, I.G., Eidesen, P.B., Broekman, R., Loonen, M.J.J.E. and Rozeman, J. (2012) No divergence in Cassiope tetragona: persistence of growth response along a latitudinal temperature gradient and under multi-year experimental warming. *Annals of Botany* 110, 653-665. doi.org/10.1093/aob/mcs123

Wei, K. and Wang, L. (2013) Reexamination of the aridity conditions in arid northwestern China for the last decade. *J. Climate,* 26, 9594–9602, doi:10.1175/JCLI-D-12-00605.1

Wei, W., Zhang, R., Wen, M., and Yang, S. (2017) Relationship between the Asian Westerly Jet Stream and Summer Rainfall over Central Asia and North Chia: Roles of the Indian Monsoon and the South Asian High. *Journal of Climate* 30, 537-552, doi: 10.1175/JCLI-D-15-0814.1

Wilby, R.L., Dawson, C.W., Murphy, C., Connor, P.O. and Hawkins, E. (2014) The statistical downscaling model-decision centric (SDSM-DC): conceptual basis and applications. *Climate Research*, 61(3), pp.259-276

Wilby, R.L and Dawson, C.W. (2007) SDSM 4.2 — A decision support tool for the assessment of regional climate change impacts. User Manual. https://sdsm.org.uk

Wilby, R.L., Dawson, C.W. and Barrow, E.M. (2002) SDSM—a decision support tool for the assessment of regional climate change impacts. *Environmental Modelling & Software,* 17(2), pp.145-157

Wilks, D. S. (2006) Statistical methods in the atmospheric sciences., Elsevier

Willkofer, F., Schmid, F.-J., Komischke, H., Korck, J., Braun, M., Ludwig R. (2018) The impact of bias correcting regional climate model results on hydrological indicators for Bavarian catchments*. J. Hydrol: Regional Studies*, 19, pp. 25-41, doi: 10.1016/j.ejrh.2018.06.010

Wigley, T.M.L., Briffa, K.R. and Jones, P.D. (1984) On the average value of correlated time series, with applications in dendroclimatology and hydrometeorology. *Journal of Applied Meteorology* 25, 201-213

The World Meteorological Organization (2022) 2021 one of the seven warmest years on record, WMO consolidated data shows. accessed 10 May 2022, https://public.wmo.int/en/media/press-release/2021-one-of-seven-warmest-years-record-wmo-consolidated-data-shows

Wu, X., Zhang, W., Li, H., Long, Y., Pan, X., and Shen, Y. Analysis of seasonal snowmelt contribution using a distributed energy balance model for a river basin in the Altai Mountains of northwestern China. *Hydrol. Proc.* 2021, 35, 14046

Xu, M., Han, H., and Kang, S. (2017). Modeling glacier mass balance and runoff in the Koxkar River Basin on the South Slope of the Tianshan Mountains, China, from 1959 to 2009. *Water*, 9(2), 100

Xu, C., Zhao, J., Deng, H., Fang, G., Tan, J., He, D., Chen, Y., Chen, Y and Fu, A. (2016). Scenario-based runoff prediction for the Kaidu River basin of the Tianshan Mountains, Northwest China. *Environmental Earth Sciences*, 75(15), 1-14

Yu, W., Wu, T., Wang, W-Z., Li, R., Wang, T., Qin, Y., Wang, W-H., and Zhu, X. (2016) Spatiotemporal changes of reference evapotranspiration in Mongolian during 1980-2006. *Advances in Meteorology*, 14, doi: 10.1155/2016/9586896

Yao, J., Tuoliewubieke, D., Chen, J., Huo, W. and Hu, W. (2019) Identification of Drought Events and Correlations with Large-Scale Ocean–Atmospheric Patterns of Variability: A Case Study in Xinjiang, China. *Atmosphere*, 10, 94, doi: 10.3390/atmos10020094

Yasutomi, N., Hamada, A., and Yatagai, A. (2011) Development of a Long-term Daily Gridded Temperature Dataset and Its Application to Rain/Snow Discrimination of Daily precipitation. Global Environmental Research 15/2011:165-172

Yatagai, A., Kamiguchi, K., Arakawa, O., Hamada, A., Yasutomi, N ad Kitoh, A. (2012) APHRODITE: Constructing a Long-Term Daily Gridded Precipitation Dataset for Asia Based on a Dense Network of Rain Gauges. American Meteorological Society., 93, 9: 1401-1415, https://doi.org/10.1175/BAMS-D-11-00122.1

Yilmaz, K. K., H. V. Gupta, and T. Wagener. (2008) A process-based diagnostic approach to model evaluation: Application to the NWS distributed hydrologic model, *Water Resour. Res.,* 44, W09417, doi:10.1029/2007WR006716

Yuan, W. and Sun, J.Q. (2009) Enhancement of the summer North Atlantic Oscillation influence on Northern Hemisphere air temperature. *Adv. Atmos. Sci.,* 26(6), 1209–1214, doi: 10.1007/s00376-009- 8148-x

Zhang, W.; Shen, Y.; Chen, A.; Wu, X. (2022) Opportunities and Challenges Arising from Rapid Cryospheric Changes in the Southern Altai Mountains, China. Appl. Sci. 12, 1406. https://doi.org/10.3390/app12031406

Zhang, T., Yuan, Y., Hu, Y., Wei, W., Shang, H., Huang, L., Zhang, R., Chen, F., Yu, Sh., Fan, Z. and Qin, L. (2015) Early summer temperature changes in the southern Altai Mountains of Central Asia during the past 300 years. *Quaternary International* 358, 68-76. doi:10.1016/j.quaint.2014.12.005

Zhang, D., Yang ,Y. and Lan, B. (2018) Climate variability in the northern and southern Altai Mountains during the past 50 years. Scientific Reports 8, 3238. doi: 10.1038/s41598-018-21637-x

Zhang, L., Dawes, W.R. and Walker, G.R. (2001) The response of mean annual evapotranspiration to vegetation changes at catchment scale. *Water Resources Research* 37, 701–708

Zhang, W., Kang S.C, Shen Y.P, He J.Q, Chen A.A. (2017) Response of snow hydrological processes to a changing climate during 1961 to 2016 in the headwater of Irtysh River Basin, Chinese Altai Mountains. *Journal of Mountain Science 14(11)*. https://doi.org/10.1007/s11629-017-4556-z

Zhang, Y. E., Hiroyuki, O., Tetsuo, K., Hideyuki, Kadota. and Tsutomu, H. Y. (2016) Projections of glacier change in the Altai Mountains under twenty-first century climate scenarios. *Climate Dynamics.* 47. 2935-2953. 10.1007/s00382-016-3006-x

Zhang, Y., Ohata T. , Yang D. , and Davaa G. (2004) Bias correction of daily precipitation measurements for Mongolia. Hydrol. Processes, 18, 2991–3005, doi:10.1002/hyp.5745.

Zhao, Y., Wang, M., Huang, A., Li, H., Huo, W. and Yang, Q. (2014) Relationships between the West Asian subtropical westerly jet and summer precipitation in northern Xinjiang. *Theoretical and Applied Climatology* 116, 403-411. Doi 10.1007/s00704-013-0948-3

Zhong, X-Y., Zhang, H.S., Xiao, X-X., Wang, Sh-F., Hu, Y-T., Wang, H-J., Zheng, L., Zhang, W., Xu, M., and Wang, J. (2021) Impacts of landscape and climatic factors on snow cover in the Altai Mountains, China, *Advances in Climate Change Research,* 12 (1), 95-107, ISSN 1674-9278, https://doi.org/10.1016/j.accre.2021.01.005

Zorigt, M., Kwadijk, J., Van Beek, E. and Kenner S. (2016) Estimating thawing depths and mean annual ground temperatures in the Khuvsgul region of Mongolia. *Environ Earth Sci* 75, 897. https://doi.org/10.1007/s12665-016-5687-1

Zorigt, M., Myagmar, Kh., Orkhonselenge, A., Van Beek, E., Kwadijk, J., Tsogtbayar, J., Jambaljav, Ya. and Dechinlkhundev, D. (2020). Modeling permafrost distribution over the river basins of Mongolia using remote sensing and analytical approaches. Environmental Earth Sciences. 79. 10.1007/s12665-020-09055-7

Zuo, J.Q., Li, W.J., Ren, H.L. and Chen, L.J. (2012) Change of the Relationship Between the Spring NAO and East Asian Summer Monsoon and Its Possible Mechanism. *Chinese Journal of Geophysics*. 55. 23-34. 10.1002/cjg2.1697

ANNEX

A. Lapse rates of temperature, precipitation and evapotranspiration observed at climate stations

In Bulgan river catchment, WATERCOPE project set up seven climate stations at heights ranging from 1133 m at state border to 2960 m on top of mountain in different periods from 2009 to 2013. Over the common period of 2013, precipitation and temperature records of four WATERCOPE stations and two official Duchinjil and Baitag climate stations are used for calculating lapse rates of seasonal and annual temperature and precipitation with change in elevation by 100 m in the southern Altai Mountain by the linear regression.

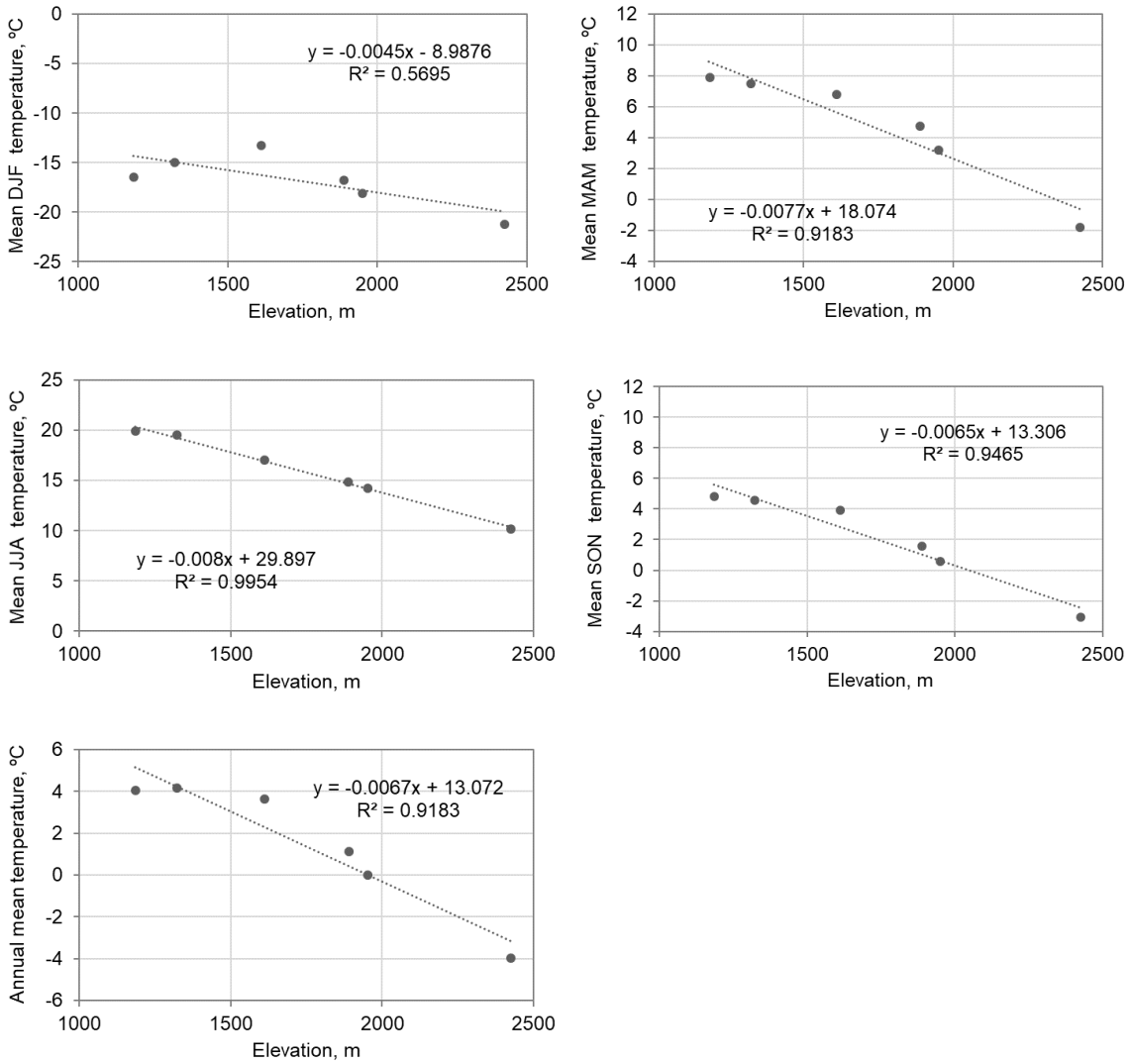

Figure A.1: Lapse rate of seasonal and annual air temperatures in the southern Altai Mountains

It is found that lapse rates of temperatures with elevation for winter, spring, summer and autumn in 2013 are -0.45ºC, -0.77ºC, -0.8ºC and -0.65ºC in 100 m, respectively. For summer and autumn, lapse rates of precipitation with elevation are identified as 3% and 4% in 100m, respectively whereas no lapse rates are found for precipitation measurement in spring and

winter, might be caused by falling small amount of precipitation in solid form. Along main valley, change of annual precipitation is 69mm/km. However, it is revealed during the snow field survey of WATERCOPE project in February 2014 that lapse rate of snow depth with elevation is 6 mm per 100 m in the southern Altai mountains (Purevdagva, 2014).

For lapse rate of precipitation, we focused on only stations along main valley of Bulgan catchment from south to north, but excluded Turgen station in tributary valley from west to east and Tsunkhel station on top of the mountain of the tributary valley.

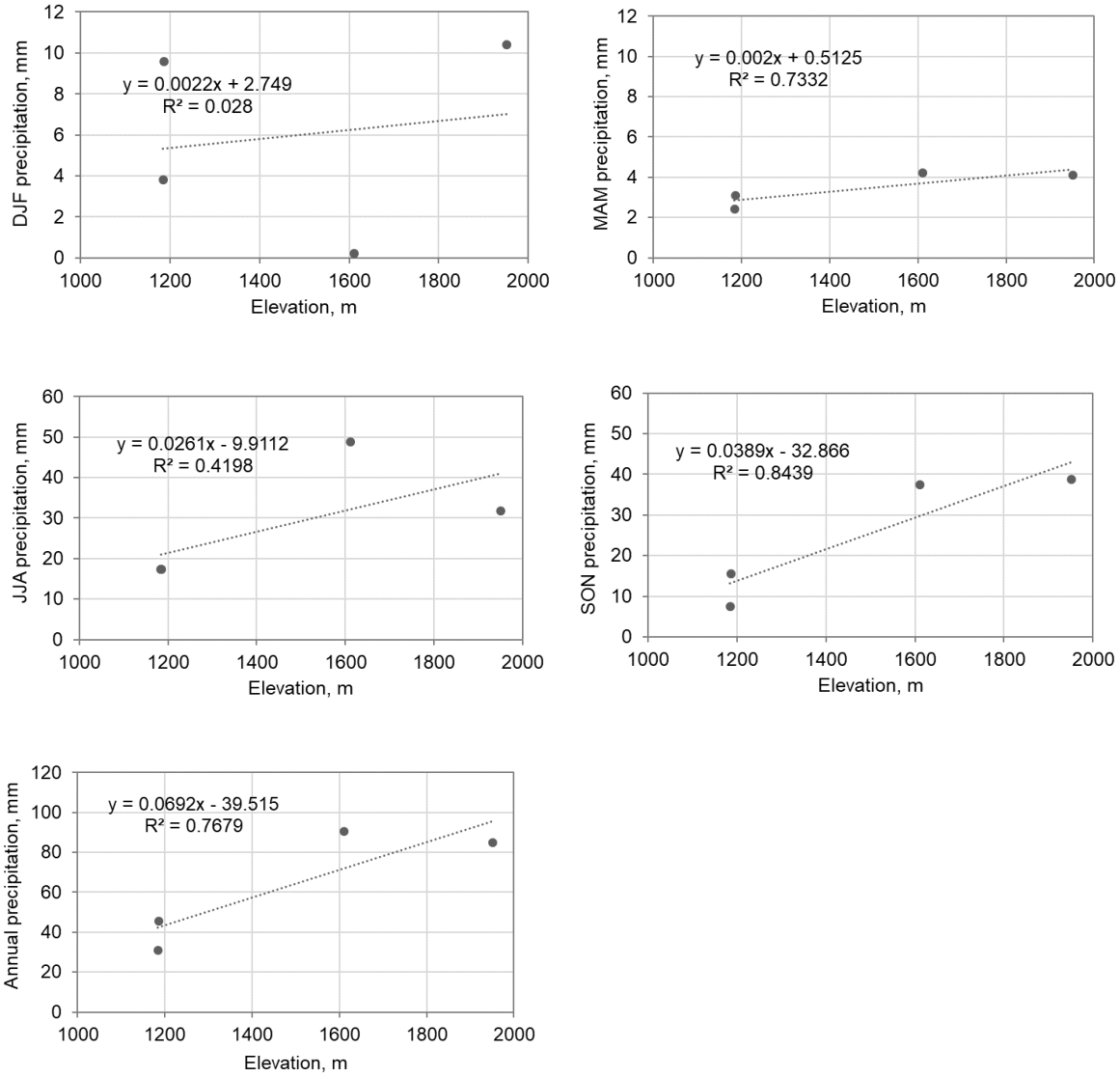

Figure A.2: Lapse rate of seasonal and annual precipitation in the southern Altai Mountains

Annual lapse rates of temperature and precipitation with elevation are defined as -0.67ºC and 7% in 100 m, respectively. We used annual lapse rates of precipitation and air temperature for areal mean climate of the catchment area for hydrological simulations.

Using ET_0 estimates of five official climate stations at different latitude and elevations in and nearby the Bulgan catchment, we found that annual lapse rates of ET_0 with elevation and

latitude are -9.9 mm (2.5%) per 100m and -112 mm (13%) per degree in the southern Altai Mountains, respectively. Also, the lapse rate of daily ET_0 with elevation is -0.003 mm (3%) per 100m.

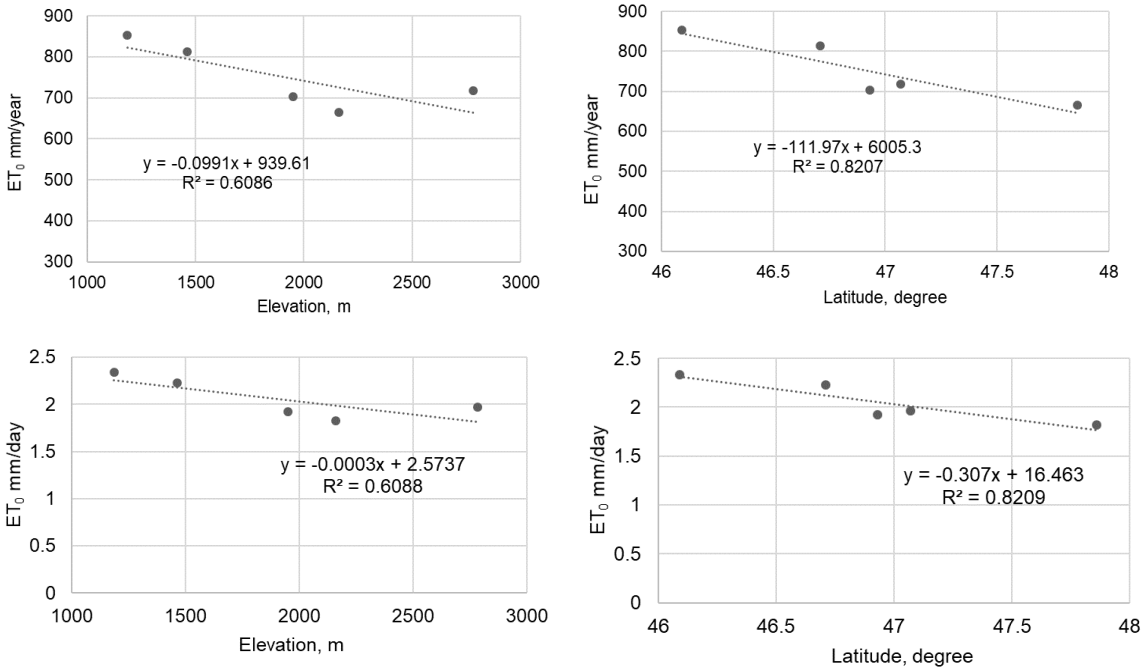

Figure A.3: Lapse rate of annual and daily evapotranspiration changes with elevation (a, c) and latitude (b, d) in the southern Altai Mountains

B. Lapse rates of temperature, precipitation and evapotranspiration of APHRODITE dataset

Over the recent period of 1993-2002, lapse rates of gridded temperature, precipitation and evapotranspiration of APHRODITE dataset over the Bulgan catchment are estimated on seasonal and annual scales (Figures B.1-3).

On annual and seasonal scales, precipitation (r=0.96-98, p<0.01) and temperature (r=0.98-99, p<0.0001) of grids (46.1º-47.3ºN) along the latitude of the catchment are more statistically significantly changed with elevations than precipitation (r= -0.12 and -0.45) and temperature (r=0.87-0.98, p=0.05-0.001) of grids (90.8ºE -91.8ºE) along the longitude of the catchment.

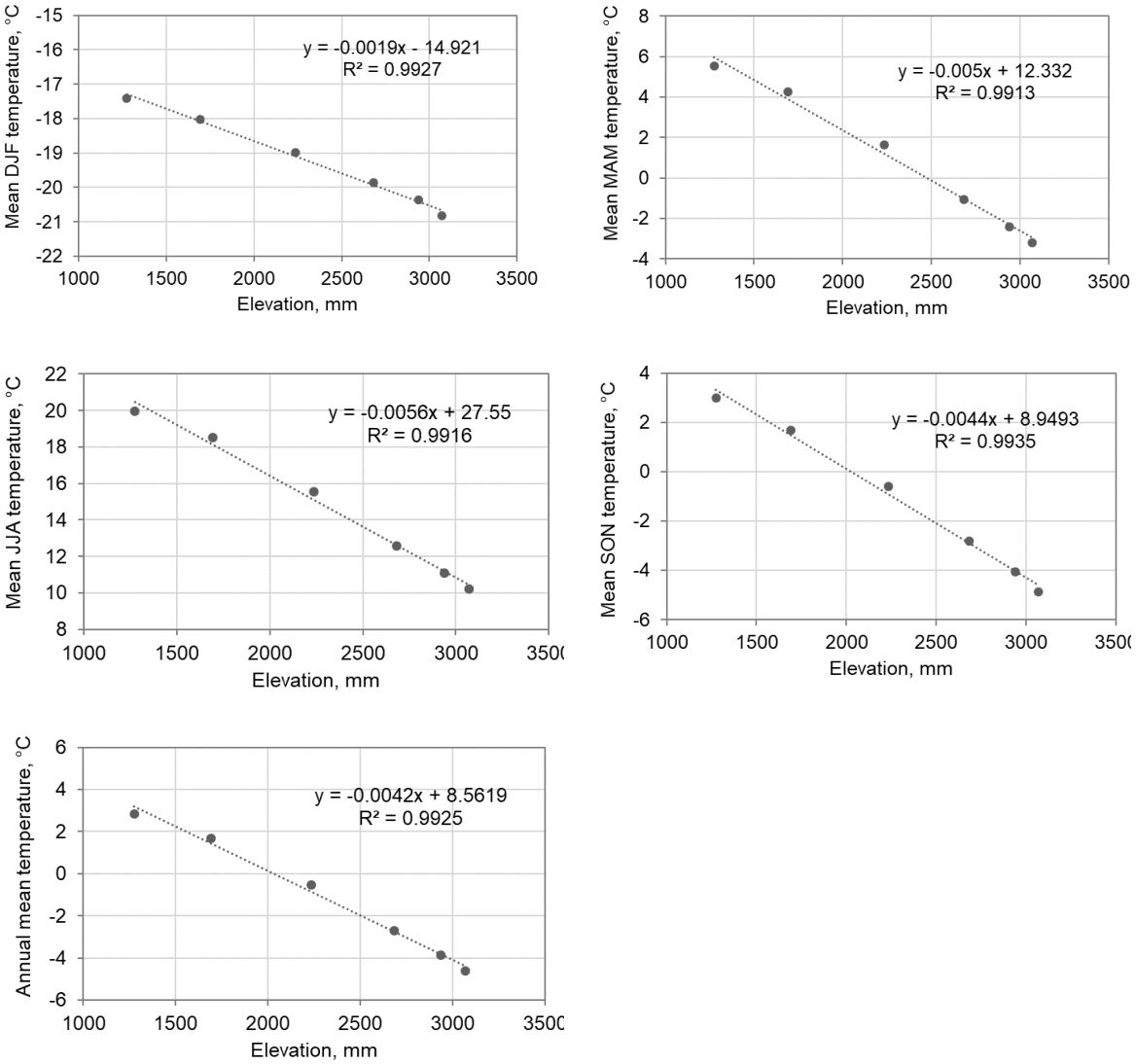

Figure B.1: Lapse rates of seasonal and annual air temperatures of APHRODITE dataset in the southern Altai Mountains

Along latitude of the catchment, changes of winter, spring, summer and autumn temperatures with elevation are -0.19ºC, -0.5ºC, -0.56ºC and -0.44ºC per 100 m, respectively (Figure B.1).

As shown in Figure B.2, lapse rates of precipitation sum during winter and summer are identified as -1.7 % ($p<0.01$) and 5% ($p<0.001$) and per 100m, respectively. But no significant lapse rates are found for spring and autumn precipitation sums.

Annual lapse rates of temperature and precipitation are defined as -0.42ºC and 2.3% per 100 m on average, respectively.

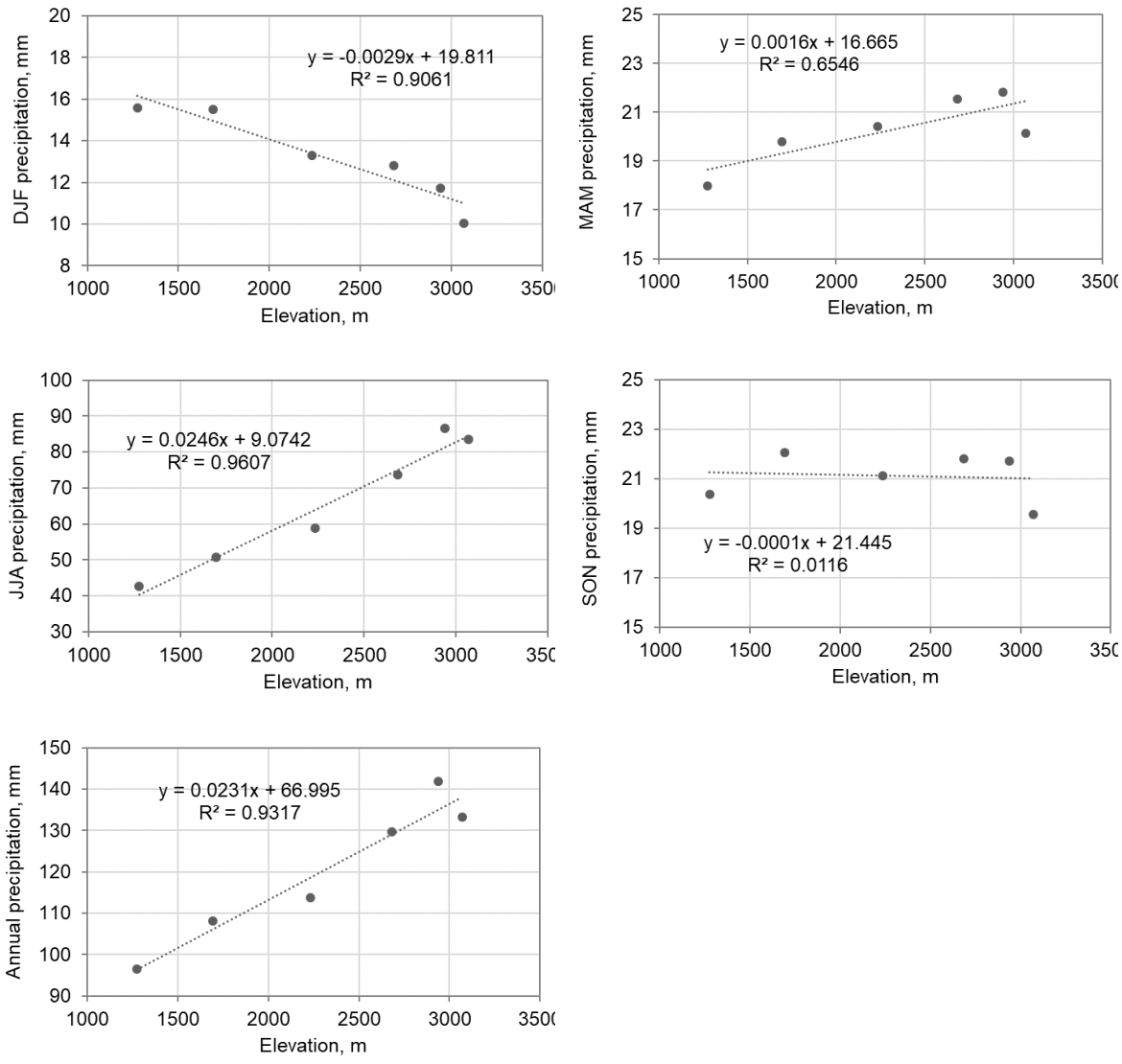

Figure B.2: Lapse rates of seasonal and annual precipitation of APHRODITE dataset in the southern Altai Mountains

Changes of the evapotranspiration for winter, spring, summer and autumn with elevation along latitude of the catchment are -4%, -2.3%, -1.6% and -2.3%, per 100 m, respectively (Figure B.3). Daily and annual lapse rates of the evapotranspiration per 100 m are found as -0.04mm (-2%) and -14.6mm (-2%), respectively.

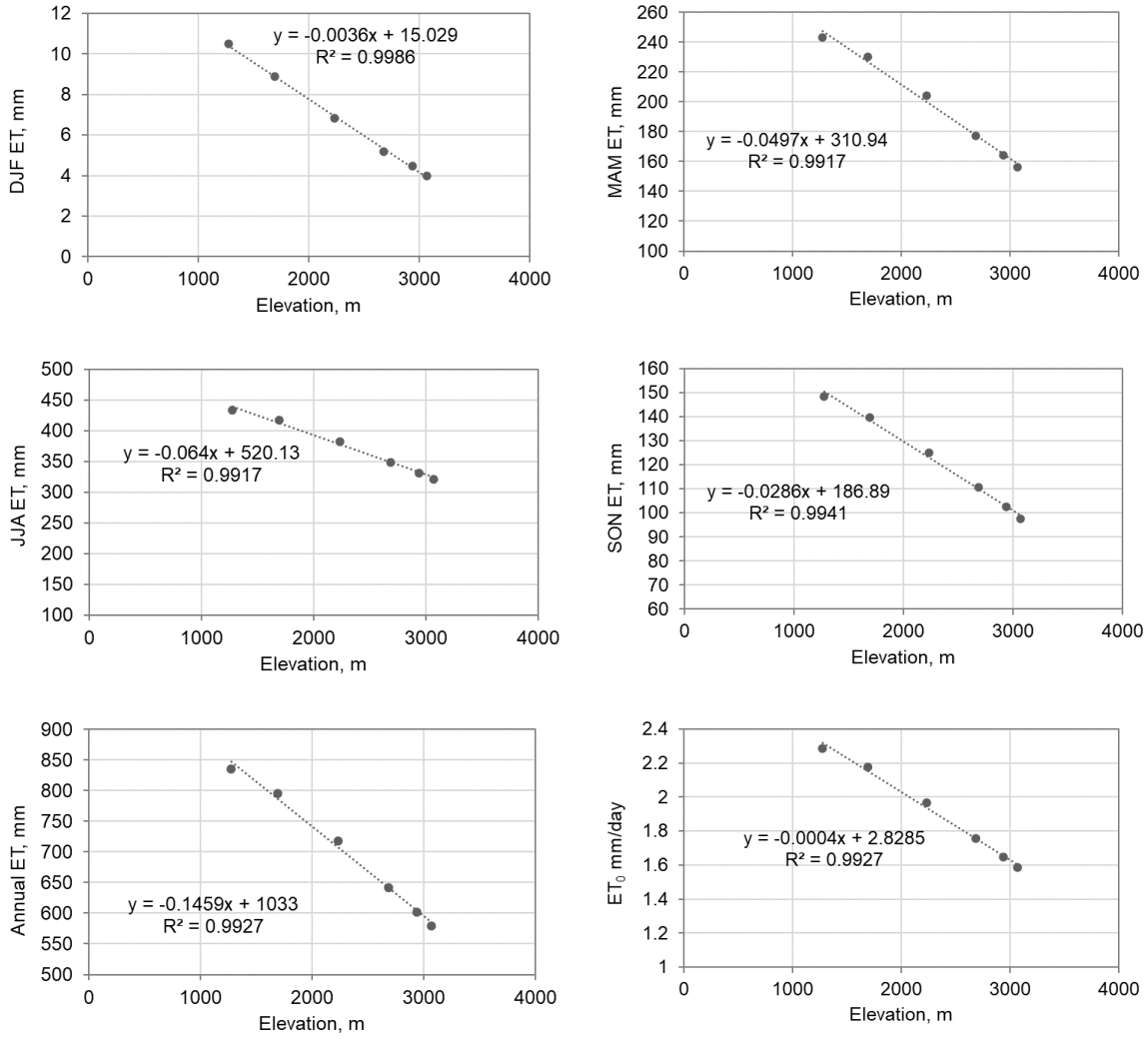

Figure B.3: Lapse rate of annual, seasonal and daily evapotranspiration changes with elevation along the latitude (46.1º-47.3ºN, 91.3ºE) of the Bulgan catchment in the southern Altai Mountains

C. Difference in the projected climate and runoff changes by raw and bias-corrected GCMs and RCMs for the period of 2030-2050

Generally, the mean of raw GCMs projected more precipitation in winter with increases of 21% and 32%, and in autumn with increases of 21% and 22% under RCP4.5 and 8.5, respectively. Moreover, intensive warming of +2.2 and +2.6°C was projected in summer. After post-processing, the mean of GCMs projected more precipitation in spring and autumn, and strong warming in summer and autumn (Figure C.1).

Raw and bias-corrected RCMs projected a larger increase in precipitation for winter by 11% and 47%, and for autumn by 20% and 29% under RCP4.5 and 8.5, respectively. Raw RCM projected spring precipitation to slightly increase (3%); in contrast, bias-corrected RCM projected it to slightly decrease (-1.5%) under RCP4.5. Furthermore, intensive warming of +2.7°C and +3.3°C in spring was projected by both raw and bias-corrected RCMs under RCP4.5 and 8.5, respectively.

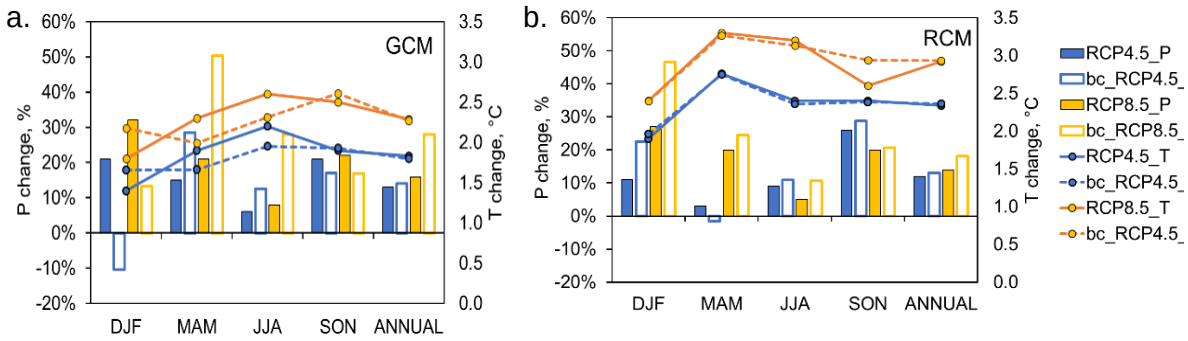

Figure C.1: Projected precipitation and temperature changes in the near future period of 2030-2050 by raw and bias-corrected GCMs (a) and RCMs(b) under RCP4.5 (blue color) and RCP8.5 (orange color) scenarios.

Raw and bias-corrected GCMs projected the same increasing trends in runoffs for all seasons from 2030 to 2050, characterized by a low increase in summer runoff. In addition, raw RCM projected a decrease and the lowest increase in summer runoff; whereas, bias-corrected RCM projected the lowest increase in autumn runoff (Figure C.2, Table 3.37).

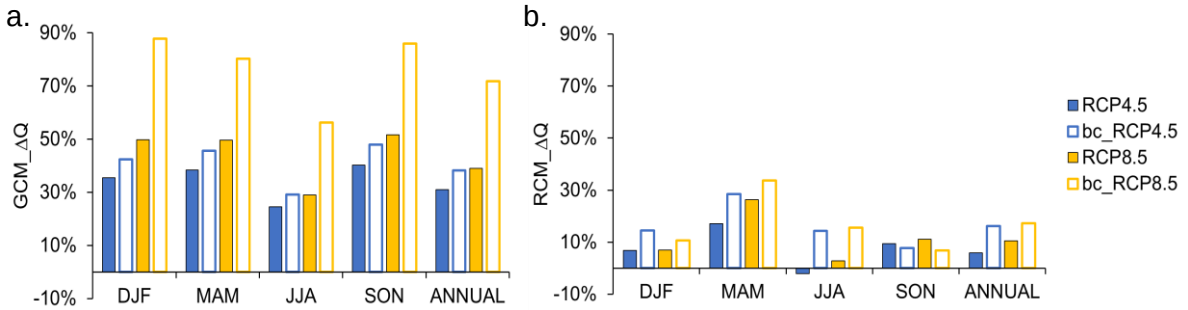

Figure C.2: Projected seasonal runoff changes (%) in near future period of 2030-2050 by raw and bias-corrected GCMs (a) and RCMs(b) under RCP4.5 (blue color) and RCP8.5 (orange color) scenarios.

After the post-processing of RCM data, a lower increase in summer runoff projected by raw RCMs is altered into a higher increase of summer runoff rather than autumn runoff. The signal change in summer runoff can be explained by more precipitation projected in summer by bias-corrected RCM (Figure C.1) since the summer runoff of Bulgan River is largely influenced by summer precipitation (See Chapter 3.3).

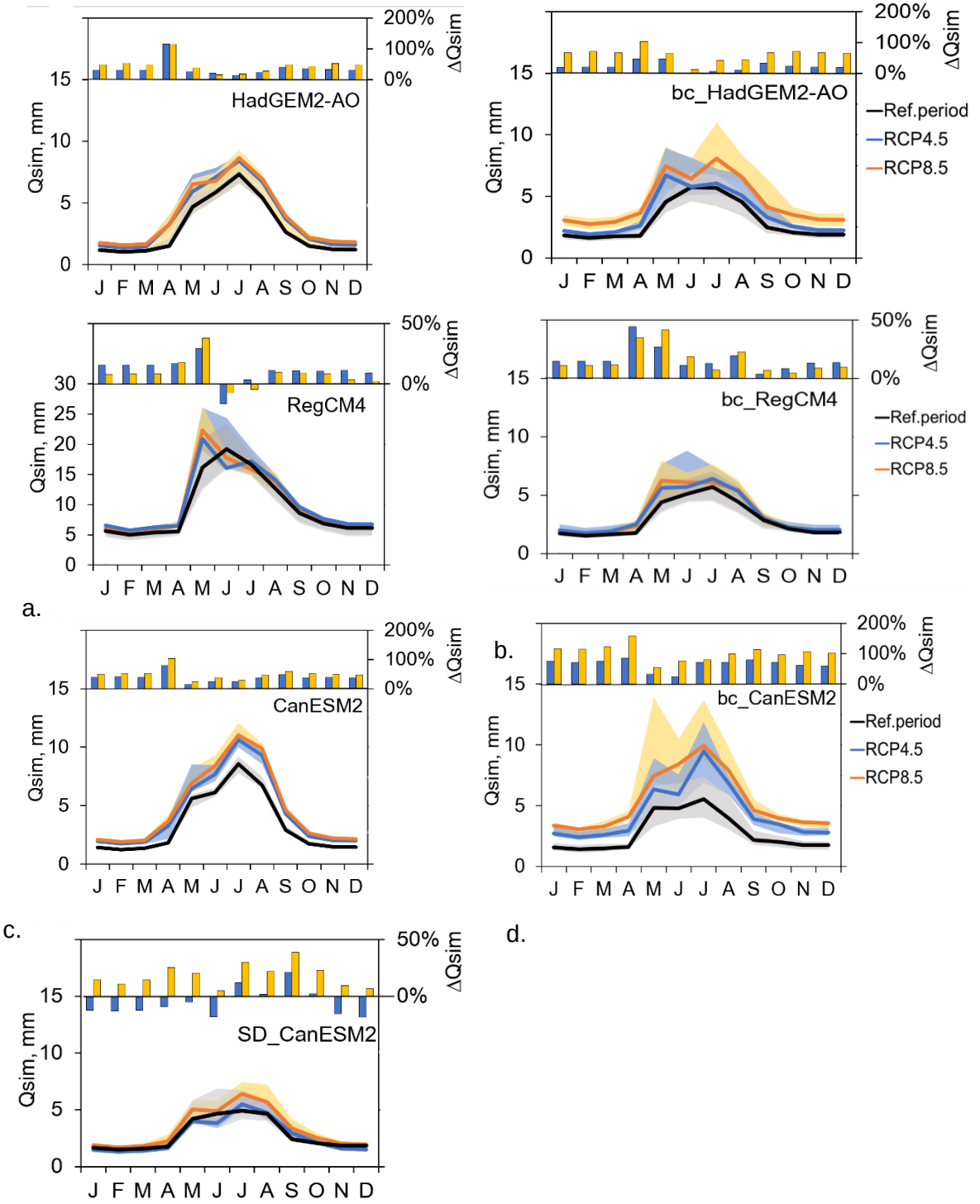

Figure C.3: Comparison of the projected monthly median runoffs (Q_{sim}, mm) and their changes (%) by raw (left panel) and bias-corrected (right panel) GCMs and RCMs for the period of 2030-2050 under RCP4.5 and RCP8.5 scenarios comparing to the reference period of 1985-2005. Shaded bands show a range between the 25th and 75th percentile of the corresponding simulated runoffs for the reference period and RCPs.

Table C.1: Seasonal runoff changes in the near future (2030-2050) under RCP 4.5 and 8.5 compared to the baseline period 1985-2005.

	GCM				RCM			
	Raw		Bias corrected		Raw		Bias corrected	
Seasons	RCP4.5	RCP8.5	RCP4.5	RCP8.5	RCP4.5	RCP8.5	RCP4.5	RCP8.5
Winter	36%	50%	42%	88%	7%	7%	14%	11%
Spring	38%	50%	46%	80%	17%	26%	28%	34%
Summer	24%	29%	29%	56%	-2%	3%	14%	16%
Autumn	40%	52%	48%	86%	9%	11%	8%	7%
Annual	31%	39%	38%	72%	6%	11%	16%	17%